technische universität
dortmund

Dissertation

Strongly interacting Rydberg excitons in Cu_2O

submitted in partial fulfillment of the
requirements for the degree of

Dr. rer. nat.

to the Faculty of Physics of the
TU Dortmund University, Germany

by

Julian Heckötter

Dortmund, July 2020

Accepted by the Faculty of Physics of the TU Dortmund University, Germany.

Day of the oral examination: 2nd October 2020

Examination board:

Prof. Dr. Marc Aßmann
Prof. Dr. Mirko Cinchetti
Prof. Dr. Harald Gießen
Prof. Dr. Heinrich Päs
Dr. Bärbel Siegmann

Summary

Excitons are fundamental electronic excitations in a semiconductor. They are bound states consisting of an electron in the conduction band and a positively charged hole in the valence band. They have hydrogen-like properties and are therefore referred to as the hydrogen analogues in solid states. In the semiconductor Cuprous Oxide, Cu_2O, highly excited states of excitons can be observed with principal quantum numbers up to $n = 25$. These states are called Rydberg excitons in analogy to their atomic counterparts, the Rydberg atoms.

The intention of this thesis is to gain new insights into fundamental properties of these Rydberg excitons by optical spectroscopy. The focus lies on one-photon absorption spectroscopy with high spectral resolution up to 5 nanoelectronvolts. The physics addressed in this thesis can be divided into three main topics.

First, the interaction of Rydberg excitons with high principal quantum numbers n with both external electric and magnetic fields is studied. In the regime of high n, the density of states becomes so large that it becomes unfeasible to use a microscopic theory that explicitly considers every single state. Instead, general n-dependent scaling laws for various fundamental properties of Rydberg excitons are derived theoretically and proven experimentally. These scaling laws provide an efficient description of Rydberg excitons in the high-n regime and give fundamental insights into similarities and differences between Rydberg excitons and Rydberg atoms.

Second, the behavior of Rydberg excitons surrounded by an electron-hole plasma is investigated. For this purpose, absorption spectra are presented, recorded at different densities of free carriers injected into the crystal by an off-resonant pump laser. Carrier densities as low as 0.01 μm^{-3} are found to lead to a lowering of the band gap and the disappearance of the highest exciton lines. A model based on screening of the Coulomb interaction by free charge carriers is presented that allows for a phenomenological description of the data. In this context, the experimental parameter space spanned by excitation power and temperature is investigated to determine the limiting factors for the observation of Rydberg excitons with principal quantum numbers higher than $n_{max} = 25$, the highest Rydberg exciton state observed so far. Indeed, at nanowatt laser powers and millikelvin temperatures, the extension of the observable exciton series to $n_{max} = 28$ is possible.

The third part of this thesis addresses mutual interactions between Rydberg excitons. Combining data from pump-probe experiments with a detailed theoretical model for the shape of these spectra for several exciton interaction mechanisms clearly shows that long-range van der Waals-type interactions are the dominant contribution to interactions between Rydberg excitons.

Zusammenfassung

Exzitonen sind fundamentale elektronische Anregungen in einem Halbleiter. Es handelt sich hierbei um gebundene Zustände aus einem Elektron im Leitungsband und einem positiv geladenen Loch im Valenzband. Aufgrund ihrer wasserstoffähnlichen Eigenschaften werden sie auch als Wasserstoff-Analogon in Festkörpern bezeichnet. In dem Halbleiter Kupferoxydul, Cu_2O, können hoch angeregte Exzitonzustände mit Hauptquantenzahlen bis zu $n = 25$ beobachtet werden. Diese Zustände werden aufgrund ihrer hohen Hauptquantenzahl, in Anlehnung an Rydberg-Atome, als Rydberg-Exzitonen bezeichnet.

Die vorliegende Arbeit befasst sich mit der Untersuchung grundlegender Eigenschaften der Rydberg-Exzitonen mittels optischer Spektroskopie. Der Schwerpunkt liegt dabei auf Ein-Photonen-Absorptionsspektroskopie mit einer hohen spektralen Auflösung von bis zu 5 Nanoelektronenvolt. Generell können die Ergebnisse dieser Arbeit in drei Themengebiete unterteilt werden.

Im ersten Teil wird die Wechselwirkung von Rydberg-Exzitonen hoher Hauptquantenzahlen n sowohl mit externen elektrischen als auch magnetischen Feldern untersucht. Aufgrund der hohen Dichte an Zuständen im Bereich hoher Hauptquantenzahlen wird die Beschreibung des Systems mit einer mikroskopischen Theorie sehr aufwändig. Aus diesem Grund werden hier Skalierungsgesetze zahlreicher exzitonischer Eigenschaften in Abhängigkeit von n entwickelt, die experimentell bestätigt werden können. Diese Gesetzmäßigkeiten erlauben eine einfache Beschreibung von Rydberg-Exzitonen mit hoher Hauptquantenzahl n und ermöglichen tiefere Einblicke in Gemeinsamkeiten und Unterschiede zwischen Rydberg-Exzitonen und Rydberg-Atomen.

Der zweite Teil der Arbeit beschäftigt sich mit der Untersuchung von Rydberg-Exzitonen in der Umgebung eines Elektron-Loch-Plasmas. Zu diesem Zweck werden Absorptionsspektren diskutiert, welche das Verhalten der Rydberg-Exzitonen bei zunehmender Elektron-Loch-Dichte zeigen. Es zeigt sich, dass bereits Dichten von 0.01 μm^{-3} zu einer Absenkung der Bandkante führen, was zu einem Verschwinden der höchsten Exziton-Linien im Spektrum führt. Es wird ein theoretisches Modell, beruhend auf der Abschirmung der Coulomb-Wechselwirkung durch freie Ladungsträger, eingeführt, das es erlaubt, die experimentellen Daten phänomenologisch zu beschreiben. Schließlich wird in diesem Zusammenhang der experimentelle Parameterraum aus Anregungsleistung und Temperatur untersucht, um die limitierenden Faktoren zu finden, welche die höchste beobachtbare Hauptquantenzahl bestimmen. Bei Anregungsleistungen im Bereich von Nanowatt und Temperaturen im Bereich von Millikelvin kann die maximal beobachtbare Hauptquantenzahl auf $n_{\mathrm{max}} = 28$ erweitert werden.

Der dritte Teil der Arbeit zielt auf die Untersuchung von gegenseitigen Wechselwirkungen zwischen Rydbergexzitonen ab. Mit der Kombination von Daten aus Pump-Probe-Messungen und einem theoretischen Modell, das die Berechnung der Linienform dieser Spektren für verschiedene Wechselwirkungs-Mechanismen ermöglicht, kann gezeigt werden, dass zwischen Rydberg-Exzitonen langreichweitige van der Waals-Wechselwirkungen dominieren.

Contents

Chapter 1

Introduction

Atomic spectroscopy played an important role in the development of quantum mechanics at the beginning of the twentieth century [Gal94; Bet+57]. Beginning with the description of spectral lines in the visible spectrum of hydrogen by Balmer in 1885 and the more general classification by Rydberg in 1890, the first model to describe the main characteristics of the hydrogen atom was proposed by Bohr in 1913 [Whi34; Ryd90]. Bohr assumed electrons to move around the atomic core in classical orbits, but restricted their angular momentum to change in an integral multiple n of the reduced Planck's constant $\hbar$ only. The integral multiple n is called the principal quantum number. This leads to discrete radii of the electron orbits and correspondingly also to discrete electron binding energies that depend on the principal quantum number n. While the radii of the orbits increase according to n^2, the binding energies of electrons moving in such orbits decrease as n^{-2}. Hence, transitions between these orbits lead to a series of discrete spectral lines, in accordance with the observations in atomic spectra, as reported by Balmer and Rydberg for example.

Despite its simplicity, the Bohr model is suitable to describe basic physical properties of atoms with an electron excited to a state of high principal quantum number n. These atoms are called Rydberg atoms. Due to their huge radii, Rydberg atoms have large dipole moments and are extremely sensitive to external fields but also to the presence of other Rydberg atoms in their surrounding [Gal+08]. Along with the development of experimental techniques that allow for the cooling and trapping of individual atoms, Rydberg atoms gained enhanced attention in the last two decades due to their mutual interactions. Since they exhibit dipole-dipole interactions that are up to about 10 orders of magnitude larger than those of ground state atoms and that act over large distances of several μm [Urb+09; Rav+14], they became promising candidates to realize quantum logical gates in the field of quantum simulation [Jak+00; Luk+01; Saf+05]. Further, Rydberg atoms gained interest in the fields of nonlinear quantum optics, where they were employed to realize all-optical switching on a single-photon level [Mur+16], and they also present a unique platform to study many-body physics [Bro+20]. In this regard, the investigation of Rydberg atoms nowadays covers a wide range of interesting research fields [Bro+16]. However, while the preparation of tailored atomic systems is possible on a laboratory scale and enables researchers to demonstrate fundamental principles that are relevant to the realization of quantum technology concepts, Rydberg states in solid state systems offer a more application friendly environment.

Such Rydberg excitations can be found in semiconductor systems. In a semiconductor, the fundamental electronic excitations consist of a negatively charged electron in the conduction band and a positively charged hole in the valence band. The electron and the hole form Coulomb-bound states, called excitons, that exhibit an hydrogen-like energy scheme. After

the proposal of the exciton concept by Frenkel [Fre31] and Wannier [Wan37] in the 1930s, they were first observed experimentally by Hayashi and Katsuki [Hay+50; Hay+52] and by Gross and Karryev [Gro+52; Gro56] in the 1950s in the semiconductor Cu_2O. The spectra shown in Ref. [Gro56] already reveal a Rydberg series of states with principal quantum numbers up to $n = 8$. The material Cu_2O is well suited to study highly excited exciton states, as it offers a remarkably high Rydberg energy of about 90 meV compared to other semiconductors, in combination with the availability of high quality natural crystals. In this context, the series of observable excitons in Cu_2O was extended to $n = 12$ in 1996 [Mat+96] and to $n = 25$ in 2014 [Kaz+14], which is by far the highest Rydberg state found in a solid-state environment. Excitons with high principal quantum numbers as large as $n = 25$ are termed Rydberg excitons and have giant extensions up to about 1 μm, covering a volume of one billion unit cells. Akin to their atomic analogues, they are expected to exhibit strong interactions both with external fields and among each other and are therefore ideal candidates to study Rydberg physics in a crystal.

In contrast to atoms, the cubic crystal structure and peculiarities of the valence band dispersion allow for the direct observation of high angular momentum states [The+15] and lead to a fine structure splitting of states with different angular momenta [Uih+81; Sch+16a; Sch+17c; Mun+18]. Furthermore, the dielectric environment of the crystal leads to a Rydberg energy, that is reduced by two orders of magnitude compared to the hydrogen case, which allows one to directly access the whole Rydberg series spectroscopically. Thus, the properties of Rydberg excitons can be studied in a systematic way in dependence on the principal quantum number n. A detailed introduction into the basic concepts of excitons and to the influence of the crystal environment on the excitonic properties is given in Chapter 2. The experimental setup used to study the excitonic Rydberg series is described in Chapter 3.

The high-field regime of the excitonic system, where the interaction energy with external fields exceeds the Coulomb interaction of the bound state, can be reached within comparably low experimental effort due to the reduced Rydberg energy compared to atoms. In this regard, the observation of Rydberg excitons triggered the investigation of quantum chaos in the range of high magnetic fields directly after their discovery [The15; Aßm+16; Fre+17]. Besides the observation of quantum chaos in the high-field regime, experiments in moderate external fields offer the possibility to uncover fundamental properties of Rydberg excitons in both electric and magnetic fields. In this context, high resolution studies of excitons in the low-n regime in external fields have been performed and described theoretically [Sch+17b; Rom+18; Hec+17a]. However, while these theoretical models succeeded to describe the excitonic states in external fields with quantum numbers $n \leq 6$ almost quantitatively, the density of states in the high-n regime, i.e. $n > 6$, becomes too large to calculate solutions of the Hamiltonian in practice.

Therefore, Chapter 4 of this thesis presents an approach for the investigation of Rydberg excitons in the high-n regime subject to electric and magnetic fields. The focus lies on the determination of scaling laws for characteristic quantities of excitons that depend on the principal quantum number n, as these scaling laws allow one to extrapolate physical concepts valid at low n to the high-n regime. Properties, such as the polarizability and the rate of ionization in electric fields, but also the crossing of states and the formation of Landau levels in magnetic fields, are addressed. Scaling laws in dependence on n are well

known for many properties of Rydberg atoms as well [Gal94]. Hence, the scaling laws found for Rydberg excitons are used to explore similarities and differences between excitonic and atomic Rydberg systems.

The strength of interaction of Rydberg states with external fields but also among each other depends directly on the dipole moments of the particular states. Since the dipole moments increase with the principal quantum number as n^2, similar to the radii, states with higher n than $n = 25$ are expected to interact even stronger than the highest excitons observed so far. This assumption directly gives rise to the question of what mechanisms limit the highest observable principal quantum number n_{max} [Höf+14]. Chapter 5 addresses this question within a comprehensive investigation of the influence of an electron-hole plasma on Rydberg excitons. An increasing density of free carriers in a semiconductor is known to result in the Mott effect, which describes a transition of bound exciton states to free electron-hole pairs, due to a band gap renormalization which shifts the continuum edge to lower energies [Mot61; Mot68]. So far, the Mott effect has been studied for excitonic ground states at plasma densities of the order of 10^6 $\mu\mathrm{m}^{-3}$[Man+10]. The system of Rydberg excitons with binding energies below 1 meV allows for the first time for the investigation of the Mott effect of highly excited states in a semiconductor environment and the general behavior of excitons surrounded by a plasma at ultralow densities on the order of 1 $\mu\mathrm{m}^{-3}$ and below. Therefore, in that chapter the impact of such a low-density plasma on the absorption spectra of Rydberg excitons is presented. Further, a model based on the Debye theory is introduced, that allows for an estimation of the relevant plasma densities and a phenomenological description of the data.

Finally, Chapter 6 of this thesis addresses mutual interactions among Rydberg excitons. Indications for strong dipole-dipole interactions, as found in atomic systems, have already been reported for Rydberg excitons along with their discovery in Ref. [Kaz+14]. The huge interaction strength between two Rydberg excitons leads to a spectral shift of the pair state resonance energy. If the shift is larger than the linewidth of the excitation light source, it becomes impossible to excite the Rydberg exciton pair state. As the dipole-dipole interaction depends on the distance between the two corresponding excitons, the existence of a Rydberg exciton can prevent the excitation of a second one within a certain volume. This is called the Rydberg blockade. The concept of the excitonic Rydberg blockade motivated various proposals that suggested to use Rydberg excitons to strongly enhance optical nonlinearities [Zie+16; Wal+18a] or as single-photon emitters based on Rydberg blockade [Kha+17]. However, while indications of the Rydberg blockade were found in Ref. [Kaz+14], it was not possible to reveal the exact type of the underlying interaction potential. Therefore, in Chapter 6, a different experimental approach than in Ref. [Kaz+14] is presented, that allows for the determination of the type of interaction potential and to rule out other possible candidates for the underlying interaction mechanism. Not only the distinction between two different potentials that describe exciton-exciton interactions but also the differentiation between an exciton-exciton and exciton-plasma interaction becomes possible within the discussed approach.

Chapter 2

Absorption spectroscopy in Cu_2O

In this chapter, all basic concepts that are necessary to understand linear absorption spectroscopy in Cu_2O are summarized. First, light-matter interaction is discussed with a focus on the electric-dipole approximation in one-photon absorption. In Sec. 2.2, detailed information about the material system Cu_2O is given with a focus on its optical properties at low temperatures. In Sec. 2.3, the concept of excitons is introduced and deviations of the excitonic energy spectrum from the hydrogen-like model are discussed with a comparison to atomic physics. Next, selection rules for optical transitions are given in Sec. 2.4 to provide an explanation of the appearance of absorption features. Finally, in Sec. 2.5, the main spectroscopic features observable in one-photon absorption are demonstrated with an exemplary high-resolution absorption spectrum of the whole yellow exciton series.

2.1 Interaction of light with matter

In this section, the interaction of light with matter is briefly summarized based on the descriptions in [Kli07]. We consider an electronic system with a ground state $|\Psi_i\rangle$ and an excited, or final, state $|\Psi_f\rangle$ as for example a two-level atom, or the electronic bands of a semiconductor. We are interested in the transition rate of an electron from the ground state to the excited state under the influence of an electromagnetic field. The light field is treated perturbatively as it results only in small changes of the eigenenergies and eigenstates. Therefore, the transition rate is given by Fermi's Golden rule

$$w_{if} = \frac{2\pi}{\hbar}|H_{if}|^2 D(E) \ , \tag{2.1}$$

with the transition matrix element $H_{if} = \langle \Psi_f | H | \Psi_i \rangle$ and the density of final states $D(E)$ as a function of energy E. H is the Hamiltonian of the system. For a single electron of mass m_e and momentum $\mathbf{p}_\mathrm{e}$ in an electrostatic potential $V(\mathbf{r})$, it is given by

$$H_{e,0} = \frac{\mathbf{p}_\mathrm{e}^2}{2m_\mathrm{e}} + V(\mathbf{r}) \ . \tag{2.2}$$

The interaction of the electron with the light field is obtained by minimal substitution $\mathbf{p}_\mathrm{e} \rightarrow \mathbf{p}_\mathrm{e} + e\mathbf{A}$ with the elementary charge e and the vector potential $\mathbf{A}$ of the electromagnetic wave. The Hamiltonian then reads

$$H_e = \frac{1}{2m_\mathrm{e}} \left(\mathbf{p}_\mathrm{e} + e\mathbf{A}\right)^2 + V(\mathbf{r}) \ . \tag{2.3}$$

With $\mathbf{p}_\mathrm{e} = \frac{\hbar}{i}\nabla$ ($\hbar$ being the reduced Planck constant) and the Coulomb gauge $\nabla \cdot \mathbf{A} = 0$ one obtains

$$\begin{aligned} H_e &= \frac{1}{2m_\mathrm{e}}\left(-\hbar^2\nabla^2 + \frac{\hbar}{i}e\mathbf{A}\nabla + e^2\mathbf{A}^2\right) + V(\mathbf{r}) \\ &= H_{\mathrm{e},0} + \frac{e}{m_\mathrm{e}}\mathbf{A}\cdot\mathbf{p}_\mathrm{e} + \frac{e^2}{2m_\mathrm{e}}\mathbf{A}^2 \ . \end{aligned} \tag{2.4}$$

The vector potential is given by

$$\mathbf{A} = A_0\hat{\mathbf{e}}\cdot e^{i(\mathbf{kr}-\omega t)} \ , \tag{2.5}$$

with an amplitude A_0 and a unit vector defining the direction of polarization $\hat{\mathbf{e}}$. Further, $\mathbf{k}$ is the wave vector with $k = |\mathbf{k}| = \frac{2\pi}{\lambda}$ and ω is the frequency of the electromagnetic wave.

To treat the light field perturbatively, we assume the amplitude of $\mathbf{A}$ to be small. Thus, the last term in Eq. (2.4) can be neglected and we focus on the linear regime. This is given by the second term $H_1 = \frac{e}{m_\mathrm{e}}\mathbf{A}\cdot\mathbf{p}_\mathrm{e}$, that is the first-order perturbation term relevant for the transition in Eq. (2.1):

$$w_{if} = \frac{2\pi}{\hbar}\left|\langle\Psi_f|\,H_1\,|\Psi_i\rangle\right|^2 D(E) = \frac{2\pi}{\hbar}\left|\left\langle\Psi_f\middle|\,\frac{e}{m_\mathrm{e}}\mathbf{A}\cdot\mathbf{p}_\mathrm{e}\,\middle|\Psi_i\right\rangle\right|^2 D(E) \ . \tag{2.6}$$

In the visible spectral range, the wavelengths $\lambda \approx 500$ nm are much larger than the relevant spatial dimensions, that are of the order of the lattice constant $r \approx a_\mathrm{l} \approx 5$ Å, and one finds for the product $k\cdot r = \frac{2\pi}{5000\ \text{Å}}\cdot 5\ \text{Å} = 2\pi\cdot 10^{-3}$. Therefore, we can expand $\mathbf{A}$ in orders of $\mathbf{kr}$ and stop after the second term

$$e^{i\mathbf{kr}} = 1 + \frac{i\mathbf{kr}}{1!} + \frac{(i\mathbf{kr})^2}{2!} + ... \approx 1 + \frac{i\mathbf{kr}}{1!} \ . \tag{2.7}$$

Thus, we find for the transition matrix element of (2.6)

$$H_{if} = \langle\Psi_f|\,H_1\,|\Psi_i\rangle \approx \frac{eA_0}{m_0}\langle\Psi_f|\,(\hat{\mathbf{e}}\cdot\mathbf{p})\,|\Psi_i\rangle + \frac{ieA_0}{m_0}\langle\Psi_f|\,(\hat{\mathbf{e}}\cdot\mathbf{p})(\mathbf{k}\cdot\mathbf{r})\,|\Psi_i\rangle \ . \tag{2.8}$$

This yields the different orders of possible optical transitions in one-photon absorption. The first term describes electric-dipole transitions while the second term includes magnetic-dipole and electric-quadrupole transitions. Typically, only the first term is considered. This is called the dipole approximation [Ell61]. Within the point group O_h, the electric-dipole operator transforms according to Γ_4^-, the electric-quadrupole operator transforms according to $\Gamma_3^+ \oplus \Gamma_5^+$ and the magnetic-dipole operator according to Γ_4^+. These relations will be used in Sec. 2.4 to develop selection rules for optical transitions.

2.2 Crystal structure of Cu_2O

Cuprous Oxide (chemical sum formula Cu_2O) is one of the oxides of copper. It is found in nature as the mineral cuprite appearing in a reddish color. An example of a μm-thin slab is shown in Fig. 2.1 (a). It crystallizes in a centrosymmetric cubic structure and can be described according to symmetry operations of the point group O_h [Mad+98]. One

possible unit cell consists of 4 copper atoms and 2 oxygen atoms as shown schematically in Fig. 2.1 (b). The copper atoms form a face-centered cubic (fcc) lattice, whereas the oxygen atoms form a body-centered cubic (bcc) lattice, shifted along the diagonal relative to the copper lattice by a quarter of the diagonal's length [Dah+66]. The lattice constant is $a_l = 4.26$ Å[Mad+98]. The optical properties considered here result from the electronic

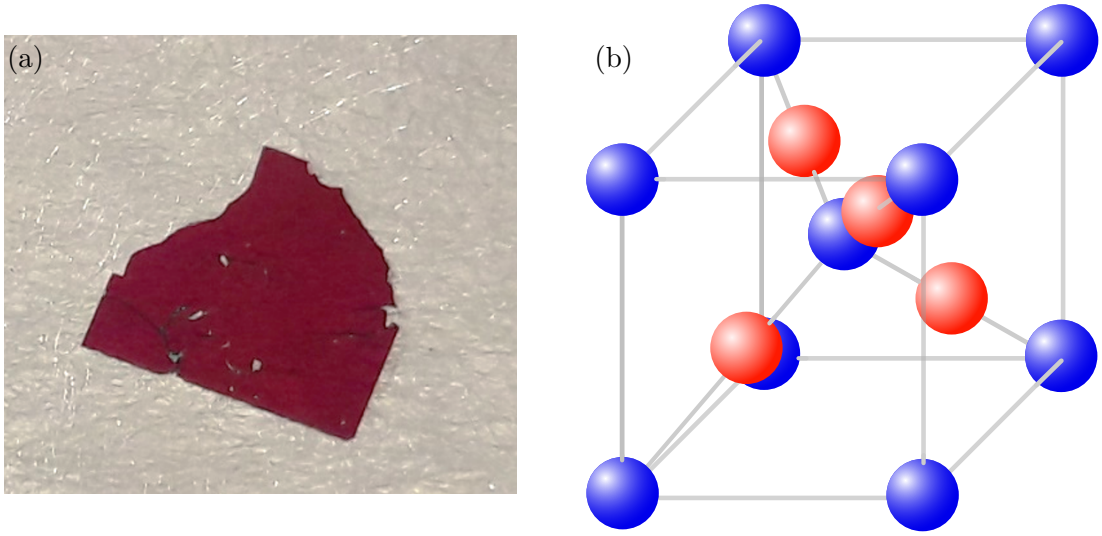

Figure 2.1 (a) Photo of a reddish shimmering crystal slab of Cu_2O with a thickness of 30 μm. (b) The unit cell of Cu_2O. Red spheres represent copper atoms in an fcc lattice, blue spheres represent oxygen atoms in a bcc lattice.

properties of the valence and conduction bands at the Γ point. Several band structure calculations of Cu_2O have been made starting with the work of [Dah+66] followed by [Kle+80] and [Rob83] and many others. The relevant dispersion of the band structure used here was finally calculated using density functional theory in [Fre+09]. For further band structure calculations, see references therein. The main properties of the electronic band structure will be summarized here, according to the works mentioned before.

In the following and throughout this work, we will use the notation of [Kos+66] to denote the symmetry representations of electronic bands, excitonic states and operators. Due to the centrosymmetry of Cu_2O, parity is a good quantum number that will be denoted by the upper indices + and - for positive and negative parity under inversion.

A schematic presentation of the relevant electronic bands is shown in Fig. 2.2 (a). The upper two valence bands stem from the fivefold degenerate copper 3d orbitals. They are split by the crystal field into the upper Γ_5^+ and lower Γ_3^+ bands. The lowest conduction band stems from copper as well, but from the copper 4s orbitals that are represented by Γ_1^+ in the crystal field. The next higher conduction band stems from copper 4p orbitals that are transformed into Γ_3^- symmetry [Rob83].

Including spin-orbit coupling (see Sec. 2.3.1), the states split further, now described by the double groups. The splitting is obtained by multiplying the symmetries mentioned above with Γ_6^+, which is the spin representation in O_h symmetry. As a result, the uppermost valence band splits into the high-lying Γ_7^+ band and the lower-lying Γ_8^+ band [Kle+80].

The Bloch amplitudes of the Γ_7^+ band read according to [Kos+66][1], ($\Gamma_5 \otimes \Gamma_6$), cf. [Hec+17a]:

$$|\Gamma_7^+, +1/2\rangle = |\uparrow_H\rangle = -\frac{1}{\sqrt{3}}\left[\left(U_x + iU_y\right)|\downarrow_h\rangle - U_z\,|\uparrow_h\rangle\right] \ , \tag{2.9}$$

$$|\Gamma_7^+, -1/2\rangle = |\downarrow_H\rangle = -\frac{1}{\sqrt{3}}\left[\left(U_x - iU_y\right)|\uparrow_h\rangle + U_z\,|\downarrow_h\rangle\right] \ . \tag{2.10}$$

Here, U_i, $i = x, y, z$ are the orbital Bloch amplitudes of the valence band which transform as $\Gamma_{5,yz}$, $\Gamma_{5,xz}$, $\Gamma_{5,xy}$ and $\uparrow_h$ and $\downarrow_h$ denote the hole spins $\pm 1/2$.

Analogue expressions can be found for the Γ_8^+ band, but are not of importance in this work. The Γ_8^+ band is shifted to lower energies by the split-off energy of $\Delta_{\mathrm{so}} = 131$ meV [Sch+16a]. Note that this value varies slightly in literature between 127.3 meV in [Fre+09] and 133.8 meV in [Uih+81]. It was shown in [Fre+09], that the spin-orbit coupling leads to an important deviation of the pure parabolic dispersion of the uppermost valence band as indicated in Fig. 2.2 (b). Next, the Γ_1^+ conduction band is described via Γ_6^+ within the double group, whereas the higher Γ_3^- band is transformed into Γ_8^-.

These energy bands result in optical band-to-band transitions, as shown in Fig. 2.2 (b). Transitions from the uppermost valence band to the lowest conduction band belong to the yellow series with a band gap of 2.17208 eV [Kaz+14]. Transitions from the second highest valence band to the lowest conduction band build the green series with a band gap of $E_{\mathrm{g}}^g = 2.3023$ eV [Ito+75]. Excitations from the highest valence band to the second lowest conduction band are called the blue series, with a gap energy of $E_{\mathrm{g}}^b = 2.6336$ eV [Tak+18] and those from the second highest valence band to the second lowest conduction band are called violet transitions, with $E_{\mathrm{g}}^v = 2.756$ eV [Dau+66].

2.3 The concept of excitons

When light of suitable energy is absorbed by an electron in a valence band of a semiconductor, the electron is excited to a state of higher energy in a conduction band. Simultaneously, a hole is created in the valence band. The description here is restrained to the effective-mass approximation, i.e. the restriction to transitions in the vicinity of the Γ point or to small values of the light's wave vector $\mathbf{k}$, respectively. Within this approximation, one assumes parabolic band dispersions meaning that electron and hole are treated as free particles with $\mathbf{k}$-independent effective masses m_{e} and m_{h}. Electron and hole interact via Coulomb interaction and form hydrogen-like bound states with quantized energy levels below the band gap E_{g}. These quantized states are called excitons. Their motion can be separated in a center-of-mass motion and a relative motion of electron and hole. In this approximation, the Hamiltonian is given by

$$H_0 = E_{\mathrm{g}} + \frac{\hbar^2}{2M}\nabla_{\mathbf{R}}^2 + \frac{p^2}{2\mu} + V(\mathbf{r}) \ . \tag{2.11}$$

The second term is the kinetic energy of the center of mass $\mathbf{R} = (m_{\mathrm{e}}\mathbf{r}_{\mathrm{e}} + m_{\mathrm{h}}\mathbf{r}_{\mathrm{h}})/(m_{\mathrm{e}} + m_{\mathrm{h}})$ with the total mass $M = m_{\mathrm{e}} + m_{\mathrm{h}}$. Here, $\mathbf{r}_{\mathrm{e}}$ and $\mathbf{r}_{\mathrm{h}}$ denote the coordinates and m_{e} and m_{h} denote the masses of the single particles. The third term describes the relative motion of

[1] Note that they are shifted in phase by (-i)

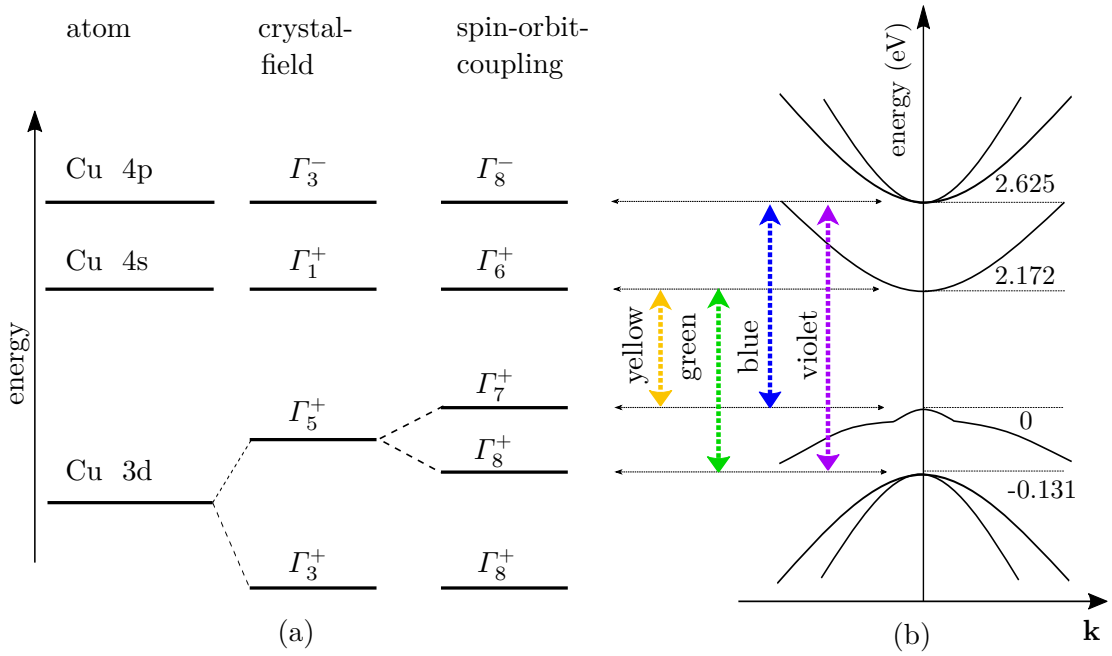

Figure 2.2 (a) Splitting of atomic orbitals into valence and conduction bands. (b) Scheme of dispersion relations of the four most important bands at the Γ point and corresponding band-to-band transitions. The uppermost valence band shows a deviation of a pure parabolicity, according to Refs. [Fre+09; Sch+16a].

electron and hole with the reduced mass $\mu^{-1} = m_e^{-1} + m_h^{-1}$ and momentum $\mathbf{p}$. The fourth term is the Coulomb potential given by

$$V(r) = -\frac{e^2}{4\pi\epsilon_0\epsilon_s r} \ , \tag{2.12}$$

with the vacuum permittivity ϵ_0 and the static dielectric constant ϵ_s reducing the Coulomb potential in material, compared to vacuum. For Cu_2O, one finds $\epsilon_s = 7.5$ [Hod+76]. The distance between electron and hole is given by $r = |\mathbf{r}| = |\mathbf{r}_e - \mathbf{r}_h|$. The Hamiltonian in Eq. (2.11) will be extended in Sec. 2.3.1.

The energy dispersion of an exciton in this approximation is given by

$$E_X = E_g + E_n^b + E_{kin} \ . \tag{2.13}$$

The second term is the excitonic binding energy

$$E_n^b = -\frac{Ry}{n^2} \ , \tag{2.14}$$

with the excitonic Rydberg energy Ry and the principal quantum number n. Ry is given by the atomic Rydberg energy $Ry_H = 13.6$ eV, modified by μ and ϵ_s:

$$Ry = \frac{\mu}{m_0}\frac{1}{\epsilon_s^2}\frac{m_0 e^4}{2(4\pi\epsilon_0\hbar)^2} = \frac{\mu}{m_0}\frac{1}{\epsilon_s^2}Ry_H \ . \tag{2.15}$$

Here, m_0 is the free electron mass. The quadratic dependence on n results in a hydrogen-like energy ladder in the spectra.

The last term in Eq. (2.13) describes the center-of-mass kinetic energy with the exciton wave vector $\mathbf{K} = \mathbf{k}_\mathrm{e} + \mathbf{k}_\mathrm{h}$

$$E_\mathrm{kin} = \frac{\hbar^2 \mathbf{K}^2}{2M} \ . \tag{2.16}$$

For the yellow series, the masses are given by $m_\mathrm{e} = 0.985\ m_0$, $m_\mathrm{h} = 0.575\ m_0$ and $M = 1.56\ m_0$ [Nak+12]. Note that these are actually polaron masses.

With increasing principal quantum number n not only the binding energy decreases but also the average distance between electron and hole increases. It is given by

$$\left\langle r_{n,l} \right\rangle = \frac{a^\mathrm{B}}{2}[3n^2 - l(l+1)] \ , \tag{2.17}$$

with the excitonic Bohr radius given by

$$a^\mathrm{B} = \frac{m_0}{\mu}\epsilon_s a_\mathrm{H}^\mathrm{B} \tag{2.18}$$

and the angular momentum quantum number l. The excitonic Bohr radius is increased by μ and ϵ_s compared to the hydrogen value $a_\mathrm{H}^\mathrm{B} = 0.53$ Å [Gru06].

For Cu_2O, the Rydberg energy of the yellow series is about 90 meV [Kaz+14]. The excitonic Bohr radius can be expressed in terms of the Rydberg energy

$$a^\mathrm{B} = \frac{1}{2}\frac{e^2}{4\pi\epsilon_0\epsilon_s Ry} \ , \tag{2.19}$$

which yields $a^\mathrm{B} = 1.11$ nm. The values of Ry and a^B given above hold for states with $n \geq 2$, but deviate for $n = 1$ as discussed in the next section. For highly excited Rydberg excitons, one finds an average distance between electron and hole up to $r_{25P} \approx 1\ \mu$m for $n = 25$.

The wave function of an exciton is given by the center-of-mass movement and the product of the electron's wave function in the conduction band with the hole's wave function in the valence band times their envelope function

$$\Psi_{nlm}(\mathbf{K}, \mathbf{r}) = \Omega^{-1/2}\ e^{i\mathbf{KR}}\ \Phi_\mathrm{e}(\mathbf{r}_\mathrm{e})\ \Phi_\mathrm{h}(\mathbf{r}_\mathrm{h})\ \Phi_{nlm}^\mathrm{env}(\mathbf{r}) \ . \tag{2.20}$$

The center-of-mass movement is described with a plane wave $e^{i\mathbf{KR}}$ and a normalization factor $\Omega^{-1/2}$. The envelope function $\Phi_{nlm}^\mathrm{env}(\mathbf{r})$ describes the relative motion of electron and hole. In spherical approximation without any crystal symmetries, it contains spherical harmonics in analogy to the solutions of the hydrogen problem. Hence, the relative motion of electron and hole is classified by angular momentum quantum numbers l and m, with $l = 0, 1, 2, ...n-1$, and can be described by S-, P-, D-...like states. Strictly speaking, the angular momentum is no longer a good quantum number in a crystal and the relative motion has to be described by irreducible symmetry representations, given by the symmetry of the material. Nevertheless, the excitonic states are usually labeled by their corresponding spherical counterpart.

2.3.1 Deviations from the hydrogen model

The excitonic energies of the yellow series in Cu_2O show deviations from the pure hydrogen-like energy ladder, in particular for low n. The degeneracy of states with the same n but different angular momenta is lifted by several effects which spread the levels over a certain energy range for a particular n. The corresponding effects are described by correction terms added to the hydrogen-like Hamiltonian H_0 (Eq. (2.11)) and shall be briefly described in this section.

We follow the notation of Refs. [Uih+81] and [The+15] in cgs- and reduced units, respectively. Further detailed descriptions are given in Refs. [Sch+16c; Sch+17c].
The Hamilton reads

$$H = H_0 + H_{\mathrm{so}} + H_{\mathrm{d}} + H_{\mathrm{exch}} \ . \tag{2.21}$$

The first new term, H_{so}, describes the spin-orbit coupling between the hole spin $\mathbf{s}_{\mathrm{h}}$ ($s_{\mathrm{h}} = 1/2$) and the quasi spin $\mathbf{I}$ (I=1) of the threefold valence band to an effective hole spin $\mathbf{j} = \mathbf{I} + \mathbf{s_h}$ with quantum numbers $j = |I \pm s_{\mathrm{h}}|$. It is given by

$$H_{\mathrm{so}} = \frac{2}{3}\bar{\Delta}\,(1 + \mathbf{I}\cdot\mathbf{s}_{\mathrm{h}}) \tag{2.22}$$

and leads to the splitting of the Γ_5^+ band into Γ_7^+ ($j = 1/2$) and Γ_8^+ ($j = 3/2$) valence bands. $\bar{\Delta} = \Delta_{\mathrm{so}}/Ry^*$ is the splitting amplitude in units of the excitonic Rydberg $Ry^* = e^4 m_0/(2\hbar^2\epsilon_s^2\gamma_1')$ with $\gamma_1' = \gamma_1 + m_0/m_e$ and the first Luttinger paramter γ_1. The term gives rise to the yellow and green series and leads to the non-parabolic dispersion discussed above of the uppermost valence band (Fig. 2.2)

The H_{d} term consists of a spherical (first line) and a cubic term (second line) and was introduced in [Bal+73; Bal+74]

$$\begin{aligned} H_{\mathrm{d}} = &-\frac{1}{3\hbar^2}\mu\left(P^{(2)}\cdot I^{(2)}\right) + \\ &\frac{1}{3\hbar^2}\delta_{\mathrm{cubic}}\left(\sum_{k=\pm 4}[P^{(2)}\times I^{(2)}]_k^{(4)} + \frac{1}{5}\sqrt{70}[P^{(2)}\times I^{(2)}]_0^{(4)}\right) \ , \end{aligned} \tag{2.23}$$

with $\mu = (6\gamma_3 + 4\gamma_2)/(5\gamma_1')$, $\delta = (\gamma_3 - \gamma_2)/\gamma_1'$ and the second and third Luttinger parameters γ_2 and γ_3. Further, $P^{(2)}$ and $I^{(2)}$ denote the second rank irreducible tensors of $\mathbf{p}$ and $\mathbf{I}$.

The H_{d} term mixes states of the yellow and green series. In spherical approximation ($\delta_{\mathrm{cubic}} = 0$), it further couples the valence band spin $\mathbf{j}$ with the relative motion of the exciton, described by the angular momentum operator $\mathbf{l}$ ($l = 0, 1, ..., n-1$). This coupling introduces a fine structure splitting for states with $l > 0$, that can be described in terms of a total angular momentum $\mathbf{f} = \mathbf{j} + \mathbf{l}$ with quantum numbers $f = |j - l|, ..., |j + l|$. Now, the particular states can be denoted by the usual terminology for atomic states of the form ${}^vL_f$, with a capital L for the angular momentum quantum number and the multiplicity $v = 2j + 1$ that denotes the yellow ($j = 1/2$, $v = 2$) and green ($j = 3/2$, $v = 4$) series. Since we are interested mainly in the yellow series here, we will neglect the index v. So far, the relevant states read $S_{1/2}$, $P_{1/2}$, $P_{3/2}$, $D_{3/2}$, $D_{5/2}$, $F_{5/2}$, $F_{7/2}$, ...

The tensor products in H_{d} lead to terms in the fourth order of $\mathbf{p}$ that describe deviations from the parabolic dispersion of the valence band. This can be understood with a descriptive example given in [Kav+97]: In tight-binding approximation, the valence band dispersion

relation is given by $E(k) \propto \cos(|\mathbf{k}|a)$. The expansion of the cosine function around $|\mathbf{k}| = 0$ leads to the typical quadratic dependence of the dispersion on $\mathbf{k}$ or $\mathbf{p}$, respectively. The next non-vanishing term is of the order p^4. The energy deviations due to the non-parabolicity of the valence band can be summarized by incorporating a quantum defect parameter $\delta_{n,l}$ in the binding energy $E^{\mathrm{b}}_{n,l}$ [Sch+16a; Sch+16b], in analogy to atomic physics [Gal94], giving the corrected energy dispersion:

$$E_X = E_{\mathrm{g}} - \frac{Ry}{(n-\delta_{n,l})^2} + \frac{\hbar^2\mathbf{K}^2}{2M} \ . \tag{2.24}$$

In atomic physics, the quantum defect $\delta_{n,l}$ appears in the description of non-hydrogenic atoms. An electron in a low-l state feels a deviation from the pure $1/r$ core potential, since the field is partially shielded by the remaining core electrons. For states with higher l, the probability to find the electron in the vicinity of the core decreases and these states are less affected by these deviations. This leads to an increase of the binding energy for states with low l in atoms.

Coming back to the excitonic case, the cubic symmetry of the crystal is considered by values $\delta_{\mathrm{cubic}} \neq 0$ and leads to an additional fine structure splitting of states, in particular into two lines for $D_{5/2}$ and into three lines for F excitons (see Sec. 2.5). In this case, f is not a good quantum number anymore and the eigenstates have to be described by the irreducible representations $\Gamma_i^{\pm}$ of the O_h group (see Sec. 2.4).

Finally, the term H_{exch} accounts for the electron-hole exchange interaction. It is relevant for S-like states ($l = 0$) or states that are mixed with these, i.e. D states in particular. The exchange interaction is given by

$$H_{\mathrm{exch}} = \bar{J}_0 \left(\frac{1}{4} - \mathbf{s}_{\mathrm{e}} \cdot \mathbf{s}_{\mathrm{h}}\right) \delta(\mathbf{r}) \ , \tag{2.25}$$

with its magnitude $\bar{J}_0 = \frac{J_0 \Omega}{R^* a^*}$, whereby J_0 is the exchange integral. Ω is the volume of the unit cell and $a^* = \frac{\hbar^2 \epsilon_0 \gamma_1'}{e^2 m_0}$. Further, $\mathbf{s}_{\mathrm{e}}$ is the electron spin. The last term, $\delta(\mathbf{r})$, gives contributions for states with non-vanishing probability density at $\mathbf{r} = 0$ only, i.e. states with an S contribution. For these states, the electron spin has to be considered within a new total angular momentum $\mathbf{f}_{\mathrm{tot}} = \mathbf{f} + \mathbf{s}_{\mathrm{e}}$ and quantum numbers $f_{\mathrm{tot}} = |f \pm s_{\mathrm{e}}|$. In particular, this term leads to the splitting of the ground state ($n = 1$) into a Para- ($f_{\mathrm{tot}} = 0$) and an Ortho-exciton ($f_{\mathrm{tot}} = 1$), see Sec. 2.4. These states are denoted by $L_f^{f_{\mathrm{tot}}}$, following the notation in Ref. [Uih+81], which reads $S_{1/2}^{(0)}$ for the S Para-exciton and $S_{1/2}^{(1)}$ for the S Ortho-exciton. The Ortho-exciton is shifted to higher energies by 12.117 meV [Hög+05] above the Para-exciton, caused by the analytic part of the exchange interaction H_{exch} [Kuw+77; Uih+81; Sch+16e]. But also states with $n \neq 1$ are affected by the exchange interaction, as for example the $3D$ states. Similar to the $S_{1/2}^{(1)}$ Ortho-exciton, the $D_{3/2}^{(1)}$ Ortho-exciton is shifted to higher energies as well. It is shifted even beyond the energy of F states and determines the highest energy of a multiplet (see Fig. 4.1 in Sec. 4.1).

Finally, S states with $n = 1$ are even more affected by correction terms due to their small size which is comparable to the lattice constant and the polaron radii [Kli07]. The resonance energy of the $1S$ Ortho-exciton is 2.03279 eV (see Fig. 2.3), resulting in a deviating Rydberg energy of $Ry_{1S} = 2.17208\ \mathrm{eV} - 2.03279 = 139.3$ meV. The Bohr radius is then found to be

smaller than the value mentioned previously with $a_{1S}^{\mathrm{B}} \approx 7$ Å $\approx 1.6 \cdot a_1$. This deviation results from a modified dielectric constant that varies between ϵ_s and the background dielectric constant ϵ_b. The small extensions of the $1S$ exciton wave functions in real space result further in a widely spread wave function in **k**-space. A description with parabolic energy dispersions (effective mass approximation) does not hold anymore and higher terms in k modify the exciton mass. Away from the zone center the bands typically flatten and the mass becomes heavier [Kav+97]. Hence, the $1S$ exciton mass is found to be $M_{1S} = 2.61\ m_0$ [Bra+07]. These deviations are typically accounted for within so called central-cell corrections. A detailed theoretical treatment is given in [Sch+17c].

All these corrections affect states with different total quantum number f_{tot} differently which leads to various deviations from the pure hydrogen series. The resulting multiplet widths are investigated theoretically and experimentally with help of external electric fields in Ch. 4. All energies of the experimentally accessible states are shown in Fig. 2.5.

2.4 Optical selection rules

Using the symmetries of the electronic energy bands and of the transition operators in Eq. (2.8) allows one to set up selection rules for optical transitions between certain energy bands. Obviously, a transition is forbidden, if the matrix element in Eq. (2.8) is zero. If it is non-zero, the transition is in principal allowed. Note that it can still show only a small oscillator strength. According to group theory, it is non-zero if the symmetry of the final state $|\Psi_f\rangle$ is contained in the direct product of the symmetries of the initial state $|\Psi_i\rangle$ and the perturbation operator H_1: $\Gamma_f \in \Gamma_{H_1} \otimes \Gamma_i$ [Kli07]. In particular, this rule can be used for the analysis of excitonic excitations as well. For optical transitions, the initial state is given by the ground state of the crystal, that has Γ_1^+ symmetry according to the O_h symmetry group, and the final state is the exciton. According to Eq. (2.20) the symmetry of an exciton is given by the direct product of the involved bands times the symmetry of electron's and holes's relative motion

$$\Gamma_X = \Gamma_{\mathrm{c}} \otimes \Gamma_{\mathrm{v}} \otimes \Gamma_{\mathrm{env}} \ . \tag{2.26}$$

The indices c and v denote the conduction and valence band, respectively. Hence, we have to consider the symmetry of matrix elements $\langle \Gamma_X | \Gamma_{H_1} | \Gamma_1^+ \rangle$. For dipole transitions, the final state must contain a Γ_4^- representation. For quadrupole transitions, we need either Γ_3^+ or Γ_5^+ representations in the symmetry of the final state.

For S-type excitons the envelope is represented by $\Gamma_{\mathrm{env}} = \Gamma_1^+$ and does not change the symmetry. Thus, their total symmetry is directly given by the involved bands. We now consider S excitons of the yellow series, i.e. transitions involving the uppermost Γ_6^+ band and the lowest Γ_7^+ band. Their symmetry is then given by

$$\Gamma_S = (\Gamma_6^+ \otimes \Gamma_7^+) \otimes \Gamma_1^+ = \Gamma_2^+ \oplus \Gamma_5^+ \ . \tag{2.27}$$

Since the Γ_1^+ contribution does not change the wave function, the states can be easily expressed by their valence band and conduction band constituents, considering the multi-

plication $|\Gamma_7^+, \pm 1/2\rangle \otimes |\Gamma_6^+, \pm 1/2\rangle$, where $|\Gamma_7^+, \pm 1/2\rangle$ is given by Eqs. (2.9) and (2.10) :

$$\Gamma_2^+ = \frac{1}{\sqrt{2}} \left(|\uparrow_e \downarrow_H\rangle - |\downarrow_e \uparrow_H\rangle \right) , \tag{2.28}$$

$$\Gamma_{5,yz}^+ = \frac{i}{\sqrt{2}} \left(|\uparrow_e \uparrow_H\rangle - |\downarrow_e \downarrow_H\rangle \right) , \tag{2.29}$$

$$\Gamma_{5,xz}^+ = \frac{1}{\sqrt{2}} \left(|\uparrow_e \uparrow_H\rangle + |\downarrow_e \downarrow_H\rangle \right) , \tag{2.30}$$

$$\Gamma_{5,xy}^+ = \frac{-i}{\sqrt{2}} \left(|\uparrow_e \downarrow_H\rangle + |\downarrow_e \uparrow_H\rangle \right) . \tag{2.31}$$

The Γ_2^+ state describes the non-degenerate $1S$ Para-exciton and is the energetically-lowest state in the yellow series. It contains only triplet states (total spin $\mathbf{s}$=1) in terms of the pure spins $|\uparrow_h \uparrow_e\rangle$, $|\downarrow_h \downarrow_e\rangle$ and $|\uparrow_h \downarrow_e\rangle + |\downarrow_h \uparrow_e\rangle$. This can be seen by inserting the relations given by Eqs. (2.9) and (2.10) into Eqs. (2.28), (2.29), (2.30) and (2.31). It is spin-forbidden for optical transitions, since we start from the ground state of the crystal with $\mathbf{s}$=0 and the electric field of the light cannot change the spin. The Γ_5^+ terms describe the threefold $1S$ Ortho-exciton. It contains also spin singlet states (total spin $\mathbf{s}$=0), that can couple to light [Kuw+77].

Since these states do not contain a Γ_4^- symmetry, they cannot be excited with the electric-dipole moment of the light wave. Thus, Cu_2O is a semiconductor with a so called forbidden direct band gap, caused by the parity of the highest valence and the lowest conduction band being the same [Age77]. However, one-photon excitations of S excitons are allowed in terms of a quadrupole transition. The quadrupole operator $(\Gamma_3^+ \oplus \Gamma_5^+)$ can excite the Ortho-exciton due to its Γ_5^+ symmetry.

For the S states (allowed transitions), the intensities of absorption lines, i.e. the oscillator strengths, are proportional to the squared modulus of the exciton wave function at the origin $\mathbf{r} = 0$ [Ell57; Age77]

$$f_S(n) \propto |\Psi_S(\mathbf{r})|^2_{\mathbf{r}=0} = \frac{1}{\pi (a^{\mathrm{B}})^3 n^3} \propto n^{-3} . \tag{2.32}$$

Hence, the oscillator strength drops with the third power of principal quantum number.

Now, excitons with a P-type relative motion are considered. Their symmetry representation is given by

$$\Gamma_P = (\Gamma_6^+ \otimes \Gamma_7^+) \otimes \Gamma_4^- = (\Gamma_2^+ \oplus \Gamma_5^+) \otimes \Gamma_4^- = \Gamma_2^- \oplus \Gamma_3^- \oplus \Gamma_4^- \oplus 2\Gamma_5^- . \tag{2.33}$$

Due to their P-type envelope they contain a Γ_4^- contribution and the dipole transition matrix element becomes non-zero. Their oscillator strengths depend on the squared derivative of the wave function at the origin

$$f_P(n) \propto \left| \nabla \Psi_P(\mathbf{r}) \big|_{\mathbf{r}=0} \right|^2 = \frac{1}{\pi (a^{\mathrm{B}})^5} \frac{n^2 - 1}{n^5} \tag{2.34}$$

and scale as n^{-3} for $n \gg 1$. These transitions belong to the group of so called direct forbidden transitions, but are allowed due to their P-type envelope function.

Beside the most prominent S- and P-like excitons, also D-, F-, G- and H-like excitons can be observed. For completeness their symmetry representation shall be given here (without Γ_2^+ contributions):

$$\begin{aligned}
\Gamma_D &= \Gamma_5^+ \otimes (\Gamma_3^+ \oplus \Gamma_5^+) \\
&= \Gamma_1^+ \oplus \Gamma_3^+ \oplus 2\Gamma_4^+ \oplus 2\Gamma_5^+ \ , && (2.35) \\
\Gamma_F &= \Gamma_5^+ \otimes (\Gamma_2^- \oplus \Gamma_4^- \oplus \Gamma_5^-) \\
&= \Gamma_1^- \oplus \Gamma_2^- \oplus 2\Gamma_3^- \oplus 3\Gamma_4^- \oplus 2\Gamma_5^- \ , && (2.36) \\
\Gamma_G &= \Gamma_5^+ \otimes (\Gamma_1^+ \oplus \Gamma_3^+ \oplus \Gamma_4^+ \oplus \Gamma_5^+) \\
&= \Gamma_1^+ \oplus \Gamma_2^+ \oplus 2\Gamma_3^+ \oplus 3\Gamma_4^+ \oplus 4\Gamma_5^+ \ , && (2.37) \\
\Gamma_H &= \Gamma_5^+ \otimes (\Gamma_3^- \oplus 2\Gamma_4^- \oplus \Gamma_5^-) \\
&= \Gamma_1^- \oplus 2\Gamma_2^- \oplus 3\Gamma_3^- \oplus 4\Gamma_4^- \oplus 4\Gamma_5^- \ . && (2.38)
\end{aligned}$$

The observation of high angular momentum F and H excitons was first reported in [The+15]. They are visible in pure absorption spectra since they are mixed with allowed P states by the H_d term and contain Γ_4^- representations (see Fig. 2.3 in Sec. 2.5 or Fig. A.1 in Appendix A.1). Even-parity D- and G-like states couple to the electric-quadrupole field. Since D states start at $n = 3$ and G states not before $n = 5$, their oscillator strength is small according to Eq. (2.32) and they are invisible in one-photon absorption without external perturbations. However, they can be optically activated either by stress or an external electric field that mixes even and odd-parity states. Among many early works (see for example Refs. [Dei+73] or [Age+74]), investigations in an external electric field were done in [Hec15] and continued as a part of this thesis with a high-resolution setup. Results are published in Refs. [Hec+17a; Hec+18c] and [Hec+18d]. They will be described in more detail in Chapter 4.

Furthermore, S and D states can be excited by two-photon absorption processes ($\Gamma_3^+ \oplus \Gamma_5^+ \in \Gamma_4^- \otimes \Gamma_4^-$) as in [Uih+81] or in a second harmonic generation (SHG) scheme respectively, which was done by Mund et al. [Mun+18]. Additionally, huge theoretical effort has been spent on the investigation of the excitonic level scheme. Especially the even exciton series was studied in Refs. [Uih+81] and [Sch+17c].

All experimentally found excitonic transitions of the yellow series are summarized in Tab. A.1 in Appendix A.1. Their energies are visualized in a level scheme in Fig. 2.5 at the end of this chapter.

The symmetry considerations can be applied to the green series as well, i.e. transitions from the second highest valence band (Γ_8^+) to the lowest conduction band (Γ_6^+). Again, due to the same parity of the bands, S-like transitions are only quadrupole allowed ($\Gamma_{1Sg} = (\Gamma_6^+ \otimes \Gamma_8^+) \otimes \Gamma_1^+ = \Gamma_3^+ \oplus \Gamma_4^+ \oplus \Gamma_5^+$). Indeed, in absorption the weak green $1S$ quadrupole transition can be seen on the high energy side of the $2P$ state (see inset II in upper panel of Fig. 2.3). However, a much stronger signal can obtained via SHG technique (cf. [Mun+18]). For the blue and violet series at higher energies, S excitons are dipole allowed as the corresponding conduction band possesses negative parity (Γ_8^-), resulting in huge optical features (see e.g. [Dau+66]). Throughout this work, the focus will be on the yellow exciton series and in particular on the P states.

Beside discrete absorption peaks, continuous absorption features arise from phonon assisted absorption bands. The excitation of a quadrupole-allowed S state can be cou-

pled to the simultaneous creation of an optical phonon. There are in total 18 phonon branches in Cu_2O. The coupling of the $1S$ Ortho-exciton with Γ_5^+ symmetry to all odd-parity phonons with Γ_2^-, Γ_3^-, Γ_4^- or Γ_5^- symmetry can result in a dipole-allowed transition ($\Gamma_4^- \in \Gamma_2^- \otimes \Gamma_5^+, \Gamma_3^- \otimes \Gamma_5^+, \Gamma_4^- \otimes \Gamma_5^+, \Gamma_5^- \otimes \Gamma_5^+$). As discussed in Ref. [Sch+17a], the most relevant couplings include the Γ_3^-- and Γ_4^--phonons, as these show the strongest transitions. The resulting absorption starts at about one phonon energy E_{Ph} above the involved S resonance with a square-root dependence on the excitation energy

$$\alpha_{nS}^{\mathrm{Ph}} = c_{nS}^{\mathrm{Ph}}(E - (E_{nS} + E_{\mathrm{Ph}}))^{1/2} \ . \tag{2.39}$$

The square-root dependence stems from the density of final states $D(E)$ in three dimensions (cf. Eq. (2.1)). The amplitude of this process is c_{nS}^{Ph} that is obtained by comparison to experimental data.

All these transitions can be observed in one-photon absorption and are shown in Fig. 2.3 and discussed in the next section.

2.5 Absorption spectrum of the whole yellow series

In this section, an overview about the absorption spectrum of the yellow series is given. The whole absorption spectrum of the yellow exciton series is measured with the high-resolution setup described in Ch. 3 and is shown in Fig. 2.3. The sample used is $H7$ cooled down to a temperature of 1.35 K and the probe power is 1 μW.

The absorption spectrum begins with the sharp quadrupole transition of the $1S$ Ortho-exciton at 2.03279 eV. A closeup is shown in inset I in the upper panel of Fig. 2.3. In this particular case, the resonance is split into two resonances with linewidths of ≈ 4 μeV and 2 μeV. This splitting was investigated in Refs. [Das+03; Das+04; Das+05] and was assigned to **K**-dependent terms of the analytic exchange interaction. Later, in Refs. [Sch+16c; Sch+16e], the **K**-dependent analytic exchange terms were shown to be in the range of neV and negligible. The splitting was rather related to the deviations from parabolicity in the valence band structure (scheme in Fig. 2.2 (b)) seen by an exciton with finite total momentum $\hbar\mathbf{K}$. A splitting can in principal be induced by strain as well, but is excluded here as a cause of the splitting due to the use of a strain-free sample holder (see Ch. 3) and the overall high quality of the sample.

The second inset II in the upper panel reveals weak quadrupole signals for the $2S$ exciton of the yellow series and the $1S$ exciton of the green series. The energies of these features agree with the values found in the SHG-spectra ($E_{2S_y} = 2.13750$ eV and $E_{1S_g} = 2.15439$ eV) [Mun+18].

At an energy of $E_{\mathrm{Ph}}^{\Gamma_3^-} = 13.5$ meV above the yellow $1S$ absorption, the phonon background starts with the Γ_3^--phonon branch. It shows a square-root dependence $\propto (E - (E_{1S} + E_{\mathrm{Ph}}^{\Gamma_3^-}))^{1/2}$, according to Eq. (2.39). Within the spectrum, contributions due to four different phonon branches can be identified, all adding up to the continuous phonon background, shown as the red curve in Fig. 2.3. The onsets of the relevant branches are indicated by dashed vertical lines. The second and third phonon branches start at $E = E_{1S_y} + E_{\mathrm{Ph}}^{\Gamma_4^-}$ ($E_{\Gamma_4^-} = 82.1$ meV [Sch+17a]) and $E = E_{2S_y} + E_{\mathrm{Ph}}^{\Gamma_3^-}$. Similar to the $1S$ Ortho-exciton of the yellow series, the green $1S$ exciton couples to Γ_3^- phonons as well, resulting in the strong fourth phonon branch starting at $E = E_{1S_g} + E_{\mathrm{Ph}}^{\Gamma_3^-}$ (middle panel of Fig. 2.3).

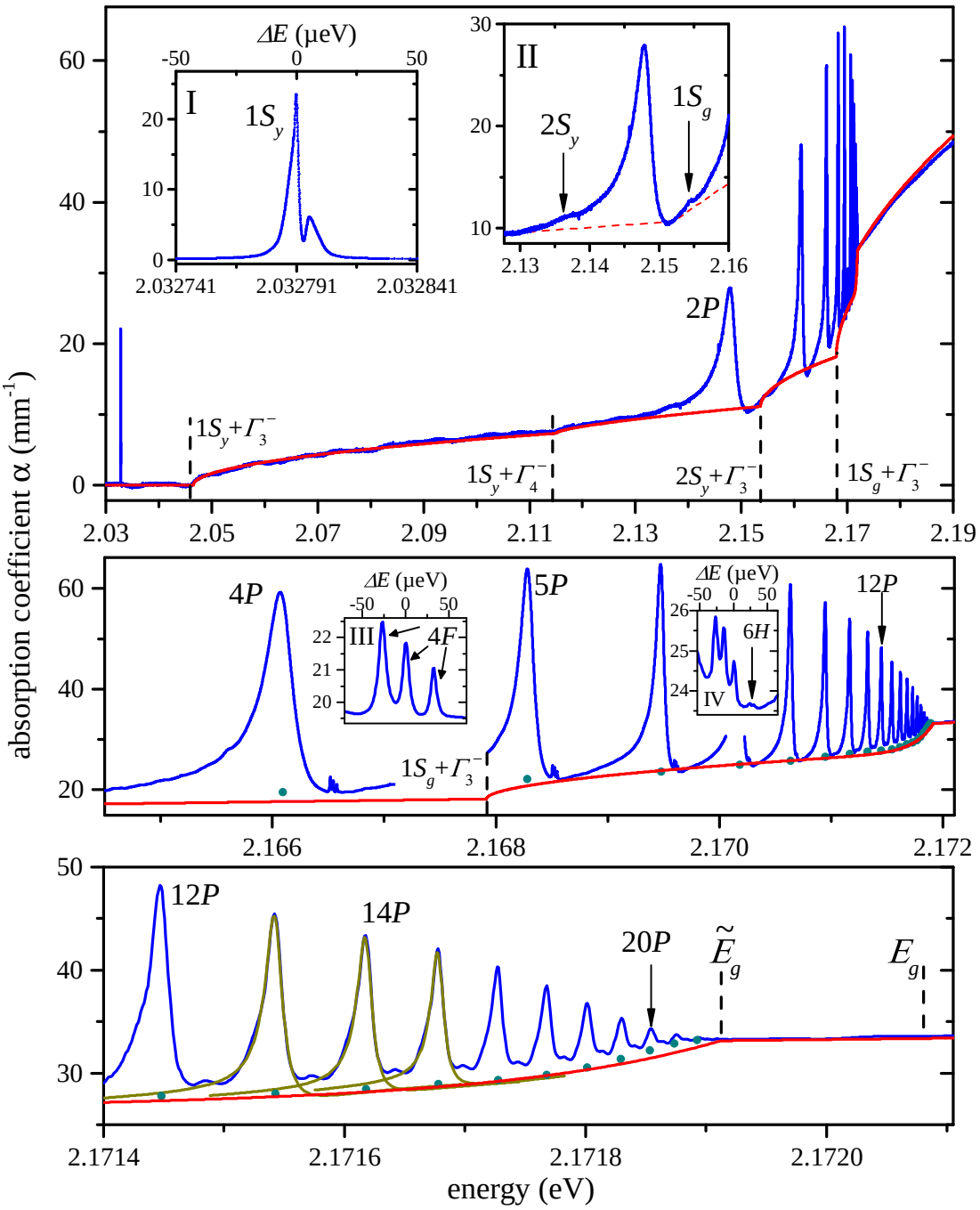

Figure 2.3 High-resolution absorption spectrum of the yellow exciton series measured with a probe power of 1 μW at $T = 1.35$ K on sample $H7$. The red line indicates the background absorption according to Eq. (2.42). Dashed vertical lines mark the beginning of a phonon branch. Green dots mark zero points $\alpha^P_{0,n}$ for every exciton line, obtained by the fitting routine described in the text. Dark yellow lines in the lower panel show fitted curves for $n = 13$, 14 and 15. $\tilde{E}_g$ indicates the end of the exciton series and the transition into the continuum at about 172 μeV below E_g. E_g is the nominal band gap at 2.172087 eV obtained by a fit to the energies according to Eq. (2.24). Insets show zooms into regions of S, F and H angular momentum states.

This branch is superimposed by an exponential increase of absorption that is observed from about $n = 10$ until an energy $\tilde{E}_\mathrm{g} = 2.171915$ eV, where the exciton series ends and the spectrum smoothly transforms into a continuum. This part is phenomenologically described with an Urbach tail-like function

$$\alpha_\mathrm{U} = c_\mathrm{U} e^{(E-\tilde{E}_\mathrm{g})/E_\mathrm{U}} \ , \tag{2.40}$$

with an amplitude c_U and the Urbach energy E_U, determining its width (see e.g. [Gru06]). Here, a width of $E_\mathrm{U} = 170$ μeV leads to a good agreement with the data.

The microscopic origin of this tail is investigated in a recent study by Krüger et al. [Krü+20]. There, the exponential tail is described quantitatively, based on earlier proposals by Dow and Redfield [Dow+72]. Within this model, charge carriers, trapped by impurities, give rise to an inhomogeneous electric micro-field distribution in the crystal. The micro-field leads to an ionization of the highest Rydberg states which transform into an exponentially increasing absorption continuum. In other words, the continuum edge is smeared out and extends exponentially to lower energies. Moreover, the presence of micro-fields results in deviations of line shape parameters of excitons with the highest n, which is discussed below. An experimental investigation of this exponential part is given in Sec. 6.7.

In the true continuum, i.e. $E > \tilde{E}_\mathrm{g}$, the absorption is described by [Sch+17a]

$$\alpha_\mathrm{cont} = c_\mathrm{cont} \cdot \frac{1}{E} \left(E - \tilde{E}_\mathrm{g}\right)^{3/2} \cdot \frac{\bar{\gamma} e^{\bar{\gamma}}}{\sinh \bar{\gamma}} \left(1 + \frac{\bar{\gamma}^2}{\pi^2}\right) . \tag{2.41}$$

Following [Ell57], the continuum absorption increases with an $(E - \tilde{E}_\mathrm{g})^{3/2}$ dependence for forbidden transitions. The third factor in Eq. (2.41) is the Sommerfeld enhancement factor with $\bar{\gamma} = \sqrt{\frac{\pi^2 Ry}{E-\tilde{E}_\mathrm{g}}}$. It accounts for the increased oscillator strength at the absorption edge given by the Coulomb interaction between (free) electron-hole pairs. The magnitude of this process is given by c_cont. Finally, the total background is given by

$$\alpha_\mathrm{back} = \alpha_{1Sy}^{\Gamma_3^-} + \alpha_{1Sy}^{\Gamma_4^-} + \alpha_{2Sy}^{\Gamma_3^-} + \alpha_{1Sg}^{\Gamma_3^-} + \alpha_\mathrm{Ur} + \alpha_\mathrm{cont} \ . \tag{2.42}$$

The chosen amplitudes for the background to fit this particular spectrum are given in Tab. A.2 in Appendix A.2 .

In [Sch+17a], the composition of the background as outlined above is extended by terms including a deformation potential. Note that these terms are neglected here. Additionally, the amplitude of the green $1S$ phonon branch is chosen to be $c_{1Sg}^{\Gamma_3^-} = 2.6 \cdot c_{2Sy}^{\Gamma_3^-}$, which is higher than predicted in [Sch+17a]. Further, the value for E_{2S_y} entering Eq. (2.42) is set to the theoretical value $E_{2S} = 2.1401$ eV given in [Sch+17c].

On this continuous background, the P exciton absorption lines arise, starting with the significant $2P$ line (upper panel in Fig. 2.3). The series of P states continues up to $n = 22$ in this particular case with a hydrogen-like energy ladder following (almost) an n^{-2} dependence. The line shapes of the P resonances are described by asymmetric Lorentzian curves of the form

$$\alpha_{nP}(E) = \frac{O_n}{\pi} \frac{\frac{\Gamma_n}{2} + 2q_n \left(E - E_n\right)}{\left(\frac{\Gamma_n}{2}\right)^2 + \left(E - E_n\right)^2} \ , \tag{2.43}$$

with the resonance energy E_n, the FWHM Γ_n and the asymmetry parameter q_n. The prefactor, O_n, is the area of the peak in eV/mm and proportional to the electron-photon interaction strength. Following [Nik+61], the oscillator strengths are given by the peak areas obtained in the experiment

$$f_{n,\mathrm{exp}} \propto \int \alpha_{nP}(E)dE = O_n \ . \tag{2.44}$$

The line shape given by Eq. (2.43) was derived by Toyozawa in Refs. [Toy58; Toy64], where the asymmetry was mainly attributed to interband scattering between different exciton bands by optical phonons. However, it was shown in [Sch+16d], that the experimentally observed asymmetries are larger than predicted by this theory and have to be rather attributed to interference effects between the continuous background states and discrete exciton states, as it is known from general theory by Fano [Fan61]. The line shape in Eq. (2.43) is used to fit the spectrum with the fitting routine described in Appendix A.3. Three fitted resonance curves for $n = 13, 14$ and 15 are exemplarily shown by the dark yellow lines in the lower panel of Fig. 2.3. First of all, the fits reveal an offset $\alpha^P_{0,n}$ for each resonance, that is indicated by green dots. Following these dots, the actual background in the lower panel of Fig. 2.3 is found to be slightly lower than one would expect from the pure spectrum. All other obtained fit parameters are visualized in Fig. 2.4.

The P exciton binding energies $E_\mathrm{g} - E_n$ are shown in the upper left panel. A fit to the resonance energies with the quantum defect formula Eq. (2.24) yields $E_\mathrm{g} = 2.172087$ eV, $Ry = 90$ meV and a quantum defect of $\delta_{n,P} = 0.08$ in this particular case. Note that $\delta_{n,l}$ is assumed to be constant here, but typically depends on n. At a photon energy of $E_\mathrm{g} = 2.172087$ eV one obtains a wave vector of $k_0 = E_\mathrm{g}\bar{n}/(\hbar c) = 3.3 \cdot 10^7$ m^{-1}, with the index of refraction $\bar{n} \approx 3$ (calculated with a first-order Sellmeier formula and a wavelength of $\lambda = 570$ nm [Ito+98]). Vice versa, the excitons near the band gap are excited at $\mathbf{K} = \mathbf{k}_0$ which gives a center-of-mass kinetic energy of $E_\mathrm{kin} = \hbar^2\mathbf{K}^2/(2M) \approx 27$ μeV. Hence, the actual value for the band gap has to be corrected to $E_\mathrm{g} = 2.172060$ eV. If not stated otherwise, the values $E_\mathrm{g} = 2.171208$ eV and $Ry = 86$ meV are used for calculations in the next chapters.

This particular spectrum shown in Fig. 2.3 ends at $n_\mathrm{max} = 22$ or at $\tilde{E}_\mathrm{g} = 2.171915$ eV, resp., i.e. $\Delta_0 = -172$ μeV below E_g. This is the shifted band gap

$$\tilde{E}_\mathrm{g} = E_\mathrm{g} + \Delta_0 \ , \tag{2.45}$$

that is attributed to the charged impurities in the sample mentioned above, that lead to a band gap renormalization. The exciton energies are not affected by this shift, as it is compensated in first order by Coulomb screening. The constant exciton energies can be described by introducing an effective Bohr radius $a^\mathrm{B}_\mathrm{eff} > a^\mathrm{B}$ and effective quantum numbers $n_\mathrm{eff} > n$ (see Sec. 5.2.4). The value for Δ_0 depends strongly on the exact constitution of the sample under consideration.

Information about the oscillator strengths is obtained from the peak areas O_n, shown in Fig. 2.4 (b) as a function of principal quantum number n. They are normalized to the measured peak area of $n = 5$, O_5=0.0101 mm^{-1}eV, yielding a theoretical scaling following $f_n/f_5 = O_n/O_5 = 130.21$ meV $\cdot \frac{n^2-1}{n^5}$ (cf. Eq. (2.34)). As known from [Kaz+14], the oscillator strengths follow this dependence roughly up to $n = 10$, while they drop drastically

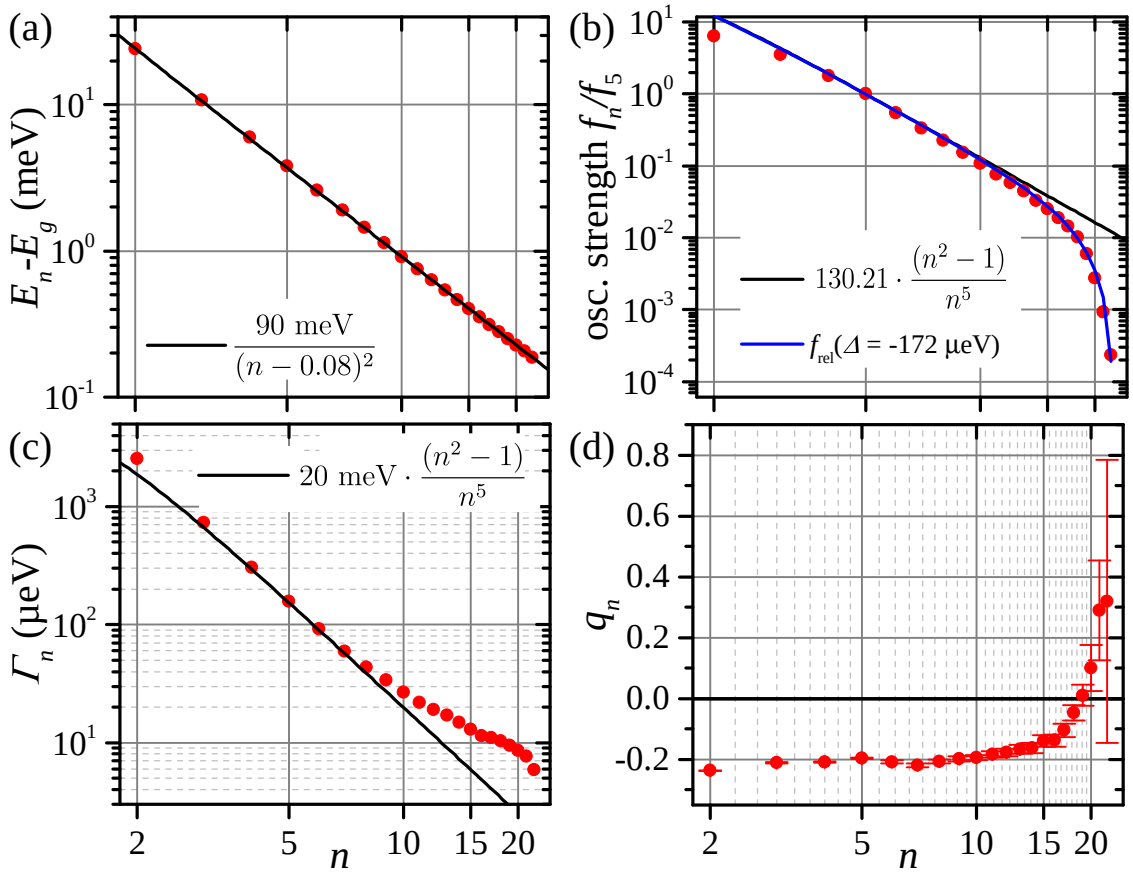

Figure 2.4 (a) Binding energies $E_g - E_n$ as a function of principal quantum number n and a fit according to Eq. (2.24) with $Ry = 90$ meV and $\delta_{n,l} = 0.08$ (b) Oscillator strengths f_n normalized to f_5. The black line shows the ideal scaling, the blue line gives the relative oscillator strength with a band gap shift of $\Delta_0 = -172$ μeV according to Eq. (5.28) (c) Linewidths Γ_n following the predicted scaling (black line) up to approximately $n = 10$. For higher n they are broader than predicted. (d) The asymmetry parameters q_n start around -0.2 for $n = 2$ and continuously approach zero around $n = 18$. For higher n they become even positive.

for higher n. As explained in detail in Sec. 5.2.4, the relative oscillator strengths can be calculated as a function of the effective Bohr radius $a^{\mathrm{B}}_{\mathrm{eff}} > a^{\mathrm{B}}$ and effective quantum numbers $n_{\mathrm{eff}} > n$, given by the intrinsic band gap shift Δ_0. Doing so, the drop of oscillator strength can be described phenomenologically. The resulting curve is shown in blue in the same panel for $\Delta_0 = -172$ μeV.

The linewidths follow an n^{-3} dependence as well. This dependence is well known from radiative decay in atomic systems. It stems from the wave function overlap between excited and ground state [Gal94]. However, in [Sto+18] it was shown that the linewidth of P excitons is mainly given by interactions with phonons, i.e. the decay of a P state into the $1S$ state by phonon scattering. The n dependence is again determined by the overlap between initial nP and final $1S$ states. The main contributions are shown to be caused

by deformation-potential scattering with Γ_3^- / Γ_5^- phonons and Fröhlich interaction with LO phonons. In an earlier calculation in Ref. [Sch+16d] the Γ_3^- / Γ_5^--process was not considered. In total, this yields the dependence [Sto+18] [2]

$$\Gamma_n = 18 \text{ meV} \cdot \frac{n^2 - 1}{n^5} \ . \tag{2.46}$$

In Fig. 2.4 (c), this dependence is shown as the black solid line, whereas the prefactor is set to 20 meV to fit the linewdiths best. The higher value results from a slightly higher temperature in the experiment (1.35 K compared to 1.2 K in [Kaz+14]). The values drop from $\Gamma_{2P} \approx 2500$ μeV for $n = 2$ down to $\Gamma_{22P} \approx 6$ μeV for $n = 22$, corresponding to ns lifetimes. However, as already mentioned in [Kaz+14], the linewidths for states with $n > 10$ are larger than predicted by the theoretical scaling. As a result, they start to overlap in the high-n regime as shown by the three dark yellow curves in the lower panel of Fig. 2.3. In Sec. 5.3, the linewidths are investigated at mK temperatures, still showing this broadening.

Finally, the obtained asymmetry parameters as a function of n are shown in Fig. 2.4 (d). They start at $q_n = -0.2$ and increase gradually to zero for $n \approx 18$, meaning that the line shapes become more symmetric in this spectral range. For higher n, i.e. closest to the band gap, the values for q_n even become positive.

The linewidth broadening and the drop of oscillator strength as well as the positive asymmetry parameters in the high-n regime can be traced back to the ionization of states due to the micro-field distribution induced by charged carriers, as explained in Ref. [Krü+20]. The vanishing oscillator strength finally results in a shifted band gap $\tilde{E}_g$ in accordance with the phenomenological description, that is used in this thesis.

Beside the P exciton Rydberg series even higher angular momentum states can be observed, shown in the insets III and IV in the middle panel of Fig. 2.3. Namely these are F excitons with $l = 3$, visible from $n = 4$ onwards on the high energy side of each P resonance. They are split into three visible lines by the cubic part of the H_d term. This is in accordance to Eq. (2.36), that involves $3\Gamma_4^-$ terms [The+15]. Their linewidths are about 10 μeV for $n = 4$. From $n = 6$ onwards, one finds even H excitons ($l = 5$) visible as a single tiny peak on the high energy side of the three F states. They can be identified up to $n = 7$ in pure absorption spectra and at $n = 8$ in differential transmission (cf. Fig. A.1).

Furthermore, in the lower panel of Fig. 2.3, one can observe additional small resonances between two P exciton lines. They were described in [Grü+16] as dressed states emerging from a coherent coupling of both adjacent Rydberg states via the ground state in a V-type level scheme by a single laser source. Due to the close spectral separation of two P states the probe laser drives both transitions with little detuning from each resonance. Since they are only predicted to appear between coherent states with low rates of dephasing, their observability serves as a signature for low levels of decoherence and dephasing in the system. This will be used in Ch. 5.

As a summary, a level scheme of resonance energies of all experimentally found exciton states of the yellow series is given in Fig. 2.5. It includes data from one-photon absorption and SHG experiments (from [Mun+18]), both with and without external fields. Their numeric values are listed in Tab. A.1 in Appendix A.1

[2] Note that the values given in [Sto+18] have to be multiplied by 2.

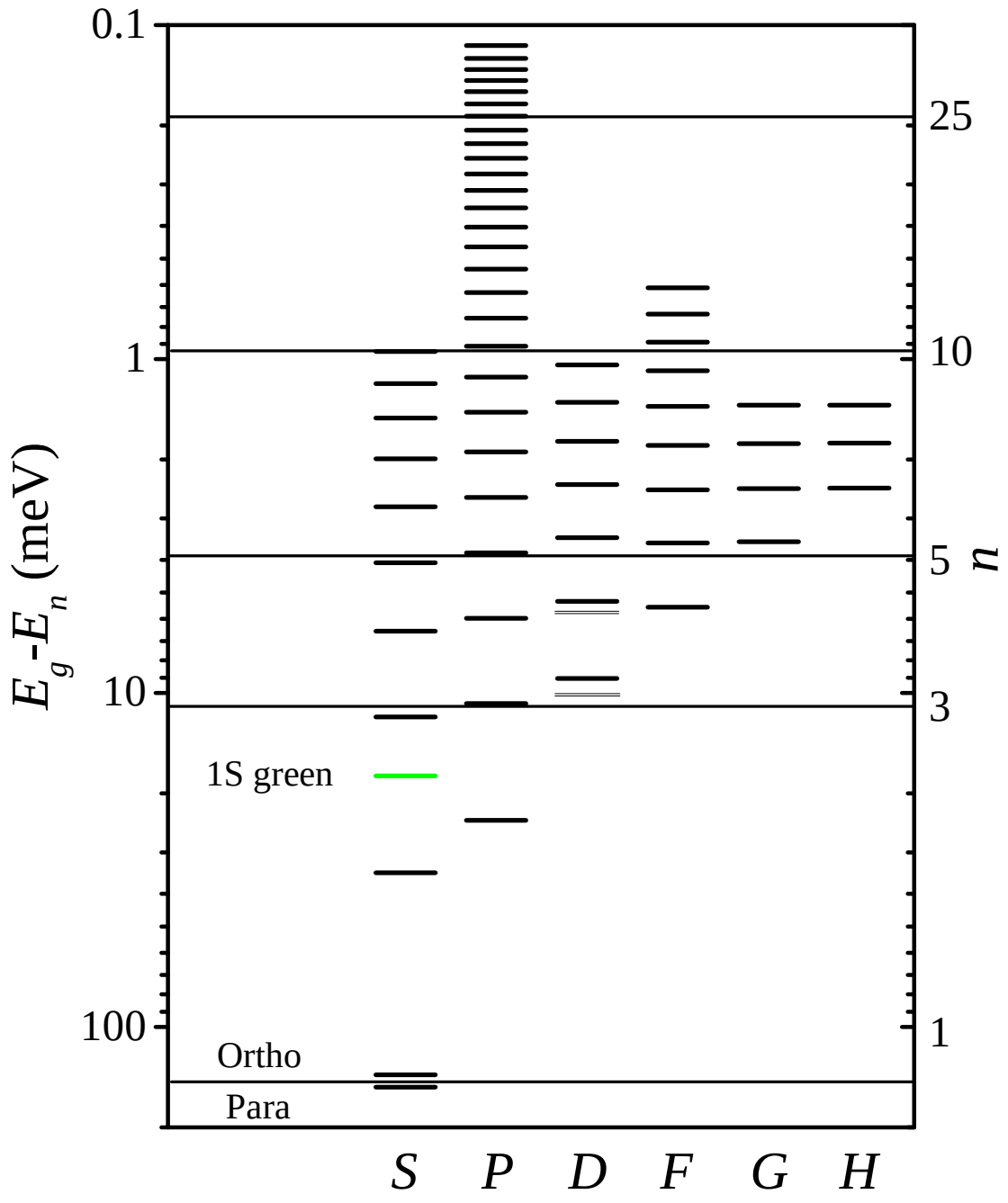

Figure 2.5 Level scheme of experimentally observable exciton states of the yellow series in Cu_2O. The energies and references are given in Tab. A.1 in Appendix A.1. For each n, states with different angular momentum are non-degenerate. They are spread over a certain energy range that decreases as n^{-3} (Sec. 4.1.1).

Chapter 3

Experimental setup

In this chapter, the experimental setup used for the experiments shown in this thesis is explained. It is optimized for continuous-wave (CW) absorption spectroscopy at low temperatures with a high spectral resolution of 1 neV. The light sources consist of two identical dye lasers and a white light source. In the first section the focus lies on the laser setup. The white light excitation is briefly explained in the second section at the end of this chapter.

3.1 Laser spectroscopy

The laser systems (Sirah Matisse DS) used offer a high spectral resolution of 1 neV in locked mode and about 5 neV in scanned mode. Figure 3.1 shows a sketch of the optical setup used for single-beam experiments as well as for pump-probe experiments. The main optical elements are explained in the following.

The dye used is Rhodamine 6G which covers the wavelength range from 620 nm to 565 nm, i.e. from energies below the 1S-Ortho resonance to energies about 30 meV above the band gap of the yellow series. This wavelength range can be scanned continuously via software control and is read out by a high-precision wavelength meter (HighFinesse WSU). The dyes are pumped by a Verdi V-10 from Coherent and a Finesse from Laser Quantum with a power of 7 W each. The laser light is coupled into a fiber to maintain a stable beam diameter for all wavelengths. To reduce fluctuations in the signal to a minimum, each light beam is stabilized by a noise eater (BEOC Laser Power Controller, short: LPC). This stabilization is important during a wavelength scan in particular, as the output intensity of the laser may vary strongly. These fluctuations become even more enhanced by the fibers. The LPC systems used maintain a noise level below 0.5 %. In the following both beams can be attenuated further to a certain power level with a combination of a half-wave plate and a Glan-Taylor prism (GTP). Unfortunately, these devices generate unavoidable Fabry-Pérot interference patterns in the signal in dependence on the scanned wavelength. In order to reduce these interferences, the devices can be slightly tilted. This reduces the amplitude of interferences to around 2%. In addition, a pellicle beamsplitter (P) is used in front of the cryostat to reflect around 4 % of the probe beam to photodiode 1 (PD1). This signal, called $V_{\mathrm{Int.}}$, contains all interference patterns generated along the optical path up to this point and serves as a reference signal to smooth the data later on. The diode should preferably be of the same type as photodiode PD2. Further, both diodes should not generate additional interferences on its surface. Another source for interference patterns are the cryostat windows. Therefore, the cryostat is typically tilted slightly around its vertical axis which allows for a complete elimination of these interferences. The remaining interferences mainly stem from the sample plate (red) itself. Both beams are focused on the sample with

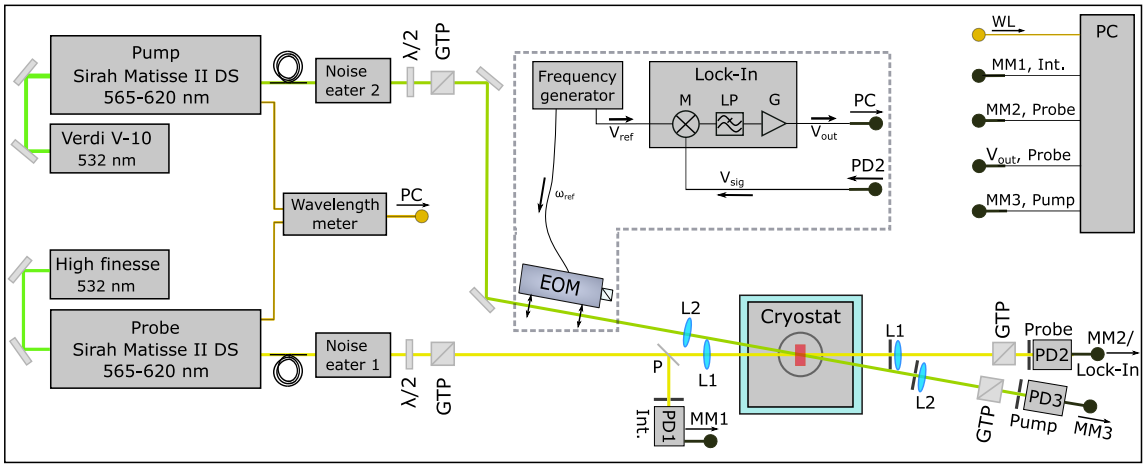

Figure 3.1 Sketch of experimental pump-probe setup. General abbreviations: $\lambda/2$: half-wave plate. GTP: Glan-Taylor prism. P: Pellicle beamsplitter. PD: Photodiode. MM: high-speed multimeter. L: achromatic lenses, WL: wavelength. Inside dashed area (optional Lock-In detection scheme): EOM: electro optical modulator. M: electronic mixer, LP: electronic low-pass filter. G: electronic gain. PD1 measures a reference signal containing interference patterns from optical devices. PD2 measures the probe laser transmission, that is passed either directly to multimeter MM2 or to the input of the Lock-In. PD3 measures the pump laser transmission. The sample (red) is mounted strain free in a cryostat.

lenses L1 and L2. The probe spot has a diameter of about 100 μm and the pump spot is set to a larger diameter of 300 μm to ensure a preferably homogeneously spread pump power density. The beam profiles are measured with a beam analyser (Coherent BeamMaster 2408) and diameters are given as the full width at half maximum. The probe laser's power is usually set to 1 μW, whereas the pump power is varied. With a probe power of 1 μW, a negligible influence of the probe power on the system is ensured, while a good signal-to-noise ratio is still obtained. The powers are measured in front of the cryostat. For an estimation of the intensity illuminating the sample, reflection losses at the cryostat windows of about 4 % at each side and of about 25 % at the sample surface (index of refraction $\bar{n} \approx 3$) have to be considered. Depending on the cryostat, 3 or 5 windows are built in with 6 to 10 surfaces. Combined with the sample surface we estimate the losses to about 40-50 %. For convenience, only laser powers will be given throughout this thesis.

Both beams are collimated behind the sample and detected by photodiodes (New Focus Large-Area Photoreciever). The probe beam is detected by photodiode PD2 and the pump beam by photodiode PD3. With a variable built-in gain they allow for the detection of signals from mW magnitudes down to tens of nW. For the detection of lower powers on the order of a few nW or even below, an avalanche diode (Hamamatsu C-5331) or a low-power photoreciever (Femto FWPR-20 SI) are used (cf. Sec. 5.3). The sample is mounted strain-free in a cryostat. For temperatures down to 1.35 K, a liquid ^{4}He cryostat is used, either with or without magnetic coils. For lower temperatures a ^{3}He-^{4}He dilution refrigerator is necessary.

In a pump-probe measurement scheme, the pump power is usually higher than the probe

power. Although both beams follow different pathways, PD2 might still detect stray light generated by the pump beam at the sample surface. To reduce the magnitude of this stray light in direction of PD2 we first use a pinhole in front of collimating lens L1. Second, the pump polarization is rotated by 90° relative to the direction of the probe polarization. Lens L1 is followed by a GTP in front of the diode. The GTP lets the probe polarization pass, but reflects the pump polarization. This is important especially in a Lock-In detection scheme (see below), since the pump stray light is modulated and will be amplified significantly by the Lock-In device. If not reduced at all, modulated stray light can give rise to significant offsets starting around 200 μW, as shown in Ref. [Sch18]. Both a pinhole and a GTP are used in the pump detection in a similar way, but with polarizations rotated by 90°. The PD voltages are read out by high-speed multimeters (Keithley 2000) connected to a PC.

To measure an absorption spectrum, the probe laser wavelength is scanned continuously and signals from all diodes are recorded simultaneously with a LabVIEW based program on a PC. The scan speed can be adjusted and is typically chosen to cover 8 μeV per second (2 GHz/s) in the spectral range between $n = 4$ and $n = 10$ and is reduced to 2 to 4 μeV per second (0.5 to 1 GHz/s) for higher n. The intensity transmitted by the sample I_T is detected by PD2 in dependence on the laser light's wavelength λ. It is given by Lambert-Beers law [Kli07]

$$I_\mathrm{T}(\lambda) = I_0 \cdot e^{-\alpha(\lambda)d} \,. \tag{3.1}$$

Here, I_0 is the light intensity without absorption in the sample and $\alpha(\lambda)$ is the wavelength- or energy-dependent absorption coefficient. The thickness of the sample is given by d. To remove interferences, the probe signal is divided by the wavelength-dependent reference voltage $V_\mathrm{Int.}(\lambda)$ measured by PD1. As all diode voltages are directly proportional to the detected light intensity $V \propto I$, we can evaluate the optical density, except for an unknown offset

$$\begin{aligned} OD(\lambda) = \alpha(\lambda)d &= -\ln\left(I_\mathrm{T}(\lambda)/I_0\right) \\ &= -\ln\left(V_\mathrm{probe}(\lambda)/c_\mathrm{loss}V_\mathrm{Int.}(\lambda)\right) \\ &= -\ln\left(V_\mathrm{probe}(\lambda)/V_\mathrm{Int.}(\lambda)\right) + \ln\left(c_\mathrm{loss}\right) \,. \end{aligned} \tag{3.2}$$

The factor c_loss comprises all gain and conversion factors and is chosen to yield an optical density equal to zero in the spectral range between the $1S$ absorption line and the beginning of the phonon background (see Fig. 2.3), as suggested in [Sch+17a]. In other words, c_loss accounts for the unknown value of I_0, which is not needed to be measured explicitly. It further takes into account all intensity losses, that occur due to reflections and scattering at both the sample surface and optical devices, in particular at the cryostat windows. The wavelength dependence of reflection and scattering is assumed to be small in this energy range and is neglected. Finally, the adjustment of c_loss as described above results in an absorption coefficient $\alpha = OD/d$ of about 33 mm^{-1} at the band gap energy of $\tilde{E}_\mathrm{g}$=2.171914 eV, cf. Fig. 2.3, comparable to the spectrum shown in [Sch+17a].

If a pump laser is added, a sufficient spatial overlap between both beams is needed. This is obtained by maximizing the signal height of the differential transmission measured with the Lock-In scheme described in the next section. The overlap should be adjusted in a daily routine and preferably measured at the same spectral positions with the same powers of

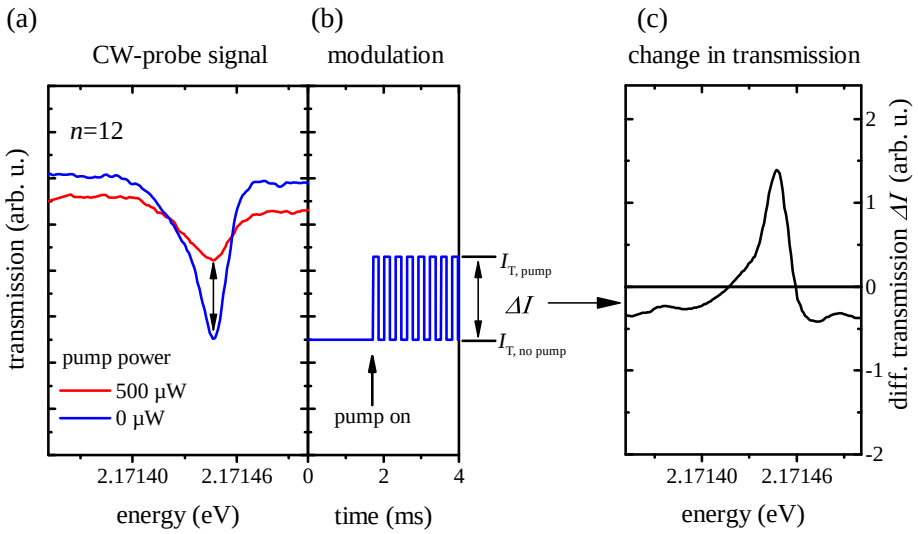

Figure 3.2 (a) Probe laser transmission around resonance $n = 12$ for zero pump power and 500 μW. The pump energy is set to $n = 16$. (b) The probe signal at the peak minimum as a function of time. The oscillations of the pump amplitude are directly transferred to the probe signal resulting in an AC-amplitude ΔI equal to the difference between the pumped and unpumped signals. (c) The difference amplitude multiplied with an arbitrary gain factor plotted against energy. This is the Lock-In signal.

pump and probe, e.g. by probing an exciton with $n = 12$ and a power of 1 μW and pumping an exciton with $n = 16$ and a power of 200 μW. Further, it should be rechecked and, if necessary, readjusted at least once per hour within a long measurement series to avoid long-term drifts in the signals and ensure comparability within the whole measurement series. In any case, it has to be checked after refilling the Helium bath.

3.1.1 Lock-In detection scheme

To detect differential spectra with high sensitivity, we use a Lock-In detection scheme. The relevant devices are indicated with the dashed box in Fig. 3.1. The Lock-In device used is a SR 830 from Stanford Research Systems. The basic concept of the scheme is explained in the following.

The transmitted probe light I_T is detected with PD2 and its output voltage V_probe is connected to the input of a Lock-In amplifier. It will be called V_sig in the following. The pump laser is optically modulated with a frequency ω_m and the modulation is assumed to be sinusoidal for simplicity. The pump laser light will induce a change in the probe transmission according to an so far unknown interaction mechanism assuming spatial overlap between both laser spots. Due to the comparably low frequency, we can neglect time-dependent dynamics in the sample and consider the probe light to follow this modulation directly, but with an arbitrary offset in phase Θ_sig. Then, the measured voltage reads $V_\mathrm{sig}\sin(\omega_\mathrm{m}t+\Theta_\mathrm{sig})$. The lock-in amplifier multiplies the input signal with a reference signal $V_\mathrm{ref}\sin(\omega_\mathrm{ref}+\Theta_\mathrm{ref})$

and we find

$$\begin{aligned} V_{\text{out}} = \quad & V_{\text{sig}} V_{\text{ref}} \sin(\omega_{\text{m}} t + \Theta_{\text{sig}}) \sin(\omega_{\text{ref}} t + \Theta_{\text{ref}}) \\ = \quad & \tfrac{1}{2} V_{\text{sig}} V_{\text{ref}} \cos\left([\omega_{\text{m}} - \omega_{\text{ref}}]t + \Theta_{\text{sig}} - \Theta_{\text{ref}}\right) \\ & -\tfrac{1}{2} V_{\text{sig}} V_{\text{ref}} \cos\left([\omega_{\text{m}} + \omega_{\text{ref}}]t + \Theta_{\text{sig}} + \Theta_{\text{ref}}\right) \ . \end{aligned} \tag{3.3}$$

Thus, we obtain two AC signals, one containing the difference frequency $\omega_{\text{m}} - \omega_{\text{ref}}$ and one containing the sum frequency $\omega_{\text{m}} + \omega_{\text{ref}}$ of both signals. Usually, the reference frequency equals the modulation frequency, $\omega_{\text{m}} = \omega_{\text{ref}}$, and the first term in Eq. (3.3) becomes a DC signal. A low-pass filter removes the second term of high frequency and the signal becomes

$$V_{\text{out}} = \frac{1}{2} V_{\text{sig}} V_{\text{ref}} \cos(\Theta_{\text{sig}} - \Theta_{\text{ref}}) \ . \tag{3.4}$$

Additionally, the reference phase is matched to obtain a maximum signal, i.e. $\Theta_{\text{ref}} = \Theta_{\text{sig}}$.

The modulation is generated either with a mechanical chopper blade or with an electro-optical modulator (Linos LM 0202) both maintaining an extinction ratio of more than 1:1000. The frequency is set to 3.333 kHz or a period of about 300 μs, while the modulators generate fast edges of about 10 ns. Hence, the pump beam can be considered to be switched on and off producing a rectangular signal with frequency ω_{ref}. The calculation given above still holds in case of rectangular signals as they can be decomposed into a Fourier sum of sinusoidal signals. The probe signal is perturbed during half a period.

The modulation scheme is schematically shown in Fig. 3.2. In panel (a), the blue curve shows the transmitted probe intensity around the absorption line of $n = 12$ and zero pump power. In a typical CW-scan of the probe energy with an unmodulated pump beam of 500 μW and a pump energy set to $n = 16$, we obtain the red curve, showing a lower amplitude of absorption on resonance and an amplified absorption on the sides. In case of a modulated pump beam, the probe laser again scans the resonance. Since the modulation with a period of 300 μs is fast compared to the scan speed of 1 GHz/s$\approx$ 1 μeV/250ms, the signal can be interpreted as varying locally at a certain probe energy in time according to the amplitude variation in the CW-picture. This is shown in Fig. 3.2 (b). The amplitude of this oscillation is directly proportional to the difference between the transmitted intensities with and without a pump beam, amplified by an arbitrary gain factor c_{gain}

$$\Delta I = c_{\text{gain}} \left(I_{\text{T, pump}} - I_{\text{T, no pump}}\right) \ . \tag{3.5}$$

The gain can be set at both the diodes and the Lock-In amplifier. The signal is integrated at the low-pass filter. A time constant of 30-100 ms turns out to be optimal. Finally, we obtain the DC-signal in Fig. 3.2 (c). Constant offsets in the signals are canceled out in the difference and only relative signals are measured.

With this scheme, small changes in transmission spectra induced by the pump laser can be measured with high accuracy and a low level of noise, since only variations around the frequency ω_{m} are amplified and others are reduced. Additionally one gets rid of interferences in the probe signal, since they do not change with varying pump power.

3.2 White light excitation and external fields

An alternative way to obtain absorption spectra is to use a broad band white light source instead of a laser. Here, we use the LDLS ("Laser Driven Light Source") from Energetiq. Before hitting the sample, the light's bandwidth is limited to the spectral range of the yellow series by a double monochromator. The light transmitted by the sample is dispersed by a second double monochromator (Spex) and detected with a CCD camera that yields a resolution of 2.6 μeV. As reported in Ref. [Kaz+14], the exciton series ends around $n = 15$ with this excitation scheme, while the exact reason is still the subject of research. However, a huge advantage compared to laser excitation is the time required to measure a spectrum of the spectral range from $n = 5$ to the band gap. It takes about 10 seconds, whereas a laser scan needs about 15 minutes. Hence, white light excitation is mainly used for measurements in external fields, where many spectra at various field strengths are taken.

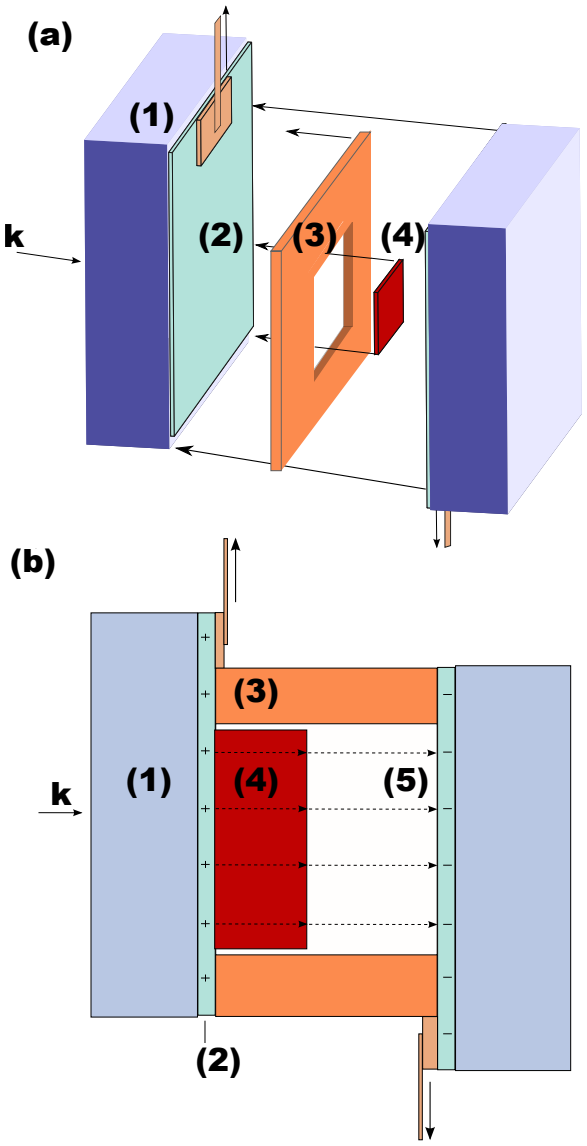

Figure 3.3 Exploded view (a) and view from the side (b) of the sample holder used for the application of electric fields along k. (1) quartz plates (2) ITO layer (3) kapton spacer (4) sample (5) free space filled with liquid helium. From [Hec+17a].

Magnetic fields are applied by the built-in superconducting magnet coils in the cryostats. For electric fields a sample holder as schematically shown in Fig. 3.3 is used. It was optimized in the context of Ref. [Hec15] and shall be briefly explained here.

The sample is mounted between two quartz plates of 5 mm thickness. They are covered with indium tin oxide (ITO), that serves as an electrically conducting but transparent electrode, and are shifted slightly relative to each other. The protruding parts are then covered by an adhesive copper foil and connected via cables to a function generator. To avoid direct contact, both plates are separated by an insulating kapton foil with a recess for the sample (see object (3) in Fig. 3.3). The thickness of the foil of 75 μm is chosen to be larger than the sample thickness of 30 or 50 μm to ensure strain-free mounting. The voltage is applied as an AC-signal of 1 MHz. The alternating sign avoids field neutralization inside the sample by surface charges.

3.3 Samples

In this work, four different samples are used. All of them are natural high-quality crystals of Cu_2O from the Tsumeb mine in Namibia and show Rydberg excitons with quantum numbers $n > 20$. They differ in thickness and orientation. They are denominated $H7$, $H93$, $H103$ and $H98$.

Sample $H7$ has a thickness of $d = 34$ μm and is known to exhibit the best spectra concerning the number of observable n. This sample is used for all measurements without external fields. The crystal is not oriented along a high symmetry axis. However, for the dipole excitation of P-shell excitons, the configuration of light vector $\mathbf{k}$ and polarization $\hat{\mathbf{e}}$ does not matter.

For investigations of quadrupole excitations or the application of external fields, typically crystals with an orientation along a high symmetry axis are used. These are the samples $H93$, $H103$ and $H98$.

In samples $H93$ and $H103$, the $\mathbf{k}$-vector is parallel to the direction [110]. The polarization of linearly polarized incident light can be oriented along both perpendicular directions $\hat{\mathbf{e}}||[1\bar{1}0]$ or $\hat{\mathbf{e}}||[001]$. Sample $H93$ has a thickness of $d \approx 30$ μm and sample $H103$ has a thickness of $d \approx 50$ μm.

Sample $H98$ is oriented along the [100]-direction with equivalent directions for the polarization of incident light $\hat{\mathbf{e}}||[010]$ and $\hat{\mathbf{e}}||[001]$.

Chapter 4

Scaling laws in external electric and magnetic fields

Atoms, excited to Rydberg states with large principal quantum numbers n, reveal astonishing properties compared to their corresponding ground states. With increasing n, not only their radius but also their dipole moments increase and the strengths of interactions among each other grow over orders of magnitude. In the same manner, their sensitivity to external fields rises, opening the possibility to study Rydberg physics and fundamental properties in the high-field regime, where the interaction energy with external fields exceeds the Coulomb interaction.

Based on this idea, the investigation of Rydberg excitons in a controlled environment of external electric or magnetic fields is an important tool to study the physics of highly excited excitonic states. Compared to atoms, the Rydberg energy of about 90 meV is reduced by two orders of magnitude which makes the high-field regime accessible with comparably low experimental effort. Therefore, the regime of ionization in electric fields or the formation of Landau levels in magnetic fields can be studied extensively.

The effects of external fields on excitons were investigated directly in the years after their discovery ([Gro62; Age+74; Age77]) with the focus on low-n states with principal quantum numbers up to $n = 9$. These experiments already revealed fundamental insights into analogies and differences to atomic physics and demonstrated the excitonic Stark effect in electric fields as well as the Zeeman splitting and formation of Landau levels in magnetic fields.

After the discovery of Rydberg excitons in 2014 [Kaz+14], analogue experiments were performed with unprecedented resolution and described by microscopic theories including the detailed aspects of the full Hamiltonian from Sec. 2.3.1 and the exact band structure. Expansive calculations taking into account the exact band structure allowed a quantitative description of the experimental data [Sch+17b; Rom+18; Hec+17a]. However, from the theoretical point of view, these investigations were limited to the regime with $n \leq 6$. In the high-n Rydberg regime, exact solutions of the Hamiltonian become more and more complex, since the number of involved states increases drastically. In magnetic fields, the high-field regime reveals signatures of chaotic behavior that was studied with the help of statistical methods in Refs. [Aßm+16; Fre+17].

To address this regime further, we focus here on scalable quantities that can be uniquely determined in the low-n regime and interpolated for the high-n regime. The validation of scaling laws for excitonic properties both experimentally and theoretically provides access to the understanding of these properties in the high-n regime.

Therefore, we study in this chapter characteristic scaling laws of Rydberg excitons mainly

by the use of external electric and magnetic fields. From Ch. 2 we already know the scaling of the radius with n^2 and binding energy with n^{-2}, or the inverse lifetime and oscillator strength with n^{-3} ($n \gg 1$). Here, we find scaling laws for various other significant physical properties in dependence on the principal quantum number n, named below, and compare the results with the analogue phenomena known from atomic physics. This allows for a more comprehensive comparison between Rydberg excitons and Rydberg atoms. Surprisingly we find mostly similarities between the scaling behaviors of excitons and atoms even though the underlying mechanisms are different in most cases. The aspects are considered from both experimental and theoretical points of view.

In Sec. 4.1, the effect of an electric field on the exciton spectrum is considered and explained within the Stark effect model. States that are optically dark without external fields can be activated by application of an electric field. First of all, this is used to study the spectral width of the exciton multiplets as a function of n. The results can be explained with the use of the Hamiltonian from Ch. 2. Next, scaling properties of the polarizability (Sec. 4.1.2), resonance voltage and anticrossing energy splittings (Sec. 4.1.3), as well as the disappearance due to ionization by the electric field (Sec. 4.1.4) are investigated.

This is followed by the study of magneto-optical properties in Sec. 4.2, where we investigate excitonic spectra in magnetic fields. We find a crossover field strength B_r from the Coulomb-dominated exciton regime to a Landau-level-dominated regime (Sec. 4.2.2) and a scaling law for the crossing of states originating from adjacent multiplets (Sec. 4.2.3).

The experimental observations are in good agreement with theoretical predictions. Finally, the results are summarized in Tab. 4.1 with a comparison to atomic physics.

The results presented here are published as parts of the following publications: [Hec+17a; Hec+17b; Hec+18c; Hec+18e]. The theoretical investigations shown here are developed by Marina Semina and Mikhail Glazov from Ioffe Institute of the Russian Academy of Sciences.

4.1 External electric fields

The spectral width of a multiplet is the energy difference between the lowest state in a multiplet and the highest. In particular these are the $S^{(1)}_{1/2}$ and $D^{(1)}_{3/2}$ Ortho-excitons (cf. Sec. 2.3.1)[1]. Without external fields, these states are forbidden in dipole but weakly allowed in quadrupole transitions (cf. see Sec.2.4). However, the quadrupole transitions are weak and negligible for $n > 3$.

To get optical access to these states we subject them to an electric field. The underlying physics is known as the Stark effect and shall be summarized briefly in the following.

For simplicity, we assume a two-state system of a dark S-shell state and a dipole allowed P-shell state with non-degenerate energies E_S and E_P. The electric field is applied parallel to the light vector $\mathbf{k}$, i.e. along the $k||[001]$ direction in this example. A scheme of the sample holder can be found in Fig. 3.3 ind Sec. 3.2. The perturbation operator is then given by

$$H_{\mathcal{E}} = -e\boldsymbol{\mathcal{E}}\mathbf{r} = -e\mathcal{E}z \tag{4.1}$$

[1]Note that in principle, the nS-Para exciton would be the lowest state of a multiplet, the energy of which is about the magnitude of exchange interaction below the Ortho-state. However, since the contribution of exchange interaction scales as n^{-3} (see below), it's non-visibility does not change the results.

with the field amplitude $\mathcal{E} = |\boldsymbol{\mathcal{E}}|$ and coordinate of relative motion $\mathbf{r}$.

Since z is a basis function of Γ_4^- the electric field is an operator of odd parity (in analogy to the electric-dipole transition in Sec. 2.1). With a linear polarization $\hat{\mathbf{e}}||[100]$ one excites the dipole-allowed wave function, according to [Kos+66]:

$$\Psi_{4x}^- = \frac{1}{\sqrt{2}} \left(\Gamma_{5xy}^+ \Gamma_{4y}^- + \Gamma_{5xz}^+ \Gamma_{4z}^- \right) \ . \tag{4.2}$$

Here, $\Gamma_{5,ij}^+$ $(i,j = x,y,z)$ represent the spin linear combinations of the Γ_7^+ valence band and the Γ_6^+ conduction band Bloch amplitudes, given by Eqs. (2.29), (2.30) and (2.31), and Γ_{4y}^- and Γ_{4z}^- can be identified with the P-shell envelopes P_y and P_z (cf. Eq. (2.33)).

Since the electric field in z direction couples to P_z states only we consider off-diagonal matrix elements of the form

$$\begin{aligned} \gamma_{SP} &= \gamma_0 \mathcal{E} \left\langle \Gamma_{5xz}^+ P_z \right| z \left| \Gamma_{5xz}^+ S \right\rangle \\ &= \gamma_0 \mathcal{E} \left\langle P_z \right| z \left| S \right\rangle \ , \end{aligned} \tag{4.3}$$

where we used $\left\langle \Gamma_{5i} \middle| \Gamma_{5j} \right\rangle = \delta_{ij}^K$ (δ_{ij}^K is the Kronecker symbol) and set $\gamma_0 = -e/\sqrt{2}$. Since they are linear combinations of the former pure states, the new eigenstates contain both an S and a P character. In particular, this leads to the visibility in absorption of the former dark S state due to its P admixture. In addition, we find new eigenenergies that can be obtained by perturbation theory up to second order (see for example [Coh+07]). For the former pure S state it reads in this particular case

$$\tilde{E}_S = E_S + \gamma_0 \mathcal{E} \left\langle S \right| z \left| S \right\rangle + \gamma_0^2 \mathcal{E}^2 \frac{\left| \left\langle P_z \right| z \left| S \right\rangle \right|^2}{E_S - E_P} \ . \tag{4.4}$$

Here, the correction term to first order describes the linear Stark effect between degenerate states and vanishes due to parity. Since z transforms as Γ_4^-, the electric field will only couple states of opposite parity. In case of degenerate states with opposite parity as given in hydrogen, this term dominates, see below. The last term describes an energy shift $\propto \mathcal{E}^2$ and is known as the quadratic Stark effect. Since $E_S - E_P < 0$, the S state is shifted to lower energies.

This is what we observe in the spectra in Fig. 4.1. It shows contour plots of the second derivative of white light transmission spectra in the spectral range of $n = 5$ and $n = 6$ as a function of applied voltage U. The spectra are recorded with the white light setup described in Sec. 3.2. For zero field, the transmission spectrum is shown in the left panel. The absorption peaks are translated into a white color coding in the panels (a) to (c), whereas darker colors denote no absorption.

The configuration discussed above with $\mathbf{k}$=[001] and $\hat{\mathbf{e}}$=[100] is shown in panel (a). We observe a Stark-splitting of non-degenerate states belonging to the multiplets of $n = 5$ and $n = 6$ with quadratically developing energies, indicated by the dashed lines. States, that are dark without electric field become visible due to the state mixing with odd-parity excitons. In particular, this can be seen for the states of lowest and highest energy. These are the $S_{1/2}^{(1)}$ and $D_{3/2}^{(1)}$ Ortho-excitons (red dashed lines).

Obviously, the system involves many more states than only two P and S states as in the simple model. For a theoretical description one needs to include matrix elements between

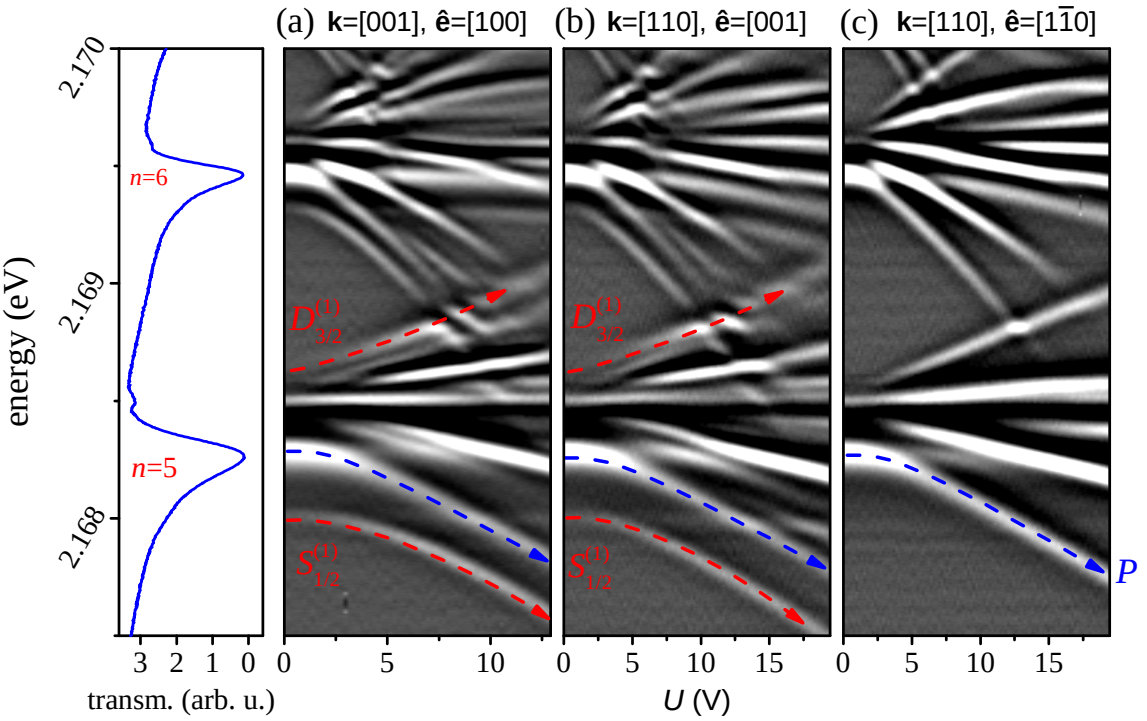

Figure 4.1 Left panel: Transmission spectrum of $n = 5$ and $n = 6$ at 1.35 K without electric field, dominated by large P and small F absorption peaks. Panels (a), (b) and (c) show contour plots of the second derivative of transmission spectra for different applied voltages. White colors denote absorption, dark colors denote no absorption. With increasing field, a Stark fan grows that includes also former dark states. In configurations (a) and (b), $S^{(1)}_{1/2}$ and $D^{(1)}_{3/2}$ excitons become visible (red dashed lines), whereas they stay dark in configuration (c). The overall number of lines is reduced in the configuration in (c). Adapted from [Hec+17a].

all involved states, namely between P and D or F and D excitons and higher angular momentum states. Strictly speaking, the electric field couples dipole-active Γ_4^- states to all states including $\Gamma_4^- \otimes \Gamma_4^- = \Gamma_1^+ \oplus \Gamma_3^+ \oplus \Gamma_4^+ \oplus \Gamma_5^+$. Additionally one needs to include states of different principal quantum numbers n. Nevertheless, the coupling to states of different n will have a minor impact on the energy corrections of a particular state due to the larger difference in energy. A detailed theoretical analysis that includes states up to $n = 6$ is given in [Hec+17a].

Now, we consider different configurations of $\mathbf{k}$ and $\hat{\mathbf{e}}$. The electric field is applied along the $\mathbf{k}||[110]$ axis, whereas the polarization is chosen to be linear and along the directions $\hat{\mathbf{e}}||[001]$ or $\hat{\mathbf{e}}||[1\bar{1}0]$. The corresponding spectra are shown in Fig. 4.1 (b) and (c).

Again, we restrict our analysis to the simple case of states with P and S character. With the polarization chosen along $\hat{\mathbf{e}}||[001]$, one excites a linear combination of dipole allowed states

$$\Psi^-_{4z} = \frac{1}{\sqrt{2}} \left(\Gamma^+_{5xz} \Gamma^-_{4x} + \Gamma^+_{5yz} \Gamma^-_{4y} \right) \ . \tag{4.5}$$

The electric field along [110] is described by

$$H_{\mathrm{E}} = -e\mathcal{E}(x+y) \tag{4.6}$$

and the matrix elements now read

$$\begin{aligned} \gamma_{SP} &= \gamma_0 \mathcal{E} \left\langle \Gamma_{5xz}^{+} P_x + \Gamma_{5yz}^{+} P_y \,\middle|\, x+y \,\middle|\, \Gamma_{5xz}^{+} S + \Gamma_{5yz}^{+} S \right\rangle \\ &= \gamma_0 \mathcal{E} \left(\langle P_x \,|\, x \,|\, S \rangle + \left\langle P_y \,\middle|\, y \,\middle|\, S \right\rangle \right) \ . \end{aligned} \tag{4.7}$$

In this configuration, we receive non-vanishing matrix elements in analogy to the configuration discussed above. Hence, the overall appearance of the spectra in panel (b) is similar to the spectra shown in panel (a).

However, in the polarization $\hat{\mathbf{e}}||[1\bar{1}0]$ (panel (c)) we find a different situation: The $S_{1/2}^{(1)}$ and $D_{3/2}^{(1)}$ Ortho-excitons do not gain oscillator strength with rising electric field. In general the Stark fan shows an overall-reduced number of states compared to the other configurations. At least for the S states, one can find an explanation within our simple model:

First, we excite all three components of Γ_4 states

$$\begin{aligned} \Psi_{ges}^{-} &= \Psi_{4x}^{-} - \Psi_{4y}^{-} = \frac{1}{\sqrt{2}} \left(\Gamma_{5xy}^{+} \Gamma_{4y}^{-} + \Gamma_{5xz}^{+} \Gamma_{4z}^{-} - \Gamma_{5xy}^{+} \Gamma_{4x}^{-} - \Gamma_{5yz}^{+} \Gamma_{4z}^{-} \right) \\ &= \frac{1}{\sqrt{2}} \left(\Gamma_{5xy}^{+} (\Gamma_{4y}^{-} - \Gamma_{4x}^{-}) + (\Gamma_{5xz}^{+} - \Gamma_{5yz}^{+}) \Gamma_{4z}^{-} \right) \ . \end{aligned} \tag{4.8}$$

Here, the electric field does not couple to the P_z component and we can write

$$\begin{aligned} \gamma_{SP} &= \gamma_0 \mathcal{E} \left\langle \Gamma_{5xy}^{+} (P_y - P_x) \,\middle|\, x+y \,\middle|\, \Gamma_{5xy}^{+} S \right\rangle \\ &= \gamma_0 \mathcal{E} \left(\left\langle \Gamma_{5xy}^{+} P_y \,\middle|\, y \,\middle|\, \Gamma_{5xy}^{+} S \right\rangle - \left\langle \Gamma_{5xy}^{+} P_x \,\middle|\, x \,\middle|\, \Gamma_{5xy}^{+} S \right\rangle \right) \\ &= 0 \ . \end{aligned} \tag{4.9}$$

Remarkably, both contributions cancel out each other and the off-matrix elements vanish. Hence, dark S states cannot be activated in this particular configuration.

This is different for other dark states as, for instance, D-shell excitons with $\Gamma_3^+ \oplus \Gamma_5^+$ envelope symmetry: The basis functions read $2z^2 - x^2 - y^2$ and $\sqrt{3}(x^2 - y^2)$, from which the latter gives non-vanishing contributions in Eq. (4.9). A detailed analysis shows that the $D_{5/2}$ excitons still obtain oscillator strength, whereas the $D_{3/2}^{(1)}$ does not [Hec+17a].

This strong polarization dependence clearly results from the cubic symmetry of our system which is different from the atomic case. It turns out to be a useful experimental tool, especially as we are interested in the physics at high n. With polarization $\hat{\mathbf{e}}||[1\bar{1}0]$ we can reduce the number of states in the Stark fan, in particular of the $S_{1/2}^{(1)}$ and $D_{3/2}^{(1)}$ states. It simplifies the analysis of the spectra and enables the investigation of the polarizability of P states (Sec. 4.1.2) as well as the identification of anticrossings between adjacent multiplets (Sec. 4.1.3). The comparison of both polarizations is shown in Fig. 4.2, now for all states $n > 4$.

Beside the differences arising due to the strong polarization dependence, we observe for both polarizations a disappearance of states with increasing voltage due to ionization. The effect is more pronounced the higher the n is. States on the high energy side within a multiplet are found to be more robust than states on the opposite side. This is discussed in Sec. 4.1.4.

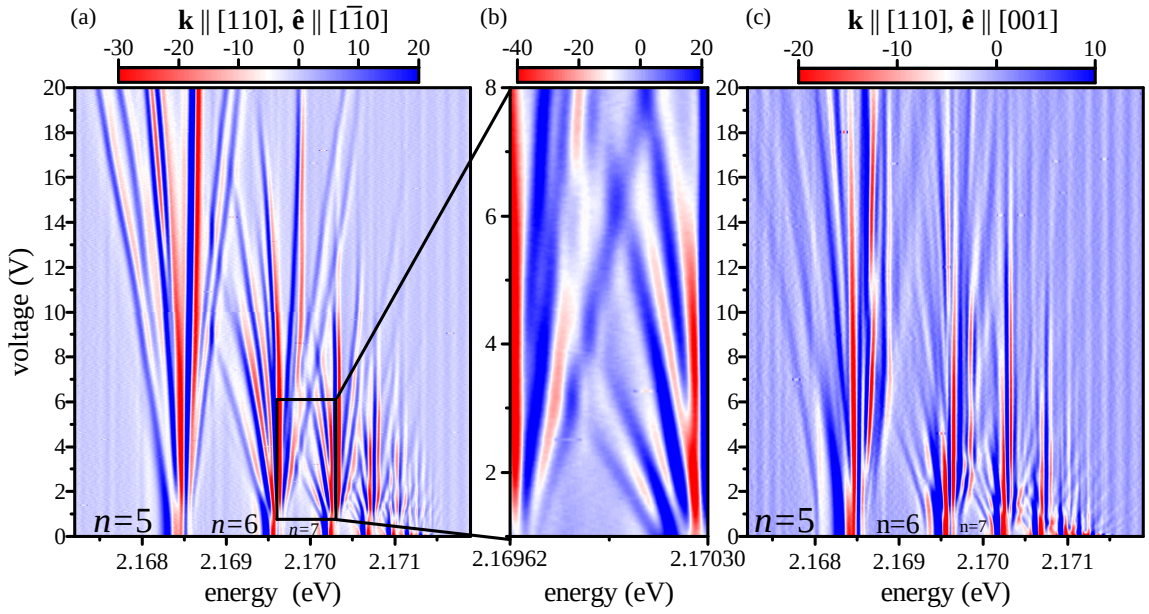

Figure 4.2 Contour plots of the second derivative of transmission spectra with $\mathbf{k}|||[110]$ at 1.35 K, for all states from $n = 5$ to the band gap. The number of visible states per multiplet is reduced for polarization $\hat{\mathbf{e}}||[1\bar{1}0]$, shown in panel (a), allowing for a better resolution of resonances between adjacent multiplets. Panel (b) shows a closeup of the resonance area between $n = 6$ and $n = 7$, revealing that the states actually anticross. Panel (c) shows the same spectral range with polarization $\hat{\mathbf{e}}|||[001]$. With increasing n, the ionization voltage decreases. Adapted from [Hec+17b].

4.1.1 Multiplet splitting

Due to the activation of dark states, we can estimate their binding energy by extrapolating the dispersions back to zero electric field. From their binding energies, we can evaluate the spectral width of a given multiplet n. This width decreases with increasing n as can be seen in Figs. 4.1 and 4.2. As discussed in Sec. 2.3.1, the energy splittings stem from deviations from a parabolic valence band dispersion that manifest in a p^4-dependence in the H_d term. The excitonic energies within a multiplet are further split by spin-orbit interactions H_so and states with $l = 0$-contribution are further affected by the exchange interaction H_exch.

In summary, the relevant contributions read (here, simplified with amplitudes A, B_e, B_h, C and in Gaussian units)

$$H_\mathrm{d} + H_\mathrm{so} + H_\mathrm{exch} = Ap^4 + \frac{e^2}{\epsilon_s r^3}[B_\mathrm{e}(\mathbf{l}\cdot\mathbf{s}_\mathrm{e}) + B_\mathrm{h}(\mathbf{l}\cdot\mathbf{s}_\mathrm{h})] + C\delta(\mathbf{r})(\mathbf{s}_\mathrm{e}\cdot\mathbf{s}_\mathrm{h}) \ . \tag{4.10}$$

Furthermore, central-cell corrections might be necessary for states with $l = 0$, that can also be included into a term $\propto \delta(\mathbf{r})$.

To derive an n dependence we consider the terms leading in the inverse quantum number

that read (see for example [Coh+07])

$$\langle p^4 \rangle_{nlm} = \left(\frac{\hbar}{a^{\mathrm{B}}}\right)^4 \frac{4}{n^3(l+1)} , \tag{4.11}$$

$$\left\langle \frac{1}{r^3} \right\rangle_{nlm} = \frac{1}{(a^{\mathrm{B}})^3} \frac{1}{n^3 l(l+1/2)(l+1)} , \tag{4.12}$$

$$\langle \delta(\mathbf{r}) \rangle_{nlm} = \frac{\delta^K_{l,0}}{\pi} \frac{1}{a^{\mathrm{B}} n^3} , \tag{4.13}$$

with the quantum-mechanical average over an exciton state $\Psi_{nlm}(\mathbf{r})$ given by $\langle ... \rangle_{nlm}$. $\delta^K_{l,0}$ is the Kronecker symbol, giving contributions only for $l = 0$. We see, that all these corrections produce level shifts and splittings decreasing as $\propto n^{-3}$.

This finding is in accordance with the quantum defect model, for which one can estimate the n-dependent scaling via a Taylor expansion of the binding energy for small $\delta_{n,l}$:

$$E^{\mathrm{b}}_{n,l} = \frac{Ry}{(n-\delta_{n,l})^2} \approx \frac{Ry}{n^2} + \frac{2\delta_{n,l} Ry}{n^3} - \frac{3\delta^2_{n,l}}{n^4} . \tag{4.14}$$

Again, the l-dependent corrections, comprised in $\delta_{n,l}$, lead in first order to changes in the binding energies following an n^{-3}-scaling.

We compare this expectation with the obtained multiplet widths from the spectra in Fig. 4.2 extrapolated to zero field. The widths are plotted against n in a double logarithmic plot in Fig. 4.3. They decrease from about 3 meV for $n = 3$ to less than 0.1 meV for $n > 10$. A fit to the data with n^{-d} yields $d = 2.75 \pm 0.02$, which is in reasonable agreement with the expected scaling. The fit error is indicated by the grey area. The red line gives a fit with the theoretical scaling following an n^{-3} law. The deviations from the expected scaling start to occur around $n = 10$ and might be traced back to the broadening of linewidths, starting around $n = 10$ as well (see Fig. 2.4 (c)), that might influence the line shapes even in the second derivative. Still, the n^{-3} fit falls within the experimental error of the data points.

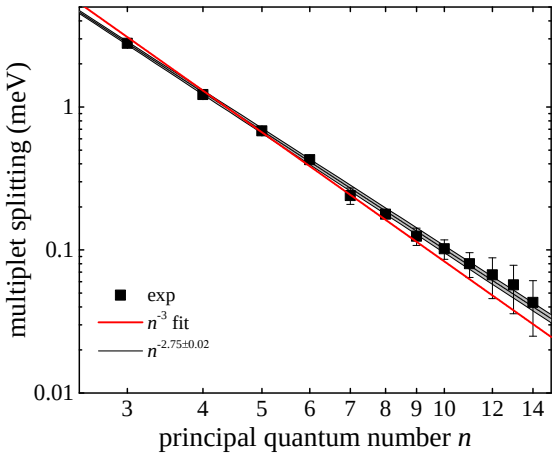

Figure 4.3 Multiplet widths as a function of principal quantum number n. Black squares give experimental data, the red line shows a fit with the expected n^{-3} scaling according to the discussion in the text. The black line is a fit to the data with $n^{-2.75\pm0.02}$. The grey shaded area indicates the fit error. From [Hec+17b].

4.1.2 Polarizability

The quadratic shift of the exciton energy in an electric field is determined by the polarizability α_{nl} of the state. In the simple two-state model discussed before, the polarizability

is given by the last term in Eq. (4.4)

$$\Delta E_{nl} = -\alpha_{nl}\mathcal{E}^2 \propto \frac{|\langle P_z|z|S\rangle|^2}{E_S - E_P}\mathcal{E}^2 \ . \tag{4.15}$$

To calculate the n dependence, the information from Sec. 4.1.1 can be used: Since states with the same n but different angular momentum quantum numbers l are spread by the H_d term and exchange interactions, their energy difference given in the denominator scales as n^{-3}. The numerator contains the dipole operator matrix element between neighboring states of the same n, that scales as n^2. Therefore $\langle r_{n,l}\rangle|^2 \propto n^4$ and we end up with

$$\alpha_{n,l} \propto n^7 \ . \tag{4.16}$$

This scaling is different for hydrogen, where states within the same multiplet are regarded as degenerate. The full solution of the Hamiltonian is typically given in parabolic coordinates n_1 and n_2, for which the Stark problem is separable and has analytical solutions. They are related to n and m via

$$n = n_1 + n_2 + |m| + 1 \ . \tag{4.17}$$

The energy of hydrogen in an electric field reads in atomic units up to second order [Lan+77; Gal94]

$$E_{nn_1n_2m} = -\frac{1}{2n} + \frac{3}{2}\mathcal{E}(n_1 - n_2)n - \frac{\mathcal{E}^2}{16}n^4[17n^2 - 3(n_1 - n_2)^2 - 9m^2 + 19] \ . \tag{4.18}$$

Here, the linear term in $\mathcal{E}$ between states of the same n and different l can give non-zero contributions. The last term describes the quadratic shift and scales as n^6, which is different from the non-degenerate case. Strictly speaking, the differentiation between linear and quadratic Stark shifts depends on the experimental resolution and the regime of applied field strengths that is considered. As long as the multiplet width and splitting of states is large compared to the energy shift induced by the field, a quadratic dispersion will be observable for low enough fields. With increasing field strength it transforms into a linear shift. Since the multiplet widths shrink with n one observes almost linear Stark fans in the high-n regime of Fig. 4.2.

Experimentally, we evaluate the polarizability $\alpha_{n,S,P}$ from the quadratic dispersions of the S and P states with increasing

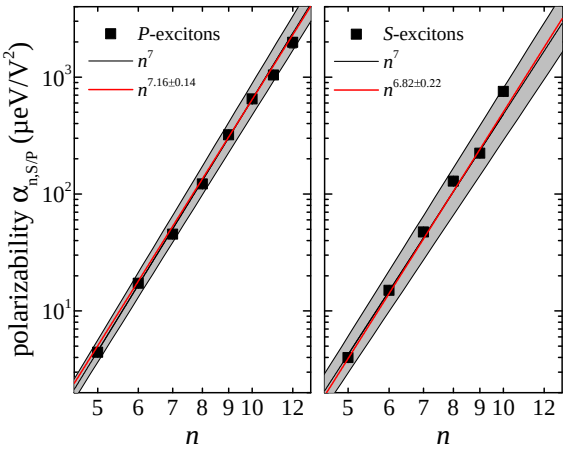

Figure 4.4 Polarizability $\alpha_{n,l}$ of P (left panel) and S excitons (right panel) as a function of n. Black squares are experimental data obtained from the dispersions in Fig. 4.2. The red lines show a fit $\propto n^7$ as predicted by theory. The black lines show a fit with n^d with $d = 7.16 \pm 0.14$ for P excitons and $d = 6.82 \pm 0.22$ for S excitons. The fit errors are indicated by the grey area. From [Hec+17b].

voltage in Fig. 4.2. We choose the configurations of $\mathbf{k}$ and $\hat{\mathbf{e}}$ where they are best observable. For P excitons this is possible up to $n = 12$ in polarization $\hat{\mathbf{e}}||[1\bar{1}0]$, whereas the dispersions of S excitons can be identified up to $n = 10$ in $\hat{\mathbf{e}}||[001]$.

The obtained values are shown in Fig. 4.4. The polarizability increases from about 5 μeV/V^2 for $n = 5$ to about 2000 μeV/V^2 for $n = 12$, following the expected scaling with n^7 as indicated by the red line. A fit with a power law $\propto n^d$ yields $d = 7.16 \pm 0.14$ for the P states, which is in perfect accord with the model within the error. For S states we find similar polarizabilities as for P states. Therefore, an n^7 law describes the data within satisfying agreement, which is confirmed by the exponent $d = 6.82 \pm 0.22$ of a variable fit.

4.1.3 Electric field-induced anticrossings

Taking a closer look at the overall appearance of the Stark structure in Fig. 4.2, one finds states of adjacent multiplets n and $n+1$ coming into resonance at a certain field strength $\mathcal{E}_r$. Fig. 4.2 (b) shows a closeup of the resonance between multiplets $n = 6$ and $n = 7$. Instead of a pure crossing - as observed in magnetic fields (cf. Sec. 4.2.3) - the states avoid each other and anticrossings appear. Since the electric field couples states of different parities, the states that come into resonance become mixed and avoid each other. First, we focus on the resonance field strengths $\mathcal{E}_r$ at which these anticrossings appear. In a next step, we analyze the spectral width of each anticrossing. To derive a scaling law for the resonance field strength, we can neglect the initially quadratic dispersions as we are interested in the regime of higher fields, where the dispersions are almost linear. Hence, we assume a linear Stark shift as it is given in first order by the hydrogen model in Eq. (4.18).

Since the states at the edge of a Stark fan belong to the quantum numbers $\{n_1 = n - 1, n_2 = 0\}$ and $\{n_1 = 0, n_2 = n-1\}$, which gives $n_1 - n_2 \approx \pm n$, one finds a first-order Stark splitting $\propto n^2$ [Lan+77]. The lowest and highest states of adjacent multiplets n and $n+1$ will cross at a field strength $\mathcal{E}_r$, that is given by

$$\begin{aligned} E_n &= E_{n+1} \\ \Leftrightarrow -\frac{1}{2n^2} + \frac{3}{2}\mathcal{E}_r n^2 &= -\frac{1}{2(n+1)^2} - \frac{3}{2}\mathcal{E}_r (n+1)^2 \\ \Leftrightarrow \mathcal{E}_r &= \frac{2n+1}{3(2n^6 + 6n^5 + 7n^4 + 4n^3 + n^2)} \ . \end{aligned} \tag{4.19}$$

The first term dominates and we find

$$\mathcal{E}_r \propto n^{-5} \ . \tag{4.20}$$

We use the experimental configuration shown in Fig. 4.2 (a), the one with a reduced number of states, to investigate the anticrossings experimentally. The field strengths $\mathcal{E}_r$ in the experiment are assumed to be directly proportional to the applied voltages U_r. These can be read out from the spectra and show a strong decrease with n. The obtained values are shown in Fig. 4.5 (a) as a function of principal quantum number n. U_r decreases from 8 V for $n = 5$ to about 40 mV for $n = 13$. The data obviously exhibits a power law. A fit $\propto n^{-d}$ yields $d = 5.33 \pm 0.11$, as shown by the black line. The error is indicated by the grey area. The fit is in reasonable agreement with the expectation of $d = 5$, that is

additionally shown by the red line. Deviations might stem from the conversion between applied voltage and field strength, whose proportionality constant might vary slightly for high and low voltages. Note that the influence of surface charges or charged defects can lead to depolarization effects in the crystal, making the exact evaluation of the present field strength complicated.

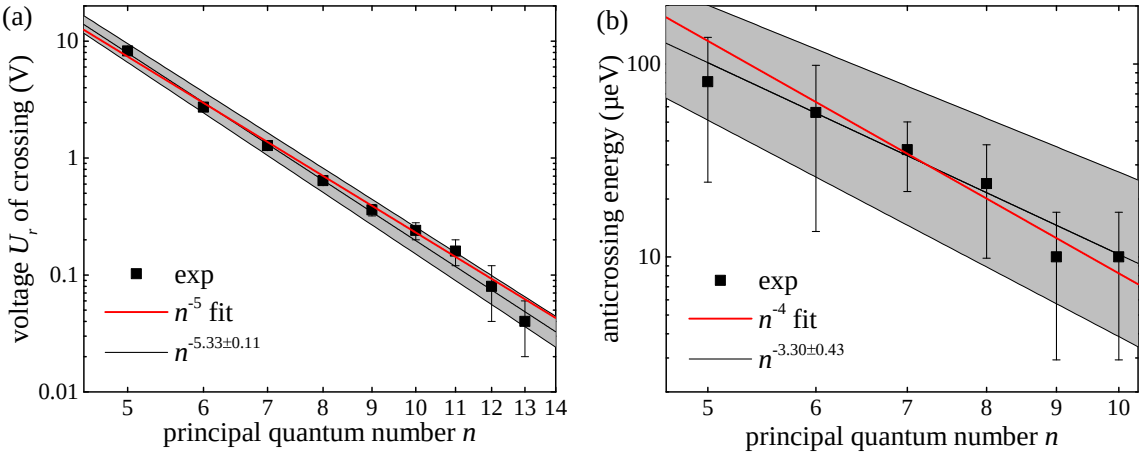

Figure 4.5 (a) Resonance voltage U_r of anticrossing between states of adjacent multiplets n and $n+1$ as a function of principal quantum number n. The values follow an n^{-d} dependence with $d = 5.33 \pm 0.11$ (black line) that is close to the theoretical expectation of $d = 5$ (red line). (b) Energy splitting of anticrossings at voltages U_r as a function of n. A fit to the data shows a scaling with n^{-d} with $d = 3.30 \pm 0.42$, which slightly deviates from the expected scaling with n^{-4}. In both panels, the grey areas indicate fit errors. From [Hec+17b].

From the data in Fig. 4.2 (a), we can even determine the energy splitting at the anticrossing, see the closeup of the anticrossing in Fig. 4.2 (b). The obtained values for the states from $n = 5$ to $n = 10$ are shown in Fig. 4.5 (b). The splitting energies decrease from about 80 μeV for $n = 5$ down to about 10 μeV. We obtain quite large error bars from the fact that the splittings are only slightly larger than the linewidths of the involved lines in the second-derivative spectra. Nevertheless, the data allows for an estimation of a scaling law. A power-law fit with n^{-d} yields $d = 3.30 \pm 0.43$ shown by the black line and grey area. The red line gives a fit to the data with the theoretical expectation $\propto n^{-4}$ that still describes the data within the experimental errors.

A derivation of the theoretical expectation for the anticrossing energy can be found in Refs. [Kom+80] and [Gal94] for non-hydrogenic atoms. In analogy, we derive the splitting for excitons from the contributions of the H_d-term of the Hamiltonian. The anticrossing energy is then given by

$$\delta E_{anti} = 2 \left| \int d\mathbf{r} \Psi^*_{n' n'_1 n'_2 m}(\mathbf{r}) H_\mathrm{d} \Psi_{n n_1 n_2 m}(\mathbf{r}) \right| . \tag{4.21}$$

We insert $\sum_l |nlm\rangle \langle nlm| = 1$ for n and n', and use the following relation between hydrogenic states with adjacent principal quantum numbers $n' = n \pm 1$ and the quantum defect

$\delta_{n,l}$ [Gal94]

$$\int d\mathbf{r}\Psi^*_{n'lm}(\mathbf{r})H_\mathrm{d}\Psi_{nlm}(\mathbf{r}) \sim \frac{\delta_{n,l}Ry}{n^3} \ .$$

Finally, taking into account that

$$\sum_l \int d\mathbf{r}\Psi^*_{n'n'_1n'_2m}(\mathbf{r})\Psi_{nlm}(\mathbf{r}) \propto \frac{1}{n-m} \ ,$$

we obtain the n-dependent scaling

$$\delta E_{anti} \sim \frac{\delta_{n,l}Ry}{n^3(n-m)} \propto n^{-4} \ , \tag{4.22}$$

that is shown in by the red line in Fig. 4.5.

4.1.4 Ionization

Another observation in Fig. 4.2 is that the emergence of Stark fans results in a disappearance of lines in the spectra, which is associated with exciton dissociation. For states with higher n the field strengths necessary for a multiplet to vanish are smaller than for states with low n. Whereas the Stark fan of the $n = 5$ multiplet is visible up to 20 V, for $n = 10$ already 2 V are sufficient to completely dissociate the multiplet.

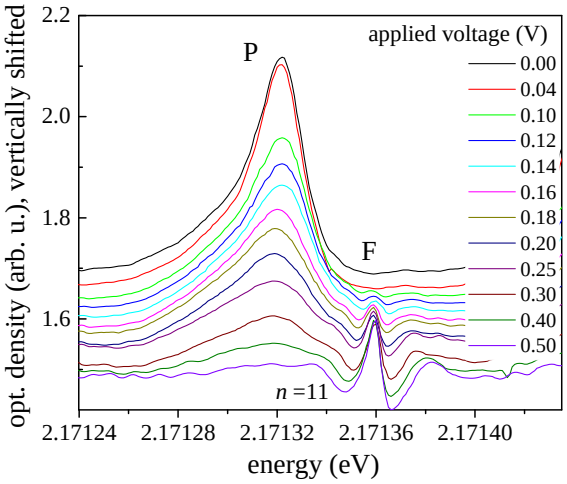

Figure 4.6 Absorption spectrum of $n = 11$ exciton multiplet for different applied voltages from 0 (top) to 0.5 V (bottom). The dominant P absorption vanishes, whereas F states mainly gain oscillator strength. Lines are shifted vertically for clarity. From [Hec+17b].

Figure 4.6 shows a closeup of the absorption spectrum around the $n = 11$ multiplet in an increasing electric field. Without electric field, the spectrum is dominated by the P absorption line. With increasing field, the P line broadens and vanishes, while on its high energy side new features appear, that are associated with high angular momentum states, such as D-, F- or G-shell states. The increase in visibility of these states is directly connected to the shuffling of oscillator strength between the excitons of different parity through the electric field as discussed at the beginning of Sec. 4.1. At high fields, the emerging feature on the high energy side starts to broaden as well.

However, it is interestingly to note that the latter is still growing, while the P exciton line already disappeared completely. We conclude, that low angular momentum states are more susceptible to ionization than high-l states.

Now, we focus on the ionization of P excitons. In analogy to atomic physics, we assume an electric field in z direction according to Eq. (4.1) that tilts the Coulomb potential along the field axis. The Hamiltonian for this process reads (in atomic units) [Gal94]

$$H = -1/|z| - \mathcal{E}z \ . \tag{4.23}$$

The potential exhibits a local maximum along the field axis at $z' = \frac{1}{\sqrt{\mathcal{E}}}$ of magnitude $H(z') = 2\sqrt{\mathcal{E}}$. Classically, ionization occurs, when the binding energy $-1/2n^2$ equals this value:

$$\begin{aligned} -2\sqrt{\mathcal{E}} &= -\frac{1}{n^2} \\ \Leftrightarrow \mathcal{E} &= \frac{1}{16n^4} \, . \end{aligned} \tag{4.24}$$

The bound exciton states are moved into the continuum and can no longer be observed.

Including additionally the first-order Stark shifts of the excitons following $n^2\mathcal{E}$ gives $\mathcal{E} = 1/(9n^4)$ [Gal94] with the same scaling on n.

Quantum-mechanically the tunneling rate through the potential barrier increases even before the classical ionization threshold and is indicated by changes in the line shape. We expect the peak area to decrease and the linewidth to increase exponentially. Both values can be determined by fits with an asymmetric Lorentzian, as described by Eq. (2.43) in Sec. 2.5. For the evaluation, care has to be taken regarding the electric-field range, since the line shape may be influenced by neighboring emerging absorption features. Hence, the analysis is restricted to field strengths where the P absorption line is still isolated from such influences. In Fig. 4.6, this regime corresponds to field strengths below 0.25 V.

The ionization voltage is given by the value, where the peak area has dropped to $1/e$. In general, the peak area will also decrease due to mixing with other angular momentum states. However, according to Fig. 4.7, the redistribution of oscillator strength seems to have a minor contribution to the absolute change in peak area in the range of the considered voltages. The obtained ionization voltages are shown in Fig. 4.7 (a).

The ionization voltage drops by about one order of magnitude from $n = 10$ to $n = 18$. The decrease is well described by a fit with a power law n^{-d} and $d = 3.79 \pm 0.34$, as shown by the black line and grey area. This is close to the expectation $\propto n^{-4}$, shown by the red line, according to Eq. (4.24).

As mentioned before, when tunneling becomes possible, the linewidth is expected to broaden, as carriers tunnel through the potential barrier into the continuum and reduce the bound states' lifetime. The extracted linewidths for $n = 10$ up to $n = 16$ are shown in Fig. 4.7 (b). The left panel gives the fit results for odd states, the right panel for even states. Following Refs. [Mer+74; Aro+78] the linewidth broadening can be described by

$$\Gamma_n \propto \exp\left(-\frac{3}{2n^3\mathcal{E}}\right) \, . \tag{4.25}$$

A fit to the data according to this dependence is shown by the dashed lines.

Indeed, the linewidths show an exponential increase, that is more pronounced at lower n. For high-lying states, a broadening can be hardly observed within experimental accuracy before the states vanish, although they are expected to be even more sensitive to the electric field. This can be understood by the fact, that the dissociation voltage decreases faster ($\propto n^{-4}$) than the critical field strength of broadening ($\propto n^{-3}$). The high-lying states simply ionize before a pronounced broadening can be seen.

Finally, we come back to the observation that states on the high energy side of a Stark fan are more stable to ionization than states on the low energy side. This can be explained by the charge distribution along the z axis. The states in a Stark fan are linear combinations of

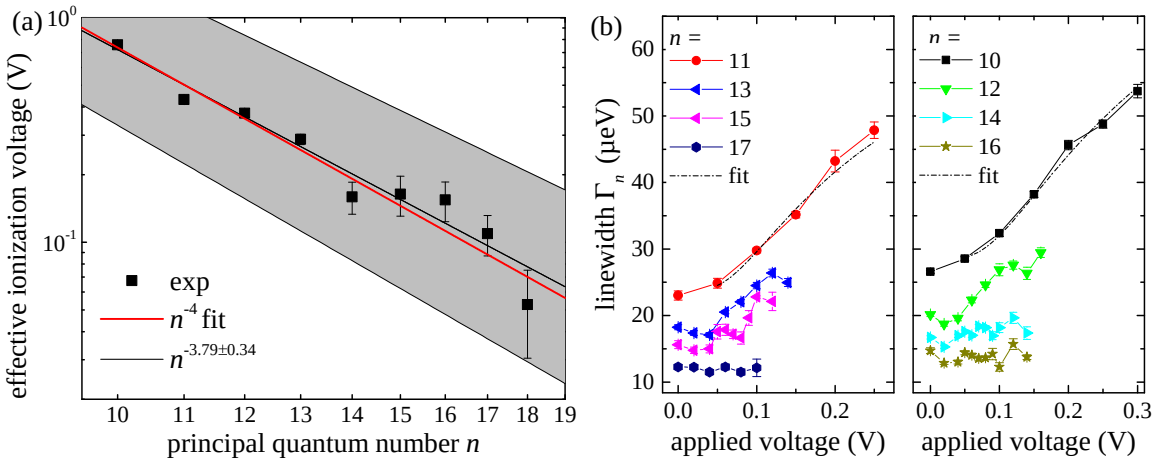

Figure 4.7 (a) Ionization voltage of P excitons as a function of principal quantum number n. At this voltage, the area below a peak has dropped to the value $1/e$. The values follow roughly an n^{-4} dependence, given by the red line, with a slight deviation at high n. A fit with n^{-d} yields $d = 3.79 \pm 0.34$, shown by the black line and grey area. (b) Linewidths of P excitons with $n = 10$ to $n = 16$ as a function of increasing voltage. Odd states are shown in the left panel, even states are shown in the right panel. Low-lying states show a broadening according to Eq. (4.25), indicated by the dashed lines. High-lying states show no broadening until they are dissociated. From [Hec+17b].

the pure exciton states of different parity without field. We find the same constituents in a state on the high energy flank than on the low energy flank, but with opposite phase. This results in a different charge distribution along the z axis. In fact, states on the high energy side of a Stark fan have a higher probability density on the opposite side of the tunnel barrier than low energy states and are therefore less affected by dissociation processes.

4.2 External magnetic fields

In this section, we focus on scaling laws in external magnetic fields. Figure 4.8 shows a contour plot of the absorption spectrum from $n = 4$ up to about 2.184 eV in a magnetic field from 0 to 7 T at 1.35 K. The field is applied in Faraday configuration ($\mathbf{B}||\mathbf{k}$, where $\mathbf{B}$ is the magnetic field strength). This spectrum is taken from Refs. [The15] and [Aßm+16]. In the regime with $n \geq 6$, the density of states becomes too large to address every eigenstate individually. Therefore, statistical methods were used in these works to analyze the distribution of level spacings between adjacent states at a fixed magnetic field strength. The spectra revealed clear signatures of quantum chaos in the regime above 2.170 eV, where the spectra are dominated by anticrossings.

In the low-n regime, from $n = 3$ to $n = 7$, the field dependence could even be reproduced quantitatively by extensive theoretical models, for both Faraday and Voigt configurations for different polarizations (Refs. [Sch+17b; Rom+18]).

In general, the effect of an external magnetic field on an exciton is obtained in the following way. In analogy to Sec. 2.1, the momentum operator is replaced by $\mathbf{p} \to \mathbf{p} + e\mathbf{A}$, whereas one typically chooses $\mathbf{B}||z$ and $\mathbf{A} = -\frac{1}{2}\mathbf{r} \times \mathbf{B}$, ($\mathbf{B} = \nabla \cdot \mathbf{A} = (0\ 0\ B_z)$).

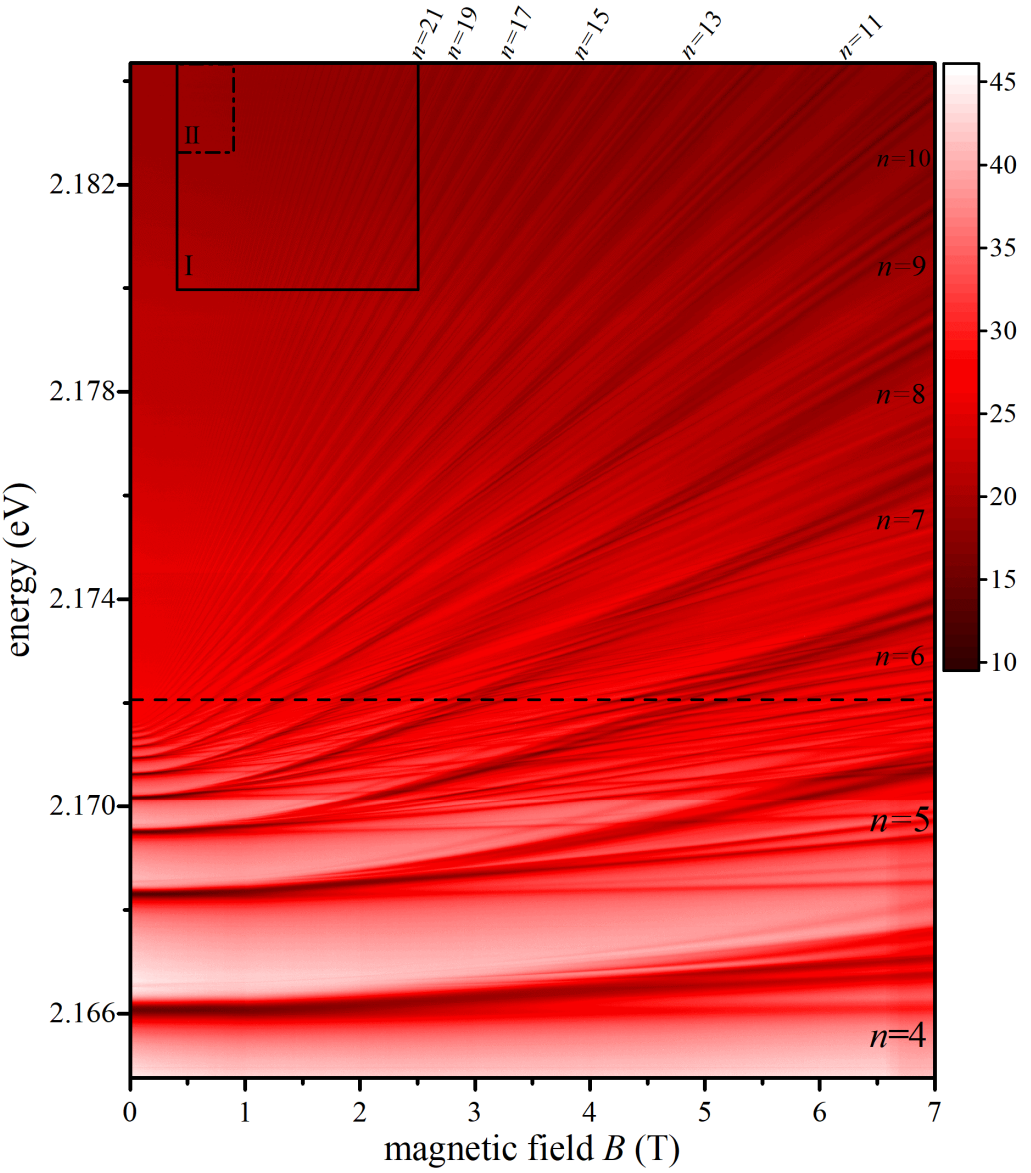

Figure 4.8 Contour plot of the yellow exctions in a magnetic field from 0 to 7 T at 1.35 K. The field is applied in faraday configuration. The dashed line indicates the band gap at zero field. The rectangles in the upper left mark spectral areas from which closeups are shown in Fig. 4.10. The level dispersions show a change from a B^2 dependence to a linear B dependence that indicates the crossover from the Coulomb-dominated regime to Landau level formation. The data is taken from Refs. [Aßm+16] and [The15] and is reanalysed here. Adapted from [Hec+17b].

The relative motion kinetic energy then reads (see, for example, Ref. [Gro+12])

$$\begin{aligned} H_{\text{kin}}^{\text{rel}} &= \frac{1}{2\mu}[\mathbf{p}+e\mathbf{A}]^2 = \frac{1}{2\mu}\left[\mathbf{p}-\frac{e}{2}\mathbf{r}\times\mathbf{B}\right]^2 \\ &= \frac{1}{2\mu}\mathbf{p}^2+\frac{e}{2\mu}(\mathbf{r}\times\mathbf{p})_z B_z+\frac{e^2B_z^2}{8\mu}(x^2+y^2)\ . \end{aligned} \tag{4.26}$$

With the angular momentum $\mathbf{l}_z = (\mathbf{r}\times\mathbf{p})_z$ we find the Hamiltonian

$$H = H_0+\frac{e}{2\mu}\mathbf{l}_z\cdot B_z+\frac{e^2B_z^2}{8\mu}(x^2+y^2)\ , \tag{4.27}$$

with the paramagnetic shift (second term) and diamagnetic shift (third term). H_0 describes the hydrogen-like unperturbed system (cf. Eq. (2.11) in Sec. 2.3), while we assume $\mathbf{K}=0$ here.

In general, the magnetic field acts also on the spins in the system. For excitons these are the quasi-spin I as well as both electron and hole spins $\mathbf{s}_\text{e}$ and $\mathbf{s}_\text{h}$. The relevant Hamiltonian reads [Sch+17b]

$$H_B = \mu_B[g_c\mathbf{s}_\text{e}+(3\kappa+g_s/2)\mathbf{I}-g_s\mathbf{s}_\text{h}]\cdot\mathbf{B}/\hbar\ . \tag{4.28}$$

Here, μ_B is the Bohr magneton and g_c and g_s are the g-factors of electron and hole. κ is the 4th Luttinger parameter. In total, the coupling to B leads to the well known Zeeman effect responsible for the splitting and shifting of lines with increasing magnetic field. This is described in detail in Refs. [Sch+17b] and [Rom+18] for different polarizations and in both Faraday and Voigt geometry.

In order to find a simple approximation for the magnetic field behavior that enables the extrapolation to the high-n regime it is sufficient to disregard Zeeman spin splittings in the analysis carried out here. In the following, the data from Fig. 4.8 is reanalyzed under a different point of view. The following studies focus on resonances of states from adjacent multiplets at intermediate field strengths as well as the formation of Landau levels in the high-field regime.

4.2.1 Crossover field strength to Landau quantization

First, the transition from the Coulomb-dominated exciton behavior at low magnetic field strengths to the magnetic field-dominated formation of Landau levels is discussed.

Both regimes can be identified in Fig. 4.8: At low fields, the absorption lines clearly show a weak diamagnetic B^2 dependence that transforms into a stronger paramagnetic shift linear in B at higher fields. Despite the splitting into a multitude of diverging lines at low fields, the states seem to appear within a bundle around a particular Landau level in the linear high-field regime.

Landau levels describe the circular movement of charged particles of mass m with a cyclotron frequency $\omega_c = eB/m$. They form quantized orbits perpendicular to the magnetic field axis. Their energy dispersion can be deduced from the model of a harmonic oscillator and is given by $E=(n+\frac{1}{2})\hbar\omega_c$. With the classical kinetic energy of the particle one finds

the extension $l_{c,n}$ of a Landau level

$$\begin{aligned} \frac{1}{2}m\omega_c^2 l_{c,n}^2 &= \left(n+\frac{1}{2}\right)\hbar\omega_c \\ \Leftrightarrow l_{c,n} &= \sqrt{2\left(n+\frac{1}{2}\right)}\sqrt{\frac{\hbar}{m\omega_c}} \approx \sqrt{2n}\sqrt{\frac{\hbar}{eB}}, n \gg 1 \ . \end{aligned} \tag{4.29}$$

The extension of the ground state Landau level is called the magnetic length l_c. It reads

$$l_c = \sqrt{\frac{\hbar}{eB}} = 25.6\text{nm}/\sqrt{B[\text{T}]} \ , \tag{4.30}$$

with B in units of Tesla. Without a magnetic field, the exciton extension is given by $r_{n,l} \approx \frac{3a^{\text{B}}}{2}n^2$ (cf. Eq. (2.17)). The crossover field strength is found where the Landau level extension and exciton extension become equal, $l_{\text{c,n}} = r_{\text{n,l}}$, and is found to scale as

$$B_{\text{c,n}} \propto n^{-3} \ . \tag{4.31}$$

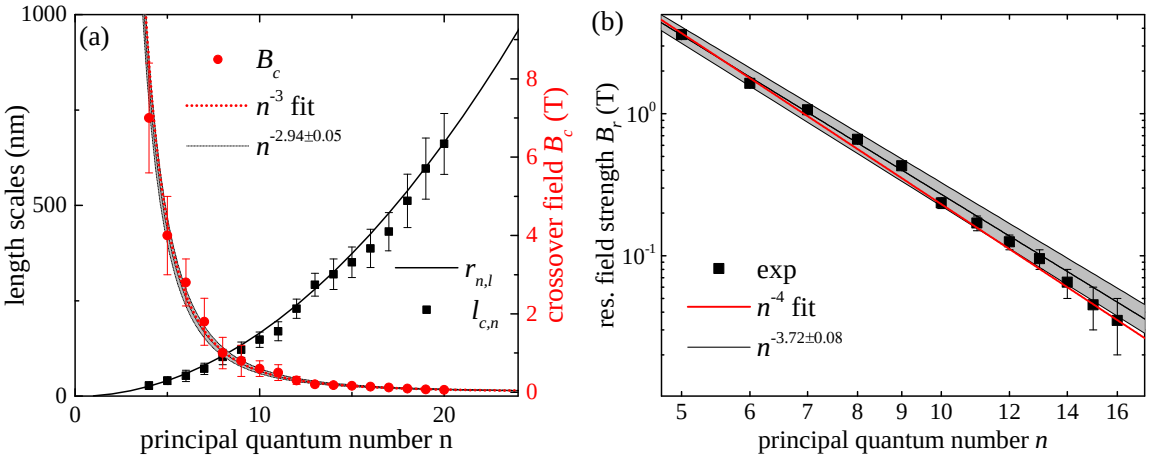

Figure 4.9 (a) Red circles, right ordinate: crossover field strength $B_{\text{c,n}}$ from B^2-like to B-linear behavior. The red curve shows a fit $\propto n^{-3}$ according to the theoretical expectation from Eq. (4.31). The trend is confirmed by the black line, that represents a fit with n^{-d} and $d = 2.94 \pm 0.05$. Black squares, left ordinate: Landau level radius $l_{\text{c,n}}$ at $B_{\text{c,n}}$ calculated with Eq. (4.29). Black solid line: Coulomb extension $\propto n^2$ with Eq. (2.17) that coincides with the Landau level extension. (b) Resonance field strengths B_{r} of the first crossing between states of two adjacent multiplets. The red line is a fit $\propto n^{-4}$ according to the expectation from Eq. (4.35), the black line and the grey area give a fit $\propto n^{-d}$ with $d = 3.72 \pm 0.08$. From [Hec+17b].

It can be roughly estimated from the spectra in Fig. 4.8. To this end, the energy of the center of a bunch of lines in the Landau regime is extrapolated linearly to lower energies for each n. The crossover field strength $B_{\text{c,n}}$ is given as the point where the dispersion deviates from the linear behavior and transforms into the quadratic B dependence at low fields. This field strength clearly drops with increasing n. At this point, an exciton with

principal quantum number n transforms into a Landau level transition with the same principal quantum number. The experimentally found crossover field strengths $B_{c,n}$ are shown in Fig. 4.9 (a).

The field strengths follow nicely the expected n^{-3}-dependence as shown by the dashed red line. A power-law fit $\propto n^{-d}$ reveals $d = 2.94 \pm 0.05$, confirming the expectations. In addition, we calculate the Landau level extension from these field strengths according to Eq. (4.29) and show them as black squares. These follow nicely the n^2-Coulomb extension of the exciton wave function, shown as the black solid line.

This finding additionally confirms the huge extension of the Rydberg exciton wave functions and shows that the description with a uniform dielectric function on these length scales is valid.

4.2.2 Landau level quantization and highest quantum number n_{max}

The transition from the excitonic regime into the Landau level regime leads to the question of the highest observable quantum number n_{max}. The magnetic field squeezes the wave function $\propto 1/\sqrt{B}$, which leads to an increasing overlap of electron and hole. Hence, especially high-lying states gain oscillator strength and their corresponding Landau level transitions are visible far above the band gap. To focus on this spectral regime, Fig. 4.10 shows closeups of the areas I and II marked in the upper left of Fig. 4.8.

In this regime, we are far away from the possibility to identify the individual states of each multiplet. We rather observe equally spaced bunches of states, each bunch belonging to a multiplet with principal quantum number n. The spacing increases, since the levels diverge linear with B and become nicely separated.

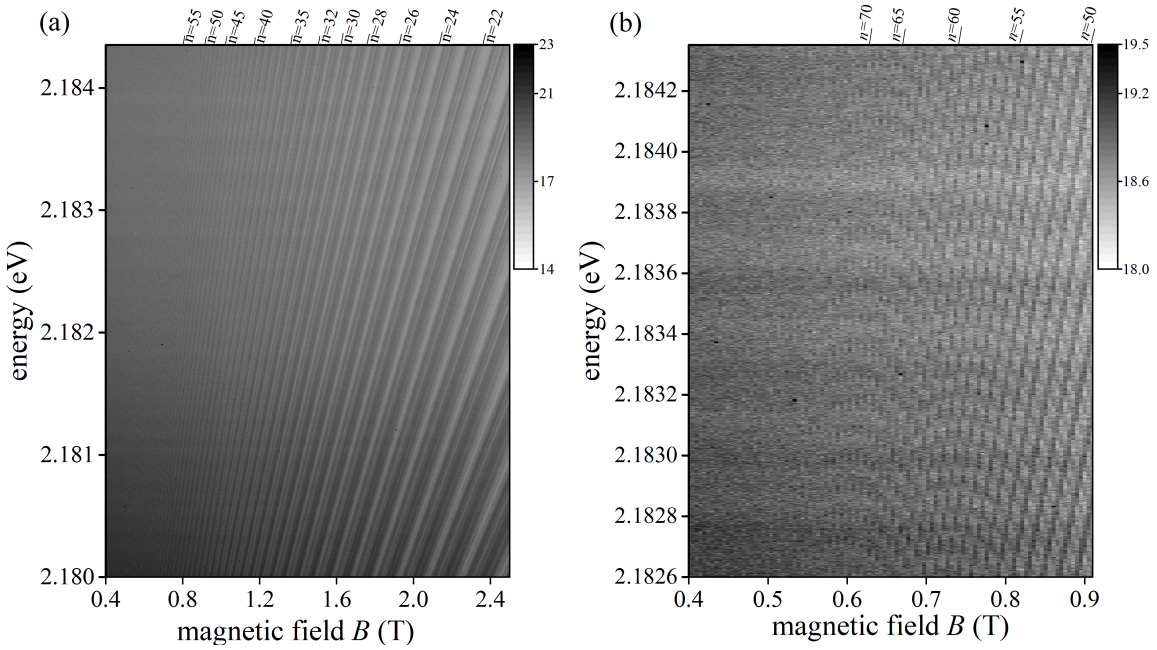

Figure 4.10 (a) Closeups of area I (a) and II (b) in Fig. 4.8. Adapted from [Hec+18e].

Each of these Landau level transitions can in principle be traced back to its excitonic

counterpart with the same quantum number at zero magnetic field and in the highest zooming level, in Fig. 4.10 (b), we can identify Landau levels up to $n = 75$ at 0.55 T, which is the highest Landau level quantum number ever observed. In [Viñ+98], a similar experiment is reported in GaAs, where the dispersions can be traced back to n around 20 or 30.

Following Eq. (4.29) one finds an extension of 425 nm at $B = 0.55$ T. The excitonic counterpart of this Landau level would, if observable, have an extension of $r_{\mathrm{n,1}} \approx 9.4$ μm. Due to the magnetic field, the wave function is squeezed by a factor of 20. With a cyclotron frequency of $\omega_c = eB/\mu = 258$ GHz, it takes 24.4 ps for a full rotation around the circumference of about 2.7 μm. Here we used the reduced mass μ and a field strength of $B = 0.55$ T. This yields a velocity of $1.1 \cdot 10^5$ m/s. For a state with $n = 75$ without magnetic field, the virial theorem leads an average velocity of $3.8 \cdot 10^3$ m/s. Thus, we find an enormous speed up by roughly two orders of magnitude through the magnetic field for these high orbits.

4.2.3 Magnetic field-induced crossings

Next, we note that states of adjacent multiplets with principal quantum numbers n and $n + 1$ come into resonance at a certain field strength in analogy to avoided crossings in electric fields.

To highlight these crossings, a contour plot of the second derivative of the data from Fig. 4.8 is shown in Fig. 4.11 with a closeup for the states $n \geq 7$ up to 2 T in the lower panel. The second derivative further increases the contrast between large P and tiny F absorption peaks. The spectra are shown in a color scale, where blue colors represent absorption features.

From this data, the resonance field strengths B_{r} can be determined with high accuracy. They are shown in Fig. 4.9 (b) as a function of n. They decrease from about $B_{\mathrm{r}} = 2$ T for $n = 6$ down to $B_{\mathrm{r}} = 0.04$ T for $n = 16$. For higher n, the crossings cannot be resolved. A fit to the data with a power law $\propto n^{-d}$ reveals $d = 3.72 \pm 0.08$ (black solid line with grey shaded area), which is close to 4, shown by the red line.

The scaling behavior can be traced back to the Hamiltonian in Eq. (4.27). We identify the term $(x^2 + y^2)$ with the squared average radius $r_{\mathrm{n,l}}$ of the exciton and obtain [Gal94]

$$\langle r^2 \rangle_{nlm} = \frac{n^2}{2}[5n^2 + 1 - 3l(l+1)] \propto n^4 \ . \tag{4.32}$$

Now we can estimate the energy of a state with quantum numbers n and l in a magnetic field (here, in atomic units, according to Ref. [Gal94])

$$E_{n,l} \approx -\frac{1}{2n^2} + \frac{mB}{2} + A_l n^4 B^2 \ . \tag{4.33}$$

Here, m denotes the magnetic quantum number and A_l is the l-dependent magnitude of the diamagnetic shift. For simplicity, we neglect fine structure splittings $\propto \mathbf{ls}$ and quantum defects, which is justified for high n due to the n^{-3} decrease of these terms (Sec. 4.1.1).

As mentioned above, we consider crossings between the highest and lowest states of adjacent multiplets n and $n+1$, i.e. states with quantum numbers $\{n, l_{\mathrm{max}} = n-1, m_{\mathrm{max}} = n-1\}$ and $\{n+1, l_{\mathrm{max}} = n, m_{\mathrm{min}} = -n\}$.

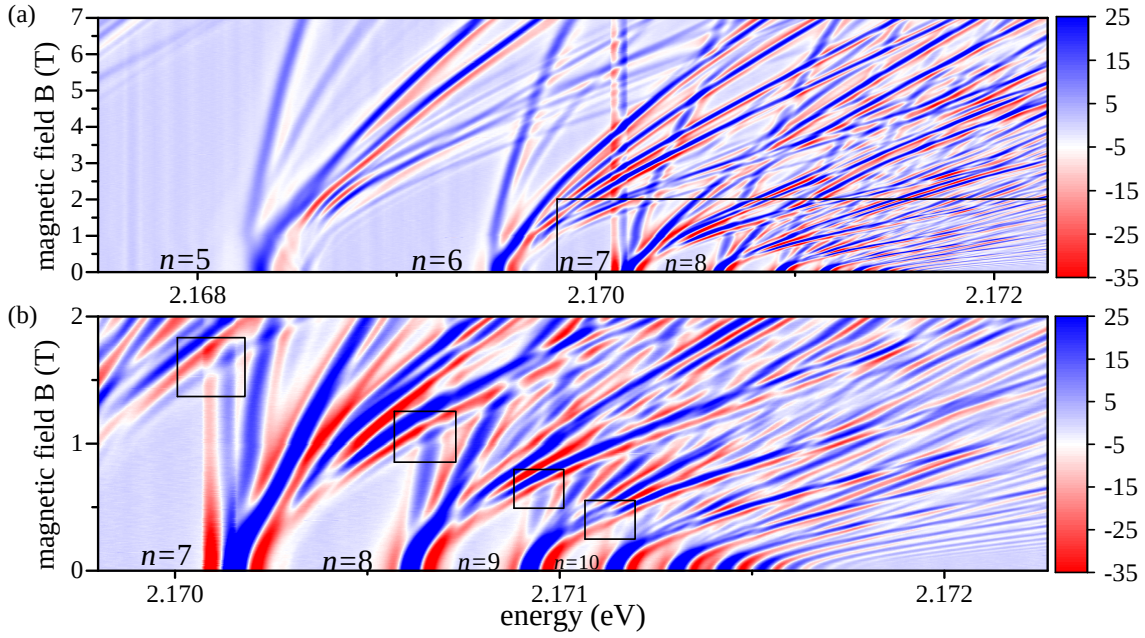

Figure 4.11 Contour plot of the second derivative of the data from Fig. 4.8. Panel (b) shows a closeup of the high-n range up to 2 T as indicated in (a). Additionally, spectral areas of crossings are marked, as discussed in the text. Adapted from [Hec+17b].

For excitons, the crossings occur at rather low magnetic fields compared to the hydrogen case. Therefore, we can neglect the diamagnetic term. The crossing occurs at

$$\begin{aligned} E_{n,m=n-1} &= E_{n+1,m=-n} \\ \Leftrightarrow -\frac{1}{2n^2} + \frac{(n-1)B_\mathrm{r}}{2} &= -\frac{1}{2(n+1)^2} + \frac{-nB_\mathrm{r}}{2} \\ \Leftrightarrow B_\mathrm{r} &= \frac{2n+1}{2n^5+3n^4-n^2} \,. \end{aligned} \tag{4.34}$$

The first term dominates, and

$$B_\mathrm{r} \propto n^{-4} \,, \tag{4.35}$$

shown as the red line in Fig. 4.9.

Due to the different optical selection rules one would only excite states with $m = 0$ or $m = \pm 1$ in the atomic case. Therefore, the paramagnetic shift is negligible and only the B^2-term has to be considered. In this case, we can neglect the second term and find for the crossing field between states n and $n+1$

$$\begin{aligned} E_n &= E_{n+1} \\ \Leftrightarrow -\frac{1}{2n^2} + A_l n^4 B_\mathrm{r}^2 &= -\frac{1}{2(n+1)^2} + A_l (n+1)^4 B_\mathrm{r}^2 \\ \Leftrightarrow B_\mathrm{r}^2 &= \frac{2n+1}{2A_l n^2 (n+1)^2} \frac{1}{4n^3+6n^2+4n+1} \,. \end{aligned} \tag{4.36}$$

Here, the dominating term gives $B_\mathrm{r}^2 \propto n^{-6}$ and we find $B_\mathrm{r} \propto n^{-3}$, which is different from the excitonic case.

4.3 Conclusions

In this chapter, properties of Rydberg excitons in external electric and magnetic fields and important scaling laws were studied.

The activation of dark states with even envelope function by application of an electric field was demonstrated. In contrast to the atomic case, the cubic symmetry gives rise to polarization-dependent optical selection rules which allow one to tune the number of visible states within a Stark fan. This turned out to be a helpful experimental tool for the further investigation of fundamental properties in external fields, in particular in the high-n regime.

The extrapolation of energy dispersions to zero field allowed us to study the multiplet width and especially its scaling with n. Its decrease with n^{-3} is in full agreement with the theoretical expectation from the full Hamiltonian in Sec. 2.3.1 and the excitonic quantum defect model. The investigation of the quadratic dispersion of states with increasing electric field strength allowed for the determination of the polarizability of S and P states in accordance with the expected n^7 scaling.

The high-field regime, where anticrossings between adjacent multiplets can be observed was shown to be reached with applied voltages below 20 V. Both the voltage of the first anticrossing and the energy splitting between the involved states are in good agreement with the theoretical expectations known from atomic physics. In this regime, also the ionization of states in an electric field was observed and discussed. The decrease of oscillator strength and the broadening of lines was shown to follow the model descriptions within good agreement.

In a magnetic field, the crossover from the Coulomb-dominated regime to a Landau level formation was observed and shown to follow an n^{-3} dependence, expected from the wave function squeezing down to the Landau orbit extension. In the high-field regime, the highest Landau level could be assigned to the quantum number $n_\mathrm{max} = 75$, the highest observed so far. An investigation of the limitation of n_max without magnetic fields is given in the next chapter.

Similar to the behavior in electric fields, crossings between adjacent multiplets could be observed in magnetic fields, the scaling of which fits to the paramagnetic shifts. Compared to atoms, the different optical selection rules due to the crystal environment allow for the observation of high angular momentum states which results in a dominating paramagnetic term. This is different from the atomic case, where the diamagnetic terms dominate. An overview of all studied properties and the underlying physical origin is given in Tab. 4.1 for both atoms and excitons.

In conclusion, Rydberg excitons show mostly similar scaling laws compared to their atomic counterparts, whereas the physical origin is different. While in the atomic case, the scaling laws originate from deviations from the $1/r$ Coulomb potential, the excitonic scaling laws result from deviations of a parabolic valence band dispersion. Differences in the scaling laws stem from the different optical selection rules of both systems. While for atoms, only transitions with $\Delta l = \pm 1$ are optically allowed, the crystal symmetry allows for the direct observation of the whole exciton multiplet. The determination and verification

	Rydberg atoms	origin	**Rydberg excitons**	origin
Zero field				
Multiplet splitting due to quantum defect	$\propto n^{-3}$ (except for hydrogen)	DCP	$\propto n^{-3}$	DPD
Electric field				
Polarizability	$\propto n^7$ ($\propto n^6$ for hydrogen)	splitting by DCP	$\propto n^7$	splitting by DPD
Resonance field of states from multiplets n and $n+1$	$\propto n^{-5}$	Stark effect	$\propto n^{-5}$	Stark effect
Anticrossing energy at first resonance	$\propto n^{-4}$	DCP	$\propto n^{-4}$	DPD
Ionization voltage	$\propto n^{-4}$	Stark effect	$\propto n^{-4}$	Stark effect
Magnetic field				
Crossover field to magnetoexciton	$\propto n^{-3}$	Landau quantization	$\propto n^{-3}$	Landau quantization
Resonance field of states from multiplets n and $n+1$	$\propto n^{-3}$	diamagnetic shift due to OSPS	$\propto n^{-4}$	paramagnetic shift due to OSDAM by DPD state mixing

Table 4.1 Legend: DCP = deviation from $1/r$ Coulomb potential; DPD = deviation from parabolic dispersion; OSPS = observation of S and P states only due to selection rules; OSDAM = observation of states with different from $l = 0, 1$ angular momenta.

of these n-dependent scaling laws allows one to extrapolate physical concepts valid at low n to the high-n regime, where the exact solutions of the Hamiltonian become too complex to calculate due to the immense density of states. In this context, the results described in this chapter serve as a basis for future studies in the high-n regime of Rydberg excitons.

Chapter 5

Rydberg excitons in an ultralow-density plasma

The impact of a plasma on Coulomb-bound states is a complex problem and was studied intensively for atoms as well as for excitons in semiconductors and is well described in the literature [Ebe+76; Kra+86; Zim88b; Kre+05].

In this chapter, the excitonic Rydberg series is investigated in the presence of an electron-hole plasma. Here, we use a pump laser with a photon energy above the band gap to create a constant density of electron-hole pairs and study the change in the absorption spectra of Rydberg excitons obtained by a second probe laser. Most of the results can be found in [Hec+18b].

First, the basic concepts for the description of a plasma are briefly summarized in Sec. 5.1. The self-energy correction (5.1.1), screening of the Coulomb interaction (5.1.2) and the Mott effect (5.1.3) are introduced, following the description in [Kre+05].

In Section 5.2 and following, the effects observed in the experiment are compared to a theory based on the Debye model, developed by the groups of Prof. Scheel and Prof. Stolz from the University of Rostock. We observe a shift of the band gap to lower energies with increasing plasma density. The bound states vanish into the continuum when the band gap crosses their energy which causes the excitonic absorption lines to disappear. Note that the model described here is based on the description given in Ref. [Hec+18a], whereas recent studies [Sem+19; Sem+] expand and improve the theoretical description beyond the Debye model. The recent studies will be discussed in Sec. 5.4.

We apply the theory also to the case of zero pump power, where the presence of residual intrinsic free electrons and holes determines the highest observable quantum number n_{max}. In this regard, two further experimental approaches are summarized in the third section of this chapter, Sec. 5.3. There, the absorption spectrum in dependence on both laser power and temperature is studied to explore the experimental factors that limit the observability of higher principal quantum numbers n_{max}. Most of the results can be found in [Hec+18a] and [Hec+20] as well as in the bachelor thesis of David Janas [Jan17]. In that section, measurements at temperatures below 1.35 K are shown that were achieved by the use of a ^{3}He-^{4}He dilution refrigerator (Oxford Kelvinox system) operated with help from Dr. Rico Schwartz from the University of Rostock.

5.1 Theoretical background

In general, the description of a plasma depends on its density ρ and can be divided into the realms of degenerate and non-degenerate plasmas. The transition between both regimes

is determined by the plasma degeneracy parameter $\rho_a \cdot \Lambda_\mathrm{a}^3$ with the thermal wavelength $\Lambda_\mathrm{a} = \sqrt{2\pi\hbar^2/(\mu_a k_B T)}$. The index a denotes the particle species. We consider a plasma to be non-degenerate, if $\rho_a \Lambda_a^3 \ll 1$ and degenerate, if $\rho_a \Lambda_a^3 \gg 1$ [Kre+05]. In the experiments presented here, we find low plasma densities ρ_eh around 1 μm^{-3}. Assuming an average plasma temperature for electrons and holes of 5 K one finds $\rho_\mathrm{eh}\Lambda_\mathrm{eh}^3 = 1.7 \cdot 10^{-4} \ll 1$, justifying a description in terms of a non-degenerate plasma model, i.e. the Debye theory in particular.

5.1.1 Self-energy

A particle with charge e_a at a position $\mathbf{r} = \mathbf{v}_0 t$, where $\mathbf{v}_0$ is its velocity and t is the time, will polarize a plasma in its surrounding, creating an induced electrostatic potential $\Phi^\mathrm{ind}(\mathbf{r}, t)$. The potential energy of this particle is changed by the interaction with the total field of all plasma particles and may be described by the so-called self-energy $\Sigma_a(v_0) = e_a \Phi^\mathrm{ind}(\mathbf{r}, t)|_{r=v_0 t}$. In the static limit for a particle at rest ($\mathbf{v}_0 = 0$), it can be shown to be $\Sigma_a(0) = -\frac{\kappa e_a^2}{4\pi\epsilon_0\epsilon_s}$, with the inverse screening length κ, that is a function of plasma-density ρ_a and given by [Kre+05]

$$\kappa = \sqrt{\rho_a e^2/(\epsilon_0 \epsilon_s k_B T_\mathrm{sc})} \ . \tag{5.1}$$

Here, k_B is the Boltzmann constant and T_sc is the screening temperature of the plasma, that will be discussed in more detail later. The total interaction energy of an electro-neutral system with N_a particles in a plasma phase is then given by

$$U_\mathrm{int} = \frac{1}{2}\sum_a N_a e_a \Phi^\mathrm{ind}(\mathbf{r}_a) = -\frac{1}{2}\sum_a N_a \frac{\kappa e_a^2}{4\pi\epsilon_0\epsilon_s} \ . \tag{5.2}$$

Thus, the mean contribution of an individual particle to the total interaction energy is given by the averaged self-energy

$$\Delta_a = -\frac{1}{2}\frac{\kappa e_a^2}{4\pi\epsilon_0\epsilon_s} \ . \tag{5.3}$$

In other words, a particle's energy in a plasma is lowered compared to that of a free particle by this self-energy correction [Kre+05]. The particle's energy is described the Hamiltonian

$$H_a^\mathrm{P}(p_\mathrm{a}) = \frac{p_\mathrm{a}^2}{2m_a} + \Delta_a \ . \tag{5.4}$$

The first term corresponds to the dispersion of the free particle's kinetic energy.

The description given above is an elementary approach to describe the self-energy correction. Much more sophisticated models using quantum theory of many-body systems can be found in [Kre+05] as well as in e.g. [Zim+78] or [Sem+19].

5.1.2 Screening of the Coulomb potential

As we are interested in the behavior of (excitonic) bound states surrounded by a plasma rather than a single particle, effects of the plasma on the binding energy E_n^b shall be considered here. The presence of free carriers leads to a shielding of the pure Coulomb

potential of the bound exciton states which now has to be described by the Debye potential

$$V_{\mathrm{Debye}}(r) = -\frac{1}{4\pi\epsilon_0\epsilon_s}\frac{e^2}{r}e^{-\kappa r} \ , \tag{5.5}$$

with the inverse screening length κ or inverse Debye radius r_D^{-1} mentioned above (Eq. (5.1)). For small values of κ the screening is weak, large values correspond to a strong screening. The Debye radius determines the length, at which the Coulomb potential has fallen to the value $1/e$. For weak screening (small values of κ), we can expand the exponential to first order, $e^{-\kappa r} \approx 1 - \kappa r$ and find

$$V_{\mathrm{Debye}}(r) \approx \frac{1}{4\pi\epsilon_0\epsilon_s}\left(-\frac{e^2}{r} + \kappa e^2\right) + \mathcal{O}(e^2\kappa^2) \ . \tag{5.6}$$

Thus, in first order, the effect of screening on the system is to increase the energy of a two-pair state by an amount $\frac{1}{4\pi\epsilon_0\epsilon_s}\kappa e^2$ as it screens the Coulomb potential. In a qualitative picture, the states close to the continuum edge will be shifted above the ionization energy. This leads to a finite number of bound states, in contrast to the bare Coulomb-like system which gives rise to an infinite number of bound states [Rog+70].

5.1.3 Mott effect

Now we consider the Hamiltonian of a bound state consisting of an electron and a hole, i.e. an exciton, surrounded by an electron-hole plasma. The energies of both electrons and holes are modified by the two effects discussed above - self-energy correction (Eq. (5.4)) and screening of the Coulomb potential (Eq. (5.5)):

$$\begin{aligned} H_{\mathrm{eh}}^{\mathrm{P}} &= \frac{p_{\mathrm{e}}^2}{2m_{\mathrm{e}}} + \Delta_{\mathrm{e}} + \frac{p_{\mathrm{h}}^2}{2m_{\mathrm{h}}} + \Delta_{\mathrm{h}} + V_{\mathrm{Debye}}(r) \\ &= \frac{p_{\mathrm{e}}^2}{2m_{\mathrm{e}}} + \frac{p_{\mathrm{h}}^2}{2m_{\mathrm{h}}} + \Delta_{\mathrm{eh}} + V_{\mathrm{Debye}}(r) \ . \end{aligned} \tag{5.7}$$

Here, the term $\Delta_{\mathrm{eh}} = \Delta_{\mathrm{e}} + \Delta_{\mathrm{h}}$ can be identified with the continuum energy E_{cont} [Kre+05],[Zim+78], which is the lowest energy of the free particles (Eq. (5.4) at zero momentum $p = 0$)

$$E_{\mathrm{cont}} = \Delta_{\mathrm{e}} + \Delta_{\mathrm{h}} = \Delta_{\mathrm{eh}} = -\frac{\kappa e^2}{4\pi\epsilon_0\epsilon_s} \ . \tag{5.8}$$

For an excitonic system in a semiconductor, this is the band gap E_{g} that is renormalized by many-particle corrections, such as the self-energy corrections, caused by the presence of a plasma. In the following, the discussion is limited to the Debye model and will only take into account self-energy corrections.

In the regime of weak screening, we see from Eq. (5.6) and Eq. (5.8) that the energy increase caused by screening is compensated in first order in κ by a decreasing band gap energy $E_{\mathrm{g}} = \Delta_{\mathrm{eh}}$

$$H_{\mathrm{eh}}^{\mathrm{P}} \approx \frac{p_{\mathrm{e}}^2}{2m_{\mathrm{e}}} + \frac{p_{\mathrm{h}}^2}{2m_{\mathrm{h}}} + \frac{1}{4\pi\epsilon_0\epsilon_s}\left(-\frac{e^2}{r} + \underbrace{\kappa e^2 - \kappa e^2}_{=0}\right) + \mathcal{O}(e^2\kappa^2) \ . \tag{5.9}$$

Thus, we see that in a first-order approximation, the energies of excitons surrounded by a plasma of small density are equal to the ones of a bare Coulomb potential. For a much more substantial description of excitonic energies influenced by a plasma, one may refer to [Sem+19].

In terms of plasma density ρ_{eh}, we find a square-root dependence of the band gap shift, connecting Eqs. (5.1) and (5.8), as long as $T_{\mathrm{sc}} = \text{const.}$:

$$\Delta_{\mathrm{eh}} \propto \kappa \propto \rho_{\mathrm{eh}}^{-1/2} \ . \tag{5.10}$$

As the band gap is decreasing with increasing plasma density ρ_{eh}, it may cross the energy of an excitonic state. At this point, the bound electron-hole state vanishes, as it is moved above the continuum edge. This is called the Mott effect and the plasma density corresponding to the crossover point is called the Mott density ρ_{Mott} [Mot61; Mot68; Sem+09]. The Mott effect of excitons in semiconductors was extensively studied theoretically (e.g. [Zim+78; Sem+09; Zim88a; Man+10; Man+12]) and experimentally (e.g. [Ego+77; Sha+77; Feh+82]), mostly with a focus on the disappearance of the ground state exciton line. The Mott condition then reads [Zim88a]

$$E_{\mathrm{cont}}(\rho_{\mathrm{Mott}}) = E_{1\mathrm{S}} \tag{5.11}$$

and is found to take place in Cu_2O at an electron-hole-density around ρ_{Mott}=3·10^{18} cm^{-3} = $3 \cdot 10^6$ μm^{-3} [Man+10]. In the following, we report on the analogue phenomenon for highly excited Rydberg excitons where the Mott effect already occurs at much smaller electron-hole densities.

5.2 Influence of an electron-hole plasma on the Rydberg exciton spectrum

Now we describe the experimental approach to study the impact of an electron-hole plasma on Rydberg excitons. We use the pump-probe setup as described in Ch. 3 with two CW laser beams. The pump laser is fixed at an energy $E_{\mathrm{pump}} = 2.20$ eV, i.e. about 28 meV above the band gap, while the probe laser scans the spectrum with a low power of 1 μW. The sample used is $H7$, cooled down to 1.35 K. The pump beam is not modulated and the non-modulated probe signal is detected by a photodiode. With a pump energy above the band gap the pump laser excites mainly free electron-hole pairs via direct excitation, whereas also an indirect creation via Auger processes is possible (see Sec. 5.2.1).

Figure 5.1 shows the recorded absorption spectra from $n = 10$ up to the band gap for pump powers starting in the μW range up to 12 mW. The absorption background is indicated with dashed lines for each pump power. As described in Chapter 2, in this spectral region it consists mainly of the sum of phonon-assisted absorption into yellow and green nS excitons and an exponentially growing Urbach tail which merges into a part with constant absorption at $\tilde{E}_{\mathrm{g}} = E_{\mathrm{g}} + \Delta$ indicating the position of the band gap. This point is marked with red arrows for every pump power. The energy is given as the difference to the nominal band gap of $E_{\mathrm{g}} = 2.17208$ eV. Already at zero pump power (red spectrum) we measure a finite band gap shift of $\Delta = \Delta_0 \approx -150$ μeV. With increasing pump power, the spectral position of the obtained band gap $\tilde{E}_{\mathrm{g}}$ shifts to lower energies and so does the

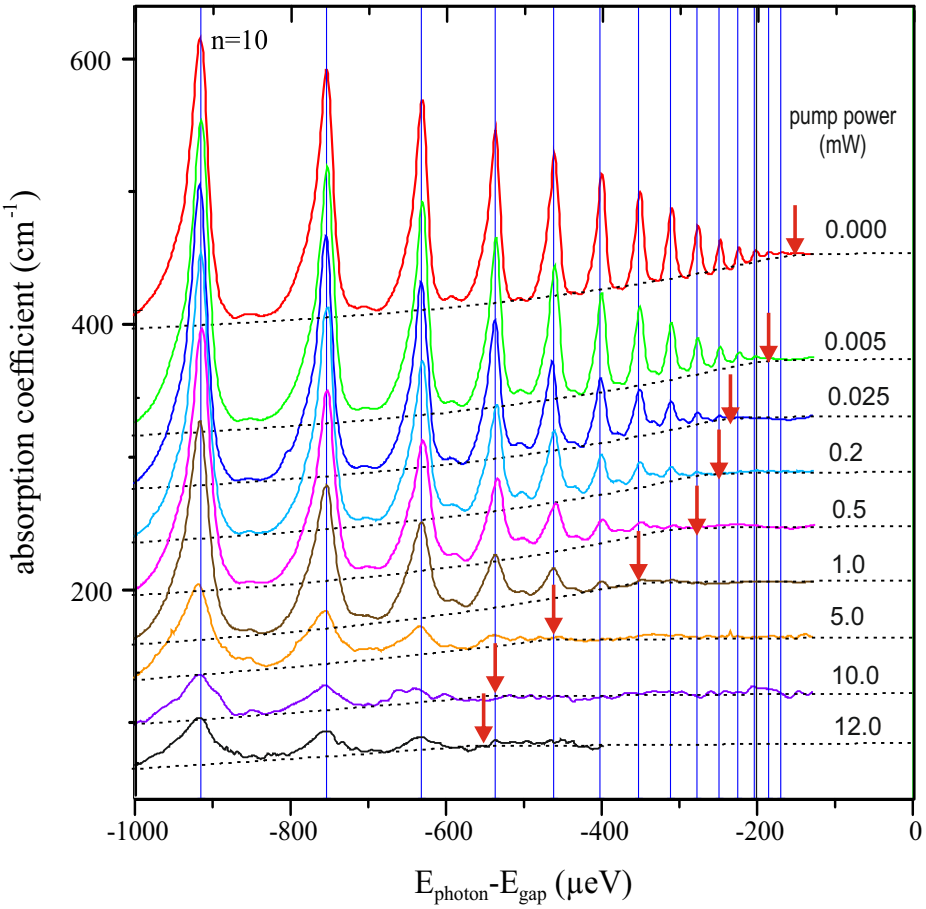

Figure 5.1 Absorption spectra of Rydberg excitons from $n = 10$ onwards for different pump laser powers. The pump laser energy is fixed at 2.20 eV. Top trace shows absorption at zero pump power. Dashed lines indicate the background with an exponentially increasing Urbach tail and a flat absorption above the band gap. The band gap is indicated by the red arrows. Traces are shifted vertically for clarity. Zero energy corresponds to $E_g = 2.17208\,\mathrm{eV}$. Recorded at $T = 1.35$ K. From [Hec+18b].

beginning of the continuum absorption. Thus, the band gap shift may be divided in a power-dependent part Δ_{eh} created by laser-induced electron-hole pairs and a constant shift Δ_0 that is attributed to charged impurities in the crystal that always contribute to a finite band gap shift, even without additional laser excitation. As mentioned in Sec. 2.5, this is confirmed by a recent publication from Krüger et al. [Krü+20], that reproduces this shift by a microscopic model based on an inhomogeneous micro-field distribution originating from these impurities. Here, we treat this shift Δ_0 phenomenologically, given by an inherent density of charged impurities ρ_0.

The laser-induced plasma density ρ_{eh} adds up to the inherent density, $\rho = \rho_0 + \rho_{\mathrm{eh}}$, leading to a total band gap shift observed in the experiment Δ given by $\Delta^2 = \Delta_0^2 + \Delta_{\mathrm{eh}}^2$ (see Eq. (5.10)). At the same time, the energies of the sharp excitonic lines do not shift with increasing pump power as indicated by the vertical blue lines. First, this is in line

with the rough approximation made before in Sec. 5.1.3 that the influence of the band gap shift on the exciton energy is compensated by a screened Coulomb potential. However, it is still remarkable that the lines do not shift at all within μeV resolution and both effects seem to compensate each other completely. As mentioned at the beginning of this chapter, a recent study by Semkat et al. [Sem+19] improves the understanding of the impact of a plasma on the exciton lines. It indeed predicts line shifts for states with principal quantum numbers $n > 10$ of the order of hundredth of μeVs at densities close to the Mott density of the corresponding state. Note that small energy shifts can be observed in more recent measurements that are extended to lower n compared to the data shown in Fig. 5.1 and that are part of current investigations (cf. Sec. 5.4).

Next, the linewidths do not change drastically before the states vanish into the continuum. Only for high pump powers around 5 mW, an emerging broadening can be observed for the lower states. Thus, up to moderate powers a possible lifetime reduction via scattering can be excluded as a possible explanation for the disappearance of the exciton states. This interpretation is in line with the behavior of the intermediate peaks arising between two Rydberg exciton states. As discussed in Sec. 2.5 in detail, these stem from the coherent coupling of the adjacent exciton states and are predicted to appear only for low levels of dephasing [Grü+16]. In the spectra in Fig. 5.1, they do not vanish before the corresponding adjacent exciton lines. Also here, carrier scattering would lead to an enhanced dephasing of excitons and suppress these lines. The observed broadening of linewidths at higher powers is still the subject of ongoing research. A recent calculation in Ref. [Sem+] predicts linewidth changes caused by the plasma on the order of 1 μeV and below only. Hence, the broadening might be caused by a different mechanism.

While the linewidths hardly change, the peak areas of the resonances decrease continuously with approaching band gap until the lines vanish completely when the band gap crosses their energy which is the equivalent of the Mott effect but for highly excited states: An exciton can be observed in the spectra as long as its binding energy E_n^{b} is larger than the band gap shift Δ leading to the following condition for the maximal visible quantum number n_{max} in analogy to Eq. (5.11)

$$n_{\mathrm{max}} = \sqrt{\frac{Ry}{|\Delta|}} \propto \rho_{\mathrm{eh}}^{-1/4} \ , \tag{5.12}$$

assuming a description within the Deybe model (Eq. (5.10)). As we will see now, the Mott densities for highly excited Rydberg excitons are orders of magnitude smaller than for the ground state, indeed justifying a description by the formulas of the Debye model described in the previous section.

Figure 5.2 shows the calculated band gap shifts Δ_{eh} as a function of plasma density ρ_{eh} for two different screening temperatures T_{sc} of 1.35 K and 10 K according to Eqs. (5.1) and (5.8). Additionally the binding energies of the states $n = 10, 15, 20$ and 25 are shown. At a temperature of 1.35 K, plasma densities of 1 $\mu\mathrm{m}^{-3}$ are already sufficient to generate a band gap shift as large as the binding energy of the state $n = 10$, while the state $n = 25$ disappears at even smaller densities around 0.01 electron-hole pairs per $\mu\mathrm{m}^3$. To further highlight the sensitivity of the Rydberg excitons to low densities of free carriers one can compare the critical plasma density ρ_{eh} necessary for the dissociation of a state with quantum number

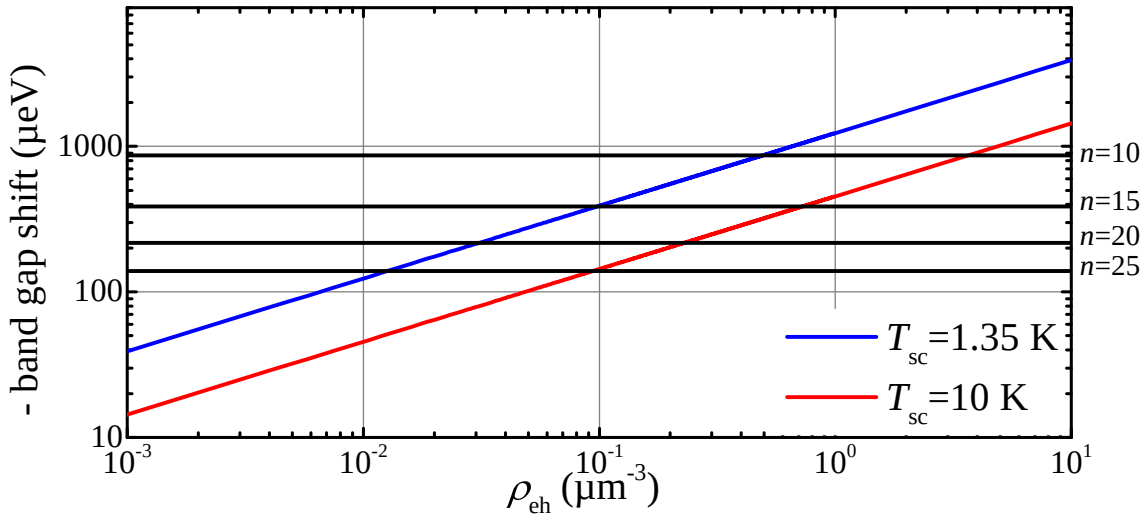

Figure 5.2 Band gap shift Δ_{eh} as a function of plasma density at $T_{\mathrm{sc}} = 1.35$ K (blue line) and at $T_{\mathrm{sc}} = 10$ K (red line). These temperatures represent the limits of equilibrium and maximal out-of-equilibrium of electrons and holes in experiment. Horizontal lines indicate the binding energies of excitons with principal quantum numbers $n = 25, 20, 15, 10$. The crossing points with the blue and red line give critical plasma densities $\rho_{\mathrm{eh,c}}$ for the dissociation of state n. From [Hec+18b].

n to the approximate volume of its wave function $V_n = \frac{4}{3}\pi r_n^3$

$$\rho_{\mathrm{eh,c}}(n) \cdot V_n \approx 10^{-4} n^2 \ . \tag{5.13}$$

For the state $n = 10$ this means that one electron-hole pair in a volume of one hundred times its own wave function is already sufficient to destroy the exciton [Hec+18a]. According to the Debye model, the screening becomes more inefficient at higher plasma temperatures and higher plasma densities are necessary to achieve a comparable band gap shift. Note that the more complex self-consistent model, given in Ref. [Sem+19], results in an opposite temperature dependence, meaning that the band gap shift increases with increasing temperature. A validation of this model is the subject of ongoing research (see discussion in Sec. 5.4).

Nevertheless, using the experimental values for the laser-induced plasma densities ρ_{eh} at a given laser power $\mathrm{P}_{\mathrm{pump}}$, a model can be derived to convert the applied laser power into an induced plasma density that will be shown in the next section. The model was introduced mainly by Prof. Stolz and Dr. Semkat in [Hec+18b]. In this context, also an estimate of the plasma temperature will be given, as it depends on the plasma density as well. Finally, it will be possible to connect the band gap shift to the applied laser power.

5.2.1 Estimation of plasma density from laser power

At an excitation energy of 2.20 eV, the absorption spectrum mainly consists of phonon-assisted absorption bands into yellow nS Ortho-excitons and the green $1S$ exciton, creating a density ρ_{ex} of excited S states that might finally relax into the $1S$ Ortho-exciton via

phonon scattering with a rate Γ_{rel} increasing its density ρ_{o}. Further a conversion of Ortho- into Para-excitons leads to a growing para exciton density ρ_{p}. With rising densities of Ortho- and Para-excitons two-body Auger processes become relevant, whereby two ground state excitons collide and the energy of one exciton is transferred to the other, ionizing it and creating energetically high-lying free electron and hole pairs of density ρ_{eh}. Additionally, a fraction of about $\gamma_{\mathrm{eh}} = 0.3$ is absorbed directly by free electron-hole pairs. This fraction can be estimated from a comparison between the height of continuum absorption and the underlying phonon background. In turn, the plasma created may decay via trapping of electrons and holes with rate Γ_{eh} or recombine to $1S$ excitons with a rate Γ_{rc}. All these coupled processes are described by the following rate equations that were mainly developed in refs. [Sch+12; Sto+12]. A relaxation into Rydberg states is neglected here, but will be discussed in Sec. 6.5.1.

$$\dot{\rho}_{\mathrm{ex}} = (1-\gamma_{\mathrm{eh}})G(P) - \rho_{\mathrm{ex}}(\Gamma_{\mathrm{op}} + \Gamma_{\mathrm{rel}}) \ , \tag{5.14}$$

$$\dot{\rho}_{\mathrm{o}} = \frac{3}{4}\Gamma_{\mathrm{rc}}\rho_{\mathrm{eh}}^2 + \Gamma_{\mathrm{rel}}\rho_{\mathrm{ex}} - \rho_{\mathrm{o}}(2A_{\mathrm{oo}}\rho_{\mathrm{o}} + A_{\mathrm{op}}\rho_{\mathrm{p}} + \Gamma_{\mathrm{o}} + \Gamma_{\mathrm{op}}) \ , \tag{5.15}$$

$$\dot{\rho}_{\mathrm{p}} = \frac{1}{4}\Gamma_{\mathrm{rc}}\rho_{\mathrm{eh}}^2 + \Gamma_{\mathrm{op}}(\rho_{\mathrm{ex}} + \rho_{\mathrm{o}}) - \rho_{\mathrm{p}}(A_{\mathrm{op}}\rho_{\mathrm{o}} + 2A_{\mathrm{pp}}\rho_{\mathrm{p}} + \Gamma_{\mathrm{p}}) \ , \tag{5.16}$$

$$\dot{\rho}_{\mathrm{eh}} = \gamma_{\mathrm{eh}}G(P) + A_{\mathrm{oo}}\rho_{\mathrm{o}}^2 + A_{\mathrm{op}}\rho_{\mathrm{o}}\rho_{\mathrm{p}} + A_{\mathrm{pp}}\rho_{\mathrm{p}}^2 - \Gamma_{\mathrm{rc}}\rho_{\mathrm{eh}}^2 - \Gamma_{\mathrm{eh}}\rho_{\mathrm{eh}} \ . \tag{5.17}$$

Here, A_{ij} $(i,j = \mathrm{o},\ \mathrm{p})$ are the Auger rates for the different combinations of $1S$ Ortho- and Para-excitons and Γ_{o} and Γ_{p} are the energy relaxation rates of the $1S$ Ortho- and Para-excitons. The pump power $\mathrm{P}_{\mathrm{pump}}$ of the circular laser spot with radius R_{spot} at pump energy E_{pump} is included in $G(\mathrm{P}_{\mathrm{pump}}) = \frac{\alpha(E_{\mathrm{pump}})}{\pi R_{\mathrm{spot}}^2 E_{\mathrm{pump}}}\mathrm{P}_{\mathrm{pump}}$. In the experiment considered here, the proportionality constant is $4 \cdot 10^{-4}\ \mu\mathrm{m}^{-3}\mu\mathrm{W}$ ns.

The following parameters are relevant for Auger scattering processes and were determined experimentally in Refs. [Sch+12; Sto+12] to be

$$A_{\mathrm{oo}} = 6.6 \times 10^{-17}\ \tfrac{\mathrm{cm}^3}{\mathrm{ns}},\ A_{\mathrm{op}} = \frac{A_{\mathrm{oo}}}{4},\ A_{\mathrm{pp}} = 2 \times 10^{-18}\ \tfrac{\mathrm{cm}^3}{\mathrm{ns}},$$
$$\Gamma_{\mathrm{o}} = 0.02\ \tfrac{1}{\mathrm{ns}},\ \Gamma_{\mathrm{op}} = 0.2\ \tfrac{1}{\mathrm{ns}},\ \Gamma_{\mathrm{p}} = 0.005\ \tfrac{1}{\mathrm{ns}} \ .$$

Further, the relaxation rate of the excited excitons into the ground state is given by $\Gamma_{\mathrm{rel}} = 0.06\frac{1}{\mathrm{ns}}$. Unfortunately, the parameters such as the specific Auger-rates, but also $1S$ exciton lifetimes can differ from sample to sample and are even stress dependent [Sno+14; Den+02]. One would rather have to evaluate these parameters for the particular sample on hand before including them in the model [Nak+02].

Nevertheless, in the range of small applied pump powers up to roughly 1 mW Auger processes can be neglected due to low densities of ground state excitons and the density of free electron-hole pairs ρ_{eh} is mostly given by their direct excitation and decay in Eq. (5.17). Setting $A_{ij} = 0$ $(i,j = \mathrm{o},\ \mathrm{p})$, the steady state of Eq. (5.17) $(\dot{\rho}_{\mathrm{eh}} = 0)$ yields

$$\rho_{\mathrm{eh}}(\mathrm{P}_{\mathrm{pump}}) = -\frac{\Gamma_{\mathrm{eh}}}{2\Gamma_{\mathrm{rc}}} + \sqrt{\left(\frac{\Gamma_{\mathrm{eh}}}{2\Gamma_{\mathrm{rc}}}\right)^2 + \frac{\gamma_{\mathrm{eh}}G(\mathrm{P}_{\mathrm{pump}})}{\Gamma_{\mathrm{rc}}}} \ . \tag{5.18}$$

The resulting densities are shown in the next section in Fig. 5.5 (a) for the eventually obtained values for Γ_{eh} and Γ_{rc} (see Sec. 5.2.3).

5.2.2 Cooling of electrons and holes

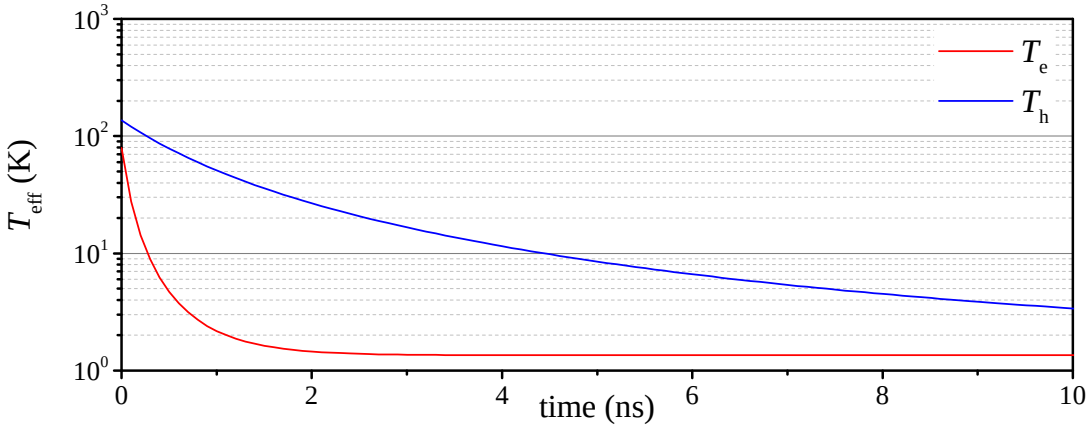

Figure 5.3 Effective temperatures for electrons (red line) and holes (blue line) as a function of time. Excitation energy $E_{\mathrm{pump}} = 2.20$ eV, crystal temperature T_{Crystal}=1.35 K. Adapted from [Hec+18b].

As shown in Fig. 5.2, the screening depends not only on the plasma density but also on its temperature T_{sc}. To estimate a final temperature for the electron-hole plasma, cooling mechanisms have to be considered, that act during the lifetime of electrons and holes. After excitation at 2.20 eV electrons and holes are in a state with high kinetic energy and might lose energy due to carrier-phonon- or carrier-carrier-scattering. Due to the low carrier densities in the experiment, carrier-carrier scattering is neglected and only acoustic phonon scattering is taken into account in the following. For both electrons or holes, separate quasi-thermal Maxwell-Boltzmann distributions with effective temperatures $T_{\mathrm{eff},i}, i = e, h$ are assumed. The carrier temperature loss rates for acoustic phonon scattering at a crystal temperature T_{Crystal} are given by [Rid82]

$$\frac{dT_{\mathrm{eff},i}}{dt} = C_{0,i}(T/T_{\mathrm{eff},i} - 1)T_{\mathrm{eff},i}^{3/2}, \text{ with } C_{0,i} = \frac{8}{3\sqrt{\pi}} k_{\mathrm{B}}^{1/2} \frac{D_i^2 (2m_i)^{5/2}}{2\pi\rho_{\mathrm{Cu_2O}}\hbar^4} . \tag{5.19}$$

Here, D_i are the acoustic phonon deformation potentials for the conduction and valence band, given by $D_{\mathrm{c}} = 3.5$ eV and $D_{\mathrm{v}} = 1.8$ eV in [Sto+18]. The parameter $\rho_{\mathrm{Cu_2O}}$ is the mass density of Cu_2O given by $\rho_{\mathrm{Cu_2O}} = 6.09$ g/cm^3 [Mad+98]. This yields a dependence on time t for the effective carrier temperatures for species i as

$$T_{\mathrm{eff},i}(t) = T_{\mathrm{Crystal}} \left[\tanh\left(\operatorname{artanh}\sqrt{T_{\mathrm{Crystal}}/T_{0,i}} + \sqrt{T_{\mathrm{Crystal}}} C_{0,i} t/2\right)\right]^{-2} . \tag{5.20}$$

Here, $T_{0,i}$ are the initial temperatures that are connected to the pump laser energy E_{pump} via

$$T_{0,i} = \tfrac{2}{3}\sigma_i (E_{\mathrm{pump}} - E_{\mathrm{g}})/k_{\mathrm{B}} , \tag{5.21}$$

with $\sigma_{\mathrm{e}} = m_{\mathrm{h}}/(m_{\mathrm{e}} + m_{\mathrm{h}})$ and $\sigma_{\mathrm{h}} = m_{\mathrm{e}}/(m_{\mathrm{e}} + m_{\mathrm{h}})$. For a crystal temperature of $T_{\mathrm{Crystal}} =$ 1.35 K and a laser light energy of $E_{\mathrm{pump}} = 2.20$ eV this yields the electron and hole cooling

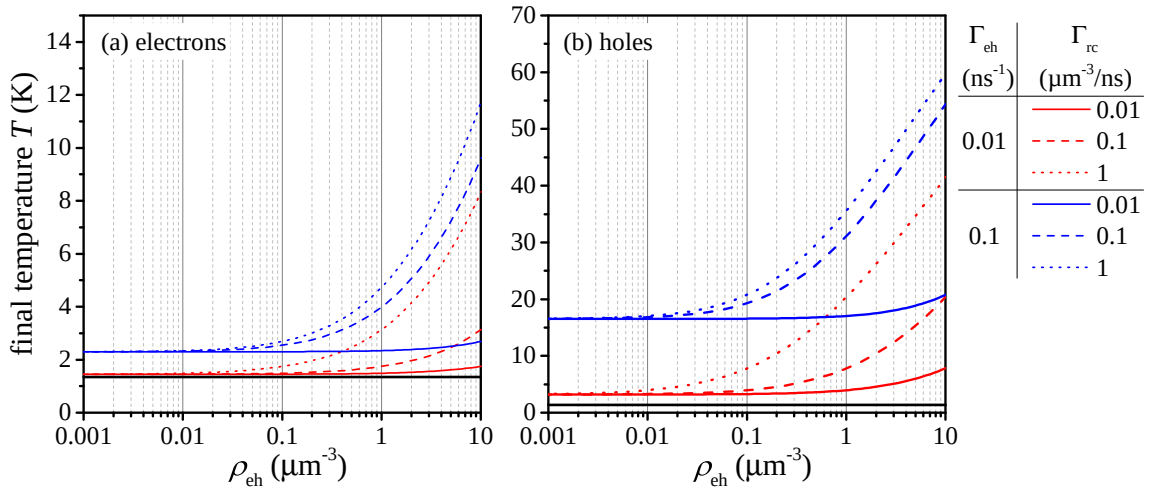

Figure 5.4 Final average temperatures of electrons (a) and holes (b) for CW excitation as a function of the electron-hole plasma density and different sets of relaxation parameters. The red curves are calculated with $\Gamma_{\mathrm{eh}} = 0.01/\mathrm{ns}$, the blue lines with $\Gamma_{\mathrm{eh}} = 0.1/\mathrm{ns}$. For each value of Γ_{eh}, three values of Γ_{rc} are shown. Crystal temperature T_{Crystal}=1.35 K. The faster the decay the higher is the temperature of the remaining plasma and the screening becomes weaker. Adapted from [Hec+18b].

curves shown in Fig. 5.3. The lighter holes start at higher temperatures and need more time to cool down compared to the electrons. To account for the finite carrier lifetime, Eq. (5.17) is solved for an excitation pulse with initial electron-hole density $\rho_{\mathrm{eh},0}$ and normalized to a time integral of 1. This leads to the following weighting function

$$f(t, \Gamma_{\mathrm{eh}}, \Gamma_{\mathrm{rc}}, \rho_{\mathrm{eh},0}) = \frac{\Gamma_{\mathrm{eh}}\Gamma_{\mathrm{rc}}}{(\Gamma_{\mathrm{eh}} + \Gamma_{\mathrm{rc}}\rho_{\mathrm{eh},0})e^{\Gamma_{\mathrm{eh}}t} - \Gamma_{\mathrm{rc}}\rho_{\mathrm{eh},0}} \frac{\rho_{\mathrm{eh}}}{\ln\left[\frac{\Gamma_{\mathrm{eh}}+\Gamma_{\mathrm{rc}}\rho_{\mathrm{eh},0}}{\Gamma_{\mathrm{eh}}}\right]} \,. \tag{5.22}$$

Next, the temporal evolution of the carrier temperatures $T_{\mathrm{eff},i}$ is weighted with $f(t)$ to describe the temperature contribution of the initially injected density $\rho_{\mathrm{eh},0}$ to the total temperature after a time t. In order to obtain the final average temperature for each species in a CW excitation scheme as in the experiment, the integral over all these contributions is taken

$$\langle T(\Gamma_{\mathrm{eh}}, \Gamma_{\mathrm{rc}}, \rho_{\mathrm{eh},0})\rangle_i = \int_0^\infty T_{\mathrm{eff},i}(t) f(t, \Gamma_{\mathrm{eh}}, \Gamma_{\mathrm{rc}}, \rho_{\mathrm{eh},0}) dt \,. \tag{5.23}$$

In the following, the brackets $\langle\rangle$ are left out for simplicity. Figure 5.4 shows average temperatures obtained by Eq. (5.23) for different parameters Γ_{rc} and Γ_{eh} as a function of plasma density ρ_{eh} for electrons (a) and holes (b) separately. As expected, with a faster decay rate of the injected carriers (higher values for Γ_{eh}, Γ_{rc}), the plasma temperature remains higher as there is less time to cool down within the limited lifetime. Further, a larger amount of hot carriers sums up to a higher final temperature as well, which renders the temperature density-dependent. At low densities and for the decay rates in Fig. 5.4, the electrons even nearly cool down to the crystal temperature, while the hole temperatures always remain higher. Thus, the contributions of electrons and holes to the total screening temperature

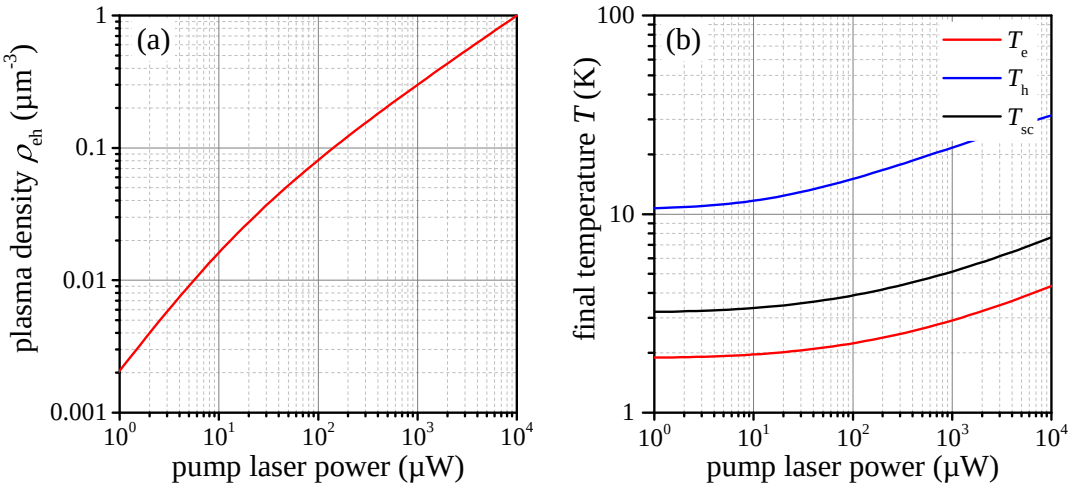

Figure 5.5 (a): Plasma density as a function of pump laser power. (b): Final plasma temperatures for electrons T_e and holes T_h as well as the total screening temperature T_{sc} for CW excitation as functions of pump laser power. Both curves are calculated with the relaxation parameters $\Gamma_{eh} = 18^{-1}$/ns and $\Gamma_{rc} = 1.15\ \mu m^{-3}$ obtained from fitting the band gap shift, see text. Crystal temperature $T_{Crystal}$=1.35 K. Adapted from [Hec+18b].

are different. Therefore the total screening temperature is given by

$$1/T_{sc} = (1/T_e + 1/T_h)/2 \tag{5.24}$$

and the inverse screening length is given by

$$\kappa = \sqrt{2\rho e^2/(\epsilon_0 \epsilon_s k_B T_{sc})}\ . \tag{5.25}$$

The carrier temperatures T_e and T_h as well as the total screening temperature T_{sc} are shown in Fig. 5.5 (b) as a function of laser power for the parameters $\Gamma_{eh} = 18^{-1}$/ns and $\Gamma_{rc} = 1.15\ \mu m^{-3}$ (see Sec. 5.2.3). As the screening and with it the laser-induced band gap shift $\Delta_{eh}(\rho_{eh}(P_{pump}), T_{sc}(\rho_{eh}(P_{pump}))$ are stronger at low plasma temperatures (Fig. 5.2) they are expected to be dominated by the electrons. Further, the effects weaken with increasing laser power due to enhanced densities and temperatures.

5.2.3 Band gap shift and n_{max} as a function of laser power

In order to reproduce the laser-induced band gap shift Δ_{eh} shown as blue dots in Fig. 5.6, we separate it from the inherent band gap shift Δ_0 by $\Delta_{eh} = \sqrt{\Delta^2 - \Delta_0^2}$ and compare it with the applied laser power. With the model presented above we can now reproduce the observed shift by adjusting the parameters to $\Gamma_{eh} = 18^{-1}$ns and $\Gamma_{rc} = 1.15\ \mu m^{-3}$/ns (blue line in Fig. 5.6). The experimentally observed maximal quantum numbers n_{max} are shown in Fig. 5.6 as well (red circles) in dependence on the applied laser power along with a comparison to the theoretical expectation after Eq. (5.12) (red bars). The upper abscissa shows the corresponding plasma densities, obtained with the parameters mentioned before.

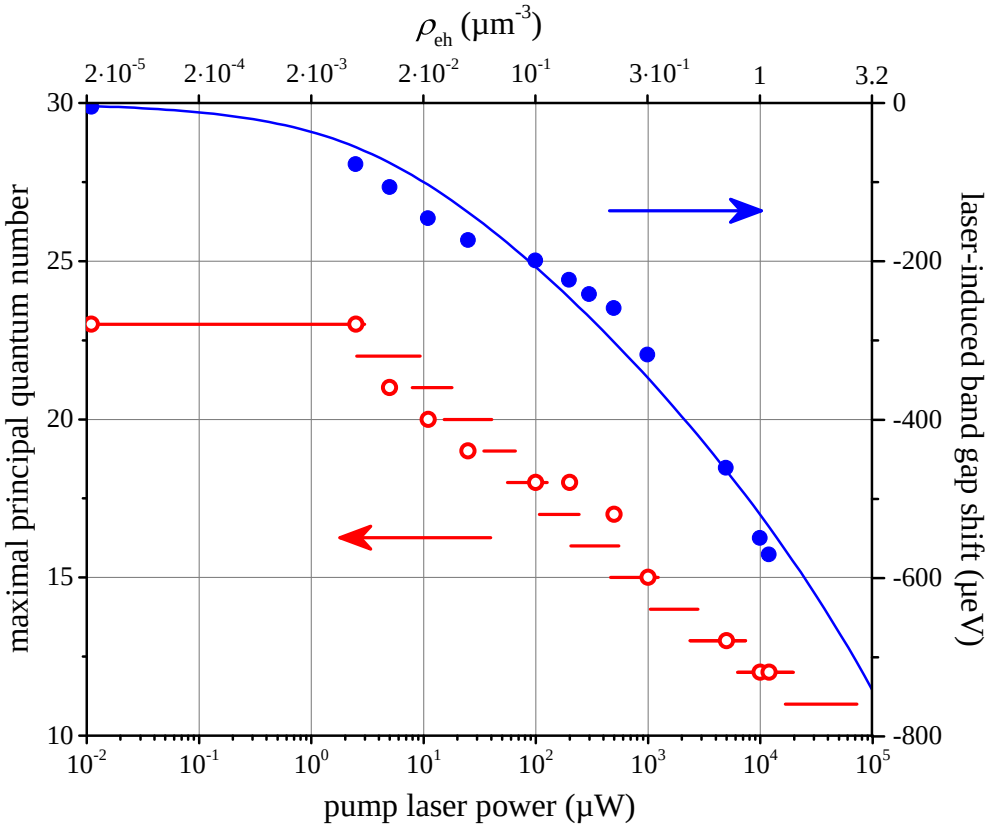

Figure 5.6 Left ordinate: Highest observed quantum number as a function of pump laser power (bottom abscissa) and corresponding laser-induced plasma density (top abscissa) as observed in the experiment (dots) compared to the theoretical prediction (bars) following Eq. (5.12). Right ordinate: Dependence of band gap shift on these parameters. Blue dots show the experimental values and the blue line shows the theoretical dependence. Adapted from [Hec+18b].

It should be noted that the values found for Γ_{eh} and Γ_{rc} depend strongly on several other input parameters. For example, the exact amount of absorbed laser power should be taken into account, including all reflections and light scattering at the sample surface and cryostat windows (cf. Ch. 3). Further, Γ_{eh} and Γ_{rc} depend on the relaxation mechanisms considered in the cooling model. Here, LO-phonon scattering is neglected in a first approach, but should be taken into account in an extended model. This extension of the cooling mechanism is still the subject of ongoing research. Finally, the rate model described above also includes Auger processes that are neglected here due to the low densities of electron-hole pairs and the corresponding density of $1S$ excitons. For a more accurate model, the Auger processes could be taken into account even for low densities. However, as already mentioned above, one would first have to evaluate the relevant Auger rates for the particular sample used [Nak+02].

Whereas the integration of all these mechanisms to a full model that converts the absorbed laser power into a plasma density is a subtle issue, the position of the band gap can also be

read out directly from the spectrum. Thus, it is possible to decouple the band gap position from the applied laser power. In the next section, the dependence of the oscillator strength on band gap position will be deduced.

5.2.4 Oscillator strength

Besides the band gap shift and the reduction of maximal observable quantum number n_{max}, the reduction of oscillator strength with increasing band gap shift is a remarkable observation and shall be described in this section.

According to studies of atomic plasmas, not only the binding energy but also the wave function of the perturbed states is changed by the Coulomb screening. As described in [Pau+09], the low plasma densities allow one to use a variational ansatz to obtain the modified wave functions as analytical solutions of the radial Schrödinger equation including a screened Coulomb potential. One uses a variational adjustment of an effective Bohr radius $a_{\mathrm{eff}}^{\mathrm{B}} = x \cdot a^{\mathrm{B}}$ to minimize the binding energy of a state with quantum number n in a plasma $E_n^{\mathrm{b,sc}}$. Adapting this idea, we find for the expectation value of the nP exciton energy in a plasma:

$$\langle E_P(n)\rangle = \Delta + \underbrace{\frac{Ry}{n^2}\cdot\left(\frac{1}{x^2} - \frac{2}{x}\frac{1}{(1+n\xi(\Delta)x)^{2n}}\,{}_2F_1\right)}_{E_n^{\mathrm{b,sc}}(\Delta)} \,. \tag{5.26}$$

Here, $\xi(\Delta) = \kappa a^{\mathrm{B}}/2 = -4\pi\epsilon_0\epsilon_s a^{\mathrm{B}}\Delta/2e^2$ is a normalized inverse screening length and ${}_2F_1(-1-n, 2-n, 1, (n\xi(\Delta)x)^2)$ is the Gaussian hypergeometric function. Note that $E_n^{\mathrm{b,sc}} \to -Ry/n^2$ for $\xi \to 0$ and $E_n^{\mathrm{b,sc}} \to 0$ for $\xi \to \infty$.

The second part of Eq. (5.26), $E_n^{\mathrm{b,sc}}$, is shown in Fig. 5.7 (a) as a function of effective Bohr radius $a_{\mathrm{eff}}^{\mathrm{B}}$ and different plasma densities for $n = 16$. For $\rho_{\mathrm{eh}} = 0$ one obtains the unperturbed binding energies with the unchanged Bohr radii. With an increasing density ρ_{eh} as well as increasing inverse screening length ξ the position of the energy minimum and $a_{\mathrm{eff}}^{\mathrm{B}}$ increases. In other words $a_{\mathrm{eff}}^{\mathrm{B}} > a^{\mathrm{B}}$ and the wave function of the excitonic state grows due to the screened Coulomb attraction. Figure 5.7 (b) shows the obtained effective Bohr radii $a_{\mathrm{eff}}^{\mathrm{B}}$ for various n as a function of both band gap shift Δ and corresponding plasma density ρ_{eh} for $T_{\mathrm{sc}} = 5$ K.

However, the exciton energies observed in Fig. 5.1 do not shift at all regardless of the band gap shift Δ until the absorption lines completely vanish. To account for this fact an effective quantum number n_{eff} is introduced such that the binding energies of the perturbed states stay equal to the unperturbed ones [1]:

$$\begin{aligned} \langle E_P(n)\rangle = -\frac{Ry}{n^2} &= \Delta + \frac{n^2}{n_{\mathrm{eff}}^2}E_{\mathrm{sc}}(\Delta, n) \\ \Leftrightarrow n_{\mathrm{eff}}^2(\Delta, n) &= \frac{-n^2 E_{\mathrm{sc}}(\Delta, n)}{\left(\Delta + \frac{Ry}{n^2}\right)} \,. \end{aligned} \tag{5.27}$$

The resulting values for n_{eff} are additionally shown in Fig. 5.7 (b) as a function of band gap shift. For small band gap shifts n_{eff} stays almost constant but increases rapidly when the band gap crosses the exciton binding energy.

[1] The quantum defect $\delta_{n,l}$ can be neglected for these high values of n

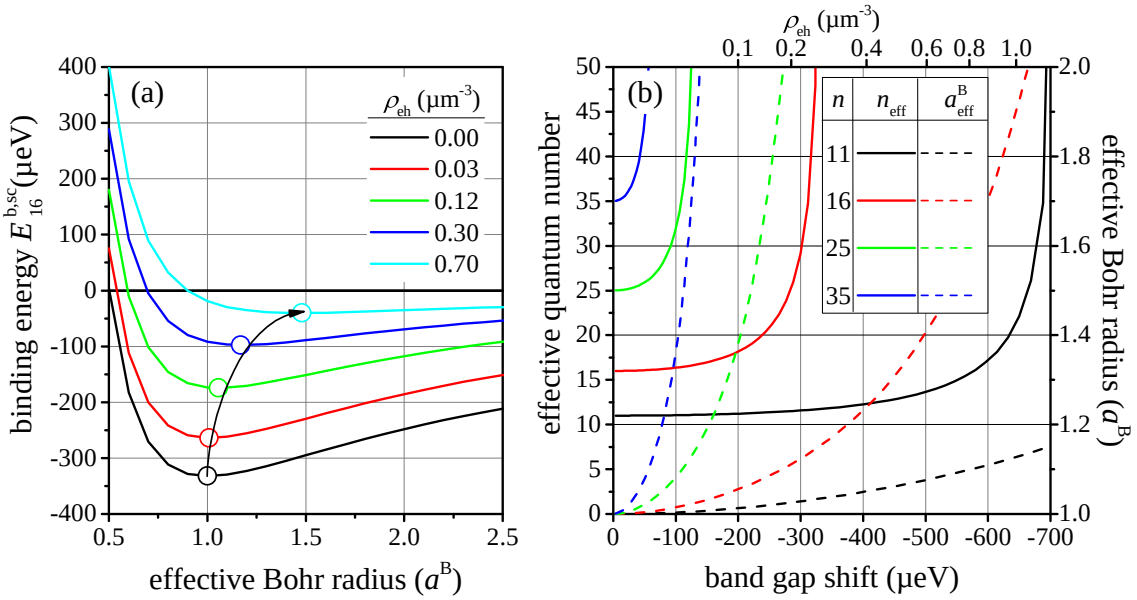

Figure 5.7 (a) Binding energy of state $n = 16$ in a plasma $E_{16}^{\mathrm{b,sc}}$ as a function of effective Bohr radius for increasing plasma density ρ_{eh} and T_{sc}=5 K for state $n = 16$. (b) Effective principal quantum number n_{eff} (full lines, left ordinate) and effective Bohr radius $a_{\mathrm{eff}}^{\mathrm{B}}$ (dashed lines, right ordinate) as a function of band gap shift Δ for $n = 11, 16, 25, 35$. The upper abscissa shows corresponding plasma density ρ_{eh} at $T_{\mathrm{sc}} = 5$ K. Adapted from [Hec+18b].

Finally, the values of $a_{\mathrm{eff}}^{\mathrm{B}}$ and n_{eff} allow us to calculate the relative oscillator strength for a particular state with quantum number n as a function of the band gap shift Δ (see Eq. (2.34))

$$f_{\mathrm{rel}}(\Delta, n) = \frac{n_{\mathrm{eff}}^2(\Delta, n) - 1}{(a_{\mathrm{eff}}^{\mathrm{B}}(\Delta)/a^{\mathrm{B}})^5 \; n_{\mathrm{eff}}^5(\Delta, n)} \; . \tag{5.28}$$

Figure 5.8 (a) shows a comparison of the experimental peak areas with the theoretical prediction of Eq. (5.28), for the states $n = 13$, 14, 15, 17 and 19. Starting at an initial band gap shift Δ_0 of about -150 μeV at zero pump power, the observed decrease of peak area follows nicely the predicted oscillator strength.

Going one step further, the influence of a remaining band gap shift or plasma density can be described. Figure 5.8 (b) shows the relative oscillator strength for the states from $n = 10$ up to $n = 30$ for different band gap shifts in terms of an inherent shift Δ_0 and corresponding plasma density ρ_0, calculated for a crystal temperature of 1.35 K. The calculated density is used as an estimate for the density of charged impurities.

Without any band gap shift, i.e. $\tilde{E}_{\mathrm{g}} = E_{\mathrm{g}}$, the values follow the expected n^{-3} dependence. Including only small shifts, i.e. small plasma densities, already leads to a strong drop of oscillator strength for the highest n, well known from experiments (see [Kaz+14] or Ch. 2). Thus, even if the band gap did not cross the binding energy yet, the oscillator strength can drop about an order of magnitude making it harder to observe a resonance in experiment. As another consequence, the wave functions of the states with highest n are always modified

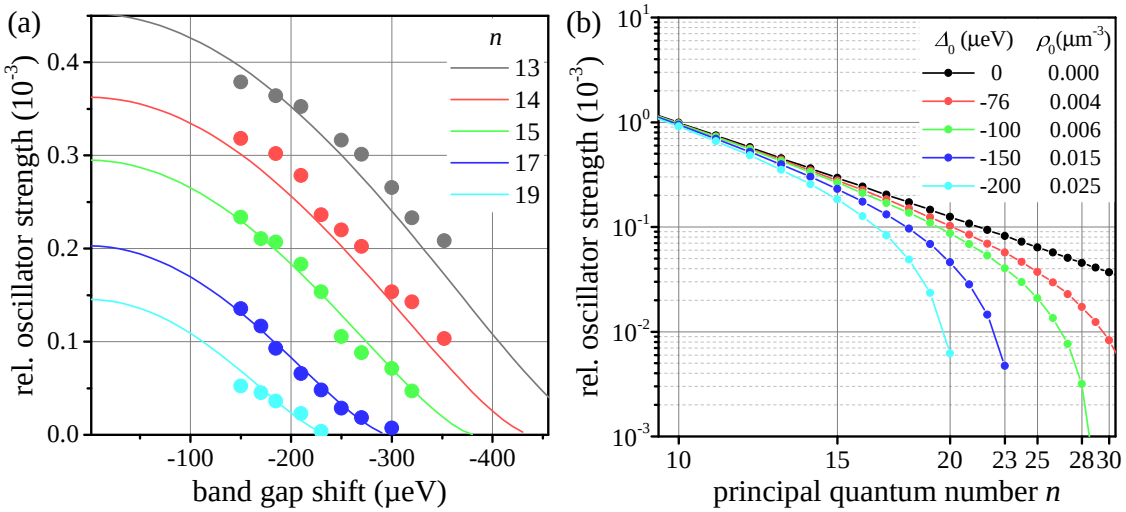

Figure 5.8 (a) Comparison of measured peak area as a function of band gap shift with theoretical prediction given by Eq. (5.28). The experimental values are scaled with a constant factor to fit the theory curves at $\Delta_0 = -150$ μeV. Adapted from [Hec+18b]. (b) Relative oscillator strengths for resonances of $n = 10$ up to $n = 30$ for different values of an inherent band gap shift Δ_0 and corresponding plasma density ρ_0 for a crystal temperature of 1.35 K. Already low plasma densities ρ_0 lead to a drop of oscillator strength for the highest n.

by the influence of this inherent plasma density.

Following the argumentation given above, the possibility to observe higher exciton states is directly connected to the inherent band gap shift Δ_0 present at zero pump power. This shift is assumed to be induced by uncompensated impurities in the sample and will differ from sample to sample. For the measurements described in this chapter, the value of $\Delta_0 = -150$ μeV corresponds to an estimated impurity density of about $\rho_0 = 0.015$ μm^{-3}, which is in line with the microscopic model in Ref. [Krü+20]. As an example, to observe an exciton with principal quantum number of $n = 30$, a band gap shift below 100 μeV would be necessary, corresponding to an impurity concentration even below $5 \cdot 10^{-3}$ μm^{-3}.

Finally, the impurity density limiting the highest observable n_{max} is expected to differ between different positions of the same sample. Figure 5.9 shows some absorption spectra measured at the same temperature of 800 mK and an excitation power of about 1 μW, but different sample positions. At exactly the same excitation conditions, the position of the shifted band gap $\tilde{E}_{\mathrm{g}} = E_{\mathrm{g}} + \Delta_0$ and with it the highest observable exciton resonance n_{max} depends on the exact sample position. Additionally, the oscillator strength of all shown resonances is lowered as the band gap is shifted to lower energies, in accordance with this model.

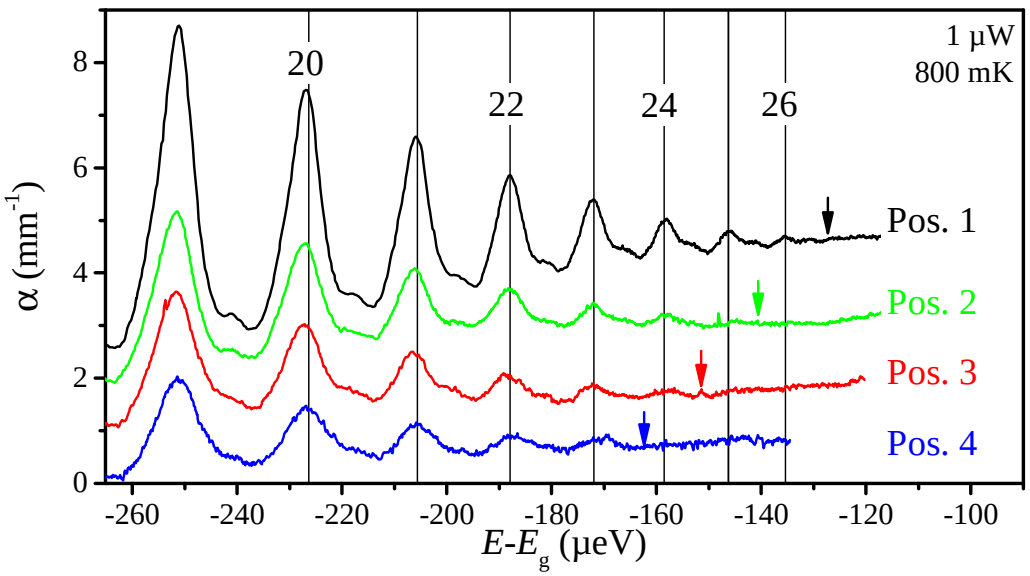

Figure 5.9 Comparison of absorption spectra recorded at the same temperature and excitation power but different sample positions. Depending on the exact condition of the illuminated area, the band gap $\tilde{E}_\mathrm{g} = E_\mathrm{g} + \Delta_0$ is shifted to lower energies followed by smaller peak areas of the highest observable resonances. Arrows indicate the band gap $\tilde{E}_\mathrm{g}$. Spectra are shifted for clarity. Adapted from [Hec+20].

5.3 Critical dependence of n_{max} on external parameters

In the previous section, the impact of an electron-hole plasma on Rydberg excitons was described. The cloud of free carriers leads to a gradual band gap renormalization and screens the Coulomb potential which modifies the exciton wave functions and leads to a disappearance of exciton lines with increasing electron-hole density. But even at zero pump power a band gap shift Δ_0 can be observed that is attributed to uncompensated impurities in the sample, which limits the observable Rydberg exciton series.

However, one can think about further external parameters that will limit the possibility to observe higher Rydberg states. In this context, the dependence of the absorption spectrum on both the probe laser's excitation power and the crystal temperature were investigated in detail and the results are given in this section. Again, all shown spectra are measured at sample $H7$.

5.3.1 Excitation power

As already reported in [Kaz+14], the existence and observability of Rydberg exciton resonances in the absorption spectrum depends strongly on the applied excitation power. In contrast to the experiment described in the section before, the resonances can be bleached out with a single laser and below band gap excitation as well. In this case, the exciton transition is driven resonantly by one laser, increasing the exciton density with rising laser power. The disappearance of exciton lines can be attributed to the Rydberg blockade mechanism, where the excitation of two or more excitons within a given volume becomes impossible as their interaction shifts the excitation energy out of the laser resonance (see Sec. 6).

However, also in experiments using a single laser, an unavoidable amount of free electron-hole pairs might be excited, leading to a band gap renormalization. The created excitons may relax towards lower-lying states and eventually form $1S$ excitons that in turn decay via the Auger mechanism into pairs of free electrons and holes. Additionally, the direct excitation of $1S$ excitons via phonon-assisted absorption is possible below the band gap (see Sec. 5.2.1). Next, even in the narrow energy range below the band gap, the direct excitation of free electron-hole pairs might be possible, due to absorption into the Urbach tail, which describes an exponentially smeared out band gap (cf. Sec. 2.5 or Fig. 5.1). Further, free electron-hole pairs may relax into Rydberg states of high principal quantum numbers, which in turn leads to an enhanced Rydberg blockade. In general, the exact density of free electron-hole pairs created by below band gap excitation remains unknown as all these processes take place independently and is still the subject of current investigations.

However, regardless of the exact blockade mechanism driven by below band gap excitation, the dependence of the absorption spectrum on laser power can be observed experimentally. While in [Kaz+14] studies were performed with a focus on the disappearance of states with increasing power, here, the low-power limit will be investigated. Figure 5.10 shows absorption spectra for various excitation powers from 25 μW down to 25 nW at a temperature of 830 mK. The lowest resonance shown belongs to the $n = 22$ exciton. With decreasing power starting from 25 μW, the oscillator strength and the total amount of visible resonances increases. Below 2.5 μW, $n = 26$ and $n = 27$ become visible. Lowering the power further leads to a reduced signal-to-noise ratio which renders the detection of higher

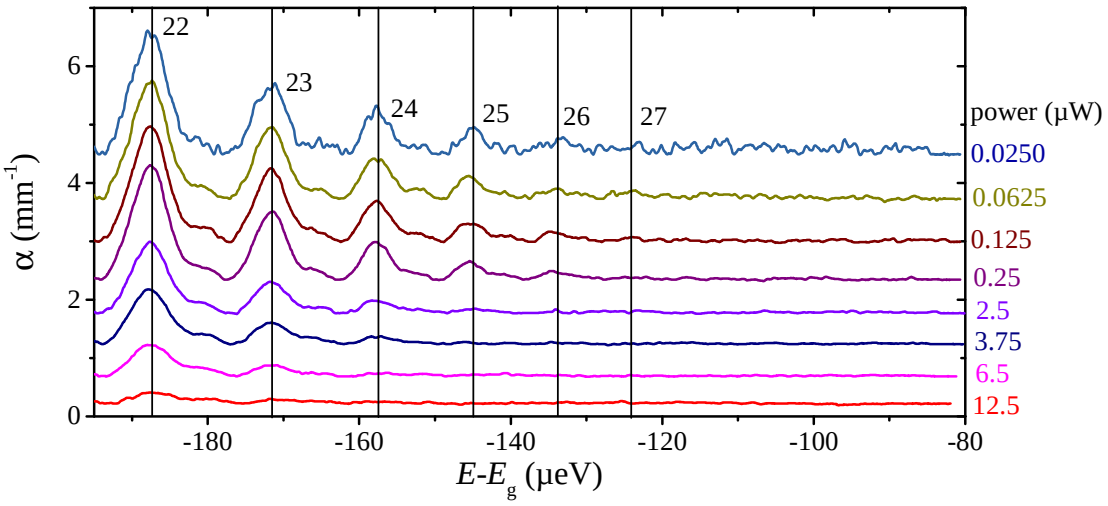

Figure 5.10 Absorption spectra for the highest observable excitons starting from $n = 22$ for different excitation powers of the probe laser. Starting with $n = 22$ as the only visible state at 12.5 μW, the number of observable states rises with falling laser power from bottom to top. Below 2.5 μW, excitons up to $n = 27$ are observable, whereas at 25 nW the signal-to-noise ratio already becomes too bad. The spectra are measured at the best sample position found and at a temperature of $T = 830$ mK. The spectra are corrected by subtracting the background and stacked vertically for better comparison. Adapted from [Jan17].

lines more complicated. The lowest applied power was 500 pW, as measured in front of the cryostat (cf. Ch. 3), which corresponds roughly to 250 pW of absorbed power at the sample (taking reflections at 5 cryostat windows into account for this particular case). Even replacing the detector by an avalanche photodiode (Hamamatsu C-5331) or a low-power photoreciever, able to detect optical powers below 20 pW (Femto FWPR-20 SI), did not improve the signal in terms of both the maximal observable quantum number and signal-to-noise ratio. Thus, a laser power between 100 nW and 1 μW seems to be well suited to avoid a major impact on the Rydberg exciton series by the possible blockade mechanisms mentioned above and provides a reasonable signal quality at the same time.

5.3.2 Temperature

The highest Rydberg excitons with principal quantum numbers higher than $n = 20$ have binding energies below 200 μeV. For the state $n = 25$ one finds a binding energy of about $E^{\mathrm{b}}_{25P} = 140$ μeV. At a typical measurement temperature in a liquid helium bath of 1.35 K, the thermal energy already amounts to $k_B T \approx 115$ μeV which is comparable to the binding energy of that state. Thus, for the highest excitons, thermal dissociation is another potential mechanism that might limit the observability of higher states, as all excitons with a binding energy in the range of the thermal energy are expected to dissociate. Thermal dissociation can result in linewidth broadening and eventually in an overlapping of resonance curves due to their small spectral separation. In turn, an increase of temperature should further reduce the number of observable exciton lines as the number of thermal phonons increases

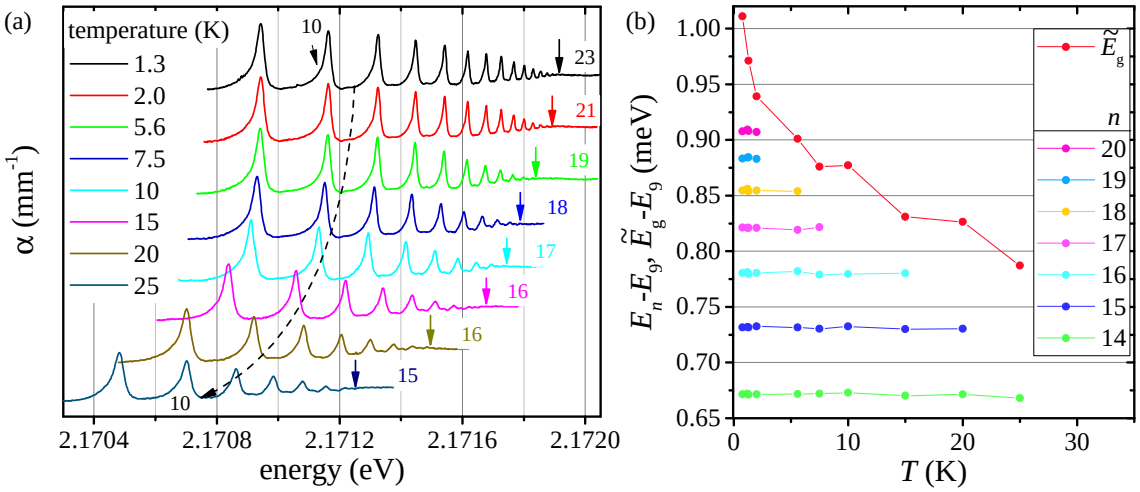

Figure 5.11 (a) Absorption spectra at various temperatures from 1.3 K up to 25 K. With increasing temperature the highest observable n_{max} vanish and resonance energies are shifted to lower energies. The numbers give n_{max}, the arrows indicate the position of the band gap $\tilde{E}_{\mathrm{g}}$. The band gap shifts are stronger than those of the exciton energies. Spectra are shifted for clarity. Adapted from [Hec+18a]. (b) Evaluated energies of excitons and band gap from panel (a), given in terms of the energy difference to the energy of the $9P$ state. While the energy difference between excitonic lines stays constant with increasing temperature, the band gap shifts about 200 μeV to lower energies.

and dissociation becomes more probable. In this context, a temperature series of absorption spectra in the range between 1.3 K to 25 K has been measured and is shown in Fig. 5.11 (a). The measurements are performed with a laser power of 1 μW. The spectra indeed show several changes with increasing temperature.

As expected, the highest observable exciton number n_{max} decreases with temperature. Starting from $n_{\mathrm{max}} = 23$ at 1.35 K, only states up to $n_{\mathrm{max}} = 16$ can be observed at 25 K. While the highest lines vanish completely, the oscillator strengths of lower lines start to drop gradually long before they completely vanish. Furthermore, the measurable band gap $\tilde{E}_{\mathrm{g}}$ is shifted to lower energies with increasing temperature (indicated by arrows). This is in line with the known temperature dependence of the nominal band gap E_{g} of a semiconductor, that is well described in the literature (see e.g. [Gru06]). Similar to the band gap, the exciton lines are also shifted to lower energies, while their spectral separation among each other stays constant within μeV-resolution. Interestingly, the band gap shift with temperature is stronger than the exciton line shift, i.e. the energy difference $\tilde{E}_{\mathrm{g}} - E_X = \frac{Ry}{n^2} + \Delta$ becomes smaller. Up to 25 K the band gap shift to lower energies amounts about 220 μeV more than the shift of exciton lines. The energies of the exciton lines from $n = 14$ to $n = 20$ and of the band gap as a function of temperature, both given in terms of the energy difference to the energy of the $9P$ state, are shown in Fig. 5.11 (b). From the constant distance between excitonic lines, a temperature-dependent change of binding energies $E_n^{\mathrm{b}} = -\frac{Ry}{n^2}$ can be excluded. Therefore, a temperature-dependent change of the band gap shift Δ seems probable.

According to Sec. 5.2, a possible explanation for the temperature dependence of Δ can be given by an electron-hole plasma, the density of which increases with rising temperature. Two possible mechanisms for the increase of plasma density with temperature are discussed in the following. One of them is the thermal dissociation of excitons into the continuum, which would increase the density of unbound electrons and holes and result in an additional band gap shift Δ. In turn, due to the reduced energy difference to the continuum, phonons of lower energy are necessary to dissociate an exciton while at the same time, assuming a Bose-Einstein distribution at higher temperatures, the amount of phonons with appropriate energy rises [Hec+18a]. In the temperature range up to 25 K, thermal dissociation might affect most of the excitons visible in Fig. 5.11, since already at 10 K the thermal energy is as large as the binding energy of $n = 10$. While an absorption line in this spectral range is still visible, it can lose oscillator strength and increase in linewidth due to dissociation. Indeed, a broadening of lines can be observed with rising temperature, that could be ascribed to additional phonon interaction. As already extremely low plasma densities of about 0.01 $\mu\mathrm{m}^{-3}$ are sufficient to shift the band gap across the resonance energies of the highest n (Sec. 5.2), the thermal dissociation of excitons seems to be a plausible explanation for the observed temperature dependence of the band gap shift that is stronger than the shift of exciton lines. However, in [Sto+18] the contribution of thermal dissociation to the total linewidth is calculated and shown to be small for temperatures up to 20 K. For lower temperatures, e.g. below 1 K, it is even said to be negligible.

Besides thermal ionization of excitons, the increased amount of unbound carriers could stem from thermal ionization of shallow impurities or defects. This is in line with the behavior of the intermediate peaks between two P lines that are still observable with rising temperatures up to 25 K, which indicates that scattering and decoherence are still low, as can be seen in the plasma-screening experiments as well (Sec. 5.2).

Finally, the exact mechanism that leads to a stronger shift of the band gap compared to the exciton lines might consist of a complex interdependence of the phenomena mentioned above and is still the subject of ongoing research. It should be noted, that on the one hand, within the Debye model, a higher temperature would lead to less effective screening ($\Delta \propto \rho_{\mathrm{eh}}^{1/2} T^{-1/2}$, see Eq. (5.1)), that would have to be overcompensated by the increasing plasma density to result in a temperature-dependent band gap shift to lower energies. On the other hand, the recent calculations in Ref. [Sem+19] predict the opposite trend, i.e. a stronger band gap shift with increasing temperature, in contrast to the Debye model. To obtain a deeper understanding of the underlying mechanisms, first of all a further validation of both models is necessary. Due to the different temperature dependence of the band gap shift in both models, experiments where a pump laser excites resonantly an electron-hole plasma at different temperatures are promising candidates to verify one of the models and are the subject of future studies (see discussion in Sec. 5.4).

Regardless of the exact mechanism that leads to the band gap shift and vanishing of exciton lines, we can conclude that a higher temperature eventually limits the observation of highly excited Rydberg states. In this context, a lowering of temperature below 1 K seems to be a reasonable experimental approach to study limitations of the observable Rydberg exciton series at ultralow temperatures. Thermal dissociation of excitons will be reduced, as the thermal energy will be as low as possible and potential thermal ionization of defects

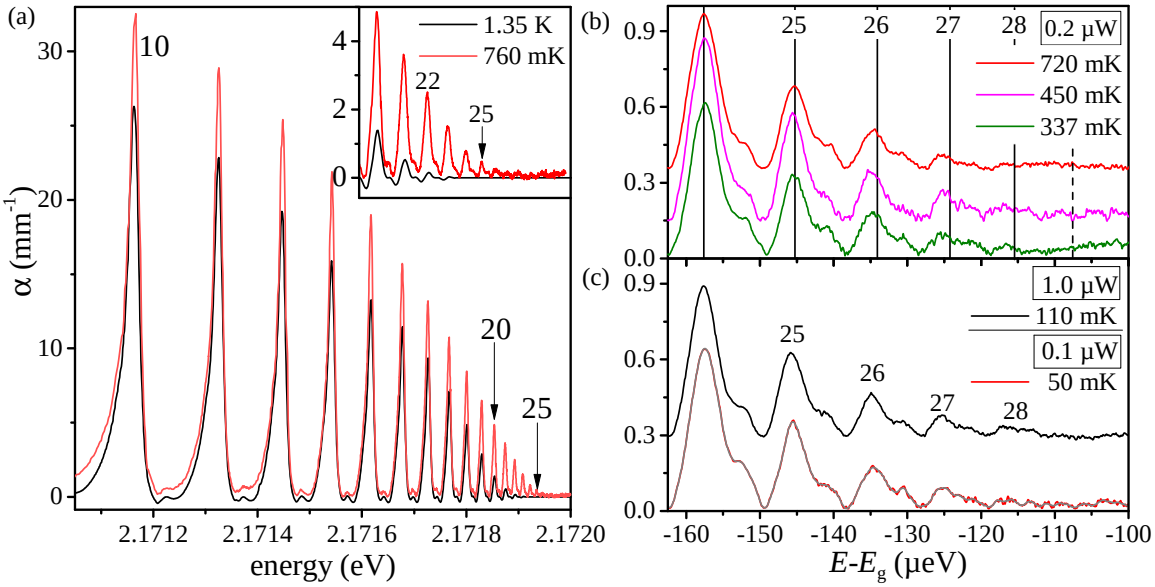

Figure 5.12 (a) Comparison of absorption spectra measured at 1.35 K and 0.76 K. Below 1 K, the absorption coefficient rises for all n. For states with $n > 20$, this results in an important improvement for their visibility. (b) Temperature series from 720 mK down to 337 mK with a low excitation power of 200 nW. Lowering the temperature below 800 mK does not enhance the absorption for states up to $n = 27$, while a tiny absorption grows for $n = 28$. Spectra are recorded at different sample positions and averaged over 10 single measurements. Vertical lines indicate expected resonance energies (dashed: $n = 29$), following Eq. (2.24) with $Ry = 90$ meV and$\delta_{n,P} = 0.08$. (c) The best visibility of $n = 28$ is obtained at 110 mK and a power of 1 μW (black), averaging 8 single measurements. At lowest temperature of 50 mK and 100 nW excitation power (red), the absorption of $n = 28$ does not improve compared to the black curve. This spectrum is averaged over 12 single measurements and additionally smoothed (grey line). In all panels the background is subtracted for better comparison. Adapted from [Hec+20].

is expected to be reduced as well. On the other hand, following the Debye model discussed before in Sec. 5.2, screening becomes more efficient at lower temperatures ($\Delta \propto T^{-1/2}$), which in turn might result in a comparable screening strength already for a smaller amount of free charges.

As reported in [Hec+20; Jan17], we performed absorption measurements in a ^{3}He-^{4}He dilution cryostat at temperatures below 1 K. The lowest temperature achieved was 47 mK. However, already at a temperature of 760 mK, certain changes in the spectra compared to 1.35 K can be observed, as shown in Fig. 5.12 (a). With falling temperature, the oscillator strengths increase while the linewidths become smaller, indicating a reduction of possible scattering effects and an increase of lifetimes. The changes are already visible for excitons with intermediate principal quantum numbers around $n = 10$, while these effects are more significant for states with $n > 20$. At temperatures of 1.35 K, these states can hardly be observed, but at 760 mK, they show pronounced lines up to $n = 27$. According to the previous discussions, this could again be related to a shift of the band gap to higher energies,

either by reduced thermal dissociation or by freezing of thermally ionized impurities.

Lowering the temperature further, from 720 mK to 337 mK, does not improve the spectra significantly as shown in Fig. 5.12 (b). Here, low powers of 200 nW were applied, and for 450 mK and 337 mK indeed one additional tiny feature on the high energy side of $n = 27$ is observed that can be assigned to the state $n = 28$. For all other states no further significant changes are seen. The best result for $n = 28$ is shown in Fig. 5.12 (c) for 110 mK. Notably, the $n = 28$ state is best visible with a higher power than in Fig. 5.12 (b). Thus, even with a slightly higher power one does not destroy the highest states. This is confirmed by the lower spectrum in Fig. 5.12 (c): This spectrum is recorded at both lowest temperature of 50 mK and lowest power of 100 nW, but shows, contrary to the expectations, an even smaller feature for $n = 28$. It is notable that, following the exciton lines to temperatures below 1.35 K, no further shift in energy is observable within μeV-resolution.Also, no further linewidth narrowing can be observed.

Finally, we conclude that temperatures below 1 K indeed improve the quality of absorption spectra. Especially for states with $n > 20$, a significant improvement is seen in terms of a higher absorption coefficient. Already temperatures around 800 mK are sufficient to observe a state with $n = 27$ (Fig. 5.10, and Fig. 5.12 (b)). The observation of an absorption feature assigned to $n = 28$ is possible at temperatures of 450 mK and below, while the best signal-to-noise ratio is obtained with a power of 1 μW. The thermal energy at 100 mK is $k_B T = 8.6$ μeV, comparable to the binding energy of the state $n = 100$, indicating that the observed limit is not given by thermal dissociation.

The spectra shown in panels (b) and (c) were recorded at slightly different sample positions in order to find the best sample position regarding the highest observable quantum number n_{max}. Hence, within an appropriate parameter space of excitation powers between 0.1 and 1 μW and a temperature below 800 mK, the final limiting factor for the highest observable quantum number n_{max} is given by the constitution of the sample itself in terms of the inherent band gap shift Δ_0. This shift is at most 110 μeV, if the $n = 28$ state is visible.

Remarkably, the intermediate peaks for the highest n are almost of the same magnitude as the corresponding exciton peaks. They are clearly shifted towards the lower-lying exciton state, which is in line with the description in [Grü+16] where this peak is expected to be shifted to the state with higher oscillator strength. However, as the oscillator strengths of the corresponding P states drop strongly with n, one would expect these intermediate peaks to decrease, too, whereas they rather seem to shrink less. Further, one would not expect to see this feature on the high energy side of $n = 28$, as there is no transition to a possible state with $n = 29$. On a closer look, especially the peak of $n = 28$ seems to be split. As calculated in [Sto+18], a polariton splitting due to an anticrossing of photon and exciton dispersions is expected to occur for states with $n > 28$. However, the splitting is predicted to be very small (≈ 10 neV). It is assumed to occur at principal quantum numbers $n > 28$, as the radiative decay starts to dominate the linewidth. Since the experimental linewidths for high n are broader than predicted by the model, such a polariton splitting might occur at even higher n in the experiment and cannot explain the observed splitting. In conclusion, the exact origin of the size of intermediate features compared to the adjacent P states at these high quantum numbers remains unclear and is the subject of ongoing research.

The spectra at 760 mK and 110 mK are evaluated by the fitting routine described in Appendix A.3 to reassess the behavior of linewidths and oscillator strengths as a function of

n, known from [Kaz+14], but now for states up to $n = 28$. The results are shown in Fig. 5.13 in comparison with the values from Fig. 2.4 in Sec. 2.5 at 1.35 K (black). For 760 mK the fits are evaluated up to $n = 25$. States with even higher n have an insufficient signal-to-noise ratio to ensure meaningful fits. As no further change in the spectra can be observed with falling temperature in Figs. 5.12 (b) and (c), the states from $n = 25$ up to $n = 28$ are evaluated at 110 mK and shown in the same panel. Due to the peaks' low visibility, error bars are given for the states with $n \geq 20$, which are estimated by the difference between the results of a fit with a single peak and with three adjacent peaks simultaneously, as described in Appendix A.3. As mentioned above, the oscillator strengths slightly increase for intermediate n up to $n = 16$, but show a more significant change for higher n, which can be seen in Fig. 5.13 (a). Although the general trend of a stronger drop in oscillator strength compared to the expected values following an n^{-3} dependence (black line) is confirmed, the oscillator strength of $n = 22$ grows about one order of magnitude at mK-temperatures compared to 1.35 K. A similar result is obtained for the linewidths (Fig. 5.13 (b)). At intermediate n, they narrow slightly at lower temperatures, while the known deviation from the expected n^{-3}-scaling is preserved, even at the lowest temperatures. The expected scaling is shown by the black solid line. The additional broadening of these lines complicates their observation additionally, as their spectral shapes smear out and overlap due to their close spectral separation. The lowest linewidth is about 2.5 μeV for $n = 28$ at 110 mK corresponding to an estimated lifetime of $\tau \approx \frac{h}{\Gamma_n} = 1.6$ ns. Still, the linewidth is 2.5 times larger than the theoretically predicted value. For the distance between electron and hole one finds a radius of $r_{28P} \approx 1.3$ μm (Eq. (2.17)). The lower temperatures improve the observability for the states $n = 20$ up to $n = 26$ while even higher ones are still hard to study due to their small oscillator strength that is still about 3 orders of magnitude below the expected value following an n^{-3}-power law (solid black line).

5.4 Discussion

The results presented in this chapter are based on the Debye model. In a simple first-order approximation, the measured band gap shift Δ and the screening of the Coulomb potential cancel out each other (Eq. (5.9)). This is in agreement with the observations in the experiment, where the exciton lines do not shift at all (Fig. 5.1). However, recent more complex numerical calculations in Ref. [Sem+19] predict strong line shifts for a particular state close to the onset of the Mott transition within the Debye model. For instance, values about 300 μeV for the state $n = 14$ are predicted, in contradiction to the experiments described here. In the same work, a more complex many-body approach for the calculation of the influence of the plasma on excitons is presented, that predicts, in contrast to the Debye model, only small exciton line shifts close to the Mott transition, which are in line with recent measurements that are extended to lower n and reveal small line shifts. Their evaluation is the subject of ongoing research. Remarkably, the recent model also predicts the opposite temperature dependence compared to the Debye model. Whereas the Debye model predicts a band gap shift according to $\Delta \propto \rho_{\mathrm{eh}}^{1/2} T^{-1/2}$ that becomes weaker at higher temperatures, the newer model predicts a shift given by $\Delta \propto \rho_{\mathrm{eh}}^{1/2} T^{1/4}$. Therefore, measurements with increasing plasma density, in analogy to the one presented in the first part of this chapter (Sec. 5.2), but at different crystal temperatures can help to get a better understanding of

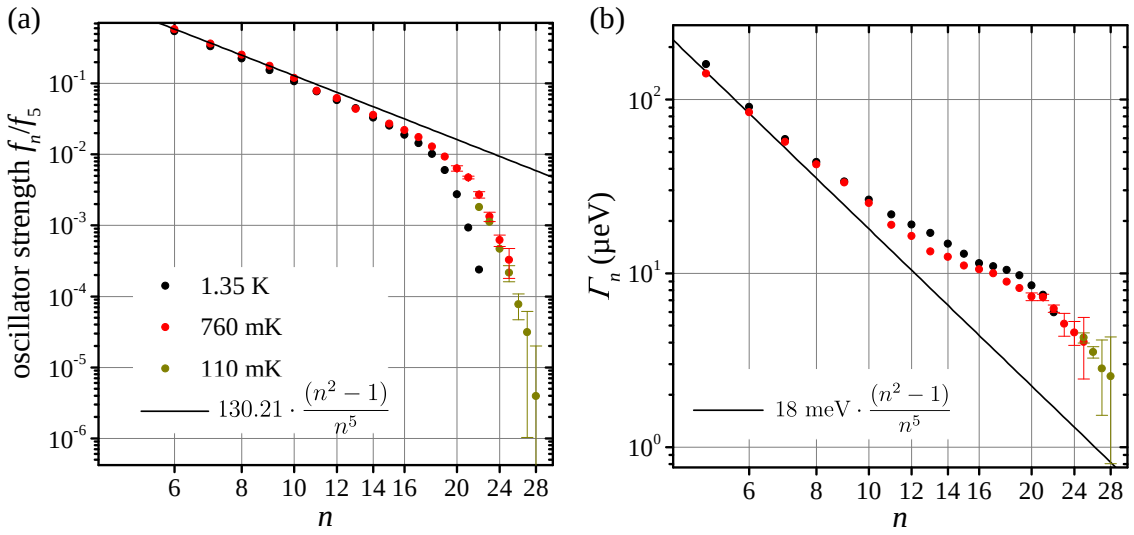

Figure 5.13 (a) Normalized oscillator strengths f_n/f_5 of $n = 8$ to $n = 28$ from spectra at 760 mK (red) and 110 mK (brown). The values for 1.35 K are shown for comparison. Error bars are given for $n \geq 20$, see text for details. Below 1 K, the oscillator strength increases most significantly for states above $n = 20$. The general trend with a strong drop in oscillator strength is confirmed up to $n = 28$. (b) The same as in panel (a) but for the linewidths. Black lines indicate the expected scaling behavior. Adapted from [Hec+20].

the underlying mechanisms and to identify one of the models as the correct one.

Further, the model discussed in this chapter allows for a phenomenological description of the exciton oscillator strength as a function of band gap shift Δ by introducing effective Bohr radii $a_{\mathrm{eff}}^{\mathrm{B}}$ and effective quantum numbers n_{eff}. In another recent work, Ref. [Sem+], the influence of an electron-hole plasma on the Rydberg exciton oscillator strength is calculated by full diagonalisation of the plasma Hamiltonian. Remarkably, it shows that the presence of an electron-hole plasma cannot cause the observed changes of the oscillator strength. The changes predicted are only on the order of 1 % of the unperturbed oscillator strength. Thus, the observed reduction of oscillator strength in the experiment might stem from additional interaction mechanisms between the excitons, see Ch. 6.

Hence, while the oscillator strength can be described phenomenologically as a function of band gap shift within the model described here, the picture of the underlying physical mechanisms is still incomplete and further investigations are necessary.

5.5 Conclusions

In this chapter, the influence of a low-density electron-hole plasma and external experimental parameters such as laser power and temperature on the Rydberg exciton series was studied.

First, changes in the absorption spectra were reported when an electron-hole plasma is injected by an external pump laser via above band gap excitation. The plasma leads to

a renormalization of the band gap via correlation effects such as a self-energy correction and to a screening of the Coulomb potential. Within a model based on the classical Debye description the observed effects could be described in good agreement with experimental data. The observed band gap shifts Δ were found to stem from very low plasma densities and the reduction of oscillator strength could be reproduced quantitatively as a function of a shifted band gap position. The Rydberg excitons are found to be extremely sensitive to low carrier densities as the highest states already vanish at plasma densities as small as 0.01 $\mu\mathrm{m}^{-3}$.

Moreover, this finding also has consequences for below band gap excitation with a single laser source, where a certain plasma density might be created, as discussed, either via Auger decay of ground state excitons or by direct excitation close to the band gap. Thus, even with below band gap excitation one will shift the band gap to lower energies. However, also deviations from this model are found in both excitation scenarios, that are discussed later in Sec. 6.5.

Second, even without external laser excitation the band gap is found to be shifted below the nominal gap E_g by an amount Δ_0, which is limiting the observation of higher Rydberg excitons. In this case, the band gap is assumed to be reduced by a density of charged impurities in the crystal in agreement with Ref. [Krü+20].

In this context, the maximal observable quantum number n_max was investigated experimentally in dependence on the applied laser power and the crystal temperature. Possible blockade mechanisms such as the excitation-power dependent Rydberg blockade on the one hand and the plasma screening on the other hand but also the thermal dissociation of Rydberg states were discussed as limiting factors. Laser powers down to several nW and temperatures as low as 50 mK were applied to minimize the influence of these effects. The highest quantum number that could be observed is $n = 28$. The best result was obtained with a power of 1 μW and a temperature of 110 mK. However, the experimental parameter space for this observation was found to be quite large, as a feature for $n = 28$ can be already identified at temperatures around 450 mK. Lowering the laser power below 1 μW did not further improve the result.

In conclusion, the inherent band gap shift Δ_0 was found to be the final limiting factor for the principal quantum number of the highest observable Rydberg exciton state. As a consequence, in order to detect higher states one needs even purer samples with an inherent band gap shift below $\Delta_0 = 110$ μeV, corresponding to an estimated impurity density even below 0.01 $\mu\mathrm{m}^{-3}$.

Chapter 6

Investigation of interactions between Rydberg excitons

In this chapter, interactions between Rydberg excitons are investigated. In analogy to highly excited Rydberg atoms, Rydberg excitons reveal giant dipole moments growing with n^2 and are therefore promising candidates to exhibit strong dipole-dipole interactions among each other. The interaction energy can become large enough to prevent the excitation of a Rydberg state in the surrounding of an existing one, since the excitation energy of the pair state is shifted out of resonance by the dipole-dipole interaction energy. This is called the Rydberg blockade mechanism [Gal+08]. In the first section of this chapter, Sec. 6.1, the dipole-dipole interaction is introduced theoretically and the concept of Rydberg blockade is explained. First indications of such strong interactions were already reported in 1981 in atomic beam experiments in Ref. [Rai+81] and gained renewed attention since the blockade mechanism was proposed theoretically as a promising candidate for the realization of quantum logical gates in Refs. [Jak+00; Luk+01; Saf+05]. Not only its importance in the field of quantum information processing, but also in quantum optics [Pri+12] and many-body physics [Bro+20] has triggered a lot of theoretical and experimental effort [Saf+10; Bro+16], so that today the observation of strong interactions between single atoms in a controlled environment is possible [Urb+09].

Along with the discovery of Rydberg excitons in 2014, indications of the excitonic Rydberg blockade were reported in Ref. [Kaz+14]. The focus laid on interactions of Rydberg states with the same principal quantum number n, which is called the symmetric blockade. It was observed in an experiment employing a single laser, that an increase in excitation power led to a bleaching of absorption lines, similar to early reports from experiments with atoms [Sin+04; Sin+05]. The corresponding blockade efficiency was shown to increase by about three orders of magnitude for excitons with principal quantum numbers from $n = 12$ to $n = 24$, following an n^{10}-scaling law. However, the determination of the exact underlying interaction mechanism was not possible as both most reasonable candidates - a short-range Förster-type or long-range van der Waals-type mechanism - would result in such a scaling, as will be shown in Sec. 6.1 as well.

Similar to the symmetric case, the excitation of Rydberg states with principal quantum numbers n can be suppressed by the presence of states with different quantum numbers $n' \neq n$. This is described by the asymmetric Rydberg blockade. In this chapter, this type of blockade is investigated. Therefore, data obtained in a two-beam pump-probe setup is presented and analyzed. Clear spectral signatures of a van der Waals-type interaction are found that exclude the Förster-type interaction as the underlying interaction mechanism. Sections 6.2 and 6.3 give an explanation of the experimental setting and general observa-

tions. In Sec. 6.4, the focus lies on measurements, in which the Rydberg state $n' = 16$ is resonantly excited and the response of other states is investigated in detail. The results are compared with a theoretical model developed by Valentin Walther from the Institute for Theoretical Atomic Molecular and Optical Physics at Harvard University and Thomas Pohl from the Department of Physics and Astronomy at Aarhus University. The model is explained in Sections 6.4.1 and 6.4.2. It is found to explain most of the observed effects by taking correlations between excitons into account, whereas a mean field model fails to explain the effects. This investigation is part of a forthcoming joint publication [Hec+].

In Sec. 6.5, the same analysis is extended to the plasma-scenario as reported in Ch. 5, where the pump laser energy is placed far above the band gap to create mainly an electron-hole plasma. Interestingly, observations are reported, that are in contradiction with the plasma model. A possible relaxation of electron-hole pairs into Rydberg states is briefly discussed on the basis of photoluminescence spectroscopy.

This is followed by Sec. 6.6, where the results of measurements are presented, in which the pump laser energy is set to the resonance energies of states with principal quantum numbers n' that are different than $n' = 16$, namely to $n' = 12, 10$ and the $1S$ Ortho-exciton. Although the observations still show an agreement with the model prediction for $n' = 12$, deviations for lower n' are observed, where the data does not agree with the model prediction and hints towards different and so far unknown interaction mechanisms.

Finally, in Sec. 6.7, an effect is described, that is visible at low pump powers in many of the pump-scenarios mentioned above. Initially, the datasets show a nonlinear increase of absorption which is neglected so far in the discussions before. In that section, the dependence on pump energy of this effect is determined from experiments in which the pump laser's energy is scanned and an explanation is presented based on recent calculations by Krüger et al., given in Ref. [Krü+20].

Preliminary studies of the shown experiments were performed in the context of Marcel Freitag's and Felix Föst's master theses (Refs. [Fre16] and [Fös18]) as well as the bachelor thesis of Steffen Schröder (Ref. [Sch18]).

6.1 Dipole-dipole interaction

In this section, the dipole-dipole interaction of two excitons with principal quantum numbers n and n' is described, following mainly Refs. [Bro+16] and [Saf+10]. The excitons are assumed to be separated by a distance $\overline{R} = |\overline{\mathbf{R}}| = \mathbf{R} - \mathbf{R}'$, where $\mathbf{R}$ ($\mathbf{R}'$) is the center of mass of the exciton with principal quantum number n (n'). The dipole-dipole interaction potential is then given by

$$V_{\mathrm{dd}}\left(\overline{R}\right) = \frac{1}{4\pi\epsilon_0\epsilon_{\mathrm{s}}} \frac{\mathbf{d}_n \mathbf{d}_{n'} - 3\left(\mathbf{d}_n \hat{\mathbf{R}}\right)\left(\mathbf{d}_{n'} \hat{\mathbf{R}}\right)}{\overline{R}^3} \,, \tag{6.1}$$

with $\hat{\mathbf{R}} = \overline{\mathbf{R}}/\overline{R}$. The electric dipole moments of the two excitons with quantum numbers n and n' are given by $\mathbf{d}_n$ and $\mathbf{d}_{n'}$, with $d_n = |\mathbf{d}_n|$. Without interaction, the excitons are described by a pair state, denoted as $|n, n'\rangle$, with unperturbed energy $E_{n,n'} = E_n + E_{n'}$.

The interaction introduces a coupling to other pair states $|k, k'\rangle$, with principal quantum numbers k and k' and energy $E_{k,k'}$. Note that due to the odd parity of the dipole operator, these are states with opposite parity, e.g. an odd difference in angular momentum quantum

number l (cf. Sec. 4.1). For simplicity, the angular momentum quantum numbers are not explicitly mentioned in the following. If the pair state energies are non-degenerate, the energy correction of the pair state $|n, n'\rangle$ is given by second-order perturbation theory and reads

$$\Delta E_{\mathrm{vdW}} = \sum_{k,k'} \frac{|\langle n, n' | V_{\mathrm{dd}} | k, k' \rangle|^2}{E_{n,n'} - E_{k,k'}} \ . \tag{6.2}$$

The denominator contains the energy difference between the energies of the involved pair states, that is called the Förster defect. Theoretically, the sum includes all possible pair states $|k, k'\rangle$ that are dipole coupled to $|n, n'\rangle$. Due to the dependence on V_{dd}^2, this shift scales as $1/\overline{R}^6$ and can be identified with the van der Waals interaction. For the expansion coefficient $C_6(n, n')$ one finds ([Mar+99; Wal+18b])

$$C_6(n, n') \propto \frac{d_{n,k}^2 d_{n'k'}^2}{\Delta_{n,k} + \Delta_{n',k'}} \ , \tag{6.3}$$

where $\Delta_{n,k}$ and $\Delta_{n',k'}$ are the energy separations between the corresponding coupled states and scale as $\Delta_{n,k} \propto n^{-3}$ (cf. Sec 4.1.1). The numerator is dominated by the dipole matrix elements of states with $k \approx n$ ($k' \approx n'$) that scale as $\langle n | \mathbf{d}_{n,k} | k \rangle \propto n^2$ ($\langle n' | \mathbf{d}_{n',k'} | k' \rangle \propto n'^2$)[1]. With these scalings, one obtains

$$C_6(n, n') \propto \begin{cases} n^7 (n')^4 \text{ for } n \ll n' \\ n^4 (n')^7 \text{ for } n \gg n' \end{cases} \ . \tag{6.4}$$

For $n \ll n'$, the denominator is dominated by the first term, $\Delta_{n,k} \propto n^{-3}$, whereas for $n \gg n'$ the denominator is dominated by $\Delta_{n',k'}$. In both cases, the interaction strength increases strongly with the principal quantum number n. This case with excitons excited initially in two different states n and n', for example by using two different lasers (see below), will be called asymmetric Rydberg blockade. If both excitons are in the same state, i.e. n=n', referred to as the symmetric Rydberg blockade, one finds the following increase with n:

$$C_6(n, n') \propto n^{11} \ . \tag{6.5}$$

If the pair state energies $E_{n,n'}$ and $E_{k,k'}$ are degenerate or quasi-degenerate, i.e. the Förster defect amounts to zero (cf. Eq. (6.2)), one obtains energy corrections of first order, called resonant dipole-dipole or Förster interaction:

$$\Delta E_{\mathrm{F}} = \pm \frac{C_3}{\overline{R}^3} = \pm \langle n, n' | V_{\mathrm{dd}} | k, k' \rangle \ . \tag{6.6}$$

Again, scaling laws can be found, which read for the both relevant cases

$$C_3(n, n') \propto n^2 (n')^2 \ , \ n \neq n' \tag{6.7}$$

$$C_3(n) \propto n^4 \ , \ n = n' \ . \tag{6.8}$$

Note that the coupled states still need to have opposite parity.

[1] For the dipole transition matrix elements between states of largely different n and k, one finds $\langle n | \mathbf{d}_{n,k} | k \rangle \propto n^{-3/2}$ [Gal+08; Bet+57]

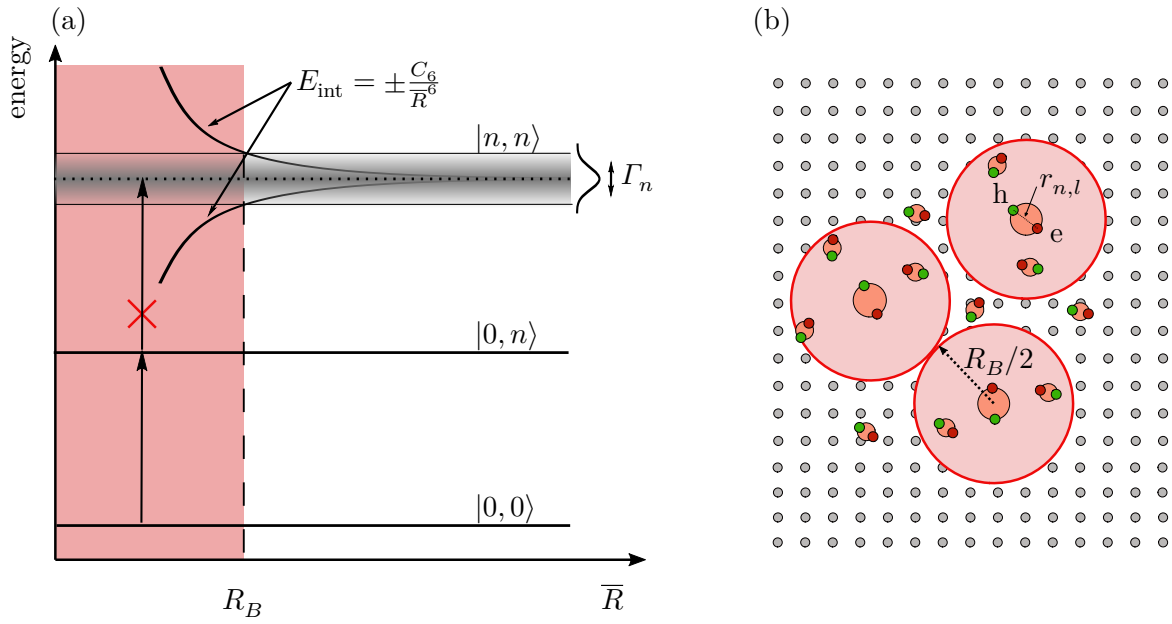

Figure 6.1 Schematic illustration of the Rydberg blockade mechanism. (a) Energy scheme of pair state energies as a function of inter-excitonic distance $\overline{R}$. At a distance smaller than the blockade radius R_B, the energy of the pair state involving two Rydberg states, $|n,n\rangle$, is shifted out of the resonance linewidth Γ_n by the interaction energy E_{int} and the excitation is not possible. (b) Grey spheres illustrate the crystal lattice, orange spheres with green (hole) and red (electron) dots illustrate excitons with a certain electron-hole separation $r_{n,l}$. Excitations of Rydberg excitons with high quantum numbers n (large $r_{n,l}$) are only possible at distances larger than the blockade radius R_B, indicated by the red spheres. Ground state excitons (small $r_{n,l}$ and negligible blockade radius) can in principle be excited within the blockade volume of the Rydberg states as well.

As mentioned above, the interaction strengths increase drastically with n. These strong interactions lead to the Rydberg blockade effect. The Rydberg blockade is schematically shown in Fig. 6.1 (a) and explained in the following. Typically, for atoms one starts from the energy of the pair state that contains the ground states of the two interacting atoms. In contrast, in the case of excitons, the ground state is given by the empty crystal. In the following it is denoted by $|0,0\rangle$. The energy of a pair state with one exciton in a Rydberg state, $|0,n\rangle$, is simply given by $E_{0,n} = E_n$, indicated by the middle horizontal line. The energy of the doubly excited pair state, $|n,n\rangle$, contains the sum of the two single energies $2E_n$, indicated by the dashed horizontal line, and an additional energy shift that is given by the interaction energy ΔE_{int} of the two excited states. The interaction energy E_{int} can be of van der Waals type or of Förster type and lead to positive (repulsive) or negative (attractive) energy shifts. If the energy shift is larger than the absorption linewidth, $\Delta E_{\text{int}} \gg \Gamma_n$, the pair state consisting of two excitons cannot be excited by a spectrally narrow laser with an energy resonant to the single exciton transition. Since the interaction strength depends on the separation $\overline{\mathbf{R}}$ of the involved excitons, one can define a radius $\mathbf{R}_{\text{B}}$ around a single Rydberg exciton within which this condition is fulfilled. This radius is called the blockade radius and the excitation of two or more Rydberg excitons is

blocked inside the corresponding blockade volume

$$V_{\mathrm{B}} = \frac{4}{3}\pi R_{\mathrm{B}}^3 = \begin{cases} (C_6/\Gamma_n)^{1/2} & \text{, van der Waals} \\ C_3/\Gamma_n & \text{, Förster} \end{cases} . \tag{6.9}$$

In Ref. [Kaz+14], the blockade radius was estimated to be of the order of 10 μm for an exciton with quantum number $n = 24$, which is about ten thousand times larger than the Bohr radius for P excitons $a^{\mathrm{B}} = 1.11$ nm (cf. Sec. 2.3) or ten times larger than the average electron-hole separation of that state $r_{24P} \approx 1$ μm.

Following this concept, the number of Rydberg excitons that can be excited by a spectrally narrow light source in a given crystal volume is limited by their interaction strength among each other and the corresponding blockade volume. The situation is schematically illustrated in Fig. 6.1 (b). The grey dots indicate the crystal lattice. Excitons are shown as orange spheres with green and red dots representing schematically electrons and holes with separation $r_{n,l}$. Rydberg excitons with large $r_{n,l}$ have large dipole moments and even larger blockade radii, that are shown by the red spheres. Hence, these excitons can only be excited outside the blockade volume of other Rydberg excitons. Excitons with small $r_{n,l}$ have negligible dipole moments and can in principle be excited anywhere in the crystal volume, as indicated by small orange spheres.

With a given density of Rydberg excitons excited, the crystal might become transparent for light with an energy equal to the resonance energy of a Rydberg state. The pair states are detuned from the laser energy and the absorption line smears out with increasing laser power, as observed for excitons in Ref. [Kaz+14], but also earlier in a similar way for Rydberg atoms in Refs. [Sin+04; Sin+05].

6.2 Experimental setting

In Ref. [Kaz+14], the bleaching of absorption lines with increasing laser power was observed in a single-beam experiment. While the laser scans a resonance, the density of excitons excited varies depending of the laser's detuning from the resonance energy. Hence, the measured spectral line shapes result from an undefined exciton density and are rather unsuitable to get information about the underlying interaction mechanism.

Here, a different experimental setting is used with a focus on the asymmetric Rydberg interaction, using states of different principal quantum numbers n and n'. For this purpose, a pump-probe-excitation scheme with two CW lasers is used, as described in detail in Ch. 3. The pump laser's energy is fixed on a resonance with principal quantum number n' while the probe laser scans a range of other states with principal quantum numbers n. The probe power is set to a low value of about 1 μW and the pump power $\mathrm{P}_{\mathrm{pump}}$ is increased. With changing pump power, the density ρ of pump excitons with quantum number n' is varied in the crystal in first-order approximation where we neglect possible decay channels into other states. Hence, this scheme allows one to observe the optical response of the probed state's line shape to a well-defined pump exciton density that can be traced back directly to the interaction between excitons with quantum number n' and n.

The pump beam's intensity is modulated and the transmitted probe beam is detected with a Lock-In amplifier. The modulation frequency of about 3 kHz is low compared to

timescales of dynamical processes in the crystal. Therefore, this scheme generates a quasi-CW signal and allows one to measure directly the pump-induced change in the transmitted intensity, i.e. the CW-differential transmission (cf. Eq. (3.5))

$$\Delta I \propto I_{\mathrm{T,\ pump}} - I_{\mathrm{T,\ no\ pump}} \ . \tag{6.10}$$

Here, positive signals correspond to an enhancement of transmission and indicate a bleaching of an absorption line. This Lock-In scheme allows one to measure small changes in the spectra with high accuracy and independent of background fluctuations. The latter could cause additional offsets distorting a precise determination of peak heights. All measurements shown in this chapter are performed at sample $H7$ and 1.35 K.

6.3 Separation of interaction regimes

The changes in the differential spectra shown throughout the next sections contain information about the underlying interactions between the pumped and probed states. In this section, the overall trend of these spectra as a function of pump power shall be described, as it will turn out to be similar in the following sections, independent of the pump laser's energy. Therefore, the changes of the resonance $n = 11$ at different pump powers are exemplarily shown in Fig. 6.2 (a). The pump laser energy is fixed on $n' = 16$ in this particular case. In general, the differential curves around the resonance $n = 11$ show an extremum strongly varying in amplitude at a constant energy E_{max} and a significant crossing on the high energy side at E_0. While a detailed line shape analysis is given in the next section, here the focus lies on the dependence of the amplitude of this extreme point $\Delta I(E_{\mathrm{max}})$ on pump power. Since the extremum does not shift in energy, it is referred to as the differential peak height in the following sections.

The dependence of the differential peak height on pump power is used to differentiate between different interaction regimes. Therefore, the differential peak height extracted from panel (a) is shown in panel (c) as a function of pump power. The signal can be divided into three regimes. For low pump powers, the trace of $\Delta I(E_{\mathrm{max}})$ reveals a nonlinear decrease meaning an increase in absorption as indicated by the arrow. This effect saturates fast at around 10 μW. Note that the value for zero pump power is added manually for a better visibility of this nonlinearity. The nonlinearity is followed by a linear increase over a wider range of powers up to approximately 100 μW. At higher powers the response starts to saturate, where full saturation corresponds to a total bleaching of the absorption line in the absolute spectrum. Since the Rydberg blockade is expected to result in a reduction of absorption at the resonance energy, which means positive values of $\Delta I(E_{\mathrm{max}})$, the second regime, in which the peak heights depend linearly on the pump power $\mathrm{P}_{\mathrm{pump}}$, will be analyzed in the following sections with regard to the dipole-dipole interaction. The initial nonlinear behavior has to be related to a different interaction mechanism, that is so far unknown, and will be neglected in the next two sections. In general, the power range where the nonlinear effect is dominant depends on the principal quantum number n of the probed state and the magnitude of it is found to be more pronounced for lower n. Moreover, the nonlinearity can be completely absent for states with $n > n'$. It is further discussed and investigated at the end of this chapter in Secs. 6.6 and 6.7, clarifying its dependence on excitation energy.

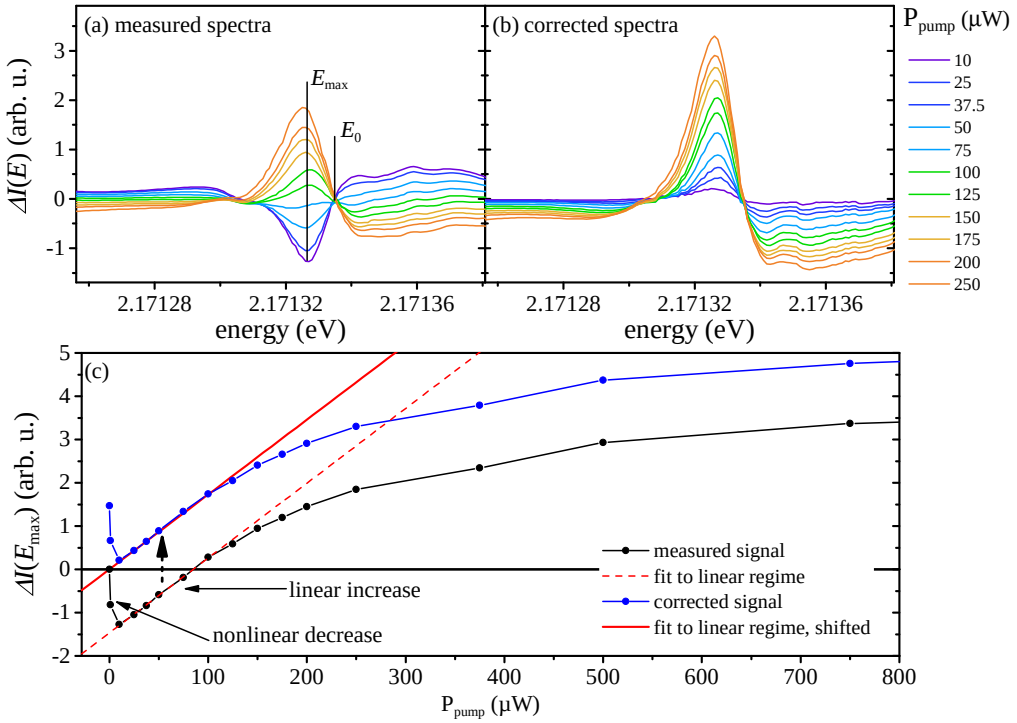

Figure 6.2 (a) Measured differential spectra around the $n = 11$ resonance. Here, we find negative peak amplitudes for low excitation powers. (b) Corrected spectra around the $n = 11$ peak after data correction as described in the text. (c) Amplitude of the extreme point of the $n = 11$ resonance from panel (a) at the energy $E_{\max}$ as a function of pump power. Black dots show the uncorrected signal. The trace can be divided into three regimes, starting with a fast saturating nonlinear decrease of transmission, followed by a linear increase over a wider range of powers up to 100 μW. At higher powers the curve flattens and finally saturates at powers around 800 μW. The value at zero pump power is added manually to obtain a better visibility of the nonlinearity. A fit to the linear regime (red dashed line) reveals an intercept, that is subtracted from the data at this energy. Blue dots show the corrected amplitudes. This procedure is repeated at every energy to correct the spectra for the initial nonlinear behavior.

In order to focus on the Rydberg interaction regime, given by the linear dependence on pump power, the spectra discussed in the following two sections are corrected for this nonlinear decrease, as shown in Fig. 6.2 (c). The measured data (black dots) is corrected by subtracting the maximum of the negative nonlinear amplitude, that is obtained by the intercept of a fit to the linear regime (red dashed line). This is done at every energy of the spectrum. As a result, in the corrected spectra (blue dots) the linear increase (red solid line) starts at $\Delta I = 0$. Panels (a) and (b) show exemplarily the corresponding differential transmission around the resonance $n = 11$ with and without correction for different pump powers.

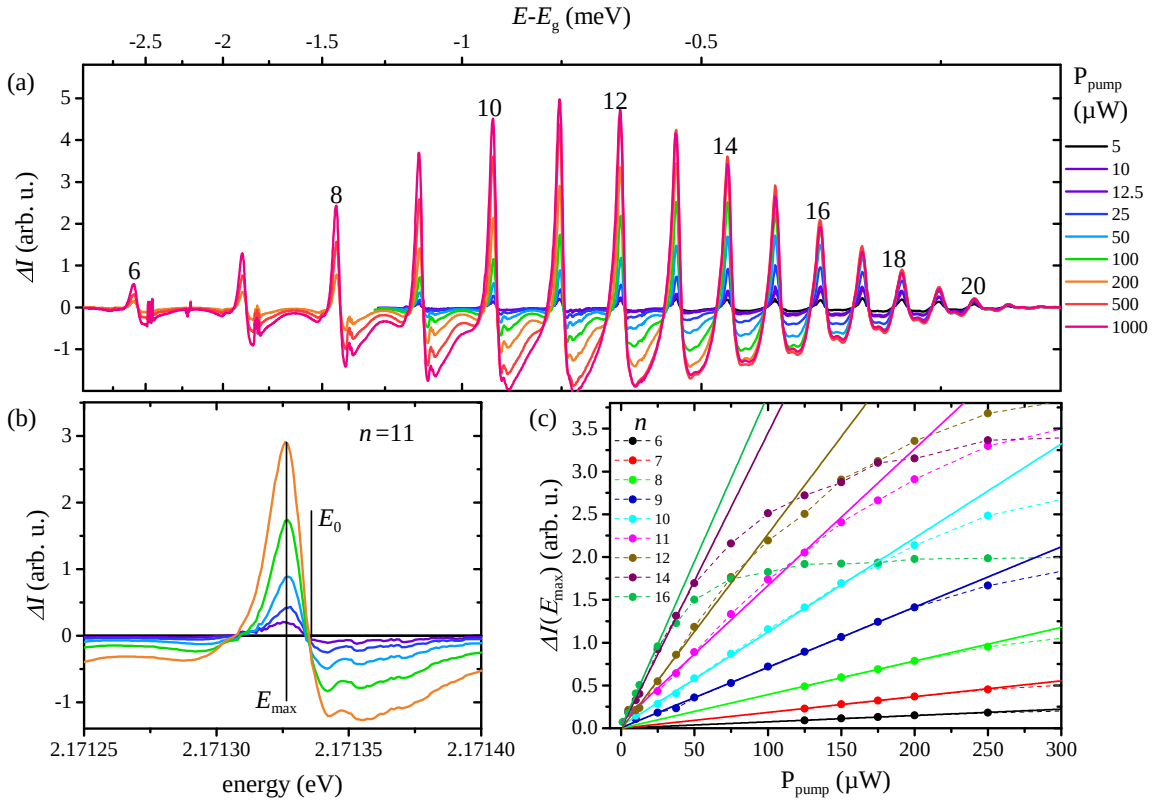

Figure 6.3 (a) Differential transmission signal ΔI for $n = 6$ to $n = 21$, recorded with a pump laser energy fixed on the $n' = 16$ P resonance. The data is corrected as described in Sec. 6.3. The pump laser power is increased from 5 to 1000 μW. For the resonances $n \leq 8$, only spectra at pump powers higher than 100 μW are shown due to the small changes at lower powers. The transmission is enhanced at the resonance energies and reduced in between the lines indicating a redistribution of oscillator strength. (b) Closeup of the $n = 11$ resonance in the linear regime (see text). The line shape exhibits a strongly increasing but non-shifting maximum at energy E_{max} and a root on the high energy side at E_0. The line shape is universal for all n. (c) Differential peak heights at E_{max} as a function of pump laser power for $n = 6$ to $n = 16$. For every n a linear increase is found that transforms into a saturation plateau. The onset of saturation shifts to lower powers with increasing n. Full saturation corresponds to a full bleaching of the absorption line. Solid lines show fits to the linear power regime with a slope $\beta(n, n')$.

6.4 Asymmetric Rydberg blockade

In the following, a series of measurements where the pump laser's energy is fixed to the resonance $n' = 16$ is analyzed in detail. The obtained differential spectra for various pump powers are shown in Fig. 6.3 (a).

While pumping the state $n' = 16$, the probe laser detects changes for all states from $n = 6$ up $n = 22$. Here, the corrected data is considered as described in the section before with a focus on changes in the linear power regime. For all n, the transmission is enhanced around the resonance energies and reduced in between. Starting from $n = 6$, these effects

become more pronounced with increasing n. Above $n = 12$, the maximum amplitude of a particular peak decreases. This simply reflects the reduction of oscillator strength in the high-n regime known from the unperturbed spectra (cf. Fig. 2.4 (b)). These states already saturate at pump powers, where lower n still show pronounced changes.

The general spectral appearance is the same for every resonance and is described in the following. Figure 6.3 (b) shows a closeup of the resonance $n = 11$. As indicated, we find a maximum strongly varying in amplitude but not shifting in energy at E_{max}. Further, the line shape reveals a root on the high energy side at E_0. Here, all the lines intersect in one point meaning that the presence of pump excitons has no effect at exactly that energy. Remarkably, the difference $E_{\mathrm{max,n}} - E_{\mathrm{0,n}}$ normalized to the linewidth Γ_n is found to be universal for all n. This quantity will be discussed later in Sec. 6.4.4. Besides the spectrally narrow increase of transmission at the center, we find a decrease of transmission or rising absorption mainly located on the high energy side of the resonance smeared out to a broad tail. An analogue tail can be observed on the low energy side as well but of lower amplitude. In addition, it is possible that the lines cross in one point on the low energy side as well, at very low pump powers. However, the data showing this crossing is less reliable due to the noise level in this spectral region. Further, the lines rather diverge continuously with increasing power.

This spectral shape describes a pump-induced redistribution of oscillator strength that is of repulsive character for most states and attractive for a few. This is in accordance with Ref. [Wal+18b], where it is shown that the potential landscape of the van der Waals interaction between two Rydberg excitons spreads into a complex pattern of attractive and repulsive potential curves for low enough separations of the involved excitons.

Next, the increase of the differential peak maximum, i.e. the differential peak height, is shown in Fig. 6.3 (c) as a function of pump power. For every n, a linear dependence on pump power is observed in a certain range of pump powers. The colored solid lines show fits in the linear power range of a particular n. Since the slopes of these fits increase with n, their dependence on n is used later in Sec. 6.4.3 for a quantitative analysis. The increase passes into saturation at higher powers, while the onset of saturation shifts to lower powers with increasing n. Note that saturation in ΔI corresponds to a total bleaching of the absorption line in pure spectra. The visibility of the root on the high energy side of a particular differential peak (panel (b)) corresponds in a good approximation to the regime of linear increase of the peak's height. For higher pump powers it begins to smear out. Furthermore, the analysis given in this section is restricted to powers below 200 μW, which is the saturation power of $n' = 16$.

In order to describe the optical response of an exciton of quantum number n to a gas of Rydberg excitons with n', a theoretical approach will be described. The model has been developed by Valentin Walther and Thomas Pohl and is summarized in the following.

6.4.1 Equations of motion

The excitation of excitons at position $\mathbf{R}$ by a light field in z direction is described by the following two equations of motion

$$\partial_t \mathcal{E}(\mathbf{R}) + c\bar{n}\partial_z \mathcal{E}(\mathbf{R}) = -ig\hat{X}(\mathbf{R}) \ , \tag{6.11}$$

$$\partial_t \hat{X}(\mathbf{R}) = -\frac{\tilde{\Gamma}}{2}\hat{X}(\mathbf{R}) - ig\mathcal{E}(\mathbf{R}) \ , \tag{6.12}$$

with the exciton and light field amplitudes $\hat{X}(\mathbf{R})$ and $\mathcal{E}(\mathbf{R})$ and the light-matter coupling strength g. Further, c is the speed of light and $\bar{n}$ is the index of refraction (cf. Ch. 2). The parameter $\tilde{\Gamma} = \Gamma - 2i\delta$ contains the linewidth Γ and a detuning from resonance frequency $\delta/\hbar = \omega - \omega_n$, where ω denotes the frequency of light and ω_n is the resonance frequency. Note that the index n, that indicates an n dependence of g and Γ, is left out here for simplicity. In the steady state, $\partial_t \hat{X}(\mathbf{R}) = 0$, Eq. (6.12) yields the steady states for the exciton annihilation operator $\hat{X}(\mathbf{R})$ and the exciton creation operator $\hat{X}^\dagger(\mathbf{R})$:

$$\hat{X}(\mathbf{R}) = -\frac{i2g}{\tilde{\Gamma}}\mathcal{E}(\mathbf{R}), \ \hat{X}^\dagger(\mathbf{R}) = \frac{i2g}{\tilde{\Gamma}}\mathcal{E}^*(\mathbf{R}) \ . \tag{6.13}$$

Further, solving for the steady state of Eq. (6.11), $\partial_t \mathcal{E}(\mathbf{R}) = 0$, with an ansatz $\mathcal{E}(\mathbf{R}) = \mathcal{E}_0 e^{ikz}$ yields the spectral shape of the absorption line of a sample of thickness d in terms of intensity ($I \propto |E|^2$)

$$I_T = I_0 \exp(-h(\delta)d) = I_0 \exp\left(-\frac{4g^2\Gamma}{c\bar{n}(4\delta^2 + \Gamma^2)}d\right) \ . \tag{6.14}$$

The first term of the exponent, $h(\delta)$, is the equivalent of the absorption coefficient in Eq. (3.1). The peak height at the resonance energy ($\delta = 0$) in terms of optical density $\mathrm{OD} = \alpha d$ is connected to g and Γ via

$$H_{\mathrm{OD}} = h(\delta = 0)d = -\ln\left(\frac{I_{\mathrm{T}}(\delta = 0)}{I_0}\right) = \frac{4g^2}{c\bar{n}\Gamma}d \ , \tag{6.15}$$

in comparison to the peak height from Eq. (2.43) in Sec. 2.5, which reads $H_{\mathrm{OD}} = \frac{O}{\pi\Gamma}$. The pump exciton density operator is given by $\hat{\rho}_p(\mathbf{R}') = \hat{X}_p^\dagger(\mathbf{R}')\hat{X}_p(\mathbf{R}')$. Pump excitons are created at position $\mathbf{R}'$ by $\hat{X}_p^\dagger(\mathbf{R}')$. Their density is connected to the pump power by

$$\rho_p(\mathbf{R}') = \langle \hat{X}_p^\dagger(\mathbf{R}')\hat{X}_p(\mathbf{R}')\rangle = \frac{4g'^2}{|\tilde{\Gamma}'|^2}|\mathcal{E}(\mathbf{R}')|^2 \overset{(\delta'=0)}{\propto} \frac{g'^2}{\Gamma'^2}\mathrm{P}_{\mathrm{pump}} \ . \tag{6.16}$$

6.4.2 Interaction of Rydberg excitons

Now, the interaction between pump and probe excitons in regard to a two-particle interaction potential $V^{\mathrm{int}}(\mathbf{R} - \mathbf{R}')$ is discussed. First, a mean-field model is considered. Here, the presence of a pump exciton density ρ_p simply leads to a mean field energy shift δ_{mf} of the probe exciton line, given by

$$\delta_{\mathrm{mf}} = \int d\mathbf{R}' V^{\mathrm{int}}(|\mathbf{R} - \mathbf{R}'|)\rho_p \ . \tag{6.17}$$

The differential curves resulting from such a mean-field interaction are shown in Fig. 6.4 (a) for three different pump powers. They are calculated in terms of the differential absorption $\Delta\alpha$. We find an increasing maximum and minimum but also a constantly shifting energy. Most importantly, the lines do not intersect in one point as found in the experiment. Thus, an interaction on the mean-field level can be ruled out as the underlying exciton interaction mechanism.

Next, we consider a more complex interaction considering correlations between pump and probe excitons. First, the exciton equation of motion (Eq. (6.12)) is expanded by the interaction term

$$\partial_t \hat{X}(\mathbf{R}) = -\frac{\tilde{\Gamma}}{2}\hat{X}(\mathbf{R}) - ig\mathcal{E}(\mathbf{R}) - i\int d\mathbf{R}' V^{\mathrm{int}}(|\mathbf{R}-\mathbf{R}'|)\hat{X}_p^\dagger(\mathbf{R}')\hat{X}_p(\mathbf{R}')\hat{X}(\mathbf{R}) \ . \tag{6.18}$$

To focus on the interaction, the last term in Eq. (6.18) is considered and one calculates

$$\begin{aligned}\partial_t \hat{X}_p^\dagger(\mathbf{R}')\hat{X}_p(\mathbf{R}')\hat{X}(\mathbf{R}) =& \underbrace{\partial_t(\hat{X}_p^\dagger(\mathbf{R}')\hat{X}_p(\mathbf{R}'))\hat{X}(\mathbf{R})}_{=0} + \hat{X}_p^\dagger(\mathbf{R}')\hat{X}_p(\mathbf{R}')\partial_t\hat{X}(\mathbf{R}) \\ =& -\frac{\tilde{\Gamma}}{2}\hat{X}_p^\dagger(\mathbf{R}')\hat{X}_p(\mathbf{R}')\hat{X}(\mathbf{R}) - ig\hat{X}_p^\dagger(\mathbf{R}')\hat{X}_p(\mathbf{R}')\mathcal{E}(\mathbf{R}) \\ & - iV^{\mathrm{int}}(|\mathbf{R}-\mathbf{R}'|)\hat{X}_p^\dagger(\mathbf{R}')\hat{X}_p(\mathbf{R}')\hat{X}(\mathbf{R}) \\ & - i\int d\mathbf{R}'' V^{\mathrm{int}}(|\mathbf{R}-\mathbf{R}''|)\hat{X}_p^\dagger(\mathbf{R}')\hat{X}_p^\dagger(\mathbf{R}'')\hat{X}_p(\mathbf{R}')\hat{X}(\mathbf{R}'')\hat{X}(\mathbf{R}) \ .\end{aligned} \tag{6.19}$$

In the first row of Eq. (6.19), a time-independent pump exciton density is assumed ($\partial_t(\hat{X}_p^\dagger(\mathbf{R}')\hat{X}_p(\mathbf{R}')) = \partial_t\hat{\rho}_p = 0$). The second and third row include correlations of lowest order. The fourth row includes interactions of higher order, i.e. between multiple pump excitons and one probe exciton, which are neglected in the following. In the steady state ($\partial_t\hat{X}(\mathbf{R}) = 0$), Eq. (6.19) then yields

$$\hat{X}_p^\dagger(\mathbf{R}')\hat{X}_p(\mathbf{R}')\hat{X}(\mathbf{R}) = \hat{\rho}_p(\mathbf{R}')\hat{X}(\mathbf{R}) = -\frac{ig\mathcal{E}(\mathbf{R})\hat{\rho}_p(\mathbf{R}')}{\frac{\tilde{\Gamma}}{2} + iV^{\mathrm{int}}(|\mathbf{R}-\mathbf{R}'|)} \ . \tag{6.20}$$

Inserted in Eq. (6.18), the steady state solution for the probe exciton reads

$$\hat{X}(\mathbf{R}) = -\frac{2}{\tilde{\Gamma}}\left(ig\mathcal{E}(\mathbf{R}) + i\int d\mathbf{R}' V^{\mathrm{int}}(|\mathbf{R}-\mathbf{R}'|)\left(-\frac{ig\mathcal{E}(\mathbf{R})\hat{\rho}_p(\mathbf{R}')}{\frac{\tilde{\Gamma}}{2} + iV^{\mathrm{int}}(|\mathbf{R}-\mathbf{R}'|)}\right)\right) \ . \tag{6.21}$$

The pump excitons are assumed to be homogeneously distributed and their density is thus independent of $\mathbf{R}'$, $\rho_p(\mathbf{R}') \to \rho_p$. Insertion of Eq. (6.21) in Eq. (6.11) leads to the probe light equation

$$\partial_z\mathcal{E}(\mathbf{R}) = -\frac{2g^2}{c\bar{n}\tilde{\Gamma}}\cdot\left[1 - i\rho_p\int d\mathbf{R}'\frac{V^{\mathrm{int}}(|\mathbf{R}-\mathbf{R}'|)}{\frac{\tilde{\Gamma}}{2} + iV^{\mathrm{int}}(|\mathbf{R}-\mathbf{R}'|)}\right]\mathcal{E}(\mathbf{R}) \ , \tag{6.22}$$

where, again, the steady state is considered ($\partial_t\mathcal{E}(\mathbf{R}) = 0$). This equation can be solved analytically and yields for the differential transmission

$$\Delta I = I_0 e^{-h(x)d}\left(e^{s_\kappa(x)d} - 1\right) \ . \tag{6.23}$$

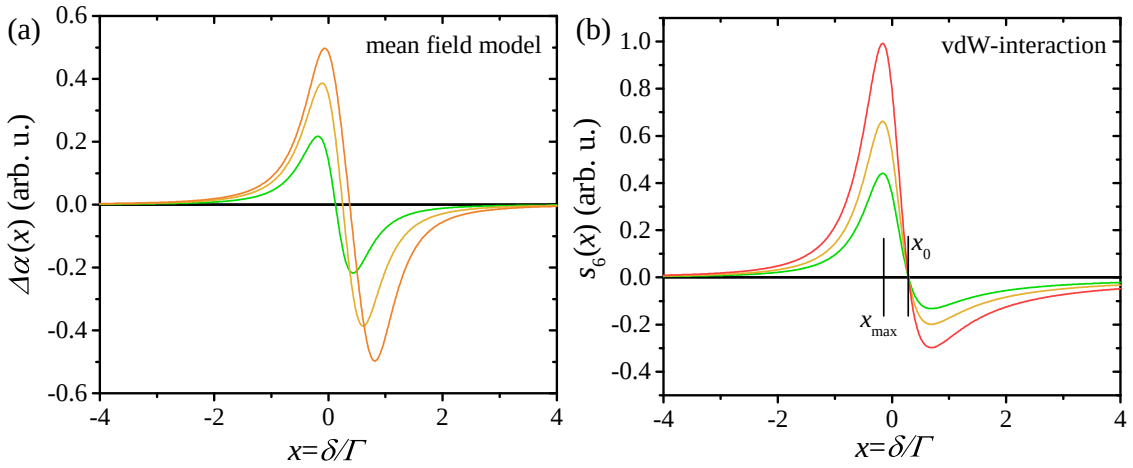

Figure 6.4 (a) Calculated differential absorption resulting from a mean-field shift shown for three different interaction strengths. The spectra show both a maximum and minimum shifting in energy and do not intersect in one point. (b) Calculated differential absorption obtained within a model including exciton correlations. Here, the line shape of a purely repulsive van der Waals potential is shown for three different interaction strengths. In agreement with the experiment, we observe a non-shifting maximum at x_{max} and a root on the high energy side at x_0 where all lines cross.

Here, $x = \delta/\Gamma$ is used as the normalized detuning. The first factor, $I_0 e^{-h(x)d}$, describes the absorption line without interaction, as given by Eq. (6.14). $s_\kappa(x)$ reflects the type of interaction, indicated by κ. Remarkably, the solution yields both a fixed maximum's position and a power-independent root on the high energy side. However, only power-law potentials of the form

$$V^{\mathrm{int}}(R) = C_\kappa / R^\kappa \tag{6.24}$$

are found to yield such a universal root at a fixed x_0 for all n as found in the experiment. For a van der Waals interaction with $\kappa = 6$, we find

$$s_6(x) = \frac{8\sqrt{2}\pi^2 g^2}{3c\bar{n}\Gamma^{3/2}}\rho_p \left[\frac{|C_6|}{\sqrt{1+4x^2}}\right]^{1/2} \frac{1}{1+4x^2}\left(\cos\frac{\phi(x)}{2} - 2x\sin\frac{\phi(x)}{2}\right), \tag{6.25}$$

with $\phi(x) = \arg(iC_6/(1-2ix))$ and the branch cut $-\pi < \phi(x) < \pi$. This function is shown in Fig. 6.4 (b) for different pump densities and a purely repulsive potential. It indeed reveals an asymmetric curve shape with a non-shifting maximum position x_{max} and a root at x_0 on the high energy side in convincing agreement with the observed spectra. In general, the universal root can be found for other types of power-law potentials as well, for instance the Förster interaction. Hence, further properties of this curve shape will be discussed in the next two sections to differentiate between the van der Waals and the Förster interaction.

6.4.3 Scaling with principal quantum number n

Besides the general line shape, one may use another criterion to identify the exciton interaction potential. It is given by the signal's dependence on the principal quantum number

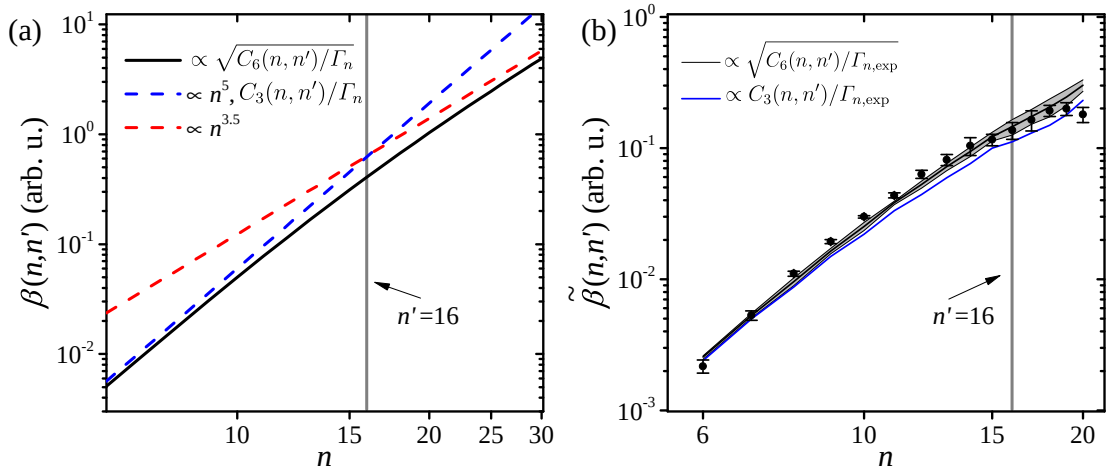

Figure 6.5 (a) Theoretical scaling of $\beta(n,n')$ for the interaction coefficient $C_6(n,n')$ with $n' = 16$ (black solid line). Blue and red dashed lines give the limits of $n \ll n'$ and $n \gg n'$. The scaling for $C_3(n,n')$ coincides with the blue dashed line, scaling as n^5. The mechanisms show different scalings for $n \gg n'$ assuming $\Gamma_n \propto n^{-3}$. Curves are shifted vertically for clarity. (b) Comparison of experimental (dots) and theoretical scalings for both van der Waals (black line) and Förster (blue line) scenarios. In both cases we find a good agreement with the data. The inclusion of experimental linewidths $\Gamma_{n,\mathrm{exp}}$ rescales $\tilde{\beta}(n,n')$ in both cases making their relative scaling almost indistinguishable in the available n regime. The grey area indicates the error for the van der Waals case, arising from the experimental linewidths. Curves are shifted vertically to coincide at $n = 6$. The grey vertical lines indicate $n' = 16$ in both panels.

n. For low interaction strengths $s_\kappa(x)d \ll 1$, the differential signal Eq. (6.23) reads

$$\Delta I \approx I_0 e^{-h(x)d} s_\kappa(x) d \,, \tag{6.26}$$

where both $h(\delta)$ and $s_\kappa(x)$ depend on n via g_n and Γ_n. Their dependence on n is from now on indicated by the index n. For the interaction coefficient $C_6(n,n')$, the n dependence is given by Eq. (6.4) in Sec. 6.1. Since the light-matter coupling strength g_n depends linearly on the transition dipole matrix element between the ground and final state, its dependence on n reads $g_n \propto d_n \propto n^{-3/2}$ and $g_n^2 \propto n^{-3}$. Thus, for an ideal system, $g_n^2/\Gamma_n \propto n^{-3}/n^{-3} = \text{const}$. However, as known from the experiment, these ideal scalings do not hold for high n (cf. Sec. 2.5). Therefore, we consider Eq. (6.26) for small detunings $|x| \ll 1$ only and can separate the n-dependent part

$$\Delta I \propto \frac{g_n^2}{\Gamma_n} \left(\frac{|C_\kappa(n,n')|}{\Gamma_n} \right)^{3/\kappa} \frac{g_{n'}^2}{\Gamma_{n'}^2} \mathrm{P}_{\mathrm{pump}} \cdot e^{\left[-\frac{4g_n^2 d}{c\bar{n}\Gamma_n}\right]} = \beta_\kappa(n,n') \mathrm{P}_{\mathrm{pump}} \,, \tag{6.27}$$

characterized by an n-dependent linear slope $\beta_\kappa(n,n')$. With the peak height of the linear spectrum in terms of optical density $H_{\mathrm{OD}} = \frac{4g_n^2}{c\bar{n}\Gamma_n} d$ (Eq. (6.15)) one finds

$$\beta_\kappa(n,n') \propto H_{\mathrm{OD}} \left(\frac{|C_\kappa(n,n')|}{\Gamma_n} \right)^{3/\kappa} \cdot e^{-H_{\mathrm{OD}}} \,. \tag{6.28}$$

In analogy to Ref. [Kaz+14], the information about the n dependence of $C_\kappa(n,n')$ enables the determination of the scaling of the slope $\beta_\kappa(n,n')$ with n and n' for the asymmetric scenario. Assuming an ideal system, $H_{\mathrm{OD}} = \text{const.}$, it reads in case of $\kappa = 6$ and the scalings derived in Eq. (6.4)

$$\beta_{\mathrm{vdW}}(n,n') \propto \sqrt{\frac{C_6(n,n')}{\Gamma_n}} \propto \begin{cases} n^5(n')^5 \text{ for } n \ll n' \\ n^{3.5}(n')^{6.5} \text{ for } n \gg n' \end{cases} . \tag{6.29}$$

For Förster ($\kappa = 3$), the scaling reads (cf. Eq. (6.7))

$$\beta_{\mathrm{F}}(n,n') \propto \frac{C_3(n,n')}{\Gamma_n} \propto n^5(n')^5 , \tag{6.30}$$

which does not depend on the relation of n and n'. The functions β_{vdW} and β_{F} are shown in Fig. 6.5 (a) in dependence on n and $n' = 16$. The black curve shows the van der Waals case β_{vdW} with both limits indicated by the blue and red dashed lines. The Förster case (β_F) is given by the blue dashed line as well, since the scalings for both types of interaction coincide for $n \ll n'$. As the dependence on n differs for $n \gg n'$ the curves for β_{vdW} and β_{F} separate for high enough n. In principle, this finding allows one to distinguish between the van der Waals interaction and the Förster interaction. Note that this is different for the symmetric Rydberg blockade ($n = n'$), where both mechanisms result in the same scaling, following an n^{10} dependence (cf. [Kaz+14]).

However, including experimental values for the linewidth, $\Gamma_{n,\mathrm{exp}}$, results in an n-dependent modification of $\beta(n,n')$, referred to as $\tilde{\beta}(n,n')$, as can be seen in Fig. 6.5 (b). The black solid line shows the resulting scaling behavior of the van der Waals interaction including experimental linewidths, $\tilde{\beta}_{\mathrm{vdW}} = \sqrt{C_6(n,n')/\Gamma_{n,\mathrm{exp}}}$. The grey area indicates the error of the expected scaling, resulting from uncertainties of the experimental linewidths. The blue line shows the scaling behavior of $\beta_{\mathrm{F}}(n,n')$ in case of a Förster-type interaction without error bars for clarity. The curves are shifted vertically to coincide at $n = 6$. Interestingly, the n-dependent broadening of the experimental linewidths in the high-n regime flattens both curves. As a result, the interaction mechanisms show an almost indistinguishable dependence on n with only a tiny difference at high n.

The experimental values of $\tilde{\beta}(n,n')$ are obtained from the slopes $\beta(n,n)$ of linear fits to the differential peak heights at E_{max} as a function of pump power, as shown in Fig. 6.3 (c) as solid lines. The fits are restricted to the linear regime. In order to obtain the intrinsic scaling law $\tilde{\beta}(n,n')$, the slopes $\beta(n,n')$ have to be corrected by the experimentally determined peak heights in terms of optical density at zero pump power $H_{\mathrm{OD,n,exp}}$ (cf. Eq. (6.28))

$$\tilde{\beta}(n,n') = \frac{\beta(n,n')}{H_{\mathrm{OD,n,exp}} \exp(-H_{\mathrm{OD,n,exp}})} . \tag{6.31}$$

The obtained values are shown as black dots in Fig. 6.5 (b) as a function of n. Within the errors, the experimentally obtained values for $\tilde{\beta}(n,n')$ are in good agreement with the expected scaling for the van der Waals interaction, while the Förster-type interaction slightly underestimates the observed trend. However, the small differences between $\tilde{\beta}_{\mathrm{vdW}}(n,n')$ and $\tilde{\beta}_{\mathrm{F}}(n,n')$ hardly allow for a clear distinction between both interaction mechanisms. In

principle, a difference would stem from the absolute values of $C_6(n, n')$ and $C_3(n, n')$, but the analysis here is restricted to a comparison of relative values, since the absolute values of $C_6(n, n')$ or $C_3(n, n')$ in case of the asymmetric Rydberg Blockade are still unknown yet. In addition, we obtain only relative values for $\tilde{\beta}(n, n')$ in the experiment since the experimental data measured with a Lock-In amplifier includes a constant but arbitrary amplification factor.

6.4.4 Exclusion of Förster interaction

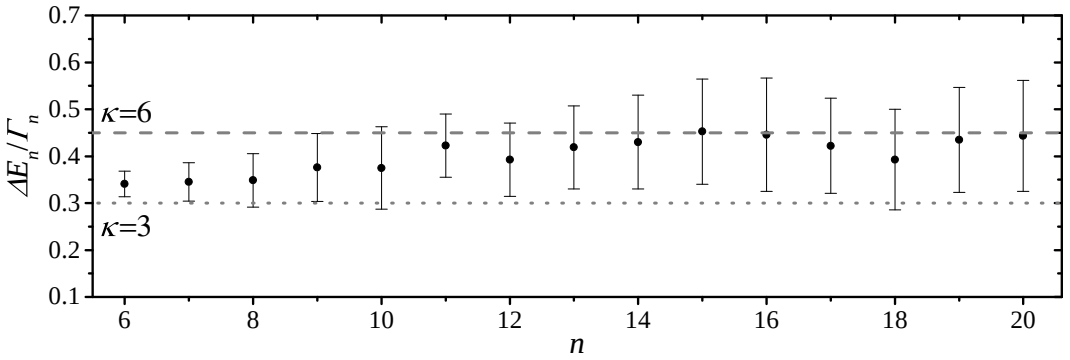

Figure 6.6 Ratio $\Delta E_n/\Gamma_n$ as a function of n obtained from differential transmission curves. Dashed lines give theoretical values for van der Waals ($\kappa = 6$) and Förster ($\kappa = 3$) interaction. The values are in good agreement with the van der Waals model. Deviations at low n can be traced back to an asymmetric line shape that is not considered in theory, see text.

So far, the general line shape of the differential transmission and the n-dependent scaling yield convincing arguments for a power-law-like interaction mechanism. In detail, the evaluation of $\tilde{\beta}(n, n')$ indicates the presence of Förster or van der Waals mechanisms, but does not allow us to distinguish between both in experiment. However, the line shape of the differential spectra gives a further possibility to rule out power-law potentials other than the van der Waals interaction. As mentioned earlier, the quantity $\Delta E_n/\Gamma_n = x_0 - x_{\max}$ is another characteristic indicator for the exciton interaction potential and has a universal value for all n in case of power-law potentials. For a Förster-like interaction potential ($\kappa = 3$) one finds $\Delta E_n/\Gamma_n = 0.3$ and for a van der Waals-like interaction potential ($\kappa = 6$) one finds $\Delta E_n/\Gamma_n = 0.45$. While it is in general possible to determine these values for power-law potentials with values of κ different than $\kappa = 3$ and $\kappa = 6$, the analysis here is restricted to the van der Waals- and Förster-type potentials, since these are the most relevant candidates for dipole-dipole interaction potentials between Rydberg-excitons. Their characteristic values for $\Delta E_n/\Gamma_n$ are shown in Fig. 6.6 in comparison to the experimentally determined numbers. The error bars mainly stem from uncertainties in the linewidths. Within the error bars, the data is mostly in accordance with the van der Waals-type value of $\Delta_n/\Gamma_n = 0.45$, rather than with the Förster-type value. Still, the data shows a constantly increasing deviation towards lower n. This deviation shows an analogue trend as the asymmetry parameter q_n, that increases continuously towards lower n as well, see Fig. 2.4 (d). Hence, the observed deviation might be traced back to the asymmetric line shape at lower n in the experiment,

whereas the theory presented so far is based on symmetric line shapes. The influence of the asymmetry on the theoretical values for Δ_n/Γ_n is the subject of ongoing theoretical research.

Nevertheless, as the data does is not in agreement with the value for $\kappa = 3$, the quantity $\Delta E_n/\Gamma_n$ can be used here to rule out the Förster-type interaction as the underlying exciton-exciton interaction mechanism. So far, the studies focusing on the symmetric case, reported in Ref. [Kaz+14], did not allow one to draw this conclusion.

Note, the shape of the exciton line resulting from the exciton-exciton interaction is not only determined by the type of power-law interaction potential but also by the ratio of repulsive and attractive energy potential curves contributing to the interaction. According to Ref. [Wal+18b], the landscape of potential energy curves depends strongly on the distance $\overline{\mathbf{R}}$ between the interacting excitons which is an unknown quantity so far. However, the value of $\Delta E_n/\Gamma_n$ holds for all configurations of repulsive and attractive potentials and thus does not depend on the exact potential landscape. Therefore it can be used as a reliable quantity to identify the interaction mechanism. A non-vanishing contribution of attractive potentials is in agreement with the observed increasing absorption on the low energy side of the peak in Fig. 6.3 (b).

6.5 Comparison with Debye screening

In Ch. 5 of this thesis, the disappearance of exciton lines as a function of plasma density is studied and explained within the Debye model. Already remarkably low plasma densities on the order of 0.01 μm^{-3} lead to the disappearance of excitonic absorption lines with high quantum numbers n. Also for pumping below the band gap, as discussed in this chapter, one might unavoidably create a certain amount of free electron-hole pairs. As described in detail in Ch. 5, these can be generated by the excitation of $1S$ states via the phonon background in combination with the Auger effect or by direct excitation via the Urbach tail below the band gap. In addition, resonantly pumped excitons might decay into $1S$ excitons via phonon interaction. These effects can lead to a certain plasma density resulting in some band gap shift Δ and a reduction of oscillator strength. Following this argumentation, the effects described in the sections before might in principle be caused by a surrounding plasma as well. However, free electron-hole pairs might in turn form bound exciton states again quickly. Whether exciton-exciton interactions or exciton-plasma interactions are dominant depends on the dynamics of the processes outlined above. Therefore, in the following various experimental observations are presented that cannot be explained by the Debye model of Ch. 5 and that help to distinguish between both regimes.

Here, the analysis of the differential transmission discussed in the section before is repeated for the plasma-scenario. The pump laser energy is fixed at 2.20 eV, which is about 30 meV above the band gap, and its power increases from 5 to 1000 μW. The resulting spectra are shown in Fig. 6.7 (a). Surprisingly, the overall spectral appearance seems to be similar to the one described in Sec. 6.4. Also here, a non-shifting but strongly varying maximum and a universal root on the high energy side of every resonance are observed, as shown in the closeup of $n = 11$ in Fig. 6.7 (b). As mentioned earlier, these observations are only expected for power-law interaction potentials and are therefore in contradiction to the Debye model.

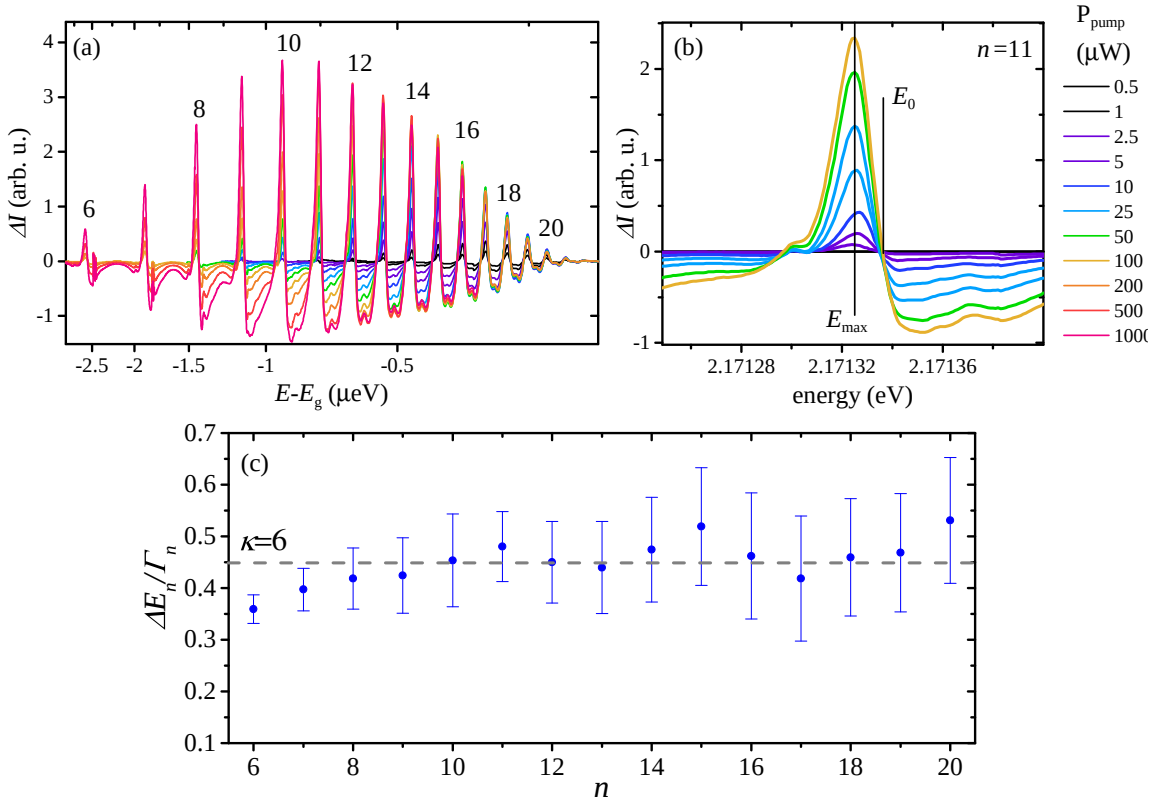

Figure 6.7 (a) Differential spectra of $n = 6$ to $n = 21$, recorded with a pump laser energy fixed above the band gap at 2.20 eV and increasing pump power from 0.5 to 1000 μW. (b) Closeup of $n = 11$ in the linear regime. Surprisingly, the curve shows a fixed relative extreme point at E_{max} and a universal root on the high energy side at E_0, which is only expected for a power-law interaction potential. (c) Also in this pump-scenario the values for $\Delta E_n/\Gamma_n$ are comparable to the theoretical value for the van der Waals interaction ($\kappa = 6$) of $\Delta E_n/\Gamma_n = 0.45$. This value is indicated by the grey dashed line. The values are extracted from the spectra in the linear power regime.

In this context, the quantity $\Delta E_n/\Gamma_n$ is evaluated for this scenario as well. The values are shown in Fig. 6.7 (c) and are found to be in good agreement with the value $\Delta E_n/\Gamma_n = 0.45$ that is expected for C_6 and is indicated by the dashed grey line. Hence, also in this pump-scenario the criteria pointing out the van der Waals mechanism as underlying interaction are confirmed.

Now, the n-dependent scaling of the slope $\tilde{\beta}(n)$ is considered. The differential peak heights are shown as a function of pump laser power in Fig. 6.8 (a). Also here, a linear dependence can be found within a narrow power range for each n. Note, the window in which the data follows a linear dependence shrinks for exciton resonances with higher quantum numbers n. For $n > 16$, it already ends below 10 μW, although the absorption lines are far away from saturation. Still, an estimate of the scaling of this slopes can be given and $\tilde{\beta}(n)$ can be calculated, which is shown in Fig. 6.8 (b). Within the Debye model from Ch. 5 one expects a rather weak n-dependent scaling of $\beta(n)$ resulting from changes of the oscillator strength

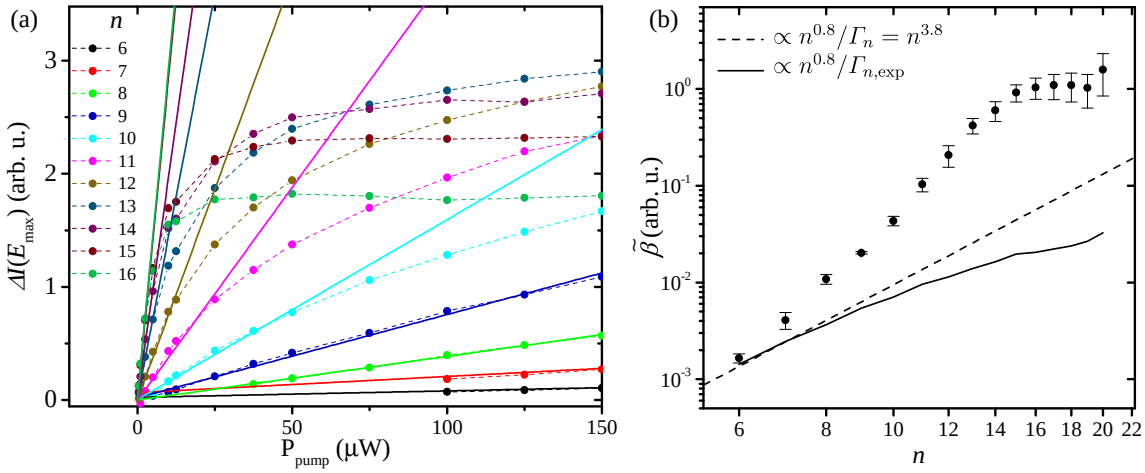

Figure 6.8 (a) Differential peak heights at E_{max} as a function of pump power $\mathrm{P}_{\mathrm{pump}}$ for principal quantum numbers $n = 6$ to 16 in the plasma-scenario. The solid curves show fits in the linear regime with a slope $\beta(n)$. (b) Experimental scaling of $\tilde{\beta}(n)$. The dashed line shows the expected scaling $\beta_{\mathrm{Debye}} \propto n^{3.8}$, following the Debye model. The solid line shows the scaling of $\tilde{\beta}(n, n')$ including experimental linewidths $\Gamma_{n,\mathrm{exp}}$. The curves are shifted by an arbitrary value for comparison. The observed scaling in the data is much stronger than predicted by the model.

according to $g_n^2 \propto n^{0.8}$. Combined with a linewidth scaling of $\Gamma_n \propto n^{-3}$ this yields for the Debye scaling

$$\mathrm{OD}_{\mathrm{pump}} - \mathrm{OD}_{\mathrm{no\ pump}} \propto \beta_{\mathrm{Debye}} \mathrm{P}_{\mathrm{pump}} \propto \frac{g_n^2}{\Gamma_n} \mathrm{P}_{\mathrm{pump}} \propto n^{3.8} \mathrm{P}_{\mathrm{pump}} \ , \tag{6.32}$$

which is shown as the dashed line in Fig. 6.8 (b). Including experimental linewidths $\Gamma_{n,\mathrm{exp}}$ in Eq. (6.32) even tilts the curve further towards a smaller increase at high n shown by the solid line. Interestingly, in the small range of a linear power dependence, the experimental data shows a much steeper slope than predicted by the Debye model. Up to $n \approx 15$ it roughly scales as n^7.

In conclusion, assuming only a Debye screening underestimates the observed changes in the spectra. Additional interactions might stem from bound exciton states generated by relaxation of free electron-hole pairs. Here, the relaxation into high Rydberg states of arbitrary principal quantum numbers n, but also high angular momentum quantum numbers l seems to be possible (cf. Sec. 6.5.1). Although the overall trend of vanishing oscillator strength could be described in accordance with the Debye model in Ch. 5, the analysis given here reveals deviations from that model at very low pump powers. These deviations are obtained by the measurement of differential transmission with a Lock-In amplifier that provides access to changes in peak heights with a higher accuracy compared to absolute signals.

Another feature observable in the experiment is given by the comparison of states with different angular momenta, namely P and F. The observations are shown in Fig. 6.9 (a). Again, the pump laser is fixed at an energy above the band gap. We focus on absorption

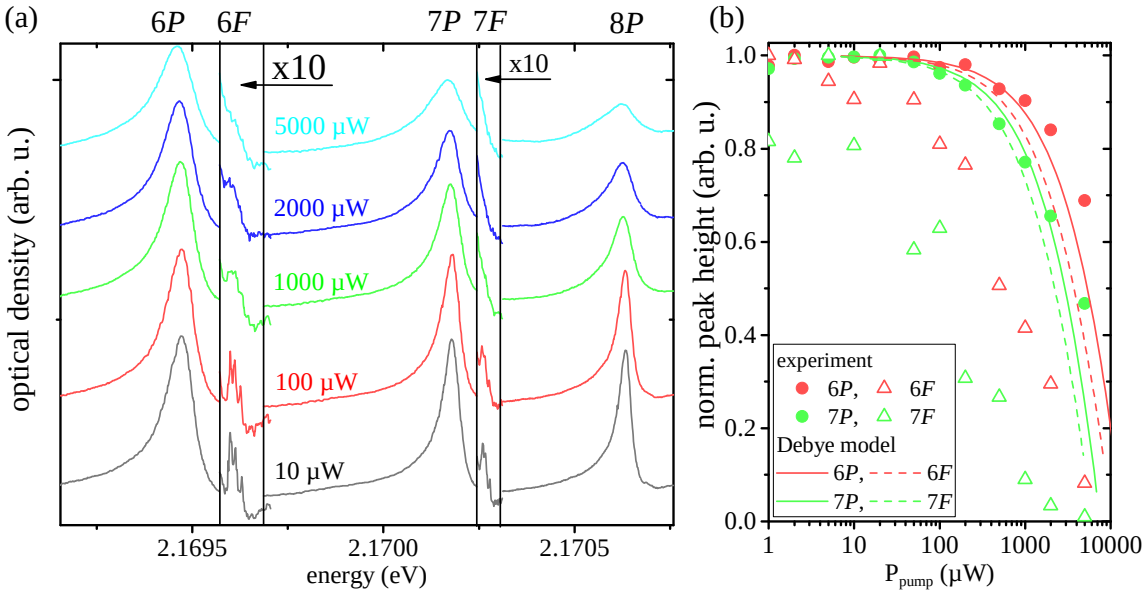

Figure 6.9 (a) Absorption spectrum of P and F excitons with $n = 6, 7$ and 8, recorded with a pump laser energy above the band gap at 2.20 eV. The spectra are stacked vertically by an arbitrary offset and magnified in by a factor of 10 in the spectral region of the $6F$ and $7F$ states. Remarkably, with increasing pump power $\mathrm{P_{pump}}$, the nF states disappear earlier than the $(n+1)P$ and $(n+2)P$ states. (b) Quantitative comparison of the normalized peak heights of $n = 6$ and $n = 7$ P and F excitons, obtained from panel (a). The Debye prediction is scaled on the abscissa to fit the P peak heights (dots). This model underestimates the drop of peak heights of the F excitons obtained from the experiment (triangles).

spectra of P and F states with principal quantum numbers $n = 6$ to $n = 8$. With increasing pump power (from bottom to top) the nF states vanish earlier than the $(n+1)P$ states and even $(n+2)P$ states. This observation is in contradiction with a plasma-induced band gap shift towards lower energies. Within that model one would expect the absorption lines to vanish one after the other starting from the high energy side, independent of their angular momentum.

A more quantitative comparison is given in Fig. 6.9 (b). Here, the normalized peak heights of P and F states (dots and triangles) are compared with the model prediction of the Debye model for different angular momentum states (solid and dashed lines). The model's power dependence is scaled by an arbitrary factor to describe the peak heights of the P excitons with minimal mismatch. Obviously, the corresponding prediction for F excitons drastically underestimates the strong drop observed in the experiment, as can be seen by the comparison between the dashed lines and the triangles. In turn, the additional interaction, that is stronger for states with high angular momenta, might stem from dipole-dipole interactions between excitons created by relaxation of free electron-hole pairs.

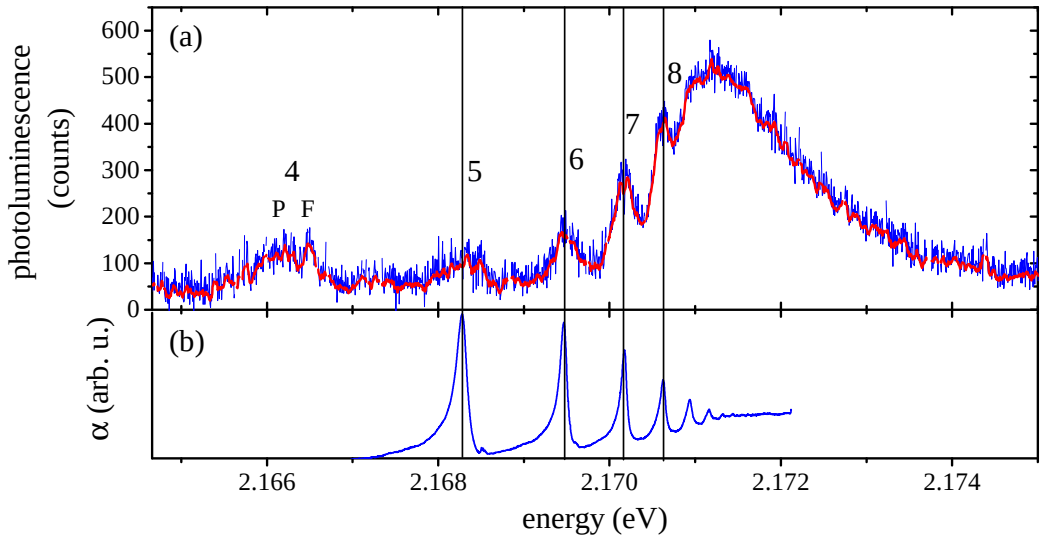

Figure 6.10 (a) Photoluminescence spectrum of the yellow series at 1.3 K. The system is excited at 2.3 eV with a power of 2 mW. The signal is integrated in 2 sets for 1.5 hours each and averaged (blue). The red line shows an additional smoothing of the data in order to achieve a better signal-to-noise ratio. Excitonic luminescence can be observed for states $n = 4$ to about $n = 8$ with a broad background starting around $n = 6$. For comparison, in panel (b) an absorption spectrum is shown recorded at an additional plasma excitation power of 2 mW at 2.20 eV. At this pump power, the band gap is shifted to lower energies and only states up to $n \approx 10$ are observable.

6.5.1 Electron-hole pair relaxation - Photoluminescence spectroscopy

The formation of bound exciton states from free electrons and holes can be studied in photoluminescence experiments. Here, free electron-hole pairs are injected by above band gap excitation around 2.3 eV (532 nm) at a crystal temperature of 1.3 K. Instead of the transmitted portion of the incident light, the spectrally resolved emission from the sample is detected. Similar experiments are reported in Refs. [Kit+17] and [Tak+18], albeit in a much more comprehensive experimental study. The pump power is set to 2 mW - a comparably high value - to achieve a good signal-to-noise ratio. The resulting spectrum is shown in Fig. 6.10 (a). The blue spectrum shows the pure measured signal which is obtained within an integration time of 2x 1.5 hours. The spectrum is smoothed, shown by the red line. We can identify P-shell exciton resonances from $n = 4$ up to $n = 8$. We find even high angular momentum states populated, since for $n = 4$ additionally $4F$ states on the high energy side of the P exciton peak are visible, similar to Ref. [Tak+18]. This finding underlines the assumption of free carrier relaxation into bound exciton states. In turn, the population of these states could give rise to a stronger dipole blockade as expected from the Debye model, resulting in effects such as the faster disappearance of high angular momentum states compared to the P excitons or the steeper scaling of the slope $\tilde{\beta}(n, n')$, discussed above.

Here, the limitation of exciton signals up to $n = 8$ in turn follows the expectations given

by a shifted band gap for an applied laser power of 2 mW. This can be demonstrated by the comparison of the photoluminescence spectrum to an absorption spectrum measured under equivalent conditions - with a pump laser energy above the band gap at around 2.20 eV. This is shown in the lower panel. At a power of 2 mW, also in absorption only peaks up to around $n = 10$ are left and have not vanished into the continuum yet. For that reason alone, we do not expect to see signals from higher-n excitons in the photoluminescence spectra. At lower pump powers as discussed in Sec. 6.5, states with higher n might additionally become populated.

Next, we find a continuous background starting to rise around $n = 6$ with a maximum height at about 2.17124 eV. This background was observed in Refs. [Tak+18] as well and partly assigned to the sum of overlapping Lorentzian curves. This is in accordance to the recent work of Krüger et al. [Krü+20] and will be discussed later in Sec. 6.7 again. Interestingly, the maximum of this background coincides roughly with the shifted band gap energy $\tilde{E}_\mathrm{g}$ of the absorption spectrum shown in the lower panel.

6.6 Variation of n'

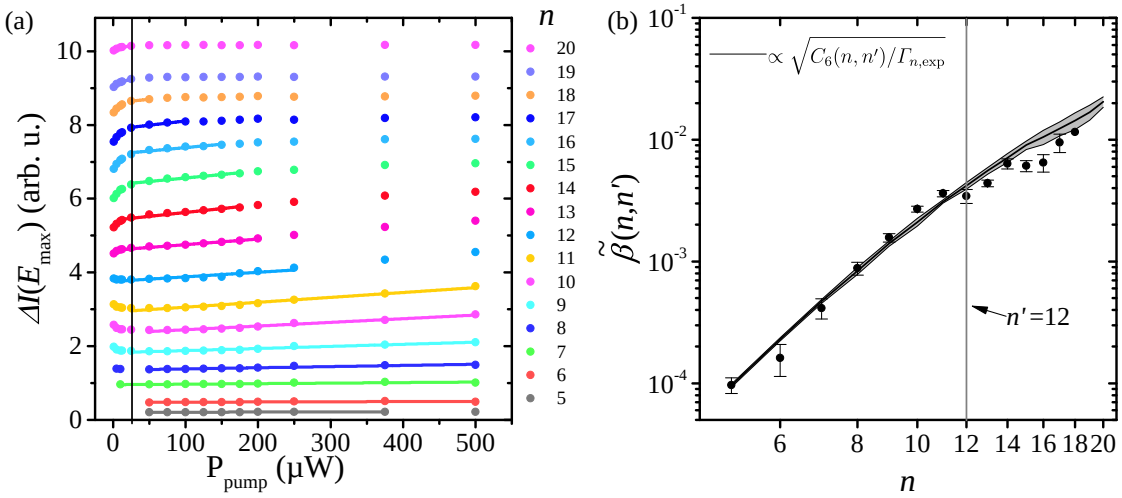

Figure 6.11 (a) Differential peak heights at E_max for a resonant excitation of $n' = 12$. The data is stacked vertically. In contrast to Fig. 6.3, the data is not corrected and thus reveals an initial nonlinearity for low pump powers. Colored solid lines show fits in the linear power regime for all resonances with $n \leq 18$. The black vertical line separates the nonlinear from the linear regime. Traces are shifted vertically for clarity. (b) Slope $\tilde{\beta}(n, n')$ as a function of n. The scaling of experimental values (dots) is in agreement with the van der Waals model for this scenario shown by the black solid line with grey area indicating the error. The vertical line indicates $n' = 12$.

In Sec. 6.4, the case of resonant excitation of pump excitons with principal quantum number $n' = 16$ was studied. A good agreement between theory and experiment was shown, revealing the van der Waals interaction as the underlying interaction mechanism. Obviously, this asks for the investigation of other pump-scenarios with n' different than $n' = 16$. Therefore various configurations with different n' are discussed in this section,

namely $n' = 12, 10$ and $1S$. Note, the spectral appearance in the differential transmission is in general the same in all of these scenarios, similar to the cases discussed before where the pump energy is set to $n' = 16$ and above the band gap. Since differences between the scenario of a resonant excitation of excitons with $n' = 16$ and the plasma-scenario turned out to be observable in the scaling of $\widetilde{\beta}(n, n')$, the discussion here is focused on the analysis of the peak heights as a function of pump power $\mathrm{P}_{\mathrm{pump}}$.

Figure 6.11 shows the analysis of the data obtained in case of resonant pumping of the state $n' = 12$. In the left panel, the evaluation of differential peak heights is shown. The data is stacked here for better comparison. Solid lines present fits to the linear pump power range. Note that the data correction from Sec. 6.3 is not used here to make differences at low pump powers visible. Interestingly, we find a nonlinear behavior at low pump powers for all n, which is - in contrast to the case of $n' = 16$ discussed in Sec. 6.3 - a nonlinear change in both directions. For $n \leq n'$ we find a nonlinear decrease and for $n > n'$ a nonlinear increase that transform into a linear behavior at higher powers, shown by the colored solid lines. The nonlinear and linear regimes are separated by the black vertical line. Restricting the analysis to the linear regime again leads to an n-dependent scaling of $\widetilde{\beta}(n, n')$ in satisfying agreement with the model prediction for $n' = 12$, as shown in Fig. 6.11 (b). The dots show the experimental values and the solid line with grey area shows the model prediction in analogy to Sec. 6.4. For $n > 18$, there is no linear power dependence at all. For these states the peak height increases nonlinearly and transforms directly into saturation.

In another scenario, the pump laser energy is set to $n' = 10$ and, again, the progression of differential peak heights as a function of pump power is extracted. The traces are shown in Fig. 6.12. In general, the behavior looks quite similar to the case of $n' = 12$. Also here, the data shows a pronounced nonlinear evolution at low pump powers. Interestingly, its sign changes around $n' = 10$, meaning a decrease of transmission for $n < n'$ and an increase for $n > n'$. Unlike in the case of $n' = 12$, a linear regime cannot be identified for $n > n'$. The nonlinear increase directly transforms into saturation and an n-dependent scaling of $\widetilde{\beta}(n, n')$ cannot be extracted in this scenario.

The nonlinear regime seems to change its sign from negative to positive at n' going from lower to higher n. However, it should be noted that it is in general possible to observe such a nonlinearity with negative sign also for $n > n'$ in the case of extremely low pump powers. This was shown in Ref. [Sch18].

The last scenario considered here is the resonant pumping of $1S$-Ortho excitons with the same analysis used above. The strength of dipole coupling between $1S$ excitons and Rydberg excitons seems to be negligible due to the small dipole moments of the ground state excitons. However, an effect of noticeable strength on Rydberg states might stem from the creation of an electron-hole plasma by Auger decay of the $1S$ excitons as considered in the rate equations (5.14)-(5.17). Hence, the direct excitation of $1S$ excitons might result in similar spectral changes as in the case of resonant excitation of electron-hole pairs (Sec. 6.5). With this in mind, we directly compare the differential peak heights from the spectra where $1S$ excitons are resonantly excited with the scenarios $n' = 16$ and pumping at 2.20 eV, which is about 30 meV above the band gap, in Fig. 6.12 (b). The traces are shifted for clarity. Open stars show the data for $n' = 16$ revealing the linear increase discussed previously for all n in the power regime starting after a short range of nonlinear decrease at the beginning. In direct comparison to the case where the pump laser energy is placed at $n' = 16$, the two other cases, namely pumping the $1S$ exciton resonantly and pumping above the band

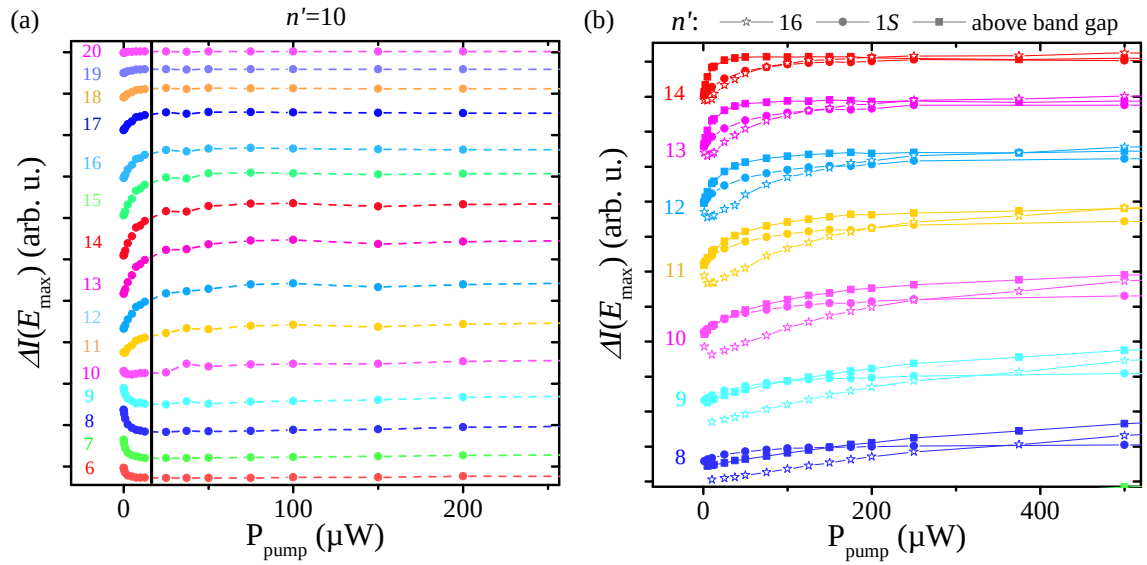

Figure 6.12 (a) Differential peak heights at $E_{\max}$ for resonant excitation of $n' = 10$. The data shows a pronounced nonlinear regime at the beginning for all n on the left side of the vertical line. For $n < 10$, the amplitude is decreasing, for $n > 10$ it is increasing. While in the first case, the nonlinearity is followed by a weak linear increase in $\mathrm{P_{pump}}$, in the second case it transforms into saturation. (b) Comparison of three pump-scenarios with a pump energy at $n' = 16$ (open stars), $n' = 1S$ (full dots) and above the band gap (full squares) for $n = 8$ to $= 14$. The scenario with $n' = 16$ deviates from the others as it shows a pronounced linear power regime for all n depicted. Traces are shifted vertically for clarity in both panels.

gap, mainly reveal a nonlinear dependence of the peak heights on pump power. Only at low pump powers, a small range of pump powers can be found for the latter cases, where the differential peak heights increase linearly with the pump power. However, this range decreases drastically with n, as mentioned earlier in Sec. 6.5. While the absolute amplitude is slightly different, the dependence on pump power seems to be quite similar when pumping the $1S$ or above the band gap, which is in accordance with the similarity of both models mentioned above.

In conclusion, the determination of an n-dependent scaling law in agreement with the model prediction of the van der Waals interaction potential is possible for $n' = 12$ as well, because a power regime can be found, where the changes of the differential peak heights depend linearly on the pump power. In case of lower n', different interaction mechanisms seem to occur since the pump power dependence of the peak heights deviates from the expectations showing no pronounced linear dependence.

6.7 Purifying effect

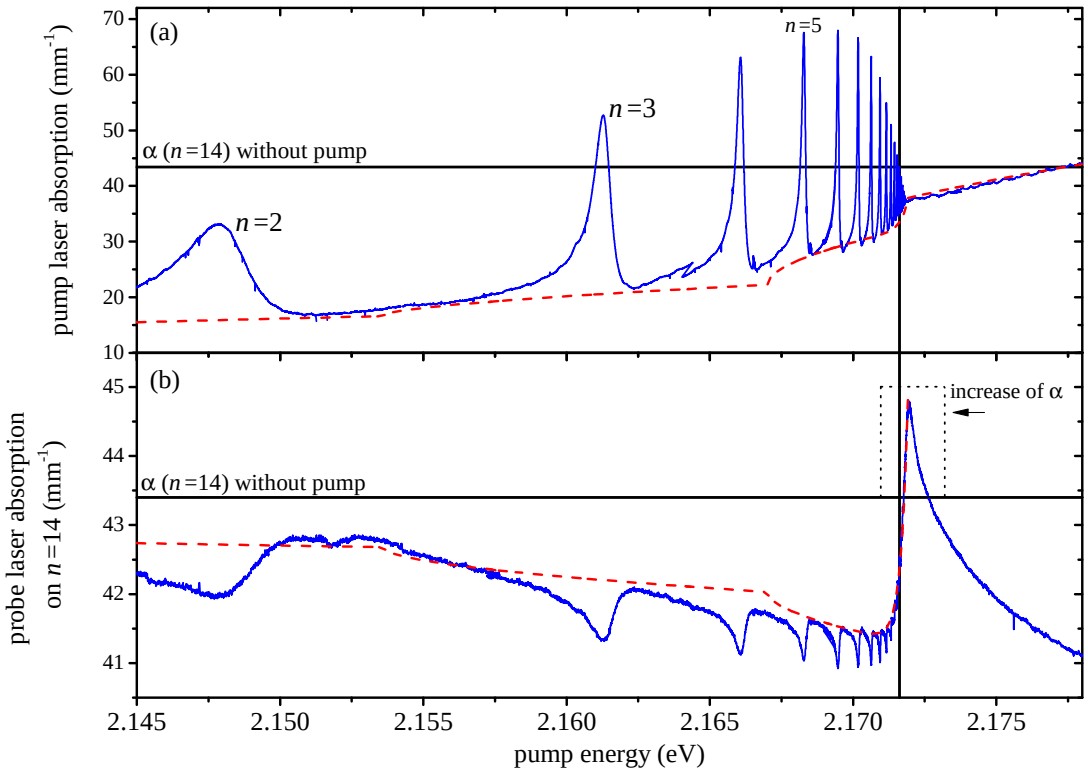

Figure 6.13 (a) Absorption of scanned pump laser light. The red dashed line shows the background absorption following Eq. (2.42) as a guide to the eye. (b) Absorption at the resonance energy of $n = 14$ as a function of pump laser energy. The absorption of $n = 14$ changes corresponding to changes in the pump laser absorption. With increasing pump energy the absorption decreases, while a sharp exponential increase of absorption (purifying) is observed in the spectral vicinity of the band gap, indicated by the dashed box. The red dashed line follows the background trace from panel (a) as a guide to the eye up to the band gap, see text for details. In both panels, the black vertical line indicates the resonance energy of the state $n = 14$. The horizontal lines indicate the amplitude of absorption at this energy without additional pump laser light obtained from Fig. 2.3.

In the sections before we noticed a nonlinear behavior of the differential transmission ΔI in dependence on pump power. It was found to occur for low pump powers and to saturate fast. It was found to be mostly an increase of absorption in case of a pump laser energy at $n' = 16$, while in the scenarios $n' = 10$ and $' = 12$ also a similar behavior of opposite sign could be observed for states with $n > n'$. Moreover, in the configurations with a pump energy above the band gap and resonant on the $1S$ Ortho-exciton it is almost absent.

Here, we focus on this observation and study the case of an increase of absorption only, i.e. a negative amplitude in the differential transmission. We will term this effect "purifying" of absorption lines, since it increases the absorption around the resonance energy. So far, a comprehensive model of the underlying physics is not yet developed and, therefore, a solely

experimental investigation is presented with a focus on the dependence on pump energy of this effect. To this end, the pump-probe setup is changed concerning two minor aspects: First, the pump laser energy is scanned continuously and the probe laser energy is fixed onto a certain resonance, i.e. $n = 14$ in this particular case. Hence, we achieve the full information about the pump energy dependence. The probe laser power stays at a low level of about 1 μW. Second, the pump laser's transmission is detected by a second photodiode (PD3 in Fig. 3.1) while scanning the spectrum. Similar experiments were already reported in [Fre16] using a differential signal, but their interpretation remained unclear. An even earlier attempt was presented in Ref. [Kaz+14], but in a quite small spectral window. Here, we achieve a deeper understanding of the data by using a more extended energy range and by measuring the absorption directly.

Since it is known that this effect occurs at low pump powers, first of all a low pump power of 2 μW is used. The pump laser energy is scanned from $n = 2$ up to 2.180 eV, i.e. about 8 meV above the band gap. The obtained data is shown in Fig. 6.13. The upper panel shows the absorption spectrum obtained by the detection of the scanned pump laser light. Due to the low pump power of 2 μW, the spectrum is comparable to the usual linear absorption spectrum, as shown for example in Fig. 2.3 in Sec. 2.5. The red dashed line traces the background absorption following Eq. (2.42). In panel (b) the absorption at the resonance energy of $n = 14$ as a function of the pump laser power is shown, measured by the probe laser fixed to the resonance energy of this absorption peak. The black vertical line indicates this energy in both panels and the black horizontal lines show the amplitude of absorption at this resonance energy with zero pump laser power of $\alpha \approx 43.5$ mm^{-1}. This value is obtained from the pure spectrum without external pump laser as shown in Fig. 2.3 in Sec. 2.5. Knowing this value allows us to obtain the probe absorption in absolute units. Now, the dependence of absorption at the resonance energy of $n = 14$ on the pump laser energy becomes visible. Starting from $n = 2$ towards higher energies, first of all a decrease of the $n = 14$ peak height below its unperturbed value is observed. The overall changes in absorption at the resonance energy of $n = 14$ follow the trace of the continuous background absorption in the upper spectrum, whereas placing the pump at the exciton absorption peaks leads to additional enhancements of this reduction within the corresponding absorption linewidth. The red dashed line serves as a guide to the eye following the general trace of the background absorption from panel (a), but with the opposite sign and arbitrary amplitudes for the different phonon contributions. However, in the regime close to the band gap the decrease of the $n = 14$ peak height is superimposed by a sharp exponential increase. This exponential trace can be described by an Urbach-tail-like function as described in detail in Sec. 2.5, reading

$$\alpha_{\mathrm{U}} \propto \exp\left(E - \tilde{E}_{\mathrm{g}}\right)/E_{\mathrm{U}} \ , \tag{6.33}$$

and is indicated by the red dashed line close to the band gap. In the spectrally small window around the band gap indicated by the rectangle in panel (b), the absorption signal even shows an increase to values higher than the unpumped one. Hence, the absorption of pump laser light in this spectral range leads to a growth of the absorption line of $n = 14$ measured by the probe laser, which corresponds to the negative signals at E_{max} in differential transmission ΔI.

We focus on this regime and show a closeup of the spectral range around the band gap in Fig. 6.14. The increase of absorption of the $n = 14$ peak follows the exponential function

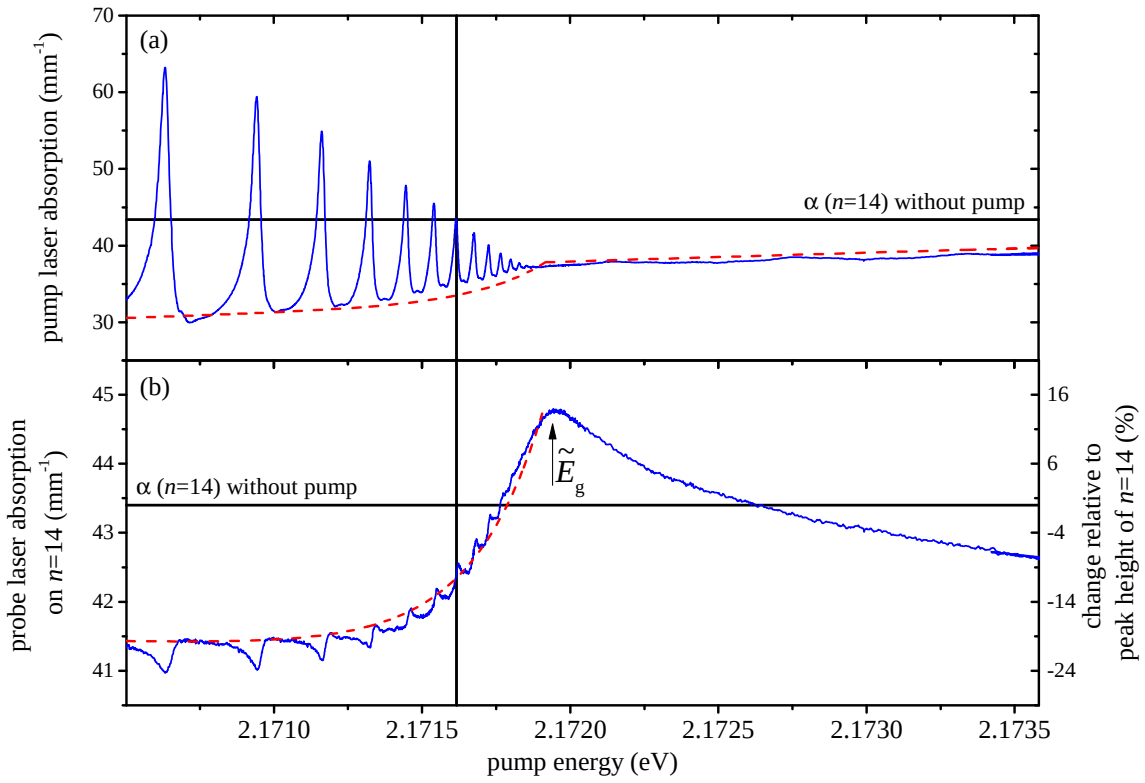

Figure 6.14 Closeup of the high energy range of Fig. 6.13. The exponentially increasing background close to the band gap in the upper panel can be obtained from the trace of the probe signal in the lower panel. The changes of the peak height of $n = 14$ compared to the height without pump of $h_{14}(\delta = 0) \approx 10$ mm^{-1} are given by the right axis in the lower panel. At a pump laser energy in the vicinity of the band gap $\tilde{E}_g$, the peak height of $n = 14$ increases by about 12 % relative to the peak height without pump.

until it saturates around 2.172 eV, which is a value comparable to the shifted band gap $\tilde{E}_g$ for zero pump power, as indicated. The width of the exponential tail is found to be $E_U = 240$ μeV which is comparable to $E_U = 170$ μeV used in Sec. 2.5 (cf. Appendix A.2). The same width is used to calculate the exponential tail of the dashed line in the upper panel. Indeed, this finding confirms the existence and width of an exponential absorption tail close to the band gap, that was found in Sec. 2.5 by the offsets $\alpha^P_{0,n}$ stemming from the peak fitting routine (green dots in Fig. 2.3).

The right axis in the lower panel gives the change of absorption relative to the peak height in terms of absorption of the $n = 14$ resonance at zero pump power $h_{14}(\delta = 0) \approx 10$ mm^{-1} (cf. Eq. (6.15)). The maximum growth of peak height is found to be about 12 %. Scanning the pump laser to even higher energies than $\tilde{E}_g$ leads to a decrease of absorption for the $n = 14$ peak height again, following an unknown nonlinear function. Moreover, also the distinct exciton-induced changes seem to change their sign, the more the closer they are to the band gap. This observation will be discussed later in the context of Fig. 6.16.

First, we conclude from these observations that the effect of purifying becomes partic-

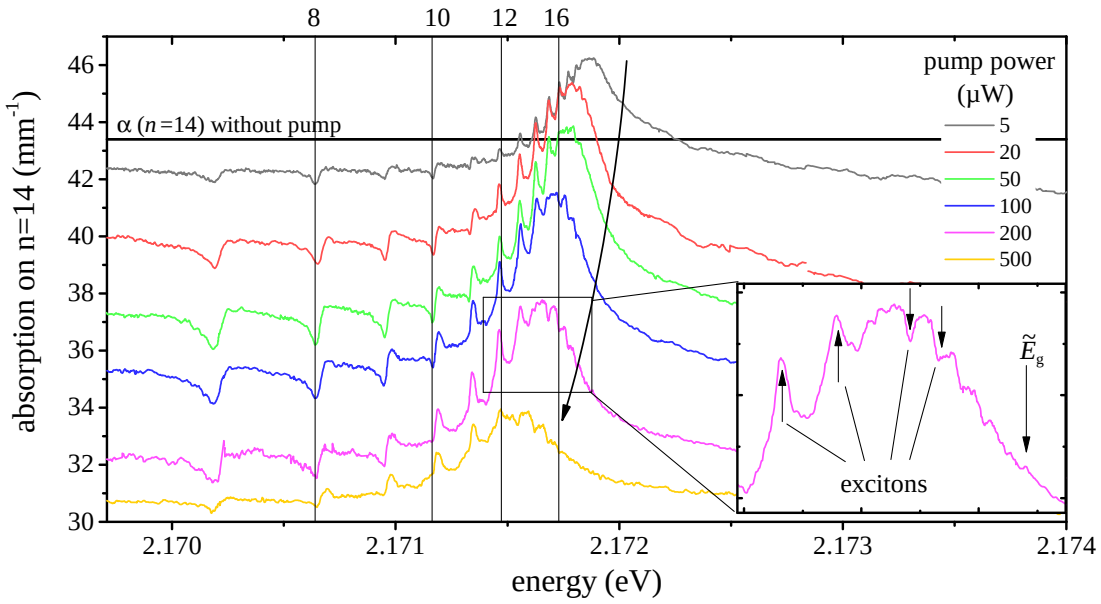

Figure 6.15 Probe absorption at the resonance energy of $n = 14$ as a function of pump energy shown for increasing pump powers from 5 μW to 500 μW from top to bottom. The solid horizontal line indicates the amplitude of absorption at the resonance energy without pump. Vertical lines mark excitonic principal quantum numbers as labeled on top. The general trend of a decrease of the probed peak height is overlaid by the purifying effect in the spectral vicinity of the band gap. Moreover, the maximum of the signal shifts to lower energies with increasing pump power (arrow). At high pump powers it does not coincide with the shifted band gap energy $\tilde{E}_g$ since distinct excitonic features are still observable at higher energies, indicated by arrows in the inset.

ularly pronounced for pump energies around the band gap. The effect seems to saturate close to the exact value of $\tilde{E}_g$ for the given pump power of 2 μW.

Next, the changes in probe absorption for increasing pump powers are investigated. The resulting spectra for pump powers from 5 to 500 μW are shown in Fig. 6.15, again as a function of pump energy. For all pump powers, we observe an increased absorption around the band gap. Interestingly, the overall trend of decreasing absorption is partially canceled out in this regime. For powers below 50 μW, this leads to the growth of absorption compared to the absorption at zero pump power, as observed at 2 μW a well. For higher powers, the growth of absorption is still present, but does not overcome the negative trend, as it saturates at a certain magnitude. Additionally, due to saturation, the maximum of this effect shifts to lower energies with increasing power, as indicated by the arrow. The spectra of pump powers 100, 200 and 500 μW even show excitonic absorption features on the maximum's high energy side. Hence, the shifted band gap E_g is located on the high energy side of this maximum as well and does not necessarily coincide with the energy of maximal purifying. This can be seen in detail for 200 μW in the inset of Fig. 6.16. The excitonic features, given by the distinct peaks lying on the continuous background, are indicated by arrows in the inset. They seem to change their sign around the saturation energy. Below

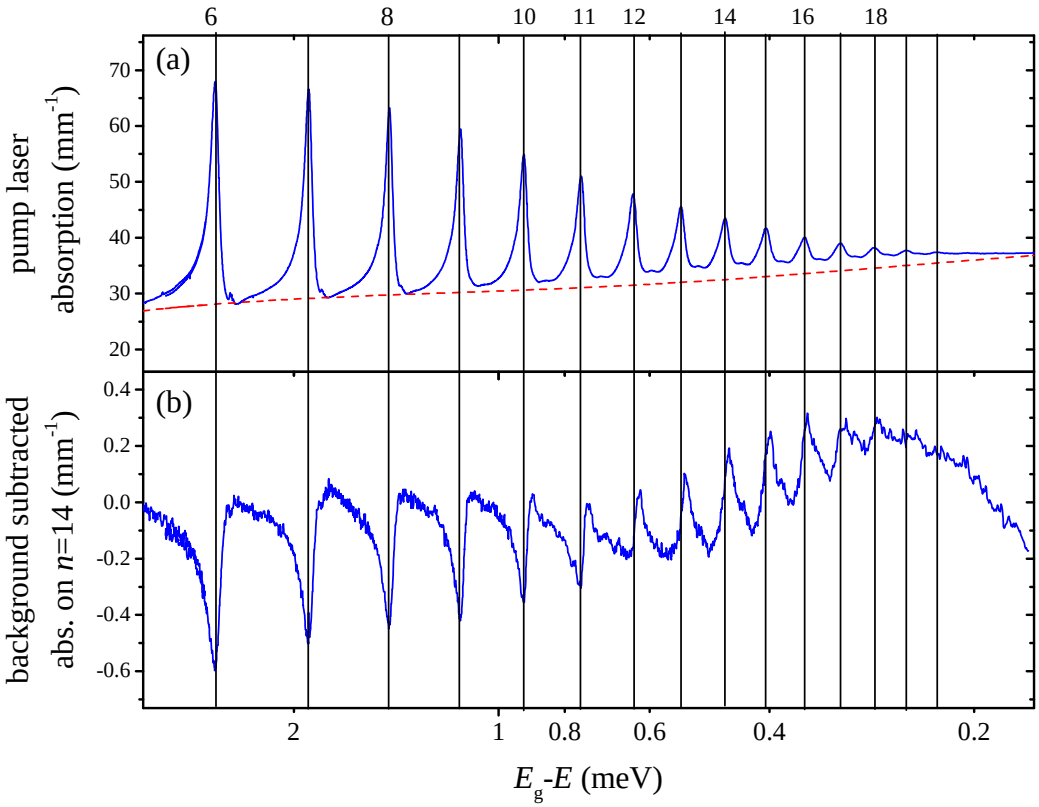

Figure 6.16 (a) High energy regime of the pump laser absorption spectrum from Fig. 6.13 with a logarithmic energy scale. (b) Probe laser absorption with subtracted background. The exciton-induced decreases of absorption in the probe signal coincide with the maxima of pump absorption. Around $n = 11$ the sign changes into an increase of absorption. Interestingly, the maximal increase is located on the high energy side of the pump resonance. Vertical lines mark excitonic principal quantum numbers as labeled on top.

saturation the exciton excitation by the pump laser induces an increase of absorption in the probe signal, whereas it induces a decrease of absorption at energies above the saturation energy. This will be discussed in the following in more detail.

Finally, we focus on the exciton-induced changes. In this regard, the data of Fig. 6.13 is used and the background-induced part of the probe absorption is subtracted, which is indicated by the red dashed line in the lower panel of that figure. The result is shown in Fig. 6.16 (b). Remarkably, differences can be observed between the spectral positions of the induced absorption features in the probe signal (lower panel) and the exciton resonances in the pump spectrum (upper panel). The comparison is indicated by the vertical lines. For low n the situation is obvious: The pump laser induces a reduction of the probe absorption when pumping an exciton. The energy of the maximum reduction in the probe signal agrees with the maximum of pump laser absorption at a particular resonance. Around $n = 11$ the sign of this effect seems to change and an increased absorption according to the purifying effect can be observed. However, exact comparison reveals that the increase

of absorption is induced by pump laser energies slightly above the resonance maximum. Hence, the maximum absorption of the pump laser on an exciton resonance does not induce the highest increase of absorption in the probe signal. A thorough explanation of this observation is out of the scope of the present work and is the subject of ongoing research.

In the following, the observations mentioned above shall be summarized. The absorption of pump laser light always leads to a change of the probed state absorption, even for primary absorption into the phonon background. Here, the probe absorption follows the background trace in a good approximation. The purifying effect is mainly caused by absorption in the spectral range around the band gap. Still, the question remains which types of particles are excited and thus are responsible for this increase in absorption. The exponential dependence on pump energy of the increase in absorption reveals a close relation between the purifying and the exponential absorption tail of the band gap. Within this tail, the linewidths are broader and the oscillator strengths are smaller than expected leading to a reduced peak height in the high n regime (cf. Sec. 2.5). This purifying may be interpreted as a partial neutralization of the effect causing this reduction.

Following the description in Ref. [Krü+20], the exponential absorption tail close to the band gap results from charged impurities in the crystal (cf. Sec. 2.5). The highest Rydberg states ionize due to the presence of spatially inhomogeneous micro-fields and lower the continuum edge which results in the exponentially smeared out band gap. Light with an energy falling into this spectral range might already excite a certain amount of free electron-hole pairs which could recombine with the bound charges causing the micro-fields. In turn, the observed reduction of peak height is partially neutralized at low pump powers leading to an increase of absorption at the resonance energy. Saturation sets in as soon as all possible recombination channels are occupied. Furthermore, this effect is superimposed by the onset of possible blockade effects which cause the absorption to decrease after saturation.

6.8 Conclusions

In this chapter, several pump-probe scenarios were studied. Resonant pumping of $n' = 16$ Rydberg states leads to distinct signatures in the differential transmission spectra that can be explained by power-law interaction potentials between excitons. While a mean field model fails to describe the spectra, the inclusion of correlations between excitons is crucial to explain the observed features in detail. The changes of differential peak heights, described by the parameter $\tilde{\beta}(n, n')$, show an n-dependent scaling behavior in agreement with dipole-dipole interactions of Förster- and van der Waals-type, but do not yield sufficient information to differentiate between both mechanisms, similar to the case of the symmetric Rydberg blockade (cf. [Kaz+14]). Finally, a detailed analysis of the resonance line's spectral shape helps to rule out the Förster-type mechanism and leaves only the van der Waals interaction as the possible interaction mechanism. To exclude a plasma influence as a cause for the observed features, the same analysis was presented for the scenario where the pump laser energy is placed above the band gap. Remarkably, spectral features were observed that might stem from a plasma relaxation into Rydberg states at low pump powers. Furthermore, the n-dependent scaling of $\tilde{\beta}(n, n')$, obtained in the range of low pump powers, was found to be in contradiction to the Debye model discussed in Ch. 5.

In addition, further pump-scenarios were discussed, namely with a pump laser energy at

$n' = 12, 10$ and the $1S$ Ortho-exciton. Also for $n' = 12$ a scaling of $\tilde{\beta}(n, n')$ in accordance with the model prediction is obtained from the data, while no agreement in the case of $n' = 10$ can be found. Here, the differential peak heights show a rather nonlinear behavior for low pump powers, the sign of which depends on n and n'. Interestingly, a linear regime, as found in the cases of $n' = 12$ and $n' = 16$ is completely missing. The same holds for the resonant pumping of the $1S$ Ortho-resonance where the results are comparable to those of the plasma-scenario. Except in a small range of very low pump powers, the differential peak heights show a mainly nonlinear behavior in dependence on pump power. The similarity of the results in both pump-scenarios leads to the assumption, that the same type of particles is created. This can be explained with the creation of an electron-hole plasma by Auger decay of the resonantly excited $1S$ excitons, that finally leads to similar changes in the spectra as in the case of a resonantly excited electron-hole plasma.

In total, various arguments were found, that the spectral changes observed while a high Rydberg state with $n' \geq 12$ is resonantly excited are caused by long-range van der Waals interactions. In order to achieve a deeper understanding of the underlying exciton-exciton interactions with respect to the disagreement between theory and experiment at lower n, comparing absolute values from the experiments to absolute values of $C_6(n, n')$ calculated within the framework of a microscopic theory, would be a promising task.

In the last section of this chapter experiments were presented that focus on a deeper understanding of the initial nonlinear behavior mentioned before, in particular the nonlinear increase of absorption, termed purifying. It was shown, that this nonlinear increase is caused by light absorption in the spectral range close to the band gap which is dominated by an exponentially growing continuum. Based on a numerical model by Krüger et al., a possible explanation for the observed increase of absorption was given: While pumping close to the band gap, i.e. on Rydberg states with principal quantum numbers $n > 10$, one always excites free carriers due to the absorption into this growing continuum. These free charges can neutralize a certain amount of charged impurities minimizing the perturbing influence of the latter on high-n Rydberg excitons. As a consequence, the absorption of Rydberg exciton resonances increases at very low pump powers. Since this effect is limited to energies close to $\tilde{E}_\mathrm{g}$, it is almost not observable in the plasma-scenario or at a pump laser energy at $n' = 1S$.

The information about the dependence of the purifying effect on pump laser energy obtained here will help to gain a better understanding of the mechanisms causing the observed increase in absorption. This is of importance for future studies since this effect is present in all absorption measurements using a laser with an energy set to a value in the spectral range close to the band gap or, more accurately, to an energy of a state with $n' > 10$.

Chapter 7

Conclusions

In this thesis, many new insights into the physics of Rydberg excitons in Cu_2O were obtained by experimental high resolution studies in external fields and by pump-probe measurements.

In Chapter 4 many aspects of the behavior of Rydberg excitons in both external electric and magnetic fields were studied. The focus laid on the evaluation of scaling laws for various characteristic quantities in dependence on the principal quantum number n. It was possible to determine scaling laws for the width of exciton multiplets by the activation of dark exciton states in an electric field. Next, the polarizability of both S and P excitons was investigated separately and the resonance field strength, where excitons from adjacent multiplets come into resonance and form an avoided crossing as well as their energy separation at this point was found to be in agreement with theoretical predictions. Finally, the electric field strength for ionization of Rydberg excitons was found to follow an n dependence as well. In an external magnetic field, the field strength for the transition from Coulomb-bound states to Landau level transitions as well as the resonance field strength of crossings between adjacent multiplets was evaluated. Interestingly, most of the scaling laws found for excitons are in agreement with known scaling laws for atoms.

The validation of these scaling laws shown in this thesis is of importance for the description of Rydberg excitons with high principal quantum numbers n in external electric and magnetic fields, where the density of states becomes too high to use a microscopic theory for the description of the system. Hence, these results lay the basis for future studies of Rydberg excitons with high principal quantum numbers n in external fields. Here, one can think about the investigation of excitonic states with giant electric dipole moments and long lifetimes, which have been predicted theoretically in crossed electric and magnetic fields [Kur+17]. Further, the study of exceptional points is a promising field as these have also been predicted theoretically to be observable in Cu_2O in combined electric and magnetic fields [Fel+16], but have not been observed experimentally yet.

Rydberg excitons are found to be not only sensitive to external fields but also to extremely low densities of electron-hole plasmas, as presented in Chapter 5. The injection of free electron-hole pairs by an additional pump laser with an energy above the band gap leads to a lowering of the band gap and the corresponding disappearance of exciton lines into the continuum, which is known as the Mott effect. The presented spectra allowed for the first time for the investigation of the Mott effect in a semiconductor for highly excited Rydberg states and with unprecedented resolution. A theory based on the Debye model was used for an estimation of the relevant plasma densities and the description of the basic observations such as the reduction of the band gap and decreasing oscillator strength in

dependence on the plasma density. The plasma densities that lead to the disappearance of the highest Rydberg excitons were found to be extremely low on the order of 0.01 μm^{-3}. Hence, Rydberg excitons might serve as ultrasensitive probes of unbound electron-hole pairs in their environment. Further, their high sensitivity can be used in future studies in the field of low-density plasma physics to get a deeper understanding of the exact interaction mechanisms of excitons with a surrounding plasma and to improve the theoretical many-body models by comparison with experimental data [Sem+19].

Even without external illumination, the band gap was found to be shifted below its nominal value, finally limiting the highest observable principal quantum number. In this regard, the experimental parameter space spanned by temperature and excitation power was investigated to find the highest observable Rydberg exciton. Temperatures down to 50 mK and laser powers on the order of nW were applied. The Rydberg series that was so far limited to $n_{\mathrm{max}} = 25$ could be extended to $n_{\mathrm{max}} = 28$, the highest Rydberg exciton state ever observed. However, the extension of the Rydberg series is found to be neither limited by thermal dissociation nor by the excitation power. Instead, the limitation stems from the quality of the sample under consideration, so far attributed to the amount of charged impurities in the crystal, which is in line with recent calculations [Krü+20]. Thus, the observation of even higher Rydberg excitons with principal quantum numbers larger than $n_{\mathrm{max}} = 28$ requires extremely pure samples with impurity densities below 0.01 μm^{-3}, which represents a challenging task for crystal growth.

Besides the investigation of the interaction with an electron-hole plasma, a comprehensive study of the interactions among Rydberg excitons of different principal quantum numbers was presented in Chapter 6. Various pump-probe experiments were discussed in which a pump laser resonantly excites Rydberg excitons of a certain quantum number n' and the response of excitons with different quantum numbers n is probed. Distinct spectral signatures are observed in the optical response of the probed states that stem from strong dipole-dipole interactions. While first indications of these were already found in Ref. [Kaz+14], the data presented here additionally allows one to identify the exact type of dipole-dipole interaction: It is found to be of long-range van der Waals-type rather than short-range Förster-type and of mostly repulsive character.

For Rydberg atoms, strong dipole-dipole interactions are widely discussed as promising mechanisms to enable a variety of applications in the field of quantum simulations [Saf+10] and nonlinear quantum optics [Mur+16]. The identification of the exact type of interaction potential reported here is a first step on the way to transfer those concepts from systems of ultracold atoms to a Rydberg system in a semiconductor.

Even in the case of plasma excitation, indications for exciton-exciton interactions were identified, as the overall line shape was found to be similar in both cases. Here, the formation of unbound electron-hole pairs into Rydberg excitons might play a role. As the experiments reported in this thesis are limited to CW-spectroscopy, future studies with time-resolved pump-probe experiments might give a deeper insight into the relaxation dynamics of the system.

Appendix

A.1 Energies of all states

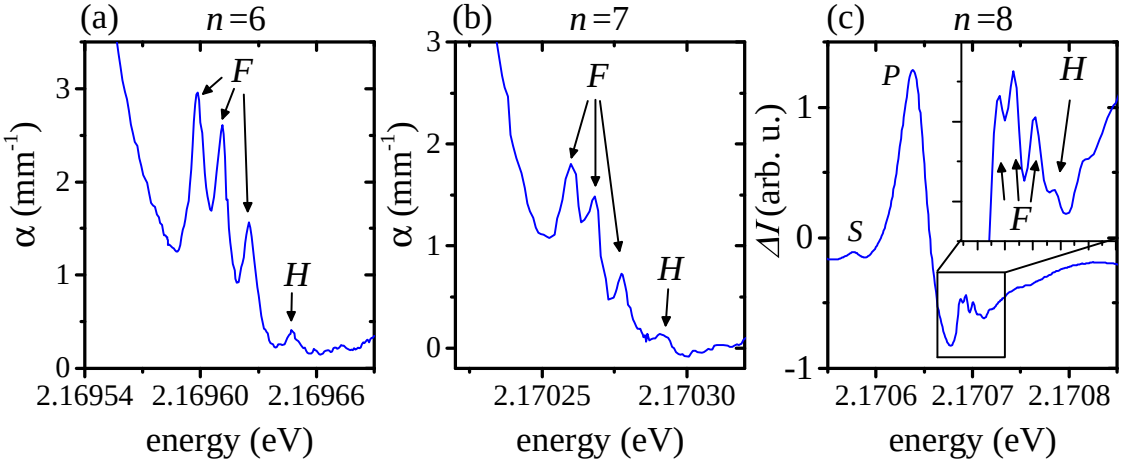

Figure A.1 Absorption spectra of high angular momentum excitons. In pure absorption, $n = 6$ (a) and $n = 7$ (b) H excitons are observable at a temperature of 760 mK. (c) The detection of differential transmission allows for the observation of $n = 8$ F and H excitons.

Table A.1 summarizes all experimentally found resonance energies of the yellow series, that are shown in Fig. 2.5 in Sec. 2.5. The $1S$ Para-exciton can be observed by the application of an magnetic field or stress. The $1S$ Ortho-exciton and the P excitons are taken from Fig. 2.3 and the measurements at temperatures below 1 K, reported in Sec. 5.3. SHG-data from Ref. [Mun+18] is used to determine the energies of the green $1S$ and the yellow $2S$ state. S and D excitons with $n > 2$ can be activated by the application of an external electric field and their dispersions in second derivative spectra can be traced back to zero field, as explained in Sec. 4.1.

The high angular momentum states, namely F and H states, were investigated in Ref. [The+15] by the application of small electric fields. To highlight the observability of high angular momentum states without external fields, the relevant absorption spectra are shown in Fig. A.1. H excitons with principal quantum number $n = 6$ and $n = 7$ are observable in pure absorption at temperatures below 1 K. For $n = 8$, they can still be observed in differential transmission spectra, obtained with a Lock-In amplifier in a pump probe scheme, as explained in Chapters 3 or 6. G-shell states were observed for $n = 5$ in Ref. [Hec+17a]. For higher n, their energy is estimated to lie between the highest F and the H state.

Table A.1 Energies of excitons in the yellow series grouped by angular momenta in eV. Green $1S$ energy: 2.15439 eV [3].

n	S	P [4]	$D_{5/2}$ [5]	D_3 [5]	F_{av} [6]	G [7]	H [8]
1	2.02066 (Para) [1] 2.03279 (Ortho) [2]						
2	2.13750 [3]	2.148022					
3	2.16027 [5]	2.161326	2.16183 2.16202	2.16305			
4	2.16555 [5]	2.166093	2.16629 2.16638	2.16677	2.166547		
5	2.16801 [5]	2.168280		2.16865	2.168525	2.168557	
6	2.16931 [5]	2.169478		2.16971	2.169611	2.169636	2.169647
7	2.17009 [5]	2.170186		2.17032	2.170267	2.170285	2.170292
8	2.17058 [5]	2.170637		2.17073	2.170695	2.170705	2.170708
9	2.17090 [5]	2.170946		2.17104	2.170995		
10	2.17113 [5]	2.171165			2.171189		
11		2.171327			2.171347		
12		2.171448			2.171467		
13		2.171543					
14		2.171618					
15		2.171678					
16		2.171727					
17		2.171768					
18		2.171801					
19		2.171830					
20		2.171854					
21		2.171874					
22		2.171893					
23		2.171908					
24		2.171922					
25		2.171934					
26		2.171944					
27		2.171954					
28		2.171965					

[1] Γ_2^+ Para-exciton, value from [Bra10].
[2] Γ_5^+ Ortho-exciton, fit to data in Fig. 2.3.
[3] From SHG-spectrum shown in[Mun+18].
[4] n = 2-22 from Fig. 2.3 at 1.35 K, n = 23-28 from Fig. 5.12 at 110 mK. Fitted with fitting routine described in A.3.
[5] From white light spectra (second derivative) shown in [Hec+17a].
[6] Mean value of three F exciton peaks for each n. From [The+15].
[7] $n = 5$: Estimated from Fig. 2b in [Hec+17a]. n = 6-8: Estimated to be centered between highest of three nF states and nH state.
[8] From Fig. A.1.

A.2 Background trace

The background in Fig. 2.3 in Sec. 2.5 is described by Eq. (2.42). The obtained fit parameters shall be given here, in Tab. A.2.

Table A.2 Parameters to describe the background shown in Fig. 2.3.

Parameter	Value	Unit
$c_{1Sy}^{\Gamma_3^-}$	28.00	$\mathrm{mm}^{-1}(\sqrt{\mathrm{eV}})^{-1}$
$c_{1Sy}^{\Gamma_4^-}$	10.00	$\mathrm{mm}^{-1}(\sqrt{\mathrm{eV}})^{-1}$
$c_{2Sy}^{\Gamma_3^-}$	51.00	$\mathrm{mm}^{-1}(\sqrt{\mathrm{eV}})^{-1}$
$c_{1Sg}^{\Gamma_3^-}$	$2.6{*}c_{1Sy}^{\Gamma_3^-}$	$\mathrm{mm}^{-1}(\sqrt{\mathrm{eV}})^{-1}$
c_{U}	5.5	mm^{-1}
E_{U}	170	μeV
$\tilde{E}_{\mathrm{g}}$	2.1719050	eV
c_{cont}	105	mm^{-1}

A.3 Fitting routine

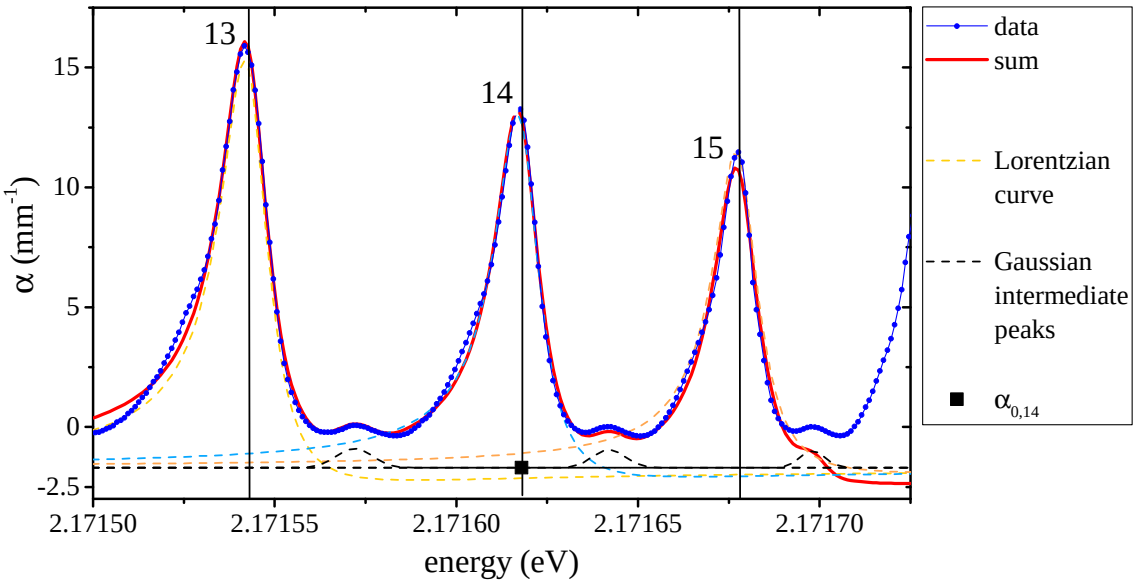

Figure A.2 The blue curve shows the absorption spectrum around $n = 14$ with subtracted background. The red curve shows the sum over all single peaks using three asymmetric Lorentzians with free fit parameters (color dashed lines) and three Gaussian peaks with fixed parameters (black dashed lines). The obtained offset α_{0n} for $n = 14$ has a negative value.

In the following, the fitting routine, used to fit the absorption spectra, is explained. The procedure was suggested by Prof. Stolz from University of Rostock. Figure A.2 shows an example of a fit to the absorption lines of $n = 13$, $n = 14$ and $n = 15$. As described in Sec. 2.5, a single absorption peak is described by an asymmetric Lorentzian with an area O_n, width Γ_n, asymmetry parameter q_n and resonance energy E_n, see Eq. (2.43). However, especially in the regime $n > 10$, the tails of adjacent Lorentzian curves overlap and contribute to a significant background, as shown by the dashed lines in Fig. A.2. Hence, to obtain meaningful fit parameters for an absorption peak, the influence of both adjacent peaks has to be taken into account by fitting three peaks at the same time. In addition, the intermediate peaks are taken into account by Gaussian curves, each located on the high energy side of a corresponding Lorentzian peak. For the Gaussian curves, the parameters of area ($O_{\mathrm{G},i}$), width ($w_{\mathrm{G},i}$) and energy ($E_{\mathrm{G},i}$) are fixed and chosen such that they reproduce the intermediate peaks best. They are shown by black dashed lines. The parameters describing the Lorentzian curves enter the fitting routine as variable fit parameters. In addition, a variable offset $\alpha_{0,n}$ is used. The fit function then reads

$$\alpha_{\mathrm{fit}}(n) = \alpha_{0,n} + \sum_{i=n-1}^{n+1} + \frac{O_i}{\pi} \frac{\frac{\Gamma_i}{2} + 2q_i\,(E - E_i)}{\left(\frac{\Gamma_i}{2}\right)^2 + (E - E_i)^2} + O_{\mathrm{G},i} \exp\left(-\frac{E - E_{\mathrm{G},i}}{2w_{\mathrm{G},i}}\right)^2 . \qquad \text{(A.1)}$$

It is fitted to the absorption spectrum with subtracted background, shown by the blue curve

in Fig. A.2. In this case, the variable offset is found to be negative in the case for $n = 14$, as indicated by the black square and the resonance energies are slightly shifted to the high energy side of each peak, shown by the vertical lines. The total fit function is shown by the red line, in good agreement with the data for the middle peak. Hence, the obtained fit parameters are used for the middle of the three peaks.

List of Symbols

symbol	meaning
α	absorption coefficient
a^{B}	exciton Bohr radius
$a_{\mathrm{H}}^{\mathrm{B}}$	hydrogen Bohr radius
$a_{\mathrm{eff}}^{\mathrm{B}}$	effective exciton Bohr radius
$a_{\mathrm{l}} = 4.26$ Å	lattice constant
$\mathbf{A}$	vector potential
$\beta(n, n')$	slope of linear response
$\tilde{\beta}(n, n')$	corrected slope of linear response
$B = \lvert\mathbf{B}\rvert$	magnetic field strength
$\Gamma_i^{\pm}$	irreducible representation according to the O_{h} symmetry group
$\tilde{\Gamma} = \Gamma - 2i\delta$	-
Γ; Γ_n	FWHM of exciton with quantum number n
c	speed of light
$C_3(n, n')$	Förster coefficient
$C_6(n, n')$	van der Waals coefficient
δ	detuning from resonance energy
$\delta_{n,l}$	quantum defect
δ_{ij}^K	Kronecker symbol
Δ_{a}	averaged self-energy of electron ($a = e$) or hole ($a = h$)
Δ	measured band gap shift
Δ_{eh}; Δ_0	laser induced and inherent band gap shift
$\Delta_{n,k}$	energy splitting of excitons with quantum numbers n and k
Δ_{so}	valence band split-off energy
d	sample thickness
$d_n = \lvert\mathbf{d}_n\rvert$	electric dipole moment of exciton with quantum number n
ϵ_0	vacuum permittivity
$\epsilon_s = 7.5$	static dielectric constant
$\mathcal{E} = \lvert\boldsymbol{\mathcal{E}}\rvert$	electric field amplitude
e	elementary charge
$\hat{\mathbf{e}}$	unit vector of polarization
E_{pump}	pump laser energy
E_n	resonance energy of exciton with quantum number n

symbol	meaning
$E_{n,n'}$	pair state energy of excitons with quantum numbers n and n'
E_{U}	Urbach tail width
E_{g}	nominal band gap energy
$\tilde{E}_{\mathrm{g}} = E_{\mathrm{g}} + \Delta$	shifted band gap energy observable in the experiment
E_X	total exciton energy
E_{kin}	excitonic kinetic energy
$E^{\mathrm{b}}_{n,l}$	excitonic binding energy
$E^{\mathrm{b,sc}}_{n}$	binding energy of an exciton in a plasma
f_n	oscillator strength of exciton with quantum number n
g; g_n	light-matter coupling strength
$\hbar$	reduced Planck's constant
$h(\delta = 0)$; $h_n(\delta = 0)$	peak height on resonance in absorption
$H_{\mathrm{OD}} = h(\delta = 0)d$	peak height on resonance in optical density
$H_{\mathrm{e},0}$	single particle Hamiltonian for the electron without perturbation
H_{a}	single particle Hamiltonian of electron ($a = e$) or hole ($a = h$)
$H^{\mathrm{P}}_{\mathrm{a}}$	Hamiltonian of single particle in a plasma
H_0	excitonic Hamiltonian in spherical approximation
H_{so}	spin-orbit coupling term of the excitonic Hamiltonian
H_{d}	H_{d} term of the excitonic Hamiltonian
H_{exch}	exchange interaction term of the excitonic Hamiltonian
I_{T}	transmitted intensity
I_0	light intensity without absorption
ΔI	differential transmission
$\mathbf{I}$	valence band quasi spin
κ	inverse screening length
k_B	Boltzmann constant
$\mathbf{K} = \mathbf{k}_{\mathrm{e}} + \mathbf{k}_{\mathrm{h}}$	exciton center-of-mass wave vector
$k = \lvert\mathbf{k}\rvert = \frac{2\pi}{\lambda}$	wave vector of incident light
λ	wavelength of light
Λ	thermal wavelength
$\mathbf{l}$	angular momentum operator
l	angular momentum quantum number
$l_{c,n}$	magnetic length
$\mu^{-1} = m_{\mathrm{e}}^{-1} + m_{\mathrm{h}}^{-1}$	reduced mass
m	magnetic quantum number
m_0	free electron mass

symbol	**meaning**
$m_\mathrm{e} = 0.985\ m_0$	electron mass
$m_\mathrm{h} = 0.575\ m_0$	hole mass
$M = m_\mathrm{e} + m_\mathrm{h} = 1.56\ m_0$	total mass
n	principal quantum number
n_eff	effective principal quantum number
$\bar{n}$	index of refraction
OD	optical density
O_n	peak area
$\mathbf{p}_\mathrm{a}$	momentum of electron ($a = e$) and hole ($a = h$)
$p = \lvert\mathbf{p}\rvert$	momentum of the relative motion of electron and hole
P_pump	pump laser power
q_n	asymmetry parameter
ρ_eh	electron-hole density
ρ_p	pump exciton density
$r_{n,l}$	exciton radius
$\mathbf{r}_\mathrm{e}$, $\mathbf{r}_\mathrm{h}$	coordinates of electron and hole
$r = \lvert\mathbf{r}\rvert = \lvert\mathbf{r}_\mathrm{e} - \mathbf{r}_\mathrm{h}\rvert$	distance between electron and hole.
$\mathbf{R} = (m_\mathrm{e}\mathbf{r}_\mathrm{e} + m_\mathrm{h}\mathbf{r}_\mathrm{h})/(m_\mathrm{e} + m_\mathrm{h})$	center of mass
$\overline{R} = \lvert\mathbf{R}\rvert = \lvert R - R'\rvert$	distance between two excitons at $\mathbf{R}$ and $\mathbf{R}'$
$R_\mathrm{B} = \lvert\mathbf{R}_\mathrm{B}\rvert$	blockade radius
Ry; Ry_H	excitonic and hydrogenic Rydberg energies
$\mathbf{s}_\mathrm{e}$; $\mathbf{s}_\mathrm{h}$	electron spin and hole spin
T_sc	plasma screening temperature
T_Crystal	crystal temperature
V_B	blockade volume
ω	frequency of light
ω_n	resonance frequency of exciton with quantum number n
ω_c	cyclotron resonance
$x = \delta/\Gamma$	normalized detuning
$\hat{X}$; $\hat{X}^\dagger$	exciton annihilation and creation operator
Φ^env_{nlm}	envelope function of the electron-hole motion
Ψ_{nlm}	wave function of excitons with quantum numbers n, l and m

Bibliography

[Age+74] V. T. Agekyan, B. S. Monozon, and I. P. Shiryapov. "The Fine Structure of Wannier-Mott Excitons in a Cubic Crystal and Its Behaviour in an Electric Field." *physica status solidi (b)* **66** (1974), pp. 359–370.

[Age77] V. T. Agekyan. "Spectroscopic Properties of Semiconductor Crystals with Direct Forbidden Energy Gap." *physica status solidi (a)* **43** (1977), pp. 11–42.

[Aro+78] A. G. Aronov and A. S. Ioselevich. "Effect of electric field on exciton absorption." *Soviet Journal of Experimental and Theoretical Physics* **47** (1978), p. 548.

[Aßm+16] M. Aßmann, J. Thewes, D. Fröhlich, and M. Bayer. "Quantum chaos and breaking of all anti-unitary symmetries in Rydberg excitons." *Nature Materials* **15** (2016), pp. 741–745.

[Bal+73] A. Baldereschi and N. O. Lipari. "Spherical Model of Shallow Acceptor States in Semiconductors." *Physical Review B* **8** (1973), p. 2697.

[Bal+74] A. Baldereschi and N. O. Lipari. "Cubic contributions to the spherical model of shallow acceptor states." *Physical Review B* **9** (1974), p. 1525.

[Bet+57] H. A. Bethe and E. E. Salpeter. *Quantum Mechanics of One and Two Electron Atoms*. Berlin: Springer, 1957.

[Bra+07] J. Brandt, D. Fröhlich, C. Sandfort, M. Bayer, H. Stolz, and N. Naka. "Ultranarrow Optical Absorption and Two-Phonon Excitation Spectroscopy of Cu_2O Paraexcitons in a High Magnetic Field." *Physical Review Letters* **99** (2007), p. 217403.

[Bra10] J. C. Brandt. "Interactions of 1S Exzitons in Cu_2O: A High Resolution Spectroscopy Study." PhD thesis. TU Dortmund, 2010.

[Bro+16] A. Browaeys, D. Barredo, and T. Lahaye. "Experimental investigations of dipole– dipole interactions between a few Rydberg atoms." *Journal of Physics B: Atomic, Molecular and Optical Physics* **49** (2016), p. 152001.

[Bro+20] A. Browaeys and T. Lahaye. "Many-body physics with individually controlled Rydberg atoms." *Nature Physics* **16** (2020), pp. 132–142.

[Coh+07] C. Cohen-Tannoudji, B. Diu, and F. Laloë. *Quantum Mechanics*. 2 vols. de Gruyter, 2007.

[Dah+66] J. Dahl and A. Switendick. "Energy Bands in Cuprous Oxide." *Journal of Physics and Chemistry of Solids* **27** (1966), pp. 931–942.

[Das+03] G. Dasbach, D. Fröhlich, H. Stolz, R. Klieber, D. Suter, and M. Bayer. "Wave-Vector-Dependent Exciton Exchange Interaction." *Physical Review Letters* **91** (2003), p. 107401.

[Das+04] G. Dasbach, D. Fröhlich, R. Klieber, D. Suter, M. Bayer, and H. Stolz. "Wavevector-dependent exchange interaction and its relevance for the effective exciton mass in Cu_2O." *Physical Review B* **70** (2004), p. 045206.

[Das+05] G. Dasbach, D. Fröhlich, H. Stolz, R. Klieber, D. Suter, and M. Bayer. "Anisotropic effective exciton mass in Cu_2O." *physica status solidi (c)* **2** (2005), pp. 886–889.

[Dau+66] A. Daunois, J. L. Deiss, and B. Meyer. "Étude spectrophotométrique de l'absorption bleue et violette de Cu_2O." *Journal de Physique* **27** (1966), pp. 142–146.

[Dei+73] J. L. Deiss and A. Daunois. "Modulated exciton spectroscopy." *Surface Science* **37** (1973), pp. 804–827.

[Den+02] S. Denev and D. W. Snoke. "Stress dependence of exciton relaxation processes in Cu_2O." *Physical Review B* **65** (2002), p. 085211.

[Dow+72] J. D. Dow and D. Redfield. "Toward a Unified Theory of Urbach's Rule and Exponential Absorption Edges." *Physical Review B* **5** (1972), pp. 594–610.

[Ebe+76] W. Ebeling, W. D. Kraeft, and D. Kremp. *Theory of Bound States and ionization Equilibrium in Plasmas and Solids*. Ergebnisse der Plasmaphysik und der Gaselektronik. Berlin: Akademie-Verlag, 1976.

[Ego+77] V. D. Egorov, G. O. Müller, H. H. Weber, R. Zimmermann, A. F. Dite, V. G. Lysenko, V. I. Revenko, and V. B. Timofeev. "Spontaneous and stimulated emission from e-h plasmas in CdS." *Il Nuovo Cimento B Series 11* **39** (1977), pp. 628–633.

[Ell57] R. J. Elliott. "Intensity of Optical Absorption by Excitons." *Physical Review* **108** (1957), p. 1384.

[Ell61] R. J. Elliott. "Symmetry of Excitons in Cu_2O." *Physical Review* **124** (1961), p. 340.

[Fan61] U. Fano. "Effects of Configuration Interaction on Intensities and Phase Shifts." *Physical Review* **124** (1961), pp. 1866–1878.

[Feh+82] G. W. Fehrenbach, W. Schäfer, J. Treusch, and R. G. Ulbrich. "Transient Optical Spectra of a Dense Exciton Gas in a Direct-Gap Semiconductor." *Physical Review Letters* **49** (1982), pp. 1281–1284.

[Fel+16] M. Feldmaier, J. Main, F. Schweiner, H. Cartarius, and G. Wunner. "Rydberg systems in parallel electric and magnetic fields: an improved method for finding exceptional points." *Journal of Physics B: Atomic, Molecular and Optical Physics* **49** (2016), p. 144002.

[Fös18] F. Föst. "Interactions of Rydberg Excitons in Cuprous Oxide." Master's thesis. TU Dortmund, 2018.

[Fre+09] M. French, R. Schwartz, H. Stolz, and R. Redmer. "Electronic band structure of Cu_2O by spin density functional theory." *Journal of Physics: Condensed Matter* **21** (2009), p. 015502.

[Fre+17] M. Freitag, J. Heckötter, M. Bayer, and M. Aßmann. "Role of phonons in the quantum chaos of Rydberg excitons." *Physical Review B* **95** (2017), p. 155204.

[Fre16] M. Freitag. “Hochauflösende Laserspektroskopie an 1S- und Rydberg-Exzitonen in Cu_2O in statischen und optischen Feldern.” Master’s thesis. TU Dortmund, 2016.

[Fre31] J. Frenkel. “On the Transformation of Light into Heat in Solids. I.” *Physical Review* **37** (1931), p. 17.

[Gal+08] T. F. Gallagher and P. Pillet. “Dipole–Dipole Interactions of Rydberg Atoms.” *Advances in Atomic, Molecular, and Optical Physics*. **56**. Elsevier, 2008, pp. 161–218.

[Gal94] T. F. Gallagher. *Rydberg Atoms*. Cambridge: Cambridge University Press, 1994.

[Gro+12] R. Gross and A. Marx. *Festkörperphysik*. München: Oldenbourg Wissenschaftsverlag, 2012.

[Gro+52] E. F. Gross and N. A. Karryev. *Dokl. Akad. Nauk SSSR* **84** (1952), pp. 471–474.

[Gro56] E. F. Gross. “Optical Spectrum of Excitons in the Crystal Lattice.” *Il Nuovo Cimento* **3** (1956), pp. 672–701.

[Gro62] E. F. Gross. “Excitons and their motion in crystal lattices.” *Soviet Physics Uspekhi* **5** (1962), p. 195.

[Grü+16] P. Grünwald, M. Aßmann, J. Heckötter, D. Fröhlich, M. Bayer, H. Stolz, and S. Scheel. “Signatures of Quantum Coherences in Rydberg Excitons.” *Physical Review Letters* **117** (2016), p. 133003.

[Gru06] M. Grundmann. *The Physics of Semiconductors: An Introduction including Devices and Nanophysics*. Berlin; New York: Springer, 2006.

[Hay+50] M. Hayashi and K. Katsuki. “Absorption Spectrum of Cuprous Oxide.” *Journal of the Physical Society of Japan* **5** (1950), pp. 380–381.

[Hay+52] M. Hayashi and K. Katsuki. “Hydrogen-Like Absorption Spectrum of Cuprous Oxide.” *Journal of the Physical Society of Japan* **7** (1952), pp. 599–603.

[Hec+] J. Heckötter, V. Walther, S. Scheel, M. Bayer, T. Pohl, and M. Aßmann. “Experimental demonstration of giant Rydberg interactions in Cuprous Oxide.” *unpublished* ().

[Hec+17a] J. Heckötter, M. Freitag, D. Fröhlich, M. Aßmann, M. Bayer, M. A. Semina, and M. M. Glazov. “High-resolution study of the yellow excitons in Cu_2O subject to an electric field.” *Physical Review B* **95** (2017), p. 035210.

[Hec+17b] J. Heckötter, M. Freitag, D. Fröhlich, M. Aßmann, M. Bayer, M. A. Semina, and M. M. Glazov. “Scaling laws of Rydberg excitons.” *Physical Review B* **96** (2017), p. 125142.

[Hec+18a] J. Heckötter, M. Freitag, M. Aßmann, D. Fröhlich, M. Bayer, P. Grünwald, and S. Scheel. “Critical Dependence of the Excitonic Absorption in Cuprous Oxide on Experimental Parameters.” *Physics of the Solid State* **60** (2018), pp. 1618–1624.

[Hec+18b] J. Heckötter, M. Freitag, D. Fröhlich, M. Aßmann, M. Bayer, P. Grünwald, F. Schöne, D. Semkat, H. Stolz, and S. Scheel. "Rydberg Excitons in the Presence of an Ultralow-Density Electron-Hole Plasma." *Physical Review Letters* **121** (2018), p. 097401.

[Hec+18c] J. Heckötter, M. Freitag, D. Fröhlich, M. Aßmann, M. Bayer, M. A. Semina, and M. M. Glazov. "Dissociation of excitons in Cu_2O by an electric field." *Physical Review B* **98** (2018), p. 035150.

[Hec+18d] J. Heckötter, M. Freitag, D. Fröhlich, M. Aßmann, M. Bayer, M. A. Semina, and M. M. Glazov. "Influence of the Wavefunction Distribution on Exciton Dissociation in Electric Field." *Physics of the Solid State* **60** (2018), pp. 1506–1509.

[Hec+18e] J. Heckötter, J. Thewes, D. Fröhlich, M. Aßmann, and M. Bayer. "Landau-Level Quantization of the Yellow Excitons in Cuprous Oxide." *Physics of the Solid State* **60** (2018), pp. 1625–1628.

[Hec+20] J. Heckötter, D. Janas, R. Schwartz, M. Aßmann, and M. Bayer. "Experimental limitation in extending the exciton series in Cu_2O towards higher principal quantum numbers." *Physical Review B* **101** (2020), p. 235207.

[Hec15] J. Heckötter. "Stark-Effekt-Messungen an Rydberg-Exzitonen in Cu_2O." Master's thesis. TU Dortmund, 2015.

[Hod+76] J. W. Hodby, T. E. Jenkins, C. Schwab, H. Tamura, and D. Trivich. "Cyclotron resonance of electrons and of holes in cuprous oxide, Cu_2O." *Journal of Physics C: Solid State Physics* **9** (1976), p. 1429.

[Höf+14] S. Höfling and A. Kavokin. "A historic experiment redesigned." *Nature* **514** (2014), pp. 313–314.

[Hög+05] G. B. H. von Högersthal, G. Dasbach, D. Fröhlich, M. Kulka, H. Stolz, and M. Bayer. "Dynamic band gap shifts and magneto-absorption of Cu_2o." *Journal of Luminescence* **112** (2005), pp. 25–29.

[Ito+75] T. Itoh and S.-i. Narita. "Analysis of Wavelength Derivative Spectra of Exciton in Cu_2O." *Journal of the Physical Society of Japan* **39** (1975), pp. 140–147.

[Ito+98] T. Ito, T. Kawashima, H. Yamaguchi, T. Masumi, and S. Adachi. "Optical Properties of Cu_2O Studied by Spectroscopic Ellipsometry." *Journal of the Physical Society of Japan* **67** (1998), pp. 2125–2131.

[Jak+00] D. Jaksch, J. I. Cirac, P. Zoller, S. L. Rolston, R. Côté, and M. D. Lukin. "Fast Quantum Gates for Neutral Atoms." *Physical Review Letters* **85** (2000), pp. 2208–2211.

[Jan17] D. Janas. "Rydberg-Exzitonen in Cu_2O bei ultratiefen Temperaturen." Bachelor's thesis. Dortmund: TU Dortmund, 2017.

[Kav+97] G. M. Kavoulakis, Y.-C. Chang, and G. Baym. "Fine structure of excitons in Cu_2O." *Physical Review B* **55** (1997), p. 7593.

[Kaz+14] T. Kazimierczuk, D. Fröhlich, S. Scheel, H. Stolz, and M. Bayer. "Giant Rydberg excitons in the copper oxide Cu_2O." *Nature* **514** (2014), pp. 343–347.

[Kha+17] M. Khazali, K. Heshami, and C. Simon. “Single-photon source based on Rydberg exciton blockade.” *Journal of Physics B: Atomic, Molecular and Optical Physics* **50** (2017), p. 215301.

[Kit+17] T. Kitamura, M. Takahata, and N. Naka. “Quantum number dependence of the photoluminescence broadening of excitonic Rydberg states in cuprous oxide.” *Journal of Luminescence* **192** (2017), pp. 808–813.

[Kle+80] L. Kleinman and K. Mednick. “Self-consistent energy bands of Cu_2O.” *Physical Review B* **21** (1980), pp. 1549–1553.

[Kli07] C. F. Klingshirn. *Semiconductor Optics*. Berlin; New York: Springer, 2007.

[Kom+80] I. V. Komarov, T. P. Grozdanov, and R. K. Janev. “Influence of the atomic core on the Stark structure of alkali atom Rydberg states.” *Journal of Physics B: Atomic and Molecular Physics* **13** (1980), pp. 573–576.

[Kos+66] G. F. Koster, J. O. Dimmock, R. G. Wheeler, and H. Satz. *Properties Of The Thirty-Two Point Groups*. M.I.T. Press, Cambridge, Massachusetts, 1966.

[Kra+86] W. D. Kraeft, D. Kremp, W. Ebeling, and G. Röpke. *Quantum Statistics of Charged Particle Systems*. Berlin; London: Akademie-Verlag and Plenum Press, 1986.

[Kre+05] D. Kremp, M. Schlanges, and W.-D. Kraeft. *Quantum Statistics of Nonideal Plasmas*. Berlin; Heidelberg; New York: Springer, 2005.

[Krü+20] S. O. Krüger, H. Stolz, and S. Scheel. “Interaction of charged impurities and Rydberg excitons in cuprous oxide.” *Physical Review B* **101** (2020), p. 235204.

[Kur+17] M. Kurz, P. Grünwald, and S. Scheel. “Excitonic giant-dipole potentials in cuprous oxide.” *Physical Review B* **95** (2017), p. 245205.

[Kuw+77] G. Kuwabara, M. Tanaka, and H. Fukutani. “Optical absorption due to paraexciton of Cu_2O.” *Solid State Communications* **21** (1977), pp. 599–601.

[Lan+77] L. D. Landau and E. M. Lifshitz. *Quantum Mechanics: Non-Relativistic Theory*. Oxford: Butterworth-Heinemann, 1977.

[Luk+01] M. D. Lukin, M. Fleischhauer, R. Cote, L. M. Duan, D. Jaksch, J. I. Cirac, and P. Zoller. “Dipole Blockade and Quantum Information Processing in Mesoscopic Atomic Ensembles.” *Physical Review Letters* **87** (2001), p. 037901.

[Mad+98] O. Madelung, U. Rössler, and M. Schulz, eds. *Landolt-Börnstein - Group III Condensed Matter*. **41C**. Berlin; Heidelberg: Springer-Verlag, 1998.

[Man+10] G. Manzke, D. Semkat, F. Richter, D. Kremp, and K. Henneberger. “Mott transition versus Bose-Einstein condensation of excitons.” *Journal of Physics: Conference Series* **210** (2010), p. 012020.

[Man+12] G. Manzke, D. Semkat, and H. Stolz. “Mott transition of excitons in GaAs-GaAlAs quantum wells.” *New Journal of Physics* **14** (2012), p. 095002.

[Mar+99] M. Marinescu and H. R. Sadeghpour. “Long-range potentials for two-species alkali-metal atoms.” *Physical Review A* **59** (1999), pp. 390–404.

[Mat+96] H. Matsumoto, K. Saito, M. Hasuo, S. Kono, and N. Nagasawa. "Revived Interest on Yellow-Exciton Series in Cu_2O: An Experimental Aspect." *Solid State Communications* **97** (1996), pp. 125–129.

[Mer+74] I. A. Merkulov and V. I. Pere. "Influence of exciton effect on electroabsorption in semiconductors." *Zh. Eksp. Theor. Fiz* **66** (1974), p. 2314.

[Mot61] N. F. Mott. "The transition to the metallic state." *Philosophical Magazine* **6** (1961), pp. 287–309.

[Mot68] N. F. Mott. "Metal-Insulator Transition." *Reviews of Modern Physics* **40** (1968), pp. 677–683.

[Mun+18] J. Mund, D. Fröhlich, D. R. Yakovlev, and M. Bayer. "High-resolution second harmonic generation spectroscopy with femtosecond laser pulses on excitons in Cu_2O." *Physical Review B* **98** (2018), p. 085203.

[Mur+16] C. Murray and T. Pohl. "Quantum and Nonlinear Optics in Strongly Interacting Atomic Ensembles." *Advances In Atomic, Molecular, and Optical Physics*. **65**. Elsevier, 2016, pp. 321–372.

[Nak+02] N. Naka and N. Nagasawa. "Two-photon diagnostics of stress-induced exciton traps and loading of 1s-yellow excitons in Cu_2O." *Physical Review B* **65** (2002), p. 075209.

[Nak+12] N. Naka, I. Akimoto, M. Shirai, and K.-i. Kan'no. "Time-resolved cyclotron resonance in cuprous oxide." *Physical Review B* **85** (2012), p. 035209.

[Nik+61] S. Nikitine, J. B. Grun, and M. Sieskind. "Etude spectrophotometrique de la serie jaune de Cu_2O aux basses temperatures." *Journal of Physics and Chemistry of Solids* **17** (1961), pp. 292–300.

[Pau+09] S. Paul and Y. K. Ho. "Hydrogen atoms in Debye plasma environments." *Physics of Plasmas* **16** (2009), p. 063302.

[Pri+12] J. D. Pritchard, K. J. Weatherill, and C. S. Adams. "Nonlinear optics using cold rydberg atoms." *Annual Review of Cold Atoms and Molecules*. **1**. World Scientific, 2012, pp. 301–350.

[Rai+81] J. M. Raimond, G. Vitrant, and S. Haroche. "Spectral line broadening due to the interaction between very excited atoms: 'the dense Rydberg gas'." *Journal of Physics B: Atomic and Molecular Physics* **14** (1981), pp. 655–660.

[Rav+14] S. Ravets, H. Labuhn, D. Barredo, L. Béguin, T. Lahaye, and A. Browaeys. "Coherent dipole-dipole coupling between two single Rydberg atoms at an electrically-tuned Förster resonance." *Nature Physics* **10** (2014), pp. 914–917.

[Rid82] B. K. Ridley. *Quantum processes in semiconductors*. Oxford: Oxford University Press, 1982.

[Rob83] J. Robertson. "Electronic structure and x-ray near-edge core spectra of Cu_2O." *Physical Review B* **28** (1983), pp. 3378–3385.

[Rog+70] F. J. Rogers, H. C. Graboske, and D. J. Harwood. "Bound Eigenstates of the Static Screened Coulomb Potential." *Physical Review A* **1** (1970), pp. 1577–1586.

[Rom+18] P. Rommel, F. Schweiner, J. Main, J. Heckötter, M. Freitag, D. Fröhlich, K. Lehninger, M. Aßmann, and M. Bayer. "Magneto-Stark effect of yellow excitons in cuprous oxide." *Physical Review B* **98** (2018), p. 085206.

[Ryd90] J. R. Rydberg. "On the Structure of the Line-Spectra of the Chemical Elements." *Philosophical Magazine* **5** (1890), pp. 331–337.

[Saf+05] M. Saffman and T. G. Walker. "Analysis of a quantum logic device based on dipole-dipole interactions of optically trapped Rydberg atoms." *Physical Review A* **72** (2005), p. 022347.

[Saf+10] M. Saffman, T. G. Walker, and K. Mølmer. "Quantum information with Rydberg atoms." *Reviews of Modern Physics* **82** (2010), pp. 2313–2363.

[Sch+12] R. Schwartz, N. Naka, F. Kieseling, and H. Stolz. "Dynamics of excitons in a potential trap at ultra-low temperatures: paraexcitons in Cu_2O." *New Journal of Physics* **14** (2012), p. 023054.

[Sch+16a] F. Schöne, S. O. Krüger, P. Grünwald, H. Stolz, S. Scheel, M. Aßmann, J. Heckötter, J. Thewes, D. Fröhlich, and M. Bayer. "Deviations of the exciton level spectrum in Cu_2O from the hydrogen series." *Physical Review B* **93** (2016), p. 075203.

[Sch+16b] F. Schöne, S. O. Krüger, P. Grünwald, M. Aßmann, J. Heckötter, J. Thewes, H. Stolz, D. Fröhlich, M. Bayer, and S. Scheel. "Coupled valence band dispersions and the quantum defect of excitons in Cu_2O." *Journal of Physics B: Atomic, Molecular and Optical Physics* **49** (2016), p. 134003.

[Sch+16c] F. Schweiner, J. Main, M. Feldmaier, G. Wunner, and C. Uihlein. "Impact of the valence band structure of Cu_2O on excitonic spectra." *Physical Review B* **93** (2016), p. 195203.

[Sch+16d] F. Schweiner, J. Main, and G. Wunner. "Linewidths in excitonic absorption spectra of cuprous oxide." *Physical Review B* **93** (2016), p. 085203.

[Sch+16e] F. Schweiner, J. Main, G. Wunner, and C. Uihlein. "K-dependent exchange interaction of the $1S$ orthoexciton in Cu_2O." *Physical Review B* **94** (2016), p. 115201.

[Sch+17a] F. Schöne, H. Stolz, and N. Naka. "Phonon-assisted absorption of excitons in Cu_2O." *Physical Review B* **96** (2017), p. 115207.

[Sch+17b] F. Schweiner, J. Main, G. Wunner, M. Freitag, J. Heckötter, C. Uihlein, M. Aßmann, D. Fröhlich, and M. Bayer. "Magnetoexcitons in cuprous oxide." *Physical Review B* **95** (2017), p. 035202.

[Sch+17c] F. Schweiner, J. Main, G. Wunner, and C. Uihlein. "Even exciton series in Cu_2O." *Physical Review B* **95** (2017), p. 195201.

[Sch18] S. Schröder. "Zwei-Farben-Pump-Probe Spektroskopie an Rydbergexzitonen." Bachelor's thesis. TU Dortmund, 2018.

[Sem+] D. Semkat, H. Fehske, and H. Stolz. "Quantum many-body effects on Rydberg excitons in cuprous oxide." *European Physical Journal Special Topics (submitted)* ().

[Sem+09] D. Semkat, F. Richter, D. Kremp, G. Manzke, W.-D. Kraeft, and K. Henneberger. "Ionization equilibrium in an excited semiconductor: Mott transition versus Bose-Einstein condensation." *Physical Review B* **80** (2009), p. 155201.

[Sem+19] D. Semkat, H. Fehske, and H. Stolz. "Influence of electron-hole plasma on Rydberg excitons in cuprous oxide." *Physical Review B* **100** (2019), p. 155204.

[Sha+77] J. Shah, M. Combescot, and A. H. Dayem. "Investigation of Exciton-Plasma Mott Transition in Si." *Physical Review Letters* **38** (1977), pp. 1497–1500.

[Sin+04] K. Singer, M. Reetz-Lamour, T. Amthor, L. G. Marcassa, and M. Weidemüller. "Suppression of Excitation and Spectral Broadening Induced by Interactions in a Cold Gas of Rydberg Atoms." *Physical Review Letters* **93** (2004), p. 163001.

[Sin+05] K. Singer, M. Reetz-Lamour, T. Amthor, S. Fölling, M. Tscherneck, and M. Weidemüller. "Spectroscopy of an ultracold Rydberg gas and signatures of Rydberg–Rydberg interactions." *Journal of Physics B: Atomic, Molecular and Optical Physics* **38** (2005), pp. 321–332.

[Sno+14] D. Snoke and G. M. Kavoulakis. "Bose–Einstein condensation of excitons in Cu_2O: progress over 30 years." *Reports on Progress in Physics* **77** (2014), p. 116501.

[Sto+12] H. Stolz, R. Schwartz, F. Kieseling, S. Som, M. Kaupsch, S. Sobkowiak, D. Semkat, N. Naka, T. Koch, and H. Fehske. "Condensation of excitons in Cu_2O at ultracold temperatures: experiment and theory." *New Journal of Physics* **14** (2012), p. 105007.

[Sto+18] H. Stolz, F. Schöne, and D. Semkat. "Interaction of Rydberg excitons in cuprous oxide with phonons and photons: optical linewidth and polariton effect." *New Journal of Physics* **20** (2018), p. 023019.

[Tak+18] M. Takahata and N. Naka. "Photoluminescence properties of the entire excitonic series in Cu_2O." *Physical Review B* **98** (2018), p. 195205.

[The+15] J. Thewes, J. Heckötter, T. Kazimierczuk, M. Aßmann, D. Fröhlich, M. Bayer, M. A. Semina, and M. M. Glazov. "Observation of High Angular Momentum Excitons in Cuprous Oxide." *Physical Review Letters* **115** (2015), p. 027402.

[The15] J. Thewes. "Hochangeregte Exziton-Zustände und Quantenchaos in Cu_2O." Master's thesis. TU Dortmund, 2015.

[Toy58] Y. Toyozawa. "Theory of Line-Shapes of the Exciton Absorption Bands." *Progress of Theoretical Physics* **20** (1958), pp. 53–81.

[Toy64] Y. Toyozawa. "Interband Effect of Lattice Vibrations in the Exciton Absorption Spectra." *Journal of Physics and Chemistry of Solids* **25** (1964), pp. 59–71.

[Uih+81] C. Uihlein, D. Fröhlich, and R. Kenklies. "Investigation of exciton fine structure in Cu_2O." *Physical Review B* **23** (1981), p. 2731.

[Urb+09] E. Urban, T. A. Johnson, T. Henage, L. Isenhower, D. D. Yavuz, T. G. Walker, and M. Saffman. "Observation of Rydberg blockade between two atoms." *Nature Physics* **5** (2009), pp. 110–114.

[Viñ+98] L. Viña, M. Potemski, and W. I. Wang. "Signatures of quantum chaos in the magneto-excitonic spectrum of quantum wells." *Physics-Uspekhi* **41** (1998), p. 153.

[Wal+18a] V. Walther, R. Johne, and T. Pohl. "Giant optical nonlinearities from Rydberg excitons in semiconductor microcavities." *Nature Communications* **9** (2018), p. 1309.

[Wal+18b] V. Walther, S. O. Krüger, S. Scheel, and T. Pohl. "Interactions between Rydberg excitons in Cu_2O." *Physical Review B* **98** (2018), p. 165201.

[Wan37] G. H. Wannier. "The Structure of Electronic Excitation Levels in Insulating Crystals." *Physical Review* **52** (1937), p. 191.

[Whi34] H. E. White. *Introduction to Atomic Spectra*. New York and London: McGraw-Hill Book Company, Inc., 1934.

[Zie+16] S. Zielińska-Raczyńska, D. Ziemkiewicz, and G. Czajkowski. "Electromagnetically Induced Transparency and slow light in media with Rydberg Excitons." *arXiv:1612.09170* (2016).

[Zim+78] R. Zimmermann, K. Kilimann, W. D. Kraeft, D. Kremp, and G. Röpke. "Dynamical Screening and Self-Energy of Excitons in the Electron–Hole Plasma." *physica status solidi (b)* **90** (1978), pp. 175–187.

[Zim88a] R. Zimmermann. "Nonlinear Optics and the Mott Transition in Semiconductors." *physica status solidi (b)* **146** (1988), pp. 371–384.

[Zim88b] R. Zimmermann. *Many-Particle Theory of Highly Excited Semiconductors*. Leipzig: BSB B. G. Teubner Verlagsgesellschaft, 1988.

List of publications

(1) J. Thewes, **J. Heckötter**, T. Kazimierczuk, M. Aßmann, D. Fröhlich, M. Bayer, M. A. Semina, and M. M. Glazov.
"Observation of High Angular Momentum Excitons in Cuprous Oxide."
Physical Review Letters **115** (2015), p. 027402.

(2) F. Schöne, S. O. Krüger, P. Grünwald, H. Stolz, S. Scheel, M. Aßmann, **J. Heckötter**, J. Thewes, D. Fröhlich, and M. Bayer.
"Deviations of the exciton level spectrum in Cu_2O from the hydrogen series."
Physical Review B **93** (2016), p. 075203.

(3) F. Schöne, S. O. Krüger, P. Grünwald, M. Aßmann, **J. Heckötter**, J. Thewes, H. Stolz, D. Fröhlich, M. Bayer, and S. Scheel.
"Coupled valence band dispersions and the quantum defect of excitons in Cu_2O."
Journal of Physics B: Atomic, Molecular and Optical Physics **49** (2016), p. 134003.

(4) P. Grünwald, M. Aßmann, **J. Heckötter**, D. Fröhlich, M. Bayer, H. Stolz, and S. Scheel.
"Signatures of Quantum Coherences in Rydberg Excitons."
Physical Review Letters **117** (2016), p. 133003.

(5) F. Schweiner, J. Main, G. Wunner, M. Freitag, **J. Heckötter**, C. Uihlein, M. Aßmann, D. Fröhlich, and M. Bayer.
"Magnetoexcitons in cuprous oxide."
Physical Review B **95** (2017), p. 035202.

(6) **J. Heckötter**, M. Freitag, D. Fröhlich, M. Aßmann, M. Bayer, M. A. Semina, and M. M. Glazov.
"High-resolution study of the yellow excitons in Cu_2O subject to an electric field."
Physical Review B **95** (2017), p. 035210.

(7) M. Freitag, **J. Heckötter**, M. Bayer, and M. Aßmann.
"Role of phonons in the quantum chaos of Rydberg excitons."
Physical Review B **95** (2017), p. 155204.

(8) **J. Heckötter**, M. Freitag, D. Fröhlich, M. Aßmann, M. Bayer, M. A. Semina, and M. M. Glazov.
"Scaling laws of Rydberg excitons."
Physical Review B **96** (2017), p. 125142.

(9) **J. Heckötter,** M. Freitag, D. Fröhlich, M. Aßmann, M. Bayer, M. A. Semina, and M. M. Glazov.
"Dissociation of excitons in Cu_2O by an electric field."
Physical Review B **98** (2018), p. 035150.

(10) **J. Heckötter**, M. Freitag, M. Aßmann, D. Fröhlich, M. Bayer, P. Grünwald, and S. Scheel.
"Critical Dependence of the Excitonic Absorption in Cuprous Oxide on Experimental Parameters."
Physics of the Solid State **60** (2018), pp. 1618–1624.

(11) **J. Heckötter**, M. Freitag, D. Fröhlich, M. Aßmann, M. Bayer, M. A. Semina, and M. M. Glazov.
"Influence of the Wavefunction Distribution on Exciton Dissociation in Electric Field."
Physics of the Solid State **60** (2018), pp. 1506–1509.

(12) **J. Heckötter**, D. Fröhlich, M. Aßmann, and M. Bayer.
"Influence of Magnetic Confinement on the Yellow Excitons in Cuprous Oxide Subject to an Electric Field."
Physics of the Solid State **60** (2018), pp. 1595–1599.

(13) **J. Heckötter**, J. Thewes, D. Fröhlich, M. Aßmann, and M. Bayer.
"Landau-Level Quantization of the Yellow Excitons in Cuprous Oxide."
Physics of the Solid State **60** (2018), pp. 1625–1628.

(14) P. Rommel, F. Schweiner, J. Main, **J. Heckötter**, M. Freitag, D. Fröhlich, K. Lehninger, M. Aßmann, and M. Bayer.
"Magneto-Stark effect of yellow excitons in cuprous oxide."
Physical Review B **98** (2018), p. 085206.

(15) **J. Heckötter**, M. Freitag, D. Fröhlich, M. Aßmann, M. Bayer, P. Grünwald, F. Schöne, D. Semkat, H. Stolz, and S. Scheel.
"Rydberg Excitons in the Presence of an Ultralow-Density Electron-Hole Plasma."
Physical Review Letters **121** (2018), p. 097401.

(16) **Heckötter**, D. Janas, R. Schwartz, M. Aßmann, and M. Bayer.
"Experimental limitation in extending the exciton series in Cu_2O towards higher principal quantum numbers."
Physical Review B **101** (2020), p. 235207.